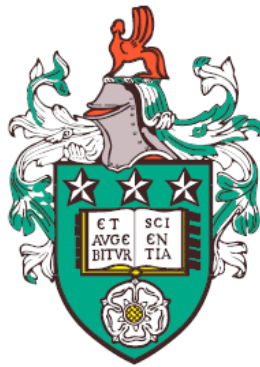


Light harvesting in low dimensional systems: application of driven Brownian ratchets in supported lipid bilayers for the creation of light harvesting mimics



Johannes Sebastian Roth
School of Physics and Astronomy

University of Leeds

Submitted in accordance with the requirements for the
degree of

Doctor of Philosophy

March 2015

Declaration

The candidate confirms that the work submitted is his own, except where work which has formed part of jointly authored publications has been included. The contribution of the candidate and the other authors to this work has been explicitly indicated below. The candidate confirms that appropriate credit has been given within the thesis where reference has been made to the work of others. Chapters 1, 3 and 5 are based on the results of previously published work jointly authored by the candidate (see the bibliography below). The atomic force microscopy experiments on one dimensional diffusion were carried out by Dr George Heath. Parts of the experiments on Brownian ratchets were carried out by Ying Zhang. Patterned electrodes were produced by Dr Peng Bao. The polymers used as supports for lipid bilayer formation were prepared by Nan Cheng and Dr Abdullah Alswieleh. This copy has been supplied on the understanding that it is copyright material and that no quotation from the thesis may be published without proper acknowledgement.

©2015 The University of Leeds and Johannes Sebastian Roth.

The right of Johannes Sebastian Roth to be identified as Author of this work has been asserted by him in accordance with the Copyright, Designs and Patents Act 1988.

Bibliography

(Bao *et al.* 2012) P. Bao, M.R. Cheetham, J.S. Roth, A.C. Blakeston, R.J. Bushby, S.D. Evans, On-chip alternating current electrophoresis in supported lipid bilayer membranes, *Analytical Chemistry*, **84**, pp. 10702-10707 (2012).

(Taylor *et al.* 2014) R.W. Taylor, F. Benz, D.O. Sigle, R.W. Bowman, P. Bao, J.S. Roth, G.R. Heath, S.D. Evans, J.J. Baumberg, Watching individual molecules flex within lipid membranes using SERS, *Scientific Reports*, **4**, 5940 (2014).

(Heath *et al.* 2014) G.R. Heath, J.S. Roth, S.D. Connell, S.D. Evans, Diffusion in low-dimensional lipid membranes, *Nano Letters*, **14**(10), pp. 5984-5988 (2014).

(Roth *et al.* 2014) J.S. Roth, M.R. Cheetham, S.D. Evans, Transport and concentration of charged molecules in a lipid membrane, *Proceedings of the 2014 COMSOL Conference*, (2014).

(Wang *et al.* 2015) L. Wang, J.S. Roth, X. Han, S.D. Evans, Photosynthetic proteins in supported lipid bilayers: towards a biokleptic approach for energy capture, *Small*, DOI: 10.1002/sml.201403469 (2015).

(Blakeston *et al.* 2015) A.C. Blakeston, A. Alswieleh, G.R. Heath, J.S. Roth, P. Bao, N. Cheng, S.P. Armes, G.J. Leggett, R.J. Bushby, S.D. Evans, New poly(amino acid methacrylate) brush supports the formation of well-defined lipid membranes, *Langmuir*, DOI: 10.1021/la504163s (2015)

(Roth *et al.* 2015) J.S. Roth, Y. Zhang, P. Bao, M.R. Cheetham, X. Han, S.D. Evans, Optimization of Brownian ratchets for the manipulation of charged components within supported lipid bilayers, *Submitted to Applied Physics Letters*, 2015

This thesis is dedicated to my family.

Acknowledgements

This work was made possible by a DTG studentship from the Engineering and Physical Sciences Research Council to myself. This research would not have been possible without the guidance and support of my supervisor Stephen Evans. His creativity and feedback have driven this work forward. I would also like to thank Richard Bushby for his continuous support and for helping me with his seemingly indefinite knowledge of chemistry. His curiosity and interest in the subject have enhanced my understanding and the quality of this project.

I have also received support from the members of the Low Dimension Chemistry Group based in Sheffield and Leeds. Particular thanks go to Matthew Cheetham for introducing me to lipid bilayers and being extremely supportive in my first months and being a constant source of intelligent input towards my work. Peng Bao has supported this work in various ways, including working late nights and early mornings. Benjamin Johnson has been invaluable because of his continuous efforts to make the experimental work in our group possible.

Personally, I would like to thank the members of the Molecular and Nanoscale Physics Group, both past and present, and the wider Physics Department that have made the last years even more enjoyable. Without the support of this group of people, this work would not have been possible.

In addition to the people mentioned before, I would also like to thank Sandra and Maddie for the infinite support and for keeping me sane in the last years.

Abstract

Supported lipid bilayers are a well known model system for the cell membrane. They allow for the investigation of the membrane in a controlled environment. The solid supported bilayer is accessible through the surface it is formed on and allows for different experimental techniques to be applied. This thesis presents work on free diffusion in the membrane and electrophoretically driven transport and concentration of charged membrane components. In addition to that, novel supports for the support of membrane proteins have been investigated and surface enhanced Raman spectroscopy is presented as a label-free method for the detection of membrane components.

Brownian ratchets have been used for applications such as molecular sorting with and without the use of lipid bilayers. So far the work has mainly been focussed on their use without a thorough investigation of their properties and the parameters influencing their efficiency. Here, the size of the ratchets and time parameters are varied in experiment and calculation and their role in the ratcheting process is discussed. The efficiency of the ratchets can be significantly reduced when the parameters are chosen in an optimal manner.

The use of electrophoresis in lipid bilayers for the concentration and separation of membrane components has focussed on using two electrodes in simple patterns such as squares or lines. This is expanded here on more complex patterns which also allow for the retention of charged material in trapping regions. The pattern was then used to demonstrate the ability to determine binding coefficients in the trapping regions even for membrane components with a low initial concentration or low fluorescence quantum yield. More complex electrode systems using four patterned electrodes are also presented which allow for the application of electric fields in two dimensions where the strength and orientation of the field can be chosen almost arbitrarily.

Polymer supports have the ability to support lipid bilayers with membrane proteins which exhibit significant extramembranous domains. Two novel supports are investigated here and different lipid bilayer formation routes are explored. To allow for label-free detection of lipids, peptides or proteins within the membrane, surface enhanced Raman spectroscopy is used. The ability of this method to distinguish between different lipids and to detect peptides within the membrane is shown, as well.

Contents

Declaration	ii
Dedication	iv
Acknowledgements	v
Abstract	vi
1 Introduction	1
1.1 Photosynthesis	1
1.1.1 Generation of Chemical Energy from Light	2
1.1.2 Rhodopsin	4
1.1.3 Light Harvesting Complexes	6
1.2 The Cell and Its Membrane	7
1.2.1 Phospholipids	8
1.2.2 Self-Assembly into Micelles and Vesicles	8
1.2.3 Aggregates of Amphiphilic Molecules	11
1.2.4 Formation of Lipid Bilayers	12
1.2.5 solid supported lipid bilayer (SLB) Formation from Vesicles	14
1.2.6 Formation of Lipid Bilayers on different substrates	16
1.3 SLB manipulation	17
1.3.1 Patterning of SLBs	18
1.3.2 SLBs Electrophoresis	20
1.4 Summary, Aims and Outline	21
2 Methods	33
2.1 Formation of Lipid Bilayers	33
2.2 Patterning of SLBs	36
2.3 Electrophoresis	37
2.3.1 Double Layer Formation	42
2.4 Impedance & Cyclic Voltammetry	44
2.5 Finite Element Analysis	47
2.6 Fluorescence Microscopy	49
2.6.1 Theoretical Principles	49
2.6.2 Experimental Details	50
2.6.3 Fluorescence Recovery after Photobleaching	51
2.7 Dark Field Microscopy	54
2.8 Plasmonics	56

2.8.1	Theoretical Background	56
2.8.2	Raman/SERS	57
2.8.3	Applications	62
2.8.4	Single Molecule Detection	63
2.8.5	Probing Lipid Membranes	63
2.9	Experimental Procedures	65
2.9.1	Surface Preparation	65
2.9.2	Vesicle Preparation	66
2.9.3	Surface Patterning	68
2.9.4	Bilayer formation and Electrophoresis Experiments	69
2.9.5	Surface Modification	70
2.9.6	Raman Experiments	71
2.9.7	Finite Element Calculations	72
3	Diffusion in Lipid Membranes	83
3.1	Measuring Diffusion in a Lipid Bilayer	83
3.1.1	Effect of the Bleach Time	84
3.1.2	Experimental Effect of Bleaching Time and Spot Size on Diffusion Coefficient	89
3.1.3	Variation of Dye Molecules	91
3.2	Special Cases of Diffusion in a Membrane	93
3.2.1	Low Dimensional Diffusion	94
3.2.2	Reduced Mobility	97
3.3	Directed Brownian Motion	103
3.3.1	Discrete Diffusion	103
3.3.2	Continuous Diffusion	104
3.4	Brownian Ratchets & Parrondo's Paradox	107
3.4.1	Brownian Ratchets	107
3.4.2	Parrondo's Paradox	109
3.5	Optimisation of Brownian Ratchets	115
3.5.1	Transport in a Brownian Ratchet	116
3.5.2	Prediction of the Ratchet Behaviour	118
3.5.3	Influence of Ratchet Parameters	128
3.6	Conclusion	143
4	Novel Electrodes and Patterns for the Concentration of Membrane Com- ponents	149
4.1	A Novel DC Pattern	150
4.1.1	Development and Calculations	150
4.1.2	Experimental Results	156
4.1.3	Application for the Determination of Binding Coefficients	164
4.2	Patterned Electrodes	177
4.2.1	Miniaturisation	177
4.2.2	New Electrode Material	183
4.3	Two-Dimensional Electric Fields	185
4.3.1	FEA Calculations	187
4.3.2	Experimental Realisation	191
4.4	Conclusion	194

5	Read-out Methods for Light Harvesting Proteins in Lipid Bilayers	199
5.1	Novel Polymeric Supports For Lipid Bilayers	199
5.1.1	PMPC	200
5.1.2	PCysMA	215
5.1.3	Polyethylene Glycol	220
5.2	SERS as a Read-Out Method	222
5.2.1	Nanopatterned Surfaces	222
5.2.2	SERS using Nanoparticles	226
5.2.3	Cyclic Voltammetry with Nanoparticles	231
5.3	Towards Light Harvesting Proteins in Lipid Bilayers	235
5.3.1	Light Harvesting Systems	235
5.3.2	Cytochrome bc1	238
5.4	Conclusion	241
6	Conclusions and Future Work	247
6.1	Concluding Remarks	247
6.1.1	Diffusion in Membranes & Brownian Ratchets	247
6.1.2	Novel Electrodes & Patterns	248
6.1.3	Polymer Supports	249
6.1.4	Read out Methods	249
6.1.5	Light Harvesting Proteins	250
6.2	Future Work	251

List of Figures

1.1	Schematic of the photosynthetic process in plants and bacteria . . .	3
1.2	Structure of adenosine triphosphate (ATP) with adenosine diphosphate (ADP) being identical to this structure without the leftmost phosphate group.	3
1.3	Absorbance spectrum of the photosynthetic membrane	4
1.4	Structures of different rhodopsins.	5
1.5	Chemical structure of retinal.	5
1.6	Structure of the RC-LH1-PufX from <i>Rhodobacter sphaeroides</i>	6
1.7	Structure of 1-palmitoyl-2-oleoylphosphatidylcholine (POPC).	8
1.8	Different structures formed by lipids	13
1.9	Schematic of electrophoresis in a lipid bilayer.	20
2.1	Vesicle adsorption to a solid support and two different paths of vesicle rupture for bilayer formation.	35
2.2	Principle of microcontact printing (μ CP)	37
2.3	Fibronectin lines produced by μ CP as barriers to electrophoretic motion of charged lipids.	40
2.4	Schematic of an impedance set-up showing the tethered SLB on a conductive (Au) support and the equivalent circuit of the membrane and the solution.	46
2.5	Jablonski Diagram of a simple fluorescence molecule.	49
2.6	Schematic of an epifluorescence microscope.	51
2.7	Schematic of a fluorescence recovery after photobleaching (FRAP) experiment on a molecular level and the observed fluorescence images.	52
2.8	Dark field microscopy set-up, the light which is being scattered off the sample is being used for imaging.	55
2.9	Principle of Raman spectroscopy showing the three different scattering mechanisms possible.	57
2.10	Vibrations possible for a water molecule.	58
2.11	Nanoparticle on a mirror geometry shown by a gold nanoparticle (NP) on top of an hybrid lipid membrane (HLM).	61
3.1	Experimental remaining fluorescence intensity for varying bleaching times.	85
3.2	Simulation layout for bleaching calculations.	86
3.3	Simulated bleaching recovery curves.	86
3.4	Correction factor c for different bleach times.	88

3.5	Diffusion coefficient D calculated from simulation data for varied bleaching times.	88
3.6	Experimentally obtained diffusion coefficients D for varied bleach spot sizes.	90
3.7	Experimental influence of the bleaching time on the measured diffusion coefficient D	90
3.8	Experimentally observed influence of the bleach spot size and the bleaching time on the diffusion coefficient D	91
3.9	Diffusion coefficient for a variation of dye molecules determined by two analysis methods.	92
3.10	Simulated FRAP images in a nano line pattern.	96
3.11	Variation of the apparent diffusion coefficient with the variation of the line width in SLBs.	96
3.12	Reduced mobility as seen in a previous experiment.	98
3.13	Pattern for the investigation of the reduced mobility	99
3.14	Experimental images and line profile of an area of reduced mobility in a trap device.	100
3.15	No reduced mobility is seen, when using nitrobenzoxadiazole (NBD) 1,2-dioleoyl-sn-glycero-3-phosphoethanolamine (DOPE) as a dye in the bilayer instead of Texas Red 1,2-dihexadecyl-sn-glycero-3-phosphoethanolamine (TxRed).	100
3.16	Fluorescence image of NBD DHPE showing no reduced mobility.	100
3.17	Line profiles comparing reduced mobility for different dyes in an SLB.	101
3.18	Line profile of the fluorescence intensity used for the Gaussian fitting to determine the movement speed of different dyes.	102
3.19	Brownian ratchet as proposed by Smoluchowski and discussed by Feynman.	107
3.20	Average capital when games A and B are played individually and combined.	110
3.21	Comparison of a DC and an AC approach for the transport of charged material in an SLB.	111
3.22	Principle of a Brownian ratchet used here.	112
3.23	A flashing ratchet moving particles towards the right. The different particles are diffusing freely while the ratchet is not activated and move into the bottom of the teeth while the ratchet is active.	113
3.24	Gaussian distribution of material in a ratchet overlaid with a Brownian ratchet pattern.	114
3.25	Calculation of the transport in Brownian ratchets based on a Gaussian distribution in each ratchet.	115
3.26	Patterned used for the calculation of transport in a patterned SLB.	116
3.27	Applied electric field in a Brownian ratchet as a function of time normalised to the period time t	117
3.28	Different states of a Brownian ratchet, showing how transport is achieved from an initial equal distribution to the final state, where a higher concentration on the right is achieved.	120
3.29	Calculated comparison of the effect of sine, sawtooth, triangular and rectangular shaped potentials on a Brownian ratchet.	121

3.30	Calculated transporting behaviour of a Brownian ratchet from finite element analysis (FEA) shown for the different ratchet regions.	121
3.31	Total flux of charged molecules in a ratchet pattern when the field is applied such that the charges move into the trapping region initially.	123
3.32	A fluorescence image of a Brownian ratchet realised as a lipid bilayer and the position of the line profile shown in red (left). Calculated values from FEA for the line profile at different times (right).	124
3.33	Fluorescence images of a Brownian ratchet showing the different states of the ratchet in experiment. The fluorescence is from the negatively charged TxRed in the membrane.	125
3.34	Two opposing ratchets showing the principle of Brownian ratcheting. The transport has occurred in different directions showing that it is caused by the ratchets. The length of an individual ratchet is 135 μm	125
3.35	Comparison of experimental results and calculated predictions from FEA for different teeth of the ratchet.	126
3.36	Comparison of the final relative increase in the different teeth in both, experiment and simulation.	127
3.37	Comparison of the normalised fluorescence intensity (for the experimental data) and the normalised concentration (for the calculated data) of a line profile just above the ratchet.	128
3.38	The design of a Brownian ratchet with the last region in which the transport is measured highlighted in red.	129
3.39	Final images of the concentration profile after 26 cycles for varied ratchet lengths.	131
3.40	Normalised relative concentration in the last tooth of ratchets of varying length over 100 cycles. For the calculations only the number of teeth was changed while all other parameters were kept constant.	132
3.41	Relative concentration in the last tooth of a Brownian ratchet achieved for different values of the asymmetry parameter λ	134
3.42	Comparison between experimental and simulation data for varied λ	135
3.43	Calculated concentration distribution at the final stage of the field reversal for a variation of the time constant τ at constant ratchet height h	138
3.44	Calculated increase of the concentration in the final ratchet with varying h'	139
3.45	Variation of h' for different values of h obtained from FEA	140
3.46	Comparison between experimental and calculated results for a variation in h' . The grey and light red points represent the individual points for the calculation and the lines are guide to the eye.	141

3.47	Comparison of the ratcheting achieved experimentally when the ratchet is perpendicular to the applied electric field (left) and when it is rotated by 30° (right). The bottom shows the relative concentration over time.	142
3.48	Combined tilted ratchet, showing how transport can be achieved with a double tilted ratchet.	143
4.1	Triangular DC pattern with concentration into the tip region. . . .	151
4.2	Several triangular concentration regions with different sized reservoirs and the concentration over time in the different triangular regions.	152
4.3	Two double triangle patterns and their respective concentration and free diffusion behaviour.	153
4.4	Double triangle pattern with an added barrier to increase retention time and concentration graph.	153
4.5	Initial state, concentration, final state and free diffusion after switch off of the electric field in a DC trap pattern.	155
4.6	Concentration and diffusion profile for the trap shown in figure 4.5 over time.	156
4.7	Optimisation of the pattern from the initial state to the final pattern. Images on the right show the effect of free diffusion after the field has been switched off for 1 h.	157
4.8	Fluorescence images for a DC trap pattern before the concentration of charged molecules and after.	158
4.9	Line profiles of the fluorescence signal in all the sub-patterns after the concentration took place.	159
4.10	Expected intensity profile of fluorescence for different interaction parameters r_0	160
4.11	Experimentally obtained concentration I_Q^c over time in the different regions marked 1-6 in figure 4.8b.	162
4.12	Behaviour of charged material in the trap region after the field has been switched off at different times.	163
4.13	Principle of cholesterol modified deoxyribonucleic acid (DNA) anchored in an SLB to which DNA is attached from solution. . . .	166
4.14	Fluorescence images from a FRAP experiment where fluorescently labelled DNA was bound to SLB anchored DNA strands and the corresponding recovery curve.	167
4.15	Fluorescence images obtained for different DNA concentrations in solution and the binding curve obtained.	168
4.16	Fluorescence image of a pattern used for the determination of binding constants, including a single, large concentrator and a parallelised pattern with multiple concentrators.	171
4.17	boron-dipyrromethene (BODIPY) labelled vancomycin bound to a lipid II containing SLB in which the charged bilayer components were moved into the trapping regions.	172
4.18	Binding curve of vancomycin binding to lipid II in an SLB.	173
4.19	Overlap of the fluorescence signal obtained from TxRed and fluorescently labelled vancomycin bound to lipid II in the SLB.	174

4.20	Binding curve for varied concentrations of streptavidin in solution.	174
4.21	Fluorescence image and binding curve obtained for streptavidin binding to a biotinylated SLB where the binding curve was obtained from a single image.	176
4.22	Left: Electric field (x component) caused by 10 V applied to patterned electrodes on a glass surface in an aqueous environment. Right: line profile of the electric field 10 nm above the surface of the cover slip	179
4.23	Relative increase in concentration/fluorescence intensity in the central region of a trapping device determined by calculation and experiment. (Experimental data courtesy of Peng Bao)	180
4.24	Comparison of the fluorescence images obtained for macroscopic and microscopic electrodes after the same concentration time. . .	181
4.25	Fluorescence images taken at different times showing the achieved transport in a concentration pattern between microscopic electrodes.	182
4.26	Chemical structure of the two isomers in PEDOT:PSS	183
4.27	Schematic of the use of a PEDOT:PSS electrode patterned directly on a glass cover slip.	184
4.28	Concentration of TxRed in a fibronectin pattern using poly(3,4-ethylenedioxythiophene) polystyrene sulfonate (PEDOT:PSS) electrodes.	185
4.29	Schematic for the electrode patterning to obtain two dimensional electric fields.	186
4.30	Calculation of the electric field caused by four electrodes close to each other.	188
4.31	Relative increase of charged material in the central region of a spiral after 10 h experimental time for different period times (shown in seconds) plotted against phase shift.	189
4.32	Relative final increase in the centre of a spiral pattern plotted against the period of the electric field for different overall experimental times.	190
4.33	Experimental realisation of the spiral pattern.	191
4.34	Relative increase in concentration of the TxRed fluorophore in the central region of a spiral pattern.	192
4.35	Two spirals connected to each other. The bottom spiral is wound up clockwise, the top spiral counter clockwise. The top spirals releases material into the bottom spiral.	193
5.1	Structure of PMPC	200
5.2	Results of vesicle fusion experiments using POPC only in vesicles on a poly(2-methacryloyloxyethyl phosphorylcholine) (PMPC) brush.	202
5.3	Comparison of the results of using the charged lipids 1,2-dioleoyl-sn-glycero-3-phospho-(1'-rac-glycerol) (DOPG) and 1,2-dioleoyl-3-trimethylammonium-propane (DOTAP) in combination with PMPC supports.	203
5.4	Comparison of the results when adding either Ca^{2+} or Cl^-	203

5.5	Patches of an SLB on a PMPC support after a single freeze thaw cycle.	205
5.6	Fluorescence images immediately after photobleaching and five minutes after bleaching for different numbers of freeze-thaw cycles.	206
5.7	Growth process of an SLB produced by freeze thaw cycles of vesicle solution on PMPC.	208
5.8	Spin coating of fluorescently labelled lipids onto a PMPC support.	209
5.9	Defects obtained when rehydrating lipids adsorbed onto PMPC using spin coating.	210
5.10	Fluorescence images from a FRAP experiment on a spin coated, rehydrated lipid layer on PMPC.	211
5.11	Lipid bilayer on PMPC formed by rehydration using moisture from the atmosphere.	211
5.12	Fully rehydrated SLB on a PMPC support. The FRAP experiment showed almost full recovery and the bilayer showed good mobility.	212
5.13	Bilayer patches formed using DHPC-C6 and the recovery curve of the associated FRAP experiment	214
5.14	Zoom in and overview of SLB formation on a PMPC support. . .	216
5.15	Structure of poly(cysteine methacrylate) (PCysMA), which was used as a polymer support.	217
5.16	Formation of an SLB on a PCysMA surface using elevated temperature and the recovery graph of a FRAP experiment.	218
5.17	Heating of PCysMA with vesicles investigated using electrochemical impedance spectroscopy (EIS) for three individual experiments.	219
5.18	Impedance spectrum obtained for the detergent removal method on PCysMA.	220
5.19	Different conditions of a polyethylene glycol (PEG) supported bilayer: before (left column) and after (right column) exposure to air. The images from FRAP experiments and their respective recovery curves are shown.	221
5.20	Microscope image and schematic of the gold nanodot pattern used.	223
5.21	An SLB was formed on a nanodot pattern with the corresponding FRAP recovery curve.	224
5.22	surface enhanced Raman scattering (SERS) data from a POPC SLB formed around gold nanoposts and nanobars on a silicon dioxide substrate.	225
5.23	Raman spectra of nanodots surrounded by lipid bilayers with varying diameters of the nanodots.	226
5.24	Schematic of the nanoparticle on a mirror arrangement with an HLM in the hot spot region.	227
5.25	Dark field image of nanoparticles on an HLM and the scattering spectra obtained from the nanoparticles circled in the dark field image.	228
5.26	SERS spectra obtained from an HLM consisting of DOTAP and POPC from different nanoparticles on the HLM.	229
5.27	SERS spectra obtained from an HLM consisting of deuterated lipids.	230

5.28	SERS spectra of HLMs containing different membrane components, gramicidin and 1-palmitoyl-2-(10,12-tricosadiynoyl)-sn-glycero-3-phosphocholine (DiPC). The bilayer was formed from POPC with 2 mol% DiPC. Gramicidin was added from solution after the formation of the SLB.	231
5.29	Nanoparticle enhanced cyclic voltammetry (CV) experiments on bilayers and bilayers containing ubiquinone Q10 (UQ).	232
5.30	Equivalent circuit used for fits and three different configuration a nanoparticle can take on or in cholesterol tethered SLBs.	233
5.31	Impedance spectra of an HLM with 80 nm gold NPs attached to the surface before and after taking CV data.	233
5.32	Impedance spectra of an SLB with 80 nm gold NPs attached to the surface before the CV measurements, 5 min after and 30 min after the CV measurements.	234
5.33	UV-Vis spectrum of light harvesting complex II (LH2) in the n-Dodecyl β -D-maltoside (DDM) containing solution as received and after dialysis in different solutions containing either DDM or octyle glucoside (OG).	236
5.34	Raman spectra of the bulk vesicle solution containing vesicles from <i>Rhodobacter sphaeroides</i> and POPC, the surface region with nanodots and the surface without nanodots.	237
5.35	Overlay of two fluorescence images of a TxRed labelled SLB with YFP-tagged RCLH1 incorporated into the membrane.	239
5.36	Dark field image of gold NPs with 5 nm diameter in solution.	239
5.37	Cytochrome bc1 labelled with 5 nm gold NPs in solution as seen under a dark field microscope.	240
5.38	Cytochrome bc1 incorporated into SLBs observed by dark field microscopy.	241

List of Tables

3.1	Distance travelled by different dye-lipid combinations after three minutes of field reversal.	102
3.2	Parameters used for the simulation and the experiment, unless stated otherwise. A schematic overview of the parameters is shown in figure 3.38.	117
3.3	Table of the parameters used for the variation of λ	133
5.1	Assignment of some of the bonds seen in the SERS spectrum. . .	225
5.2	Relative peak height of the Raman peaks seen at 1100 cm^{-1} and 1400 cm^{-1}	226
5.3	Main Raman peaks seen in figure 5.26 and their assignment. . . .	230
5.4	Resistances and capacitances obtained from the fits to the data shown in figure 5.31 and figure 5.32.	235

List of Abbreviations

AFM	atomic force microscopy
ADP	adenosine diphosphate
ATP	adenosine triphosphate
ATPase	ATP synthase
ATRP	atom-transfer radical-polymerisation
BLM	black lipid membrane
BODIPY	boron-dipyrromethene
CCD	charge coupled device
COMSOL	COMSOL® Multiphysics
D291	4-(4-(didecylamino)styryl)-n-methylpyridinium iodide
DHPC-C6	1,2-hexanoyl-sn-glycero-3-phosphocholine
CMC	critical micelle concentration
CPE	constant phase element
CV	cyclic voltammetry
DDM	n-Dodecyl β -D-maltoside
DHPE	1,2-dihexadecyl-sn-glycero-3-phosphoethanolamine
DiPC	1-palmitoyl-2-(10,12-tricosadiynoyl)-sn-glycero-3-phosphocholine
DNA	deoxyribonucleic acid
DOPC	1,2-dioleoyl-sn-glycero-3-phosphocholine
DOPE	1,2-dioleoyl-sn-glycero-3-phosphoethanolamine
DOPG	1,2-dioleoyl-sn-glycero-3-phospho-(1'-rac-glycerol)
DOPS	1,2-dioleoyl-sn-glycero-3-phospho-L-serine
DOTAP	1,2-dioleoyl-3-trimethylammonium-propane
DPPC	1,2-dipalmitoyl- sn-glycero-3-phosphocholine
DPN	dip pen nanolithography
EIS	electrochemical impedance spectroscopy

FEA finite element analysis

FEM finite element method

FITC fluorescein isothiocyanate

FRAP fluorescence recovery after photobleaching

FWHM full-width-half-maximum

HLM hybrid lipid membrane

ITO indium tin oxide

LB Langmuir-Blodgett

LB-LS Langmuir-Blodgett, Langmuir-Schäfer

LH light harvesting protein

LH1 light harvesting complex I

LH2 light harvesting complex II

LS Langmuir-Schäfer

LSP localised surface plasmon

MLV multi-lamellar vesicle

NBD nitrobenzoxadiazole

NP nanoparticle

ODT 1-octadecanethiol

OG octyle glucoside

PBS phosphate-buffered saline

PCysMA poly(cysteine methacrylate)

PDMS polydimethylsiloxane

PEDOT:PSS poly(3,4-ethylenedioxythiophene) polystyrene sulfonate

PEG polyethylene glycol

PMPC poly(2-methacryloyloxyethyl phosphorylcholine)

POPC 1-palmitoyl-2-oleoylphosphatidylcholine

PS photo system

QCM-D quartz crystal microbalance with dissipation

RC reaction centre

ROI region of interest

SAM self-assembled monolayer

SER surface enhanced Raman

SERS surface enhanced Raman scattering

SLB solid supported lipid bilayer

SPR surface plasmon resonance

SUV small unilamellar vesicle

TLB tethered lipid bilayer

TxRed Texas Red 1,2-dihexadecyl-sn-glycero-3-phosphoethanolamine

μCP microcontact printing

UQ ubiquinone Q10

Chapter 1

Introduction

The sun constantly emits energy and sends a portion of it towards earth. The total amount of energy arriving on earth's surface is around 23 PW (Smil, 1991). A small portion of this large amount of energy is used by plants and bacteria in photosynthesis. The total amount of the solar energy used in these biological processes amounts to around 120 TW (Field, 1998). This is much more than the energy demand of the population of the earth which is currently around 15 TW (IEA, 2010). Therefore, using solar energy can be a way to reduce the current dependency on fossil fuels or even become totally independent from non-renewable energy sources. Despite this still being a challenge, developing new biokleptic methods is a very promising approach, since a variety of methods to use solar energy with a high efficiency have evolved in nature.

1.1 Photosynthesis

Living organisms have found many ways of generating energy in their natural environments. Apart from the consumption of food or the exothermic conversion of oxygen and carbon into carbon dioxide, another possible way is to convert light into chemical energy. This chemical energy is then stored and used at a later point by the organism. One of the most important properties of the light harvesting proteins in these organisms is that the conversion of light into excited

electronic states has a quantum efficiency close to unity (Fleming et al., 2012; Hogewoning et al., 2012). Compared to silicon based solar cells, which have doubled their efficiency in the last 40 years to the current world record of 44.7 % efficiency for four junction solar cells (Dimroth et al., 2014), the proteins involved in light harvesting are much more efficient. This renders them of high interest for future use in artificial devices for energy generation and storage and opens up a variety of research questions in order to make these proteins usable on a large scale.

Even the very first life-forms on earth developed the ability to convert light into energy usable by their organism (Blankenship, 2010). The first form of photosynthesis occurred in cyanobacteria and from there on the mechanism has evolved into different forms which we see today. It is even suggested that the light harvesting as it exists today in eukaryotes appeared through endosymbiosis. Despite the fact that the evolutionary path from the cyanobacteria to the current form of photosynthesis in the organisms which have light harvesting proteins is still under debate (Bjorn and Govindjee, 2009), the conversion process from light to chemical energy is well understood and has been studied in great detail.

1.1.1 Generation of Chemical Energy from Light

Plants and bacteria have evolved the ability to generate energy for themselves by converting light into chemical energy, mostly via the synthesis of adenosine triphosphate (ATP) (see figure 1.2). This process can be achieved in different ways and there are different proteins in different organisms. A basic schematic of a cell using light to generate glucose is shown in figure 1.1. The solar energy is harvested by light harvesting proteins (LHs) or by photo systems (PSs) and is used to convert adenosine diphosphate (ADP) into ATP by ATP synthase (ATPase). The ATP is then used in the Calvin cycle to produce glucose, which can then be used in other parts of the organism. The systems with the fewest components consist of two proteins: proteorhodopsin, which uses the incoming

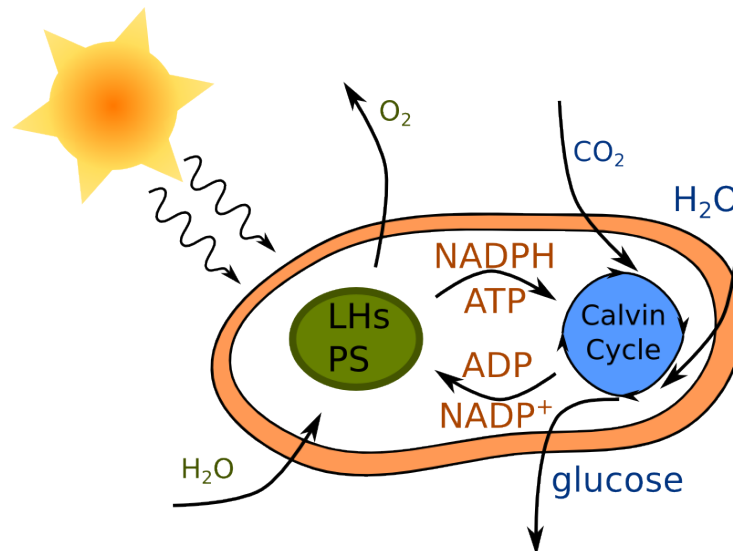


Figure 1.1: Schematic of the photosynthetic process as it happens in plants or in bacteria. Light harvesting systems and photosystems (green) capture light and convert ADP to ATP which is then used in the Calvin cycle (blue) to produce glucose for the organism. This process also consumes H_2O and CO_2 while O_2 is a side product.

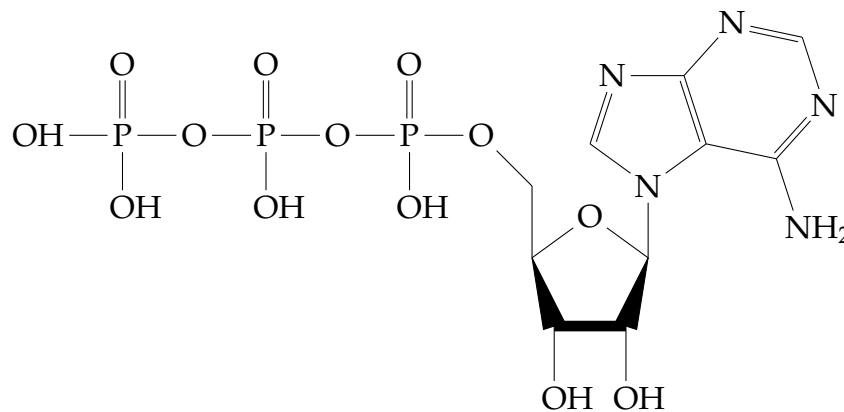


Figure 1.2: Structure of ATP with ADP being identical to this structure without the leftmost phosphate group.

light to generate a proton gradient across the cell membrane which is then being used by a second protein, ATPase, which uses the proton gradient to convert ADP to ATP.

Multiple protein systems also occur in nature. These exhibit a more complex mechanism of light capture and gradient formation. One example is present in *Rhodobacter sphaeroides*. Here, the incoming light is captured by LHs, which convert the light into excited electronic states. This process is enhanced by the reaction centres (RCs) allowing the organism to capture a larger portion

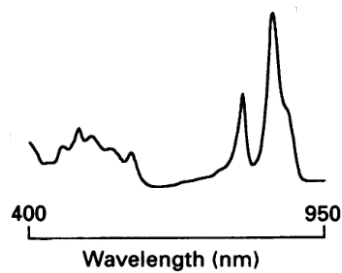


Figure 1.3: Absorbance of the photosynthetic membrane of the wild type *Rhodospirillum rubrum* showing the weak absorption in the blue/green part of the spectrum and two strong peaks in the red/infrared region. Taken from (Lang et al., 1994).

of the solar spectrum. The absorption spectrum of the whole photosynthetic membrane combining the absorption of all proteins within the membrane is seen in figure 1.3. The spectrum shows that the LHs have their main absorption in the red to infrared region of the electromagnetic spectrum, but also absorb in the lower wavelength regions of the electromagnetic spectrum. The only part of the spectrum which is not covered is the green to yellow region.

1.1.2 Rhodopsin

As discussed before, the simplest system consists of rhodopsin and ATPase to generate chemical energy from light. Rhodopsin, belonging to the class of G-protein coupled receptors (GPCRs), is one of the best characterised light sensitive proteins. It was discovered in 1876 by Boll (Broda, 1941) and has since then been extensively studied (Alves et al., 2005; Heyse et al., 1998; Subramaniam et al., 2005). Rhodopsin itself is a light activated protein which is best known for its activity in the eye. Initial work focussed on the investigation of rhodopsin in native membranes (Fung and Hubbell, 1978; Hong and Hubbell, 1972; Poo and Cone, 1974; Rudzki and Peters, 1984) while later it was more commonly reconstituted into artificial membranes such as black lipid membranes (BLMs) (Brown, 1994; Jastrzebska et al., 2011), solid supported lipid bilayers (SLBs) (Subramaniam et al., 2005, 2008) or polymer cushioned/tethered membranes (Heyse et al., 1998; Naumann et al., 1999).

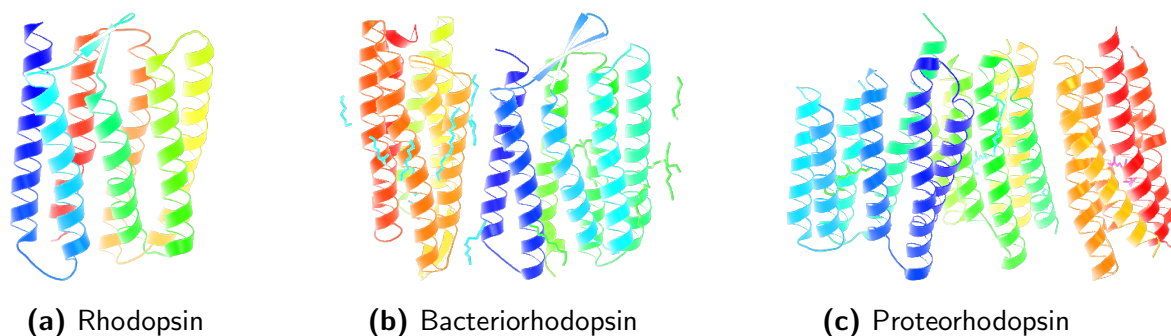


Figure 1.4: Structures of different rhodopsins. The respective PDB codes are 1JGJ, 4HYX, 4JQ6.

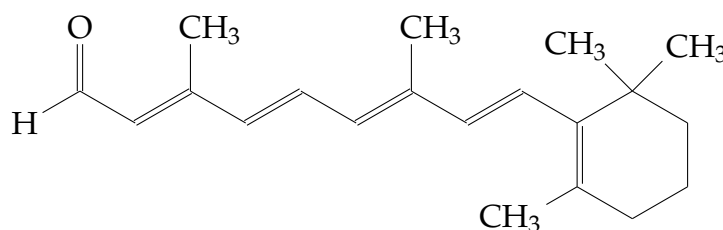


Figure 1.5: Chemical structure of retinal.

Rhodopsins are an important example for light harvesting proteins; they are part of the family of retinal (see figure 1.5) binding proteins which all use the retinal as the chromophore. Bacteriorhodopsin and proteorhodopsin belong to the same family and work as light driven proton pumps in some *archae*. Proteorhodopsin was first discovered in 2000 (Béja et al., 2000) in oceanic bacteria. In both, proteorhodopsin and bacteriorhodopsin the retinal is bound to the protein via a Schiff base. Several models have been proposed for the complete photocycle of proteorhodopsin (Dioumaev et al., 2002; Krebs et al., 2002; Martinez et al., 2007). The structure of the different types of rhodopsins are shown in figure 1.4.

Although it was shown that the charge on proteorhodopsin can be used to directionally insert the protein into vesicles (Tunuguntla et al., 2013), there is a lack of comparable work for proteorhodopsin in SLBs. This is probably due to the fact that, in order to achieve effective proton pumping, the orientation, which can be achieved in the proteoliposomes, has to be maintained when forming SLBs. As is shown in section 2.1, this can be a challenging task and the way in which a vesicle unravels to form a lipid bilayer is not yet fully understood.

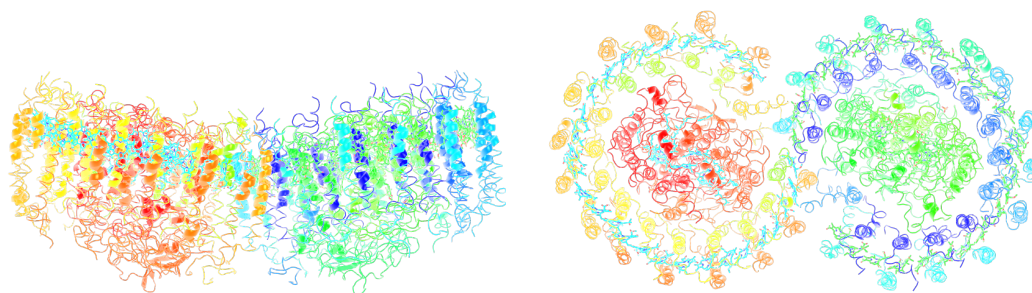


Figure 1.6: Structure of the RC-LH1-PufX from *Rhodobacter sphaeroides*. Left: side view, right: top view; the ring structure of the RC-LH1 superstructure can easily be seen. PDB code 4V9G.

1.1.3 Light Harvesting Complexes

In spite of the fact that the RCs would be able to capture light and convert the energy to a proton gradient, this process can be aided to be more efficient with the use of LHs. The LHs absorb a higher fraction of the spectrum of the light than the RCs would on their own. After the absorption of the incident light, the energy is then being transferred to the RC in the form of excited electronic states.

Initial work on LHs in artificial membranes focused on using SLBs made via the Langmuir-Blodgett, Langmuir-Schäfer (LB-LS) method and some groups continue to use this method in more recent work (Gruszecki et al., 1999; Imahori et al., 2000; Kamran et al., 2014; Li and Hollingshead, 1982). Although there has been some work on the reconstitution of LH1 (Dewa et al., 2006; Milhiet et al., 2006) and LH2 (Nagata et al., 2003; Stamouli et al., 2003) into SLBs separately and some work on the combination of LH1 and LH2 in a single membrane (Dewa et al., 2013; Lang et al., 1994; Sener et al., 2007; Sumino et al., 2011), there is a lack of work on the full photosynthetic system in a single, artificial membrane, where all elements of the natural photosynthetic membrane are combined and light is converted into ATP.

The first incorporation of LHs into an SLB was shown in 1994 and the fluorescence life time of light harvesting complex II (LH2) was measured using near-field fluorescence imaging (Dunn et al., 1994). In later work, light harvesting complex I (LH1) was also incorporated into SLBs on indium tin oxide (ITO),

a transparent and conductive substrate, which allowed for the measurement of the photocurrent of LH1 in its native membrane environment (Nagata et al., 2003). With the help of high resolution atomic force microscopy (AFM), it was possible to see the difference in the endoplasmic and periplasmic sides of LH2 (Stamouli et al., 2003). In addition to that, AFM has revealed the spatial arrangement of LH1 and its associated RCs showing a very specific structure of the two different proteins with respect to each other (Milhiet et al., 2006). LH2 was also incorporated into SLBs and it was shown that LH2, even when incorporated into the fluid domain of the SLB, will diffuse into gel domains and remain there (Dewa et al., 2006). More recently, the influence of the supramolecular structure of the arrangement of LH1, RCs and LH2 has been studied. It was shown that the clustering of the proteins, which is dependent on the lipid composition in the bilayer, plays an important role for the energy transfer. The RC-LH1 clusters (the individual complex is shown in figure 1.6) form hexagonal patterns which seem to facilitate very efficient energy transfer (Dewa et al., 2013).

1.2 The Cell and Its Membrane

In addition to the proteins discussed in the previous section, a cell which needs to create a proton gradient also requires an impermeable layer. In bacteria, plants, eukaryotes and animals this layer is the phospholipid membrane. It serves many purposes including internal separation of the cell into different compartments, shielding the cell from the outside, and allowing for the possibility to create chemical or electrical gradients (Luckey 1948, 2008).

The cell membrane mainly consists of lipid molecules which govern the behaviour of this vital part of any organism. It allows for the cell to be isolated from the outside and keep the inside of the cell at the required conditions for its own life. Membrane proteins can regulate the internal condition of the cell by acting as gatekeepers, channelling only certain molecules through while

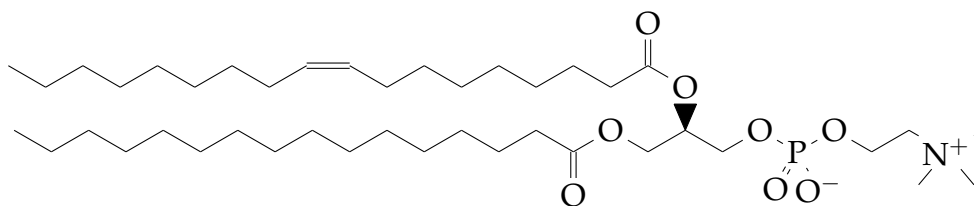


Figure 1.7: Structure of POPC. A commonly used lipid in this thesis. The tail consisting of hydrocarbon chains is hydrophobic while the polar head group is hydrophilic leading to the amphiphilic nature of this type of molecule.

stopping others from passing. This also means that the membrane itself has to be able to withstand diffusion of most molecules through itself (Phillips, 2013).

1.2.1 Phospholipids

Phospholipids are so called amphiphilic molecules. Amphiphilic stems from the Greek and translates as “loving both”, meaning that the molecules are both, hydrophilic and lipophilic at the same time. Phospholipids have a hydrophilic head group and lipophilic chains. Figure 1.7 shows the structure of a very common lipid, POPC. The tail consists of two carbon chains with a single unsaturated bond in one of the tails. The carbon chain induces the hydrophobicity of the molecule, as this part of the lipid molecule is non-polar. In contrast to this, the head group of the lipid molecule is polar (the N^+ atom and the O^- form a dipole) and is therefore hydrophilic (Boal, 2012).

Amphiphilic molecules, like lipids, self assemble into various forms when dispersed in water. The exact form amphiphilic molecules in water go into is determined by critical micelle concentration (CMC) of these molecules in water. It can be vesicles, (inverse) micelles, or sheets of bilayers. These forms are further discussed in the following section (Lodish, 2013).

1.2.2 Self-Assembly into Micelles and Vesicles

Self-assembly is the main driving forces for natural nano scale objects. It relies on energy minimisation on a molecular scale to achieve the formation of certain

patterns or objects. One of the earliest discoveries of self assembly into monolayers was when Benjamin Franklin dropped a small amount of oil into a pond and thus changed the surface tension of the water, resulting in fewer waves and the formation of a macroscopically large oil layer on top of the water (Franklin et al., 1774).

Lipid molecules in water self assemble into different structures such as micelles, bilayers or vesicles. The hydrophobic tail groups are driven out of contact with surrounding water molecules and the hydrophilic head groups are energetically favouring to be in contact with water.

Vesicles and Self-Assembly

For micelles to form through self-assembly, this formation has to be energetically favourable. Using the approach of Israelachvili (Israelachvili, 2011), a derivation of the driving forces behind the aggregation of several molecules will be given here.

Thermodynamic equilibrium is reached when all molecules, no matter in what kind of aggregate they are in, have the same chemical potential μ :

$$\mu = \mu_0^1 + k_B T \log X_1 = \mu_0^2 + \frac{1}{2} k_B T \log \frac{1}{2} X_2 = \dots \quad (1.1)$$

$$\mu = \mu_N = \mu_0^N + \frac{k_B T}{N} \log \left(\frac{X_N}{N} \right) = \text{constant}, \quad (1.2)$$

where N is the aggregation number, X_N the concentration of molecules in aggregates of the number N , μ_0^N the mean interaction-free energy per molecule, k_B is the Boltzmann constant and T is the temperature. Molecules form aggregates when the energy of the aggregated state is lower than for monomers. This means the free energy μ_0^N has to decrease with increasing N . For chains, circles and spheres the interaction free energy is given through (Israelachvili, 2011):

$$\mu_0^N = \mu_0^\infty + \frac{\alpha k_B T}{N^p}, \quad (1.3)$$

where α denotes a constant proportional to the intermolecular forces, p is the dimensionality and μ_0^∞ is the bulk energy per molecule. As required, this equation decreases with increasing N .

Conditions to Form Aggregates

Using equation 1.3 alone is not enough to explain the minimal concentration needed for aggregates to form. With equation 1.2 the following relation for the concentration of molecules in aggregates X_N can be derived (Israelachvili, 2011):

$$X_N \approx N (X_1 e^\alpha)^N. \quad (1.4)$$

If the monomer concentration X_1 is low enough so that the approximation $X_1 e^\alpha \ll 1$ is true, it follows that $X_1 > X_2 > X_3 > \dots$ for all values of α . This implies that most of the molecules in the solution will be monomers and therefore $X_1 \approx C$. But there is a restriction to this: once X_1 gets close to $e^{-\alpha}$ the value of $(X_1 e^\alpha)$ gets close to 1. By definition none of the X_N is allowed to be larger than 1, the value of X_1 cannot increase any further than $e^{-\alpha}$. Therefore, the aggregations states with $N > 1$ have to be used from this point on. The concentration at which this process starts is the so-called critical micelle concentration (CMC). In general it is true that

$$\text{CMC} \approx \exp\left(-\frac{\mu_0^1 - \mu_0^N}{k_B T}\right). \quad (1.5)$$

With equation 1.3 this becomes

$$\text{CMC} \approx e^{-\alpha} \quad (1.6)$$

independent from the dimensionality looked at. For any concentration of solute molecules higher than this value the concentration of monomers will be almost constant and the concentration of aggregates will increase.

1.2.3 Aggregates of Amphiphilic Molecules

In order to obtain bilayers, or other aggregates, such as vesicles, the molecules have to be amphiphilic. This means that the molecule is both hydrophilic and lipophilic at the same time. The structures can change from one to another, so a micelle can change into a bilayer, depending on the surrounding conditions and how they are changed. In order to understand more about the formation of a lipid bilayer from other structures, the forces between the amphiphilic molecules have to be understood first. When in an aqueous environment, there are hydrophilic and hydrophobic forces between either the lipid molecules themselves or the lipid and the water molecules. Since the hydrophobic tails try to minimise the interfacial area they share with the surrounding water, their free energy in water can be represented by a positive free energy per unit area, typically around 50 mJ m^{-2} . Due to the hydrophilic interaction of the head groups, this is reduced and is closer to 20 mJ m^{-2} . The attractive contribution to μ_0^N can be written as $\gamma_i a$ where a is the interfacial area of the head group (Israelachvili, 2011). On the other hand, the repulsive forces are much more difficult to calculate (Israelachvili et al., 1980) and have to include the double layer that forms above the lipid bilayer if the head groups are charged (see section 2.3.1). Here the fact that the energy expansion will be inversely proportional to the head group area is used for further discussion of the free energy:

$$\mu_0^N = \gamma a + \frac{K}{a}, \quad (1.7)$$

where K denotes the proportionality constant. The minimum of μ_0^N can be found when $\frac{d\mu_0^N}{da} = 0$. This leads to

$$\frac{d\mu_0^N}{da} = \gamma - \frac{K}{a^2} \quad (1.8)$$

and therefore the optimal surface energy per molecule a_0 is $\sqrt{\frac{K}{\gamma}}$. The minimum of μ_0^N can then be found by

$$\min(\mu_0^N) = 2\gamma a_0. \quad (1.9)$$

Replacing the unknown constant K in equation 1.7 with the measurable a_0 gives

$$\mu_0^N = 2\gamma a_0 + \frac{\gamma}{a}(a - a_0)^2. \quad (1.10)$$

Although several approximation have been made to obtain this result, it has fitted experimental data very well in several cases (Gallot and Skoulios, 1966; Lewis and Engelman, 1983; Reiss-Husson, 1967).

1.2.4 Formation of Lipid Bilayers

With the above considerations, several structures are energetically favourable in different conditions. The actual structure being formed will very much depend on geometric properties of the lipid molecule, the most important of them being the ratio of the interfacial area a , the head group covers, to the chain volume v and l_c , the length of the chain. The underscore c denotes the critical chain length because the maximum effective length of the chain is considered. As an estimate of the size of the hydrocarbon chain with n carbon atoms, the following approximations can be used (Tanford, 1980):

$$l_c \leq l_{\max} \approx (0.154 + 0.1256 \cdot n) \text{ nm} \quad (1.11)$$

$$v \approx (27.4 + 26.9 \cdot n) \cdot 10^{-3} \text{ nm}^3 \quad (1.12)$$

These parameters can be determined for each molecule and then, similar to solid state packing calculations, the geometric packing possibilities can be considered. The literature generally introduces a dimensionless value, called packing factor, $\frac{v}{a_0 l_c}$, where a_0 denotes the optimal surface area of the head group. While the

packing factor itself may allow for a lot of different shapes for the aggregates to form, the constraints from entropy lead to only one possibility. Only if the ratio

$$\frac{v}{a_0 l_c} \quad (1.13)$$

is very close to unity, a bilayer will form (Israelachvili, 2011). In case the head group is large compared to the tail volume ($\frac{v}{a_0 l_c} < 1$), the lipid forms a spherical micelle where the heads face the outer solvent and the tails stick together and a droplet of lipid within the solvent is formed. With increasing values the micelles become first ellipsoidal and then cylindrical. For values of $\frac{v}{a_0 l_c}$ greater than 1 the micelles become inverted micelles meaning that now the solvent forms droplets within the lipid. The configuration head groups facing the solvent and tails in contact with each other stays the same. Figure 1.8 shows the different structures an amphiphilic molecule can form.

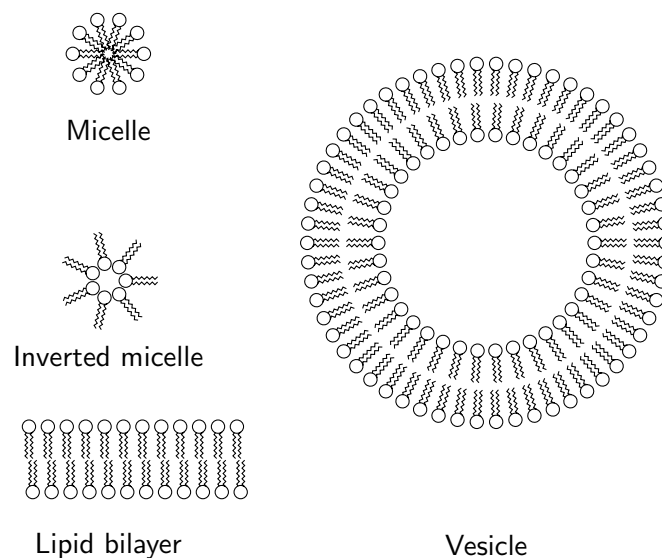


Figure 1.8: Different structures formed by lipids. Depending on the surface conditions or the solution the molecules are in and the geometry of the molecules, different aggregates are formed by lipids.

In general, single chain lipids form micelles. The packing factor for this structure is about 0.5 and has to be double the amount in order to form a bilayer. This means that a lipid that forms a micelle only has to double its hydrocarbon

volume v . This is why a lot of double chain molecules are used to form bilayers as the second chain doubles v and leads to an increase in the packing factor.

1.2.5 SLB Formation from Vesicles

Vesicles on a suitable surface (such as glass, mica or silicon) will spontaneously fuse and rupture to form a planar lipid bilayer. In a bilayer lipids are free to diffuse in two dimensions while they can not leave the bilayer structure to move in the third dimension. (Israelachvili, 2011)

Planar lipid bilayers can be formed in different ways. These include Langmuir-Blodgett (LB) deposition of individual monolayers on a support followed by the subsequent deposition of a second monolayer using the Langmuir-Schäfer (LS) method, black lipid membranes covering different openings, interfacial bilayers formed between a surface and a droplet and SLBs formed through vesicle rupture. Most SLBs in this work were formed through vesicle fusion and rupture on different supports.

Vesicles are formed in solution through the self assembly of lipid molecules which avoid the energetically unfavourable contact of their tail groups with water. The tail groups are in contact with each other and exclude the water from this region, while the head groups can be in contact with the surrounding aqueous solution. When dry lipid molecules are brought in contact with an aqueous solution, they spontaneously aggregate into multi-lamellar vesicles. These vesicles are then used to form smaller, unilamellar vesicles through either tip sonication or through extrusion of the multi lamellar vesicles through pores of various sizes, but smaller than the original vesicles.

In general, there are two different ways of vesicle spreading that will result in large bilayer regions. First, a vesicle on the surface can spontaneously rupture, unravel and form a patch of an SLB. Second, there is the possibility of vesicles sticking to the surface, flattening and forming a stack of two bilayers. The upper bilayer can then roll over the lower bilayer, which is stuck to the surface due to

pinning centres, to form larger patch of an SLB (Richter et al., 2006; Sackmann, 1996).

The process of rupture and SLB formation can follow different pathways and is dependant on the surface and the lipid composition in the vesicles. On silica, for example, it has been shown, that vesicles consisting of 1,2-dioleoyl-sn-glycero-3-phosphocholine (DOPC) and 1,2-dioleoyl-sn-glycero-3-phospho-L-serine (DOPS) (at a concentration of 80 mol% and 20 mol% respectively) will first attach to the surface and only rupture once a critical surface concentration has been reached (Richter et al., 2006). The same effect has been shown in both, experiment and computer simulation for Egg PC vesicles on a silica surface (Zhdanov et al., 2000). This effect can be explained by the enhanced stress on the individual vesicles upon the adsorption of other vesicles in their vicinity (Zhdanov and Kasemo, 2001). When the lipid composition of the vesicle is changed, the process of rupture and SLB formation can change as well. Vesicles consisting of 1,2-dioleoyl-3-trimethylammonium-propane (DOTAP) on silica show immediate rupture when they come into contact with the surface (Richter et al., 2006).

Once a single vesicle has ruptured on the surface, the small patch of bilayer on the surface will expose its edges to the surrounding liquid. From a thermodynamic standpoint these edges are energetically unfavourable and can therefore induce further rupture from closely adsorbed vesicles. This can then lead to a chain reaction which results in a high coverage of the solid support. In addition to the rupture of additional vesicles, the unfavourable edges also lead to neighbouring SLB patches fusing and the formation of larger SLB covered regions. Ideally, the combination of the processes will lead to a complete coverage of the solid support with an SLB. On some solid supports, for example silica, the time frame of this formation process is supposed to be of the order of several seconds (Richter et al., 2003).

Although the method of vesicle rupture on solid supports is well known and has been used for several years, it is far from being perfect. Different errors can introduce defects in the lipid membrane. During the formation process, even if the support is perfectly flat and hydrophilic, some of the vesicles may not rupture but be stuck to the surface and immobile. Although probably less than 1 % of the area will be covered by such defects, they have to be taken into account since they can be very important for biological applications (Grandbois et al., 1998).

1.2.6 Formation of Lipid Bilayers on different substrates

There are several surfaces on which SLBs can easily be formed, these include glass (Tamm and McConnell, 1985), quartz (Cremer and Boxer, 1999), mica (Richter and Brisson, 2005), silica (Briand et al., 2010), ITO (Hoyo et al., 2013) and many others. SLBs form especially easily on surfaces with a high free surface energy and an associated surface charge. It was shown that the possibility of bilayer formation on a given substrate depends on the surface charge and the interaction of the vesicles with the surface. Depending on these interactions the conditions which support formation of an SLB can vary and can depend on the ion concentration in solution or on the charged lipids in the vesicles in solution (Cho et al., 2010).

Apart from ITO the substrates on which lipid bilayers can be formed from vesicles fusion are non conductive as most conductive surfaces do not support lipid bilayer formation. These surfaces can be modified using self-assembled monolayers (SAMs) to change their properties such that lipid bilayer formation can be achieved. Surfaces which have been used with this approach include gold (Marquês et al., 2014), silver (Salamon et al., 1994) or platinum (Puu et al., 1995). They can be modified with different SAMs to achieve hybrid lipid membranes (HLMs), tethered lipid bilayers (TLBs) or SLBs. In the case of HLMs, the formation uses hydrophobic SAMs, which lead to the formation of a lipid mono-

layer on top of the SAMs. The formation of TLBs is driven by SAMs which are mainly hydrophilic but include tether molecules which are hydrophobic and will self-insert into the membrane, thus promoting vesicle adsorption and fusion. First used in the 1990s (Heyse et al., 1995; Raguse et al., 1998), HLMs have been extensively studied and are in wide use now. Despite their ease of use they come with the disadvantage of changing the properties of the HLM compared to an SLB. The SAM layer is more crystalline than a leaflet of a lipid bilayer which leads to the distal leaflet of the HLM being less mobile in comparison with an SLB making the environment less natural for membrane proteins. In addition to this, the water layer between the SLB and the support is very thin in this system making the incorporation of transmembrane proteins difficult and only achievable for proteins with a small extramembranous domain (Glazier et al., 2000). This can be overcome by using SAMs which are hydrophilic and have a small fraction of a hydrophobic tether inserting into the membrane. The combination of the hydrophilic surface and the hydrophobic tether leads to a lipid membrane being formed on top of the SAM such that there is a cushioning water layer between the substrate and the membrane in which small extramembranous domains of proteins can reside. This system resembles the natural membrane more closely and allows for a more direct comparison (Kastl et al., 2002). In contrast to the solid supports without a SAM, these systems can easily be formed on conductive surfaces, which allows for the direct electrochemical investigation of both, the membrane and the associated proteins via the surface.

1.3 SLB manipulation

In order to investigate the behaviour of artificial membranes in a more detailed and comprehensive way, different ways for the manipulation of SLBs have been developed. The need for these methods arises as vesicles rupturing on a surface form a continuous SLB without a pattern if the surface properties are not locally

changed. In addition to that, some membrane proteins stop the formation of an SLB when they are incorporated into vesicles at a significant concentration (van Meer et al., 2008). Therefore, methods which allow for the formation of the SLB with a low concentration of a membrane protein and subsequent concentration of this protein in pre-defined regions of interest were developed. Here, the methods for the patterning of SLBs and the creation of membrane component gradients by electrophoresis are discussed.

1.3.1 Patterning of SLBs

Several different methods have been used to achieve patterning of SLBs. The simplest method is the formation of the SLB and subsequent selective removal of certain regions. The simplest method of achieving the removal of the SLB, is mechanical scratching of the surface. This method was used to create barriers in an SLB and observe the spreading of the SLB into these barriers in different conditions (Cremer and Boxer, 1999). It was also shown that the mechanically created barriers could then be closed again through the lowering of the pH and spreading of the SLB (Cremer et al., 1999).

Mechanical scratching of SLBs has obvious shortcomings such as possible pattern size and accuracy. Therefore, other methods for the patterning of SLBs have been developed. Mechanical scratching can be improved by using an AFM tip to achieve the selective removal of the SLB. This allows for the resolution of the pattern to reach the nano scale but leads to complicated experiments and requires specialised equipment (Shi et al., 2008). Metal patterns on surfaces lead to a change in the surface properties, such that SLB formation can be inhibited in regions where the metal has been deposited. The patterning of the metal can be achieved through standard photolithography (Lee and Nam, 2012; van Oudenaarden and Boxer, 1999). The pattern size can further be reduced by using electron beam patterning of the photoresist prior to the deposition of the metal (Tsai et al., 2008). By forming metal lines with small intersections between the

lines, non-Brownian diffusion was observed in the SLB which was formed in the gaps between the metal.

Despite photolithography being an accurate and reproducible way for the formation of patterned SLBs, using photolithography and clean room technology to form an individual pattern is time consuming and expensive. Therefore, other methods for the patterning of SLBs were developed. Instead of mechanical scratching using tweezers, the selective removal of the SLB can also be achieved by using stamps on the micro-scale. Such stamps can be made from polydimethylsiloxane (PDMS) by casting the PDMS into molds made by photolithography (Hovis and Boxer, 2000). Since the stamp removes the SLB in the regions where the PDMS is in contact with the surface, the method can be extended to the formation of patterned SLBs from the same stamp (Hovis and Boxer, 2000). The overall process is similar to inking and printing with a conventional stamp.

Stamping for the formation of SLBs can be further improved by not stamping the SLB directly which requires the sample to be in liquid during the whole experiment but by stamping other molecules onto the surface which change the surface properties in specified regions. Different molecules can be stamped onto the surface. Patterned SAMs can be produced in this way to achieve the selective formation of monolayers and bilayers (Jenkins et al., 2002). In this work, a PDMS stamp was used to print the protein fibronectin onto surfaces (Bernard et al., 1998). In previous work, this has been used to create corals of SLBs and these patterns were used in combination with electrophoresis (Yoshina-Ishii and Boxer, 2006).

Other methods of patterning SLBs include the formation of selectively oxidised PDMS surfaces. This leads to varying hydrophilicity across the surface and therefore formation of SLBs in regions of high hydrophilicity and lipid monolayers in regions of low hydrophilicity. Some lipids have the ability to cross-link with each other and withstand the removal through detergents. Since

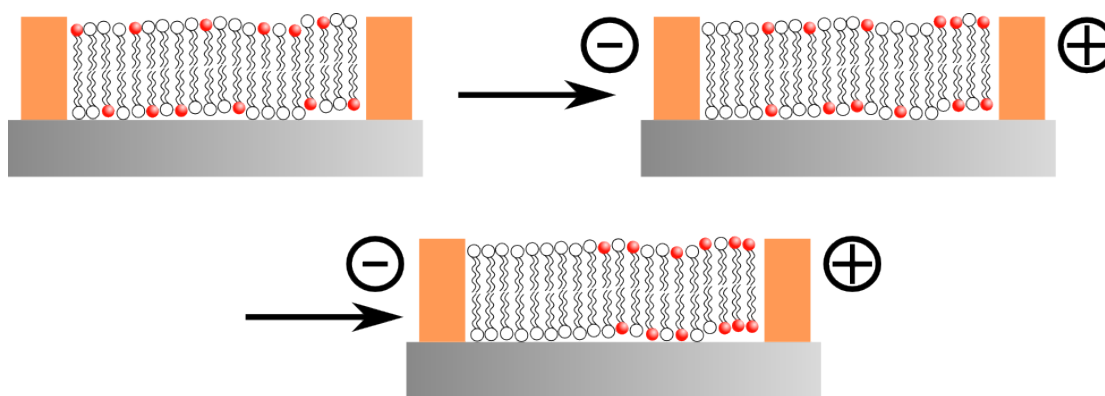


Figure 1.9: Schematic of electrophoresis in a lipid bilayer. The dye molecules are negatively charged and move along the electric field which is applied. The final distribution will be an exponential decay away from the barriers.

the cross-linking can be achieved locally through photomasks, SLBs can also be patterned in this manner (Okazaki et al., 2009). The regions, where the SLB has been removed can be back-filled using vesicles of different compositions through ink-jet printing and arrays of SLBs with varying composition can be produced (Yamada et al., 2013).

1.3.2 SLBs Electrophoresis

Initial work on electrophoresis on SLBs combined fluorescence recovery after photobleaching (FRAP) with the application of an electric field in the plane of the membrane. The bleaching of fluorescent molecules was carried out in a pattern consisting of several lines and an electric field was applied afterwards. This allowed for the measurement of the electrophoretic mobility of a combination of dyes and membrane compositions. In addition to that, when electrically neutral probes were used, the influence of drag exerted by the liquid onto the SLB through electroosmosis could also be measured (Stelzle et al., 1992).

When this method is combined with patterned surfaces, such as Brownian ratchets, molecular separation in an SLB can be achieved (van Oudenaarden and Boxer, 1999). Here, a combination of the difference in diffusion coefficient of two different membrane bound dyes and the application of electrophoresis

lead to the lateral separation of the two membrane components. This concept can lead to different applications as the separation of membrane components not only by their charge, but also by their diffusion coefficient is of great interest to the scientific community. The concept of electrophoresis used in conjunction with a patterned SLB is shown in figure 1.9, where charged dye molecules are concentrated against a barrier.

It has been shown that not only lipids in the membrane can be manipulated through electrophoresis, but also membrane bound proteins (Tanaka et al., 2007) which can even be extended to membrane proteins Cheetham et al. (2011). As this allows for the creation of regions with a high protein concentration, this could lead to the formation of protein crystals. Such crystals are required for the determination of the protein structure by diffraction techniques such as X-ray crystallography. Especially for membrane proteins the formation of crystals has proven to be very difficult and the structure of many membrane proteins is still unknown.

Another application of electrophoresis in lipid bilayers is the separation of membrane components based on their electrophoretic mobility. The idea is very similar to gel electrophoresis. An SLB which acts as the matrix is formed, vesicles with different components are then used to form an SLB at the starting point where the matrix SLB was removed and an electric field is applied. As different molecules have different electrophoretic mobilities in the membrane, this leads to the formation of bands containing a certain species, as was subsequently shown using mass spectrometry (Pace et al., 2013).

1.4 Summary, Aims and Outline

The phospholipid membrane plays an important role in the life of many organisms. It can act as barrier, an internal compartmentalisation, or as an ion-selective channel. Around 60% of current drug targets are on the surface of the mem-

brane and are mainly membrane proteins (Overington et al., 2006). This makes the phospholipid membrane an exciting research area that has been actively studied for a long time and will remain in the focus of many scientists for a long time. Here, we also focus on light harvesting proteins within this membrane. These proteins have evolved in certain bacteria and allow them to survive without the need for oxygen. The combination of several proteins enables the bacteria to not only generate energy from electromagnetic radiation but also store it in the form of ATP for later use of the organism.

This work aims to widen the understanding of diffusion within the lipid membrane as this is the main mechanism of transport *in vivo*. In order to obtain a better understanding of protein function, it is important to know their structure. This knowledge is most commonly generated through diffraction experiments from protein crystals. Such crystals can easily be created from water soluble proteins but are very difficult to obtain from membrane proteins as these are not very likely to form crystals within the membrane and, once taken out of their natural environment, denature, and therefore the information gained is very hard to interpret. This can be overcome if proteins can be concentrated and crystallised within their membranous environment. This work presents new understanding of the transport mechanism used in Brownian ratchets. Such ratchets can be used to build long channels suitable for membrane protein transport without the need of a strong electric field as it would be needed for direct electrophoretic transport. A new approach to the concentration and trapping of membrane molecules is also presented. Instead of using alternating electric fields, constant fields and new pattern designs are used to trap membrane components at different concentrations in pre-defined regions of interest. In order to develop a read-out method for changes in membrane composition and protein concentration, surface enhanced Raman spectroscopy is used to show the potential of determining a variety of membrane properties without the need for additional markers.

The methods used in this work are presented in chapter 2.

In chapter 3, diffusion in lipid membranes and Brownian ratchets are investigated. It is shown in both, calculations and experiment, how the efficiency of these ratchets is governed by a combination of geometrical properties of the pattern and external parameters such as the periodicity of the electric field.

Chapter 4 presents new approaches towards the build-up and concentration of membrane components in confined environments. These include the use of new patterns which allow for shorter experimental times, direct measurement of binding constants using fluorescence microscopy and new methods for the use of electrodes with lipid bilayers.

Alternative read-out methods for the characterisation of lipid bilayers and embedded proteins are presented in chapter 5. It is first discussed why lipid bilayers containing membrane proteins need new supports. It is then shown how surface enhanced Raman scattering (SERS) can be used for the determination of lipid and peptide components in an SLB.

References

- Alves, I. D., Salgado, G. F. J., Salamon, Z., Brown, M. F., Tollin, G., and Hruby, V. J. (2005). Phosphatidylethanolamine enhances rhodopsin photoactivation and transducin binding in a solid supported lipid bilayer as determined using plasmon-waveguide resonance spectroscopy. *Biophysical Journal*, 88(1):198–210.
- Béja, O., Aravind, L., Koonin, E. V., Suzuki, M. T., Hadd, A., Nguyen, L. P., Jovanovich, S. B., Gates, C. M., Feldman, R. A., Spudich, J. L., Spudich, E. N., and DeLong, E. F. (2000). Bacterial rhodopsin: evidence for a new type of phototrophy in the sea. *Science*, 289(5486):1902–1906.
- Bernard, A., Delamarche, E., Schmid, H., Michel, B., Bosshard, H. R., and Biebuyck, H. (1998). Printing Patterns of Proteins. *Langmuir*, 14(9):2225–2229.
- Bjorn, L. O. and Govindjee (2009). The evolution of photosynthesis and chloroplasts. *Current Science*, 96(11):1466–1474.
- Blankenship, R. E. (2010). Early evolution of photosynthesis. *Plant physiology*, 154(2):434–8.
- Boal, D. H. (2012). *Mechanics of the cell*, volume 2. Cambridge University Press, Cambridge; New York.
- Briand, E., Zäch, M., Svedhem, S., Kasemo, B., and Petronis, S. (2010). Combined QCM-D and EIS study of supported lipid bilayer formation and interaction with pore-forming peptides. *Analyst*, 135(2):343–350.
- Broda, E. (1941). The role of the phospholipin in visual purple solutions. *Biochemical Journal*, 35(8-9):960–964.
- Brown, M. F. (1994). Modulation of rhodopsin function by properties of the membrane bilayer. *Chemistry and physics of lipids*, 73:159–180.
- Cheetham, M. R., Bramble, J. P., McMillan, D. G. G., Krzeminski, L., Han, X., Johnson, B. R. G., Bushby, R. J., Olmsted, P. D., Jeuken, L. J. C., Marritt, S. J., Butt, J. N., and Evans, S. D. (2011). Concentrating Membrane Proteins Using Asymmetric Traps and AC Electric Fields. *Journal of the American Chemical Society*, 133(17):6521–4.
- Cho, N.-J., Frank, C. W., Kasemo, B., and Höök, F. (2010). Quartz crystal microbalance with dissipation monitoring of supported lipid bilayers on various substrates. *nature protocols*, 5(6):1096–1106.

- Cremer, P. S. and Boxer, S. G. (1999). Formation and spreading of lipid bilayers on planar glass supports. *The Journal of Physical Chemistry B*, 103(13):2554–2559.
- Cremer, P. S., Groves, J. T., Kung, L. A., and Boxer, S. G. (1999). Writing and erasing barriers to lateral mobility into fluid phospholipid bilayers. *Langmuir*, 15(11):3893–3896.
- Dewa, T., Sugiura, R., Suemori, Y., Sugimoto, M., Takeuchi, T., Hiro, A., Iida, K., Gardiner, A. T., Cogdell, R. J., and Nango, M. (2006). Lateral organization of a membrane protein in a supported binary lipid domain: direct observation of the organization of bacterial light-harvesting complex 2 by total internal reflection fluorescence microscopy. *Langmuir : the ACS journal of surfaces and colloids*, 22(12):5412–8.
- Dewa, T., Sumino, A., Watanabe, N., Noji, T., and Nango, M. (2013). Energy transfer and clustering of photosynthetic light-harvesting complexes in reconstituted lipid membranes. *Chemical Physics*, 419:200–204.
- Dimroth, F., Grave, M., Beutel, P., Fiedeler, U., Karcher, C., Tibbits, T. N. D., Oliva, E., Siefer, G., Schachtner, M., Wekkeli, A., Bett, A. W., Krause, R., Piccin, M., Blanc, N., Drazek, C., Guiot, E., Ghyselen, B., Salvetat, T., Tauzin, A., Signamarcheix, T., Dobrich, A., Hannappel, T., and Schwarzburg, K. (2014). Wafer bonded four-junction GaInP / GaAs // GaInAsP / GaInAs concentrator solar cells with 44.7 % efficiency. *Progress in Photovoltaics Research and Applications*, 22(January):277–282.
- Dioumaev, A. K., Brown, L. S., Shih, J., Spudich, E. N., Spudich, J. L., and Lanyi, J. K. (2002). Proton transfers in the photochemical reaction cycle of proteorhodopsin. *Biochemistry*, 41:5348–5358.
- Dunn, R. C., Holtom, G. R., Mets, L., and Xie, X. S. (1994). Near-field fluorescence imaging and fluorescence lifetime measurement of light harvesting complexes in intact photosynthetic membranes. *The Journal of Physical Chemistry*, 98(12):3094–3098.
- Field, C. B. (1998). Primary Production of the Biosphere: Integrating Terrestrial and Oceanic Components. *Science*, 281:237–240.
- Fleming, G., Schlau-Cohen, G., Amarnath, K., and Zaks, J. (2012). Design principles of photosynthetic light-harvesting. *Faraday Discussion*, 155:103–14.
- Franklin, B., Brownrigg, W., and Farish, M. (1774). Of the Stilling of Waves by means of Oil. Extracted from Sundry Letters between Benjamin Franklin, LL. D. F. R. S. William Brownrigg, M. D. F. R. S. and the Reverend Mr. Farish.
- Fung, B. K. and Hubbell, W. L. (1978). Organization of rhodopsin in photoreceptor membranes. 2. Transmembrane organization of bovine rhodopsin: evidence from proteolysis and lactoperoxidase-catalyzed iodination of native and reconstituted membranes. *Biochemistry*, 17:4403–4410.

- Gallot, B. and Skoulios, A. (1966). Interactions électriques dans les phases mésomorphes des systèmes amphiphile-eau: Rôle de la teneur en eau, de la longueur de la chaîne paraffinique, de la nature du cation, et de la température. *Colloid & Polymer Science*, 208(1):37–43.
- Glazier, S. A., Vanderah, D. J., Plant, A. L., Bayley, H., Valincius, G., and Kasianowicz, J. J. (2000). Reconstitution of the Pore-Forming Toxin α -Hemolysin in Phospholipid/18-Octadecyl-1-thiahexa(ethylene oxide) and Phospholipid/n-Octadecanethiol Supported Bilayer Membranes. *Langmuir*, 16(26):10428–10435.
- Grandbois, M., Clausen-Schaumann, H., and Gaub, H. (1998). Atomic force microscope imaging of phospholipid bilayer degradation by phospholipase A2. *Biophysical journal*, 74(5):2398–404.
- Gruszecki, W. I., Grudzinski, W., Banaszek-Glos, A., Matula, M., Kernen, P., Krupa, Z., and Siewiesiuk, J. (1999). Xanthophyll pigments in light-harvesting complex II in monomolecular layers: localisation, energy transfer and orientation. *Biochimica et Biophysica Acta (BBA)-Bioenergetics*, 1412(2):173–183.
- Heyse, S., Ernst, O. P., Dienes, Z., Hofmann, K. P., and Vogel, H. (1998). Incorporation of rhodopsin in laterally structured supported membranes: observation of transducin activation with spatially and time-resolved surface plasmon resonance. *Biochemistry*, 37(2):507–522.
- Heyse, S., Vogel, H., Sanger, M., and Sigrist, H. (1995). Covalent attachment of functionalized lipid bilayers to planar waveguides for measuring protein binding to biomimetic membranes. *Protein science : a publication of the Protein Society*, 4(12):2532–2544.
- Hogewoning, S. W., Wientjes, E., Douwstra, P., Trouwborst, G., van Ieperen, W., Croce, R., and Harbinson, J. (2012). Photosynthetic quantum yield dynamics: from photosystems to leaves. *The Plant cell*, 24(5):1921–35.
- Hong, K. and Hubbell, W. L. (1972). Preparation and properties of phospholipid bilayers containing rhodopsin. *Proceedings of the National Academy of Sciences*, 69(9):2617–2621.
- Hovis, J. S. and Boxer, S. G. (2000). Patterning Barriers to Lateral Diffusion in Supported Lipid Bilayer Membranes by Blotting and Stamping. *Langmuir*, 16(3):894–897.
- Hoyo, J., Gaus, E., Oncins, G., Torrent-Burgués, J., Sanz, F., and Torrent-Burgués, J. (2013). Incorporation of ubiquinone in supported lipid bilayers on ITO. *The journal of physical chemistry. B*, 117(25):7498–506.
- IEA (2010). Key World Energy Statistics 2010. Technical report, OECD.
- Imahori, H., Norieda, H., Yamada, H., Nishimura, Y., Yamazaki, I., Sakata, Y., and Fukuzumi, S. (2000). Light-Harvesting and Photocurrent Generation by Gold Electrodes Modified with Mixed Self-Assembled Monolayers of

- Boron–Dipyrrin and Ferrocene–Porphyrin–Fullerene Triad. *Journal of the American Chemical Society*, 123(1):100–110.
- Israelachvili, J. N. (2011). *Intermolecular and Surface Forces*. Elsevier, 3rd edition.
- Israelachvili, J. N., Marcelja, S., and Horn, R. G. (1980). Physical principles of membrane organization. *Quarterly reviews of biophysics*, 13(2):121–200.
- Jastrzebska, B., Debinski, A., Filipek, S., and Palczewski, K. (2011). Role of membrane integrity on G protein-coupled receptors: Rhodopsin stability and function.
- Jenkins, A. T. A., Bushby, R. J., Evans, S. D., Knoll, W., and Ogier, S. D. (2002). Lipid Vesicle Fusion on μ CP Patterned Self-Assembled Monolayers : Effect of Pattern Geometry on Bilayer Formation. (7):3176–3180.
- Kamran, M., Delgado, J. D., Friebe, V., Aartsma, T. J., and Frese, R. N. (2014). Photosynthetic Protein Complexes as Bio-photovoltaic Building Blocks Retaining a High Internal Quantum Efficiency. *Biomacromolecules*, 15(8):2833–2838.
- Kastl, K., Ross, M., Gerke, V., and Steinem, C. (2002). Kinetics and Thermodynamics of Annexin A1 Binding to Solid-Supported Membranes: A QCM Study. *Biochemistry*, 41(31):10087–10094.
- Krebs, R. A., Alexiev, U., Partha, R., Devita, A. M., and Braiman, M. S. (2002). Detection of fast light-activated H⁺ release and M intermediate formation from proteorhodopsin. *BMC physiology*, 2:5.
- Lang, H. P., Hunter, C. N., Bank, W., and Sheffield, S. (1994). The relationship between carotenoid biosynthesis and the assembly of the light-harvesting LH2 complex in *Rhodobacter sphaeroides*. *The Biochemical journal*, 205:197–205.
- Lee, Y. K. and Nam, J.-M. (2012). Electrofluidic lipid membrane biosensor. *Small (Weinheim an der Bergstrasse, Germany)*, 8(6):832–7.
- Lewis, B. A. and Engelman, D. M. (1983). Lipid bilayer thickness varies linearly with acyl chain length in fluid phosphatidylcholine vesicles. *Journal of Molecular Biology*, 166(2):211–217.
- Li, J. and Hollingshead, C. (1982). Formation of crystalline arrays of chlorophyll a/b-light-harvesting protein by membrane reconstitution. *Biophysical Journal*, 37(1):363–370.
- Lodish, H. (2013). *Molecular cell biology*, volume 7. W.H. Freeman, Basingstoke; New York.
- Luckey 1948, M. (2008). *Membrane structural biology: with biochemical and biophysical foundations*. Cambridge University Press, Cambridge.
- Marquês, J. T., de Almeida, R. F. M., and Viana, A. S. (2014). Lipid bilayers supported on bare and modified gold – Formation, characterization and relevance of lipid rafts. *Electrochimica Acta*, 126(0):139–150.

- Martinez, A., Bradley, A. S., Waldbauer, J. R., Summons, R. E., and DeLong, E. F. (2007). Proteorhodopsin photosystem gene expression enables photophosphorylation in a heterologous host. *Proceedings of the National Academy of Sciences of the United States of America*, 104:5590–5595.
- Milhiet, P.-E., Gubellini, F., Berquand, A., Dosset, P., Rigaud, J.-L., Le Grimellec, C., and Lévy, D. (2006). High-resolution AFM of membrane proteins directly incorporated at high density in planar lipid bilayer. *Biophysical Journal*, 91(9):3268–3275.
- Nagata, M., Yoshimura, Y., Inagaki, J., Suemori, Y., Iida, K., Ohtsuka, T., and Nango, M. (2003). Construction and photocurrent of light-harvesting polypeptides/zinc bacteriochlorophyll a complex in lipid bilayers. *Chemistry Letters*, 32(9):852–853.
- Naumann, R., Schmidt, E. K., Jonczyk, a., Fendler, K., Kadenbach, B., Liebermann, T., Offenhäusser, a., and Knoll, W. (1999). The peptide-tethered lipid membrane as a biomimetic system to incorporate cytochrome c oxidase in a functionally active form. *Biosensors and Bioelectronics*, 14(7):651–662.
- Okazaki, T., Inaba, T., Tatsu, Y., Tero, R., Urisu, T., and Morigaki, K. (2009). Polymerized lipid bilayers on a solid substrate: morphologies and obstruction of lateral diffusion. *Langmuir : the ACS journal of surfaces and colloids*, 25(1):345–351.
- Overington, J. P., Al-Lazikani, B., and Hopkins, A. L. (2006). How many drug targets are there? *Nat Rev Drug Discov*, 5(12):993–996.
- Pace, H. P., Sherrod, S. D., Monson, C. F., Russell, D. H., and Cremer, P. S. (2013). Coupling supported lipid bilayer electrophoresis with matrix-assisted laser desorption/ionization-mass spectrometry imaging. *Analytical chemistry*, 85(12):6047–52.
- Phillips, R. -R. B. (2013). *Physical biology of the cell*, volume 2. Garland Science, New York; London.
- Poo, M. and Cone, R. A. (1974). Lateral diffusion of rhodopsin in the photoreceptor membrane. *Nature*, 247:438–441.
- Puu, G., Gustafson, I., Artursson, E., and Ohlsson, P. A. (1995). Retained activities of some membrane proteins in stable lipid bilayers on a solid support. *Biosensors and Bioelectronics*, 10(5):463–476.
- Raguse, B., Braach-Maksvytis, V., Cornell, B. A., King, L. G., Osman, P. D. J., Pace, R. J., and Wieczorek, L. (1998). Tethered lipid bilayer membranes: formation and ionic reservoir characterization. *Langmuir*, 14(3):648–659.
- Reiss-Husson, F. (1967). Structure des phases liquide-cristallines de differents phospholipides, monoglycerides, sphingolipides, anhydres ou en presence d'eau. *Journal of Molecular Biology*, 25(3):363–382.

- Richter, R., Mukhopadhyay, A., and Brisson, A. (2003). Pathways of lipid vesicle deposition on solid surfaces: a combined QCM-D and AFM study. *Biophysical journal*, 85(5):3035–47.
- Richter, R. P., Bérat, R., and Brisson, A. R. (2006). Formation of solid-supported lipid bilayers: an integrated view. *Langmuir : the ACS journal of surfaces and colloids*, 22(8):3497–505.
- Richter, R. P. and Brisson, A. R. (2005). Following the formation of supported lipid bilayers on mica: a study combining AFM, QCM-D, and ellipsometry. *Biophysical journal*, 88(5):3422–33.
- Rudzki, J. E. and Peters, K. S. (1984). Picosecond absorption studies on rhodopsin and isorhodopsin in detergent and native membrane. *Biochemistry*, 23:3843–3848.
- Sackmann, E. (1996). Supported membranes: scientific and practical applications. *Science*, 271(5245):43–8.
- Salamon, Z., Wang, Y., Tollin, G., and Macleod, H. A. (1994). Assembly and molecular organization of self-assembled lipid bilayers on solid substrates monitored by surface plasmon resonance spectroscopy. *Biochimica et Biophysica Acta (BBA)-Biomembranes*, 1195(2):267–275.
- Sener, M. K., Olsen, J. D., Hunter, C. N., and Schulten, K. (2007). Atomic-level structural and functional model of a bacterial photosynthetic membrane vesicle. *Proceedings of the National Academy of Sciences of the United States of America*, 104(40):15723–8.
- Shi, J., Chen, J., and Cremer, P. S. (2008). Sub-100 nm patterning of supported bilayers by nanoshaving lithography. *Journal of the American Chemical Society*, 130(9):2718–9.
- Smil, V. (1991). *General energetics : energy in the biosphere and civilization*. WILEY-VCH Verlag.
- Stamouli, A., Kafi, S., Klein, D. C. G., Oosterkamp, T. H., Frenken, J. W. M., Cogdell, R. J., and Aartsma, T. J. (2003). The ring structure and organization of light harvesting 2 complexes in a reconstituted lipid bilayer, resolved by atomic force microscopy. *Biophysical Journal*, 84(4):2483–2491.
- Stelzle, M., Miehlisch, R., and Sackmann, E. (1992). Two-dimensional microelectrophoresis in supported lipid bilayers. *Biophysical Journal*, 63(5):1346–1354.
- Subramaniam, V., Alves, I. D., Salgado, G. F. J., Lau, P.-W. W., Wysocki, R. J., Salamon, Z., Tollin, G., Hruby, V. J., Brown, M. F., and Saavedra, S. S. (2005). Rhodopsin reconstituted into a planar-supported lipid bilayer retains photoactivity after cross-linking polymerization of lipid monomers. *Journal of the American Chemical Society*, 127(15):5320–5321.

- Subramaniam, V., D'Ambruso, G. D., Hall Jr, H. K., Wysocki Jr, R. J., Brown, M. F., and Saavedra, S. S. (2008). Reconstitution of rhodopsin into polymerizable planar supported lipid bilayers: Influence of dienoyl monomer structure on photoactivation. *Langmuir*, 24(19):11067–11075.
- Sumino, A., Dewa, T., Kondo, M., Morii, T., Hashimoto, H., Gardiner, A. T., Cogdell, R. J., and Nango, M. (2011). Selective assembly of photosynthetic antenna proteins into a domain-structured lipid bilayer for the construction of artificial photosynthetic antenna systems: structural analysis of the assembly using surface plasmon resonance and atomic force microscopy. *Langmuir : the ACS journal of surfaces and colloids*, 27(3):1092–9.
- Tamm, L. K. and McConnell, H. M. (1985). Supported phospholipid bilayers. *Biophysical journal*, 47(1):105–13.
- Tanaka, M., Hermann, J., Haase, I., Fischer, M., and Boxer, S. G. (2007). Frictional drag and electrical manipulation of recombinant proteins in polymer-supported membranes. *Langmuir : the ACS journal of surfaces and colloids*, 23(10):5638–44.
- Tanford, C. (1980). *The hydrophobic effect: formation of micelles and biological membranes*. WILEY-VCH Verlag GmbH, 2nd edition.
- Tsai, J., Sun, E., Gao, Y., Hone, J. C., and Kam, L. C. (2008). Non-Brownian diffusion of membrane molecules in nanopatterned supported lipid bilayers. *Nano letters*, 8(2):425–30.
- Tunuguntla, R., Bangar, M., Kim, K., Stroeve, P., Ajo-Franklin, C. M., and Noy, A. (2013). Lipid Bilayer Composition Can Influence the Orientation of Protorhodopsin in Artificial Membranes. *Biophysical Journal*, 105(6):1388–1396.
- van Meer, G., Voelker, D. R., and Feigenson, G. W. (2008). Membrane lipids: where they are and how they behave. *Nature reviews. Molecular cell biology*, 9(2):112–124.
- van Oudenaarden, A. and Boxer, S. G. (1999). Brownian Ratchets: Molecular Separations in Lipid Bilayers Supported on Patterned Arrays. *Science*, 285(5430):1046–1048.
- Yamada, M., Imaishi, H., and Morigaki, K. (2013). Microarrays of phospholipid bilayers generated by inkjet-printing. *Langmuir : the ACS journal of surfaces and colloids*, 29(21):6404–6408.
- Yoshina-Ishii, C. and Boxer, S. G. (2006). Controlling two-dimensional tethered vesicle motion using an electric field: interplay of electrophoresis and electroosmosis. *Langmuir*, 22(5):2384–91.
- Zhdanov, V. P. and Kasemo, B. (2001). Comments on Rupture of Adsorbed Vesicles. *Langmuir*, 17(12):3518–3521.
- Zhdanov, V. P., Keller, C. A., Glasmästar, K., and Kasemo, B. (2000). Simulation of adsorption kinetics of lipid vesicles. *The Journal of Chemical Physics*, 112(2).

Chapter 2

Methods

This chapter gives an introduction to the experimental methods used in this work. The chapter begins with the formation of lipid bilayers, continues with the mechanisms used for the investigation of the bilayers, and shows how nanoparticles (NPs) can be used to enhance the signal obtained in Raman spectroscopy.

2.1 Formation of Lipid Bilayers

There are different ways for the formation of solid supported lipid bilayers (SLBs). They all include the deposition of lipids on a solid which then acts as the support for the artificial membrane. The lipids can be used in a dispersed form in a suitable solvent such as methanol or isopropanol. This solution can then be spin coated onto a support. Depending on the strength of the lipid solution and the spin coating speed, either single bilayers or stacks of bilayers can be formed (Mennicke and Salditt, 2002; Pompeo et al., 2005). Another way of depositing the lipids onto the substrate is to disperse the lipids in a water based solution and to add detergent to the solution. The detergent will stop the formation of multi-lamellar vesicles (MLVs), dissolve the lipids and will ensure that patches of lipids form on the surface. When the solution is then exchanged so that it contains less detergent, the formation of a continuous lipid bilayer on the substrate is triggered (Mennicke and Salditt, 2002; Pompeo et al.,

2005; Subramaniam et al., 2005). The method mainly used in this work is the formation of lipid vesicle solutions which are then brought into contact with the solid support. Dry lipids are firstly mixed to the desired amounts in a solvent, such as isopropanol. This is then dried under a continuous stream of nitrogen for at least 30 min to obtain dried lipids arranged in stacks and sticking to the wall of the vial, the so called lipid cake. The desired buffer is then added and the vial is vortexed until there is no lipid left on the wall of the vial and the solution becomes cloudy. This results in the formation of MLVs. These are then tip sonicated for a further 30 min in a cooling bath at 4 °C to obtain lipid vesicles of approximately 25 nm diameter (Zhu et al., 2013). The solution is then centrifuged at 14 500 g to remove any titanium residue from the sonication tip and the supernatant is used in the experiments. Lipid vesicles can be stored in a fridge at 4 °C for up to a week.

The vesicles then adsorb to the surface, fuse, and rupture to form a continuous lipid bilayer. This process is triggered when the vesicle coverage on the surface reaches a critical point and the vesicles start interacting with each other.

The way vesicles rupture on a surface is not precisely understood and still under debate (Hamai et al., 2007; Richter et al., 2006; Schönherr et al., 2004). There are different mechanisms which are proposed and both are shown in figure 2.1. When the vesicle is attached to the surface, it could open up at one point and unfold so that the inside of the vesicle forms the distal leaflet of the bilayer (upper path of figure 2.1). In contrast to that another mechanism is possible where the vesicle flattens and ruptures at two points and the top part slides to the side of the bottom layer. This will also result in a continuous lipid bilayer but with a mixed distribution of the leaflets. For the bottom part of the vesicle the inner leaflet of the vesicle becomes the distal leaflet of the bilayer while for the top part of the vesicle the inner leaflet becomes the proximal leaflet of the bilayer (bottom path of figure 2.1). Despite the fact that the exact rupture mechanism is not of high importance for some experiments, other experiments rely on the

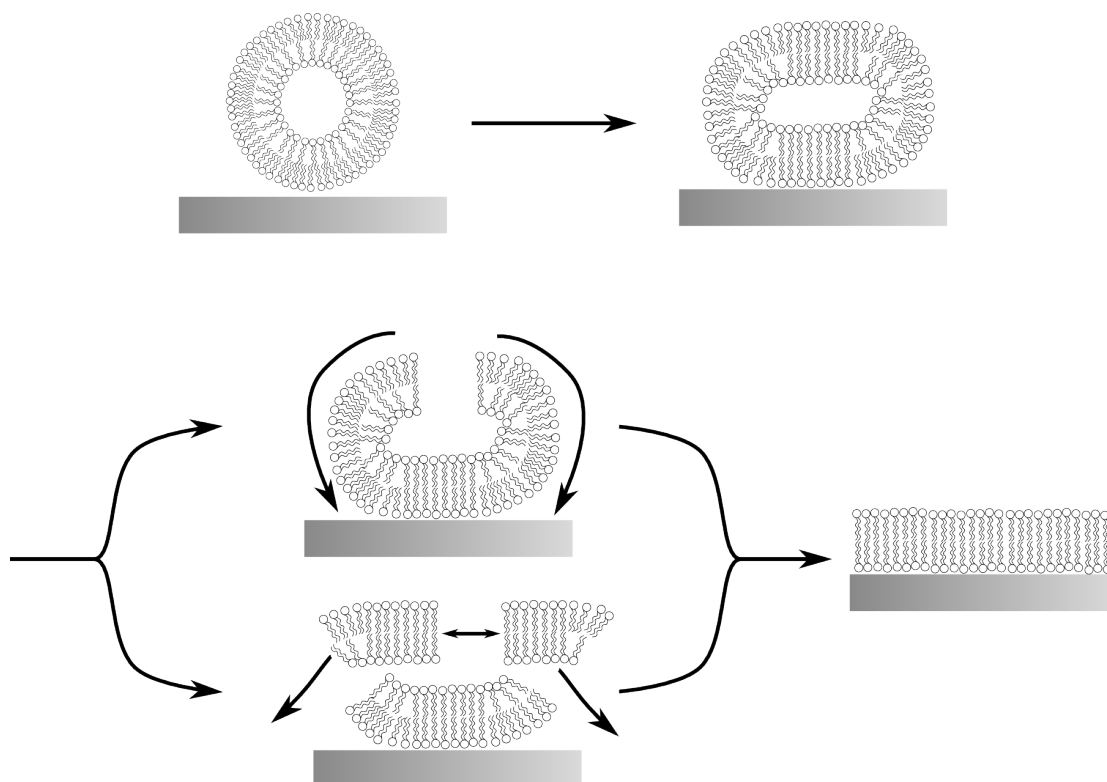


Figure 2.1: Vesicle adsorption to a solid support and two different paths of vesicle rupture for bilayer formation. In both paths the initial surface adsorption is identical. Rupture then occurs in two different ways: (top) the vesicle opens up at one point and unravels forming a bilayer patch on the surface; (bottom) the membrane in the vesicle ruptures at two points and the upper bilayer patch slides over the one below forming a continuous bilayer patch.

orientation of the contents of the vesicle with the respect to the SLB formed later. When protein pumps, for example, are incorporated into the vesicle, in order for them to have a net effect, they need to be incorporated in a preferential orientation. If this was not the case and every ion pump had a counter part which was pumping in the opposite direction, no net ion-pumping would occur. For experiments like this, it is important in which direction the proteins are oriented on the surface. But so far no conclusive results have been presented which indicate which mechanism is preferred under which circumstances (Hamai et al., 2007; Johnson et al., 2002; Richter et al., 2006; Richter and Brisson, 2005).

2.2 Patterning of SLBs

There are several ways of patterning SLBs. The most obvious way to form a patterned lipid bilayer is to create a smooth bilayer over a surface and then mechanically remove parts of the bilayer, e.g. with tweezers (Cremer and Boxer, 1999; Cremer et al., 1999). This method has obvious disadvantages when it comes to small or accurate patterns and improvements were needed. The underlying principle for these methods is to change the surface properties in two domains, one which facilitates bilayer formation and one which stops bilayer formation. This can be achieved in different ways, by photolithography directly onto the solid support for the lipid bilayer (Bao et al., 2012; Groves, 1997), by the deposition of metals where no bilayer should form (Tsai et al., 2008; van Oudenaarden and Boxer, 1999) or by microcontact printing (μ CP) of a barrier material (Abraham et al., 2014; Bernard et al., 1998, 2000; Cheetham et al., 2011; Hovis and Boxer, 2000) or by stamping the lipid bilayer directly (Hovis and Boxer, 2000).

In this work, μ CP was used in most experiments. As can be seen in figure 2.2, the method involves a stamp being made from polydimethylsiloxane (PDMS), which can be re-used several times. This allows for the cheap production of several samples. In short, the method works as follows: a photoresist pattern on a silicon wafer is formed by standard photolithography, the pattern is used as a PDMS mold, which allows for the creation of a PDMS master, which is inked with a fibronectin solution, the solution is then removed and the stamp is brought into contact with the cover slip which will act as the support, and finally the fibronectin is transferred to the cover slip where the stamp and the glass made contact but not in any other regions. The fibronectin stops bilayer formation while the bilayer will form on the glass cover slip when a vesicle solution is added to the system.

This method is not limited to the printing of protein patterns but can also be used for the blotting of lipid bilayers (Hovis and Boxer, 2000). Different

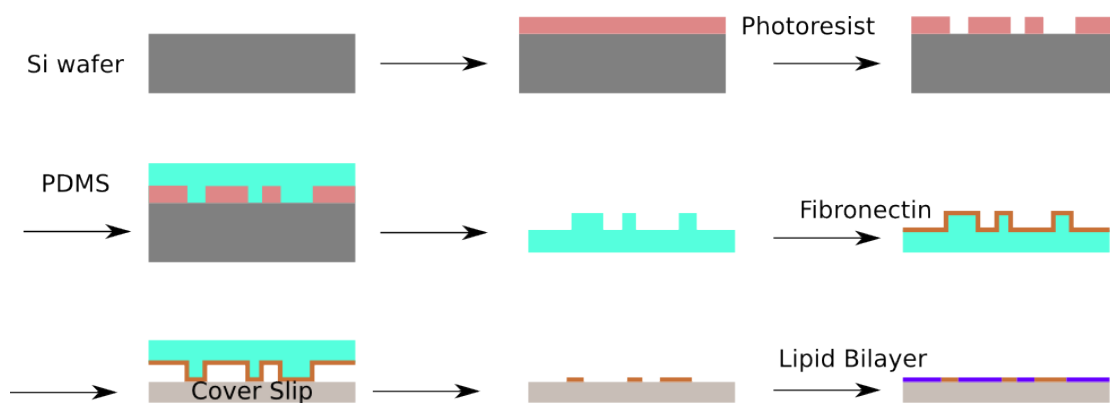


Figure 2.2: Principle of μ CP. From top left to bottom right: A silicon wafer is patterned with a photoresist. The pattern is then used to create a PDMS master, which in turn is being used to stamp fibronectin on a glass cover slip. The fibronectin inhibits bilayer formation and a lipid bilayer is formed where no fibronectin was printed.

molecules can also be printed and resolutions of the order of 100 nm can be reached using μ CP (Michel et al., 2002).

Other methods of patterning lipid bilayers include the partial polymerisation of an SLB and subsequent refilling of the layers removed using a detergent (Yamada et al., 2013), pre-patterned polymer brushes (Nakai et al., 2010), or air bubble collapse (Mager and Melosh, 2007) among others.

2.3 Electrophoresis

Electrophoresis is a way to achieve transport within membranes. Electrically charged molecules in the membrane are moved through an applied external field. If the charges are tagged by a dye or fluoresce themselves, their movement can be monitored using fluorescence microscopy.

The first time this effect was observed for membranes and proteins was in 1977, when Poo and Robinson showed that concavalin A receptors could be moved along a cell membrane with an externally applied electric field of 4 V cm^{-1} (Poo and Robinson, 1977). Later works achieved determination of the mobility of the membrane molecules μ by measuring steady state drift velocity using a supported bilayer (Stelzle et al., 1992). This means a lipid bilayer was

formed above a solid support such as glass, silicon oxide or silicon. The typical distance between the bilayer and the support is between 10 Å to 15 Å and filled with water molecules (Bayerl and Bloom, 1990; Johnson et al., 1991; Koenig et al., 1996). The use of a solid support allows the bilayer to keep some of its main properties such as fluidity and diffusion range of the free membrane (Groves et al., 1997) while it is a well localised and accessible through the surface for various analytical methods.

Later concentration gradients were used to determine the mobility of fluorescently tagged lipids. The gradients were achieved through the ongoing competition between diffusion and the field induced by the electric field. Put into an equation this means

$$\frac{\partial C}{\partial t} = D\Delta C - \mathbf{v} \cdot \nabla C, \quad (2.1)$$

where C is the concentration, D the diffusion coefficient and \mathbf{v} the drift velocity achieved through the electric field. The steady state condition

$$\frac{\partial C}{\partial t} = 0 \quad (2.2)$$

and

$$\mathbf{J} = -D\nabla C + \mathbf{v}C = 0 \quad (2.3)$$

have to be met, as both the change in concentration and the flux \mathbf{J} have to be zero. Under these conditions, the solution to equation 2.1 is

$$C(\mathbf{r}) = C_0 e^{\mathbf{v}\mathbf{r}/D} \quad (2.4)$$

with \mathbf{r} being the position vector in the membrane. This result is not only interesting for the case of DC electric fields but also for alternating fields. The distribution of the charged particles within the membrane is very similar then.

The distribution will have a maximum C_0 and then decay exponentially. The general principle of the movement of charged molecules within a lipid bilayer can be seen in figure 1.9. Initially the negatively charged dye molecules have an even distribution along the membrane and will then, under the force of the externally applied field, move towards the anode. Finally, an exponential decay in the distribution of charged molecules is reached. Figure 2.3 shows the effect of an applied electric field after two minutes onto charged fluorescent lipids within a bilayer. The initially even distribution of negatively charged Texas Red 1,2-dihexadecyl-sn-glycero-3-phosphoethanolamine (TxRed) has changed to an exponential profile against the fibronectin barrier.

The electrophoretic drift velocity can be determined via

$$\mathbf{v} = \mu z q \mathbf{E}, \quad (2.5)$$

where the mobility μ is defined by the Einstein relation

$$\mu = \frac{D}{k_B T}. \quad (2.6)$$

When considering bilayer membranes, the drift velocities or the mobility is reduced by a factor α , which is generally attributed to drag within the membrane (Groves and Boxer, 1995; Stelzle et al., 1992). This factor has so far been purely experimental, that has no theoretical explanation other than the drag in a membrane.

Stelzle *et al.* first discovered this effect and carried out a range of experiments to find the explanation for this factor (Stelzle et al., 1992). They ruled out the possibility of an error due to bleaching of the fluorescent dye as they found a maximum error of 5% due to bleaching. Also, the concentration of ions in the buffer was ruled out as an error source. The ions in the buffer form an oppositely charged cloud around the charged molecules in the bilayer and the

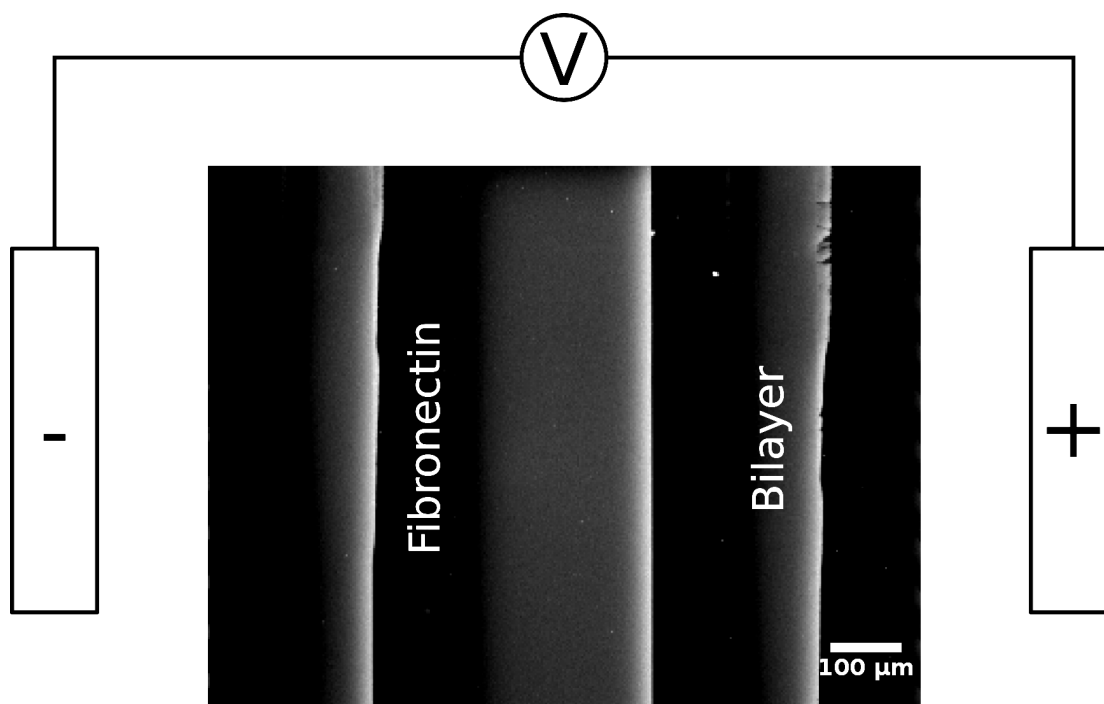


Figure 2.3: Fibronectin lines produced by μ CP as barriers to electrophoretic motion of charged lipids. The field of 62 V cm^{-1} was applied in horizontal direction. The movement of the charged fluorescent molecules can be seen through the increase of the fluorescence intensity towards the fibronectin barriers.

drag of the cloud that has to move with the charges in the bilayer could have been responsible for the drag. Using different concentrations of buffer solutions, no significant difference could be seen. In order to exclude electro-osmotic effects, oppositely charged types of molecules were used within the bilayer but no significant difference could be found.

Groves *et al.* used nitrobenzoxadiazole (NBD) labelled cholesterol to investigate the influence of electro-osmosis. NBD is fluorescent but uncharged and will therefore not be affected by the electric fields directly but will be hit randomly by the molecules from the double layer moving toward the electrode. Their experiment showed that the electro-osmosis has no significant influence on the movement of the NBD (Groves and Boxer, 1995).

Electrophoresis in lipid bilayers can be used for several applications. Corralled lipid bilayers in an electric field will have their charged components moved to one side of the corral, depending on the charge of the respective component. Such corrals can be arrayed and allow for the measurement of several

different quantities or different components in one single experiment. This has been shown using square bilayers in chromium corrals which were exposed to electric fields. Fluorescently labelled cholera toxin subunit (CTB) was used as marker for ganglioside (GM₁) tethers in the bilayer. The device had a sensitivity of up to 1 pmol dm⁻³, which is ten times higher than previously presented sensor platforms (Lee and Nam, 2012).

In addition to the electrophoretic force, the electroosmotic force can be used for transport purposes. It occurs near charged surfaces in fluid with ions in it, which will form a screening layer. This layer has the opposite charge compared to the surface and will therefore move into the opposite direction than the molecules in the surface. Yoshina-Ishii and Boxer used this to move tethered vesicles to one side and charged lipids to another (Yoshina-Ishii and Boxer, 2006). Just as the lipid molecules, the tethered vesicles are able to move in an electric field and the whole process can be reversed and repeated. Han *et al.* used the electro-osmotic effect on streptavidin to move it and to then determine its charge. This was achieved through careful adjustment of the zeta potential until electro-osmosis and electrophoresis cancel each other out. When this is the case, the zeta potential of the membrane equals the zeta potential of the protein. The change of the zeta potential of the bilayer was achieved by using different amounts of positively charged 1,2-dioleoyl-3-trimethylammonium-propane (DOTAP) (Han *et al.*, 2008).

Applications for electrophoresis in lipid bilayers include not only the movement of bilayer components, but it is also possible to determine the charge (Poyton and Cremer, 2013) or the zeta potential (Han *et al.*, 2009) of charged components (e.g. dyes or proteins) in the lipid bilayer. Both methods use the variation of drift velocity under an electric field to determine the apparent charge of a molecule in an SLB with the Einstein-Smoluchowski equation, which relates

the mobility μ with the charge of a molecule q :

$$\mu = \frac{Dqe}{k_{\text{B}}T} \quad (2.7)$$

with the diffusion coefficient D , the elementary charge e , the Boltzmann constant k_{B} and the temperature T .

Recently, electrophoresis has been used to separate different bilayer components which have different electrophoretic mobilities. Firstly, an SLB with high cholesterol content and therefore low mobility was formed, then a line of the SLB was removed using a PDMS stamp. This region was then refilled with lipids from vesicles containing a mixture of proteins and lipid dyes. After the SLB has formed in the line, an electric field was applied to move the charged components of the SLB in the line into the high cholesterol region of the SLB. Similar to gel electrophoresis, this resulted in a distribution of the different lipids and proteins according to their electrophoretic mobility. After freeze drying the samples and using mass spectrometry, it could be shown that the uncharged lipids had not moved into the high cholesterol region while the charged proteins and the dye have moved different distances into the matrix. This work shows how electrophoresis can be used for the separation of membrane components not just by their charge, but also by their electrophoretic mobility (Pace et al., 2013).

2.3.1 Double Layer Formation

Whenever a material is brought into a liquid, even if it is uncharged, there is the possibility of surface charges emerging on the material, e.g. due to chemical reactions on the surface. Other materials are uncharged in bulk but have a dipole that is orientated perpendicular to the surface. This can effectively be the same as a charged top layer on the material. The charges directly adsorbed to the surface make up the so-called first layer. Then a second layer spontaneously

forms from the ions in the liquid to shield the charges on the surface. In standard buffer solutions there are many ions, which can easily form a double layer but even in purified water, such as Milli-Q®, there are some ions, and a double layer will still form around charged surfaces.

An exact description of the electrostatic interactions between lipid head groups and the surrounding fluid is still not available. However, several approximations have been made and they give some insight on the physics of a double layer (Israelachvili et al., 1980). Gouy and Chapman introduced a theory in which the Poisson equation

$$\Delta\phi(x) = -\frac{\rho(x)}{\epsilon_r\epsilon_0} \quad (2.8)$$

is used. Here ϕ is the electric potential, ρ the charge density, ϵ_0 the permittivity of free space and ϵ_r the relative permittivity. In an ionic solution the charges ρ will be distributed as predicted by the Boltzmann law:

$$\rho(x) = -N_A q \sum_i Z_i c_i \exp\left(\frac{Z_i q \phi(x)}{k_B T}\right). \quad (2.9)$$

The sum is over all types of ions present, c_i denotes their respective concentrations and Z_i their charge number. Combining the last two equations for an electrolyte with only two ions, A^{Z+} and B^{Z-} the Poisson-Boltzmann equation is (Cevc and Marsh, 1987)

$$\Delta\phi(x) = \frac{2qN_A Z}{\epsilon_r\epsilon_0} \sinh\left(\frac{Zq\phi(x)}{k_B T}\right). \quad (2.10)$$

This is a very popular model, but it is limited in its possibilities. The interface of the bilayer and the water are not respected here and surface polarity is also neglected. Another shortcoming of this model is the treatment of the short range interactions; according to the model the attraction of charges at the surface is infinite. To avoid this problem, the so-called Stern layer, a hard core shell of the

ions, is introduced. But then the model differs again from reality, in assuming interactions only between the ions and the water, and simplifies both of them to be point charges in media of continuous dielectric permittivity. All of these simplifications make the Gouy-Chapman model valid only for highly diluted bulk solutions.

Going from theory to experimental applications, Kashimura *et al.* recently showed how to use the electric double layer for practical applications (Kashimura *et al.*, 2011). Here nanogap electrodes were fabricated and then used to control the diffusion of lipid bilayers. The small gap between two electrodes has been shown to be able to stop the spreading of a bilayer through it when an electric field is applied, and open again by turning the electric field off. The field applied at the electrodes induces a double layer around the electrodes, which in turn is able to stop the bilayer diffusion.

The combination of electrophoretic and electro-osmotic forces can lead to the independent control of the composition of the SLB and attached vesicles even if both are composed of lipids of the same charge (Yoshina-Ishii and Boxer, 2006). The lipid molecules in the SLB are mainly under the influence of the electrophoretic force while the attached vesicles are moved in the opposite direction by the electro-osmotic force. This allows for the measurement of membrane-membrane interactions by moving the vesicles into regions of the membrane with a different composition than the region they were attached to initially. In addition to that, the vesicle-vesicle interactions are increased since the vesicles can be concentrated to a higher relative concentration than initially.

2.4 Impedance & Cyclic Voltammetry

The proteins involved in the light harvesting process undergo or facilitate redox processes either in the membrane itself or in the direct environment, as the proteins themselves are membrane proteins. First measurements on membrane

enzymes were undertaken on a graphite electrode (Sucheta et al., 1992). Initially these electrodes were successfully used for different membrane enzymes.

To overcome this problem, modified gold electrodes were developed. They allow for the enzymes to be incorporated into a membrane while being attached to an electrode at the same time. The first systems used to do this were self-assembled monolayer (SAM) modified electrodes (Kalb et al., 1992; Plant, 1993). In these systems, a hydrophobic SAM is formed on a conductive (mainly gold) electrode, rendering the surface conductive and hydrophobic at the same time. This then allows for the formation of a hybrid lipid membrane (HLM) on the surface where the distal layer consists of lipids which have their hydrophobic chains now in contact with the previously formed SAM thus completing the HLM. These systems can be used for the determination of the redox properties of membrane enzymes but have the disadvantage of not leaving enough space for many transmembrane proteins on the proximal side of the membrane. For the incorporation of of transmembrane proteins, the SAM can be changed to a hydrophilic one which is combined with hydrophobic membrane tethers. The hydrophilic SAM will allow the lipid head groups to be close to the surface of the solid support while the hydrophobic tethers aide bilayer formation as they self insert into the hydrophobic core and help to induce vesicle fusion and rupture.

The formation of a lipid bilayer on a modified gold electrode can be followed by impedance spectroscopy. In this process the complex impedance Z is measured depending on the frequency ω and is defined as

$$Z_R = \frac{U}{I}, \quad Z(\omega) = \frac{U(\omega)}{I(\omega)}, \quad (2.11)$$

where U is the voltage and I the current. For a resistor this is the same as the resistance R since a resistor does not change its ratio between applied voltage and current through the resistor for different frequencies. In contrast to that, the

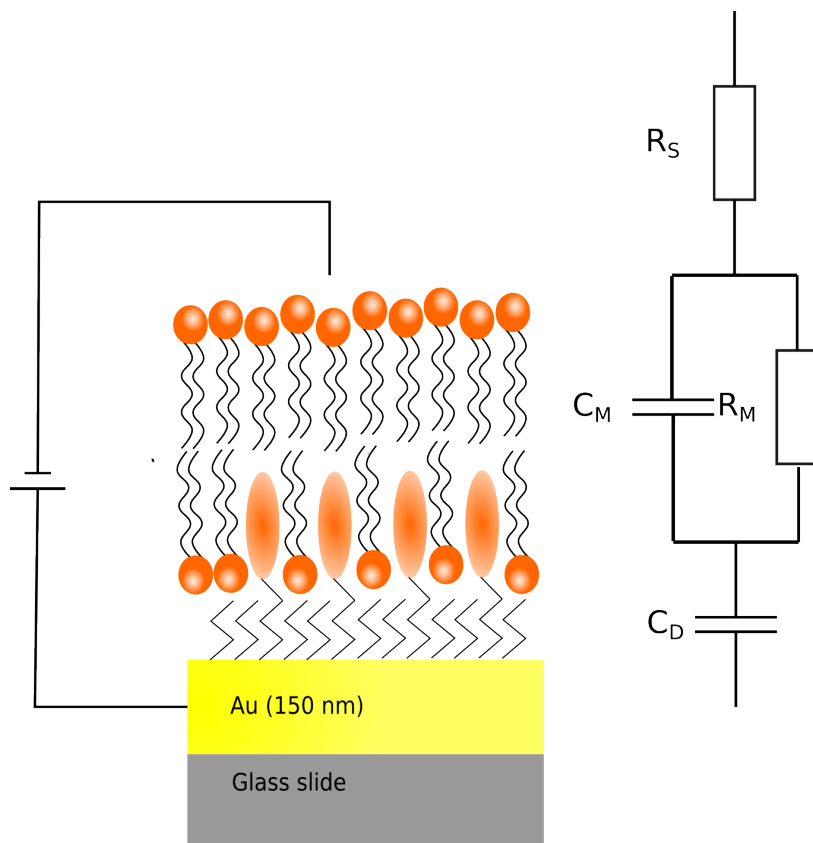


Figure 2.4: Schematic of an impedance set-up showing the tethered SLB on a conductive (Au) support on the left and the equivalent circuit of the membrane and the solution on the right. The membrane is represented through a capacitor and a resistor in parallel (C_M and R_M respectively), the solution is represented by a resistor R_S and the double layer forming on the solid support is represented through a capacitance C_D .

impedance of a capacitor is frequency dependant:

$$Z_C(\omega) = \frac{1}{i\omega C}, \quad (2.12)$$

where C denotes the capacitance. Complex systems are usually represented by an equivalent circuit. The representation of an SLB on a metal surface is shown in figure 2.4. The ions in the double layer above the metal create a capacitance C_D . The bilayer itself is equivalent to a parallel circuit of a capacitance C_M and a resistance R_M . The solution only exhibits a resistance R_S . The impedance of a circuit consisting of two elements in parallel and two elements in series is given through

$$Z = Z_1 + \frac{Z_2 Z_3}{Z_2 + Z_3} + Z_4. \quad (2.13)$$

When substituting the impedance of a capacitance for Z_1 and Z_2 and the impedance of a resistor for Z_3 and Z_4 , one obtains

$$Z = \frac{1}{i\omega C_D} + \frac{R_M}{1 + R_M i\omega C_M} + R_S. \quad (2.14)$$

In order to take the fact into account that an SLB is not a perfect bilayer, it can be modelled by a constant phase element (CPE). The impedance of a CPE is defined as

$$Z = \frac{1}{Q(i\omega)^{n'}}, \quad (2.15)$$

with Q being the pre factor for the CPE and n being the exponent which is an empirical factor. For a perfect capacitor n is 1 while n is zero for a resistor. To represent the obtained data, in this work Cole-Cole plots are used, in which the real part of the admittance Y' is plotted against the imaginary part of the admittance Y'' ; both are divided by the frequency ω . The admittance is defined as:

$$Y = \frac{1}{Z}. \quad (2.16)$$

2.5 Finite Element Analysis

Partial differential equations can be solved with finite element analysis (FEA) with the help of suitable boundary conditions. The whole problem over a given area (domain) is divided into smaller regions, the finite elements, for which the problem is solved individually. The solution for the whole domain is then found using variational methods to minimise the error associated with the approximation.

The diffusion in a two dimensional lipid membrane is governed by Fick's law

$$\mathbf{J} = -D\nabla\phi, \quad (2.17)$$

where \mathbf{J} is the diffusive flux and ϕ the concentration of any species. This shows that diffusion will always work against the concentration of a species into a certain region, as the diffusive flux is always pointing away from regions of high concentration.

When an external electric field is applied, the problem can be described with the Nernst-Planck equation (Han et al., 2008):

$$\frac{\partial c}{\partial t} = \nabla \cdot \left(D \nabla c - uc + \frac{Dze}{k_B T} c \left(\nabla \phi + \frac{\partial \mathbf{A}}{\partial t} \right) \right), \quad (2.18)$$

with t being time, D the diffusion constant, c the concentration of a given species, z the charge number, e the charge of an electron and T the temperature. This partial differential equation has to be solved to determine the concentration of the species of interest at a given time.

In order to solve the partial differential equation, the geometry in question is divided into smaller domains, the finite elements. This process is called meshing. In each of the mesh cells the equation will be solved and the solutions will then be combined to find an overall solution. The degrees of freedom scale with the amount of mesh cells, therefore the calculations will take longer the more mesh cells there are in the model. On the other hand, the mesh cells determine the accuracy to which the problem will be solved. To optimise this trade off between computational cost and accuracy of the results, the regions which are of least interest to the experiment can be meshed with larger cells while the regions of high interest can be meshed with smaller cells.

A good example of the use of the finite element model can be seen in section 3.5. In this section finite element modelling is used to determine the concentration of charged molecules of interest in a Brownian Ratchet.

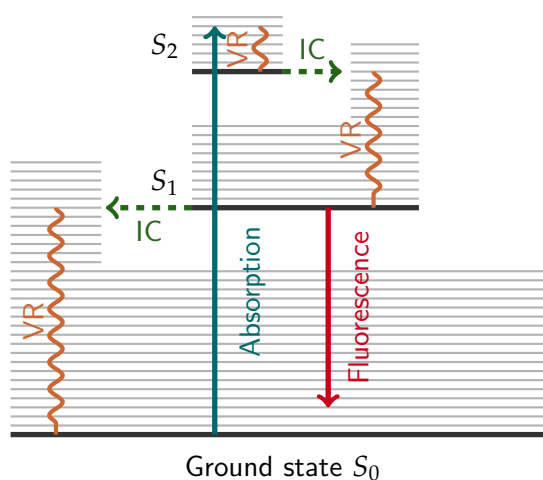


Figure 2.5: Jablonski Diagram of a simple fluorescence molecule. The excitation is marked in blue, the fluorescence in red. IC stands for internal conversion where the molecule changes its state $S_i \rightarrow S_j$ in a non-radiative way, VR denotes vibrational relaxation of the molecule, again non-radiative.

2.6 Fluorescence Microscopy

The first observations of fluorescence were made in 1560 and 1565 by Bernardino de Sahagún and Nicolás Monardes respectively (Acuña et al., 2009). It took a few hundred years from then until the phenomenon was understood as the change of the wavelength of light while interacting with a material in 1852 by George Stokes (Stokes, 1852).

2.6.1 Theoretical Principles

Fluorescence is based on the difference in excited and relaxed states of electrons in molecules. When a molecule has energy states for electrons with an energy difference equivalent to the energy of a photon $h\nu_{ex}$, an electron can change from the ground state S_0 into an excited state S_1 upon illumination of light of suitable wavelength. The electron will then, after some time, decay back into its original state. When this occurs, the electron loses energy and can emit it in the form of electromagnetic radiation (i. e. light). The energy difference of the molecular electron levels determine what wavelength the emitted photon

has. In a more detailed view, as seen in figure 2.5, the system is excited from its ground state S_0 to an excited electronic state S_2 through the absorption of a photon. The grey lines indicate vibrational states. The system is excited into a higher level of vibrational state and then relaxes back to the vibrational ground state in S_2 . From S_2 the system goes into an energetically lower state S_1 . Here the system also goes through vibrational transitions into a vibrational ground state. From S_1 the system can go to S_0 via the emission of a photon. This emitted photon is of lower energy than the absorbed photon.

Problems with this can occur if the system undergoes too many inter-system crossings (non radiative decay paths in figure 2.5). These transitions allow for a non-radiative loss of the energy stored in the excited states. This means that the system goes back to the ground state without the emission of a photon. The effect can occur when the molecule of the fluorophore has a high quantum mechanical probability for these transitions to happen. Sometimes the fluorescence photon cannot be observed because it is being absorbed before it reaches the detector. This can be due to several reasons. Firstly, the fluorophore molecules have electronic transitions which are of a suitable energy difference to absorb photons emitted by other fluorophores. This effect of self-quenching occurs especially, when the concentration of fluorophore in a certain region is very high and an emitted photon there are many other fluorophore molecules in the vicinity of the emitting fluorophore molecule.

2.6.2 Experimental Details

In an epifluorescence microscope the light source usually is either a white light, such as a high pressure mercury arc lamp, which is then being filtered by an excitation filter so that only the relevant part of the electromagnetic spectrum is transmitted towards the sample, or the light source is a laser which is already monochromatic and thus removes the need for further filtering of the excitation

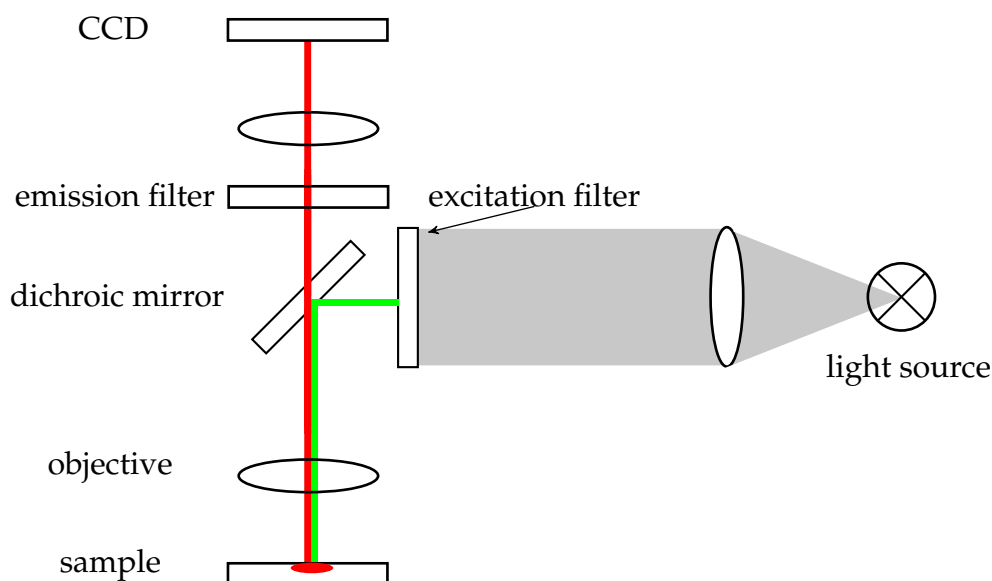


Figure 2.6: Schematic of an epifluorescence microscope. The white light from the light source is filtered, directed onto the sample where light of a different wavelength is emitted and passes through a second filter into the CCD where it is detected.

light. The excitation light is then reflected of a dichroic mirror, which reflects short wavelength light, and focused onto the sample, where it interacts with the sample and emits light of a longer wavelength. The emitted light is then being passed through the objective and the dichroic mirror as it is of a longer wavelength than the excitation light. A charge coupled device (CCD) camera records the fluorescence photons. The set-up of a fluorescence microscope is shown in figure 2.6.

2.6.3 Fluorescence Recovery after Photobleaching

In order to investigate the diffusive behaviour of fluorescent samples, fluorescence recovery after photobleaching (FRAP) can be used. This method allows for the determination of the diffusion coefficient of a fluorescent probe in a sample. It works through photobleaching of a region of the sample by short wavelength light (usually UV) which cleaves covalent bonds in the fluorophore molecules. Subsequently, the recovery of the fluorescence in the same region is monitored. As can be seen in figure 2.7, initially all fluorophore tagged molecules are fluorescing (red head groups), after bleaching, the central region is no longer

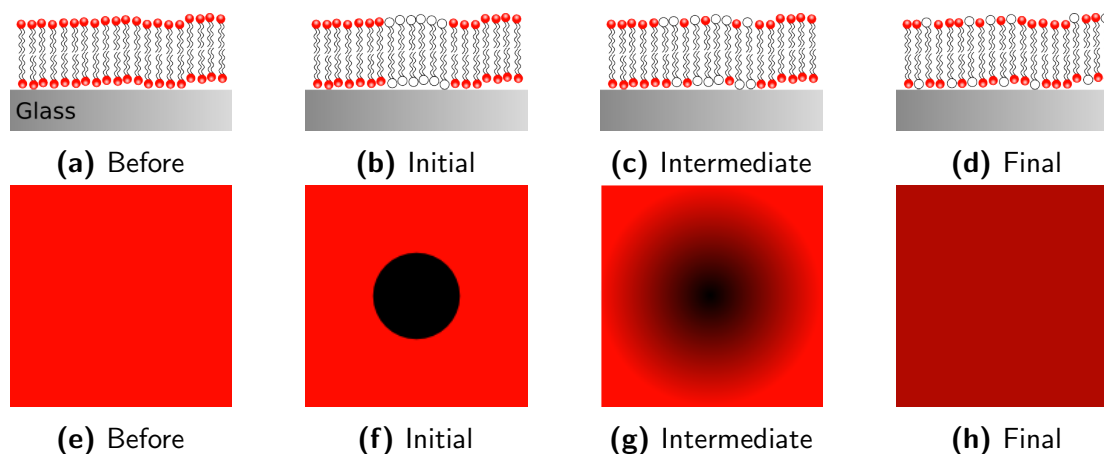


Figure 2.7: Schematic of a FRAP experiment and the observed fluorescence images. The top row shows the side view of the lipid bilayer, the bottom row the images as they would be captured by a fluorescence microscope. For clarity, all lipids in the top row have been drawn as fluorescently labelled in an experiment this would only be the case for a small fraction of the molecules. Initially all dye molecules are fluorescent, after the bleach the molecules in the bleach region are no longer fluorescent. Over time the bleached molecules exchange with the fluorescent molecules until no difference between the bleach region and the remaining bilayer can be observed.

fluorescent. In the intermediate state, the bleached lipid molecules have started to diffuse out of the central bleached region and have been replaced with fluorescing molecules. Finally, the bleached molecules will distribute evenly over the whole lipid bilayer and the bleached region will no longer be visible. An overall loss of intensity can sometimes be noted (depending on the reservoir size of unbleached molecules). The speed at which the fluorescence signal in the bleached region changes relates to the diffusion constant D of the sample. As shown in equation 3.10, the mean square displacement in two dimensions is proportional to $4Dt$, where t is the time the sample is observed for.

The diffusion coefficient is both a measure of the quality of the bilayer itself and a measure for the chemical interactions between the different molecules in the lipid bilayer. When the lipid bilayer consists only of one main component tagged with a small amount of fluorophores, the diffusion coefficient D can highlight small defects, which otherwise would not be seen optically. The diffusion coefficient will decrease with an increase in defects as these will hinder diffusion, which decreases the observed macroscopic diffusion coefficient.

The diffusion coefficient can be calculated in several different ways. Here the two methods which were mainly used are explained. Firstly the Axelrod method and then, secondly the Gaussian method.

In the Axelrod method (Axelrod et al., 1976), the diffusion is measured directly through the fluorescence counts in the previously bleached region. The pre-bleach fluorescence counts from the region of interest (ROI) are normalised to one and the first image after the bleaching process is taken as the zero value. Then the fluorescence counts are observed while the lipids are free to diffuse. This recovery curve is then plotted against time and a Box-Lucas curve is fitted to it (Dodd et al., 2008):

$$I(t) = A \left(1 - e^{-b(t-c)} \right). \quad (2.19)$$

The parameters are the amplitude of the Box-Lucas curve A , the time constant b and the offset c . The amplitude A is equivalent to the mobile fraction of the lipids in the bilayer and gives an indication of both the quality of the bilayer and the interactions with the underlying substrate. From the time constant b the diffusion coefficient D can be calculated as follows (Axelrod et al., 1976)

$$D = k \frac{bkr^2}{-4 \ln(1/2)}, \quad (2.20)$$

where k is a correction factor for different bleach spot shapes (Gaussian, top-hat, etc.) and r the radius of the bleach spot.

This method can be expanded to the analysis of two diffusion coefficients, which can be useful, when the interaction between the proximal leaflet of the lipid bilayer is strongly interacting with the support and has a significantly different diffusion coefficient to the distal leaflet. This is done by introducing a second term in the Box-Lucas curve:

$$I(t) = A_1 \left(1 - e^{-b_1(t-c_1)} \right) + A_2 \left(1 - e^{-b_2(t-c_2)} \right). \quad (2.21)$$

Here, A_1 and A_2 are the respective mobile fractions of the two diffusion coefficients, $A_1, A_2 < 1/2$ needs to be fulfilled. The time constants b_1 and b_2 can now be used to determine the individual diffusion coefficients.

A second method to determine the diffusion coefficient of a lipid bilayer using FRAP uses the change of the shape of the bleach spot over time. Immediately after bleaching, a top-hat function for the intensity can be expected. Shortly thereafter diffusion will change this from a top-hat into a Gaussian distribution. Initially, this will be a very sharp Gaussian peak, as the bleached lipids diffuse out of the bleaching region and non-bleached lipids start diffusing in, the Gaussian peak will become wider. Therefore, the full-width-half-maximum (FWHM) of the Gaussian peak will change from the size of the initial bleach spot to a larger radius until the difference between noise and the Gaussian peak becomes too small to obtain fits with reasonable confidence values.

The diffusion coefficient is then obtained from a linear fit of the FWHM (ω) squared against time. D is then equal to half the slope of the linear fit (Seiffert and Oppermann, 2005).

This method is more reliable in determining the diffusion coefficient. It will give more consistent results between different experiments on the same sample and is less prone to being influenced by changing of parameters such as the bleach spot size or the bleaching time. In contrast to the Axelrod method, this method does not return a value for the mobile fraction.

2.7 Dark Field Microscopy

In contrast to bright field imaging, in dark field microscopy the light being detected is not directly reflected from or transmitted through the sample but is scattered of it. The principle of a dark field microscope is shown in figure 2.8. The central part of the light beam is blocked out by an annular aperture which only allows the the outer part of the beam to interact with the sample. The light

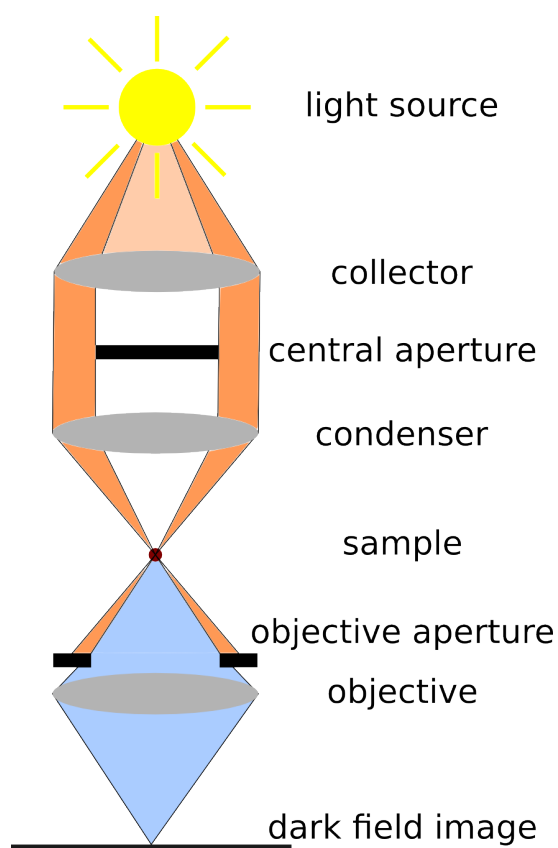


Figure 2.8: Dark field microscopy set-up, the light which is being scattered off the sample is being used for imaging. The light is guided onto the sample such that the central part of a parallel beam is blocked out, for imaging this central region is then used to only see the scattered light while blocking out the outer region of beam.

then interacts with the sample and can scatter off the sample. This will result in the path of the scattered light being changed and going through the central path where there would be no light otherwise. The outer part of the light is then blocked out before it goes to the objective by a second aperture. Therefore, only the scattered light is passed through to the image plane, making the background of the image appear dark, which has led to the name of the method.

The main disadvantage of dark field microscopy is its need for a strong light source for the illumination as most of the light is blocked off and only the scattered part is being used to form the image. Using dark field scattering allows for the imaging of different properties than the use of bright field microscopy. Parts of an object which might be dark in a conventional bright field image may appear in a dark field image, as they scatter, but do not reflect light, such as small walls of pits and groves. Also, small particles which scatter light can

become visible in dark field microscopy. Individual NPs are invisible in bright field microscopy (due to their size) but scatter light and can become visible in the dark field. In addition to that the plasmonic properties of NPs can be made visible. The scattering of an individual NP strongly depends on its surrounding, as the plasmon resonance changes with the refractive index and the possibility of plasmonic coupling to materials close to the NP.

2.8 Plasmonics

The plasmonic nature of metals and semiconductors have been used for a long time. Different applications of the localised electric field have been shown so far. These include surface enhanced Raman scattering (SERS), metamaterials, plasmonic waveguides or plasmonic antennas. They all make use of the same properties of metals and semiconductors.

2.8.1 Theoretical Background

Electrons in the conduction band of a metal or a semiconductor can move within the bulk material. An external electric field will therefore displace the electrons in the free electron plasma from their original position, leaving behind a positively charged region of the bulk material, whereas the region where the electrons have moved to is now negatively charged. This will then drive the electrons back into their original position again, leaving behind a positively charged region of the bulk material. This oscillation then continues until it is stopped through damping forces. The quantum of this plasma oscillation is called a “plasmon”. The energy of a bulk plasmon can be estimated through

$$E_p = \hbar \sqrt{\frac{ne^2}{m\epsilon_0}} = \hbar\omega_p, \quad (2.22)$$

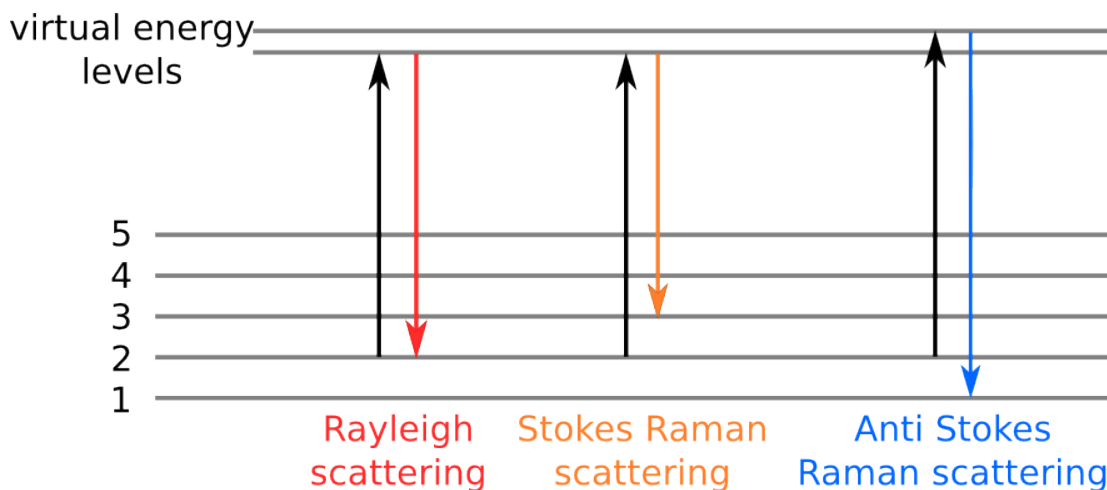


Figure 2.9: Principle of Raman spectroscopy showing the three different scattering mechanisms possible. The black arrow denotes the absorbed photon and the coloured arrows denote the scattered photons for the different processes. In Rayleigh scattering the energy of the absorbed and scattered photon is identical while for both Stokes and Anti Stokes scattering the energy of the scattered photon is different to the absorbed photon. This energy difference is used to gain information about the vibrational levels in a molecule.

with \hbar being the reduced Planck constant, n the free electron density, e , m the electron charge and mass, ϵ_0 the permittivity of free space and ω_p the plasmon frequency.

2.8.2 Raman/SERS

In Raman spectroscopy, the inelastic scattering of light is used to obtain information about vibrational modes present in the system. From the vibrational modes more information can then be extracted, such as phase, chemical composition, bonds or sensing of certain molecules.

Different interactions between the incident photons and the molecules under investigation are possible in vibrational spectroscopy. Light can interact in different ways with atoms. An incident photon with the energy $h\nu$ can be absorbed by an atom only if the difference between the ground state and the first excited state $E_1 - E_0$ is less or equal to the energy of the photon:

$$h\nu \geq E_1 - E_0. \quad (2.23)$$

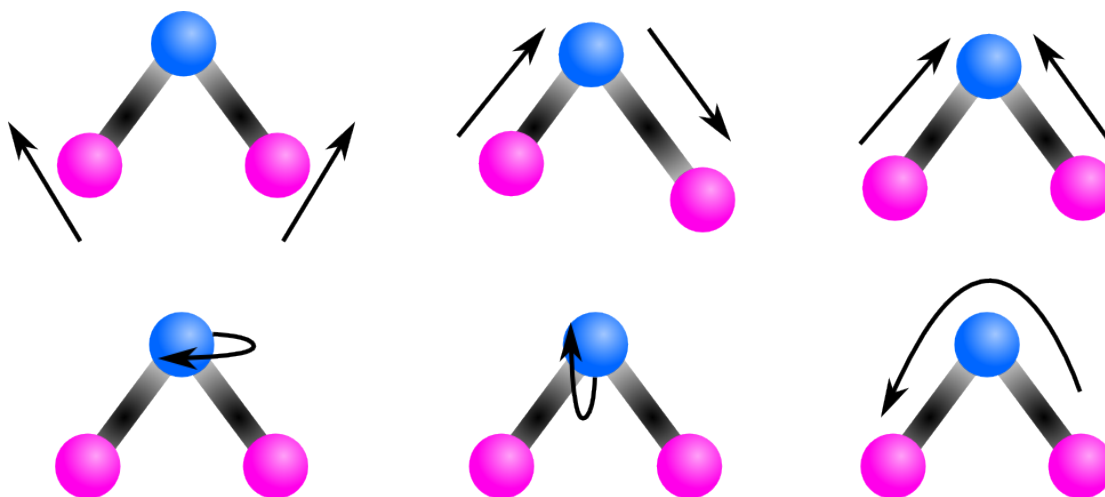


Figure 2.10: Vibrations possible for a water molecule. From top left to bottom right the following vibrations are shown: bending, asymmetric stretch, symmetric stretch, and the three rotations around the x,y and z axis.

$E_1 - E_0$ is usually of the order of several electron volts and therefore this condition is not always met for visual light. Therefore, quantum mechanics does not allow photons with energies less than $E_1 - E_0$ to be absorbed and they undergo scattering processes as shown in figure 2.9. Most of these are elastic scattering processes resulting in the same energy, and therefore wavelength, for incident and scattered photons. This process is called Rayleigh scattering and generally occurs when a photon interacts with particles much smaller than its wavelength, but can also happen from single molecules. A less likely process (around 1 in 10 000 000 photons) is Stokes Raman scattering. In this process a molecule absorbs an incident photon, changes into a virtual energy state, and then goes back into an energetically higher vibrational state than the original one, and emits a photon of a different wavelength. The virtual energy levels E_v lie below the molecular excitation levels used in fluorescence microscopy. This shift, which is generally given in inverse wavelengths (cm^{-1}) is then measured with a spectrometer. The difference between the two photons is called the Stokes shift. An even less likely process is Anti-Stokes scattering. In contrast to Stokes scattering, the molecule is excited from a vibrational excited state into a virtual energy level

and then relaxes into an unexcited state. In this case, the wavelength is not red- but blue-shifted.

Different vibrational modes are possible in different molecules. A straight molecule like $O=C=O$ cannot rotate along the $C=O$ axis as this rotation cannot be excited. The possible vibrational modes for a water molecule are shown in figure 2.10. The two hydrogen atoms can bend against the oxygen, or can stretch symmetrically or asymmetrically. In addition to that, the whole molecule can also rotate along all three axis, x , y and z .

Although Raman spectroscopy itself has many advantages and can be used for Raman microscopy, which gives spatial information with a high resolution, the inherent problem of the very unlikely Stokes scattering process cannot be resolved. To get a larger quantum yield, different mechanisms have to be used. A very promising approach is the use of surface effects. First discovered in 1974 (Fleischmann et al., 1974), the surface enhanced Raman (SER) effect occurs on any given rough metal surface. Since then it has become clear that silver and gold are the most effective substrates for SERS¹. Their roughness has to be in the order of the wavelength of the excitation.

The strong and localised electric field produced by the surface plasmons is very sensitive to changes on or close to the surface of the metal. Very small changes in the composition or even single molecules passing by the metal island can be sensed using this effect.

The exact enhancement factor achieved from this process is still under debate in the scientific community. Generally, factors between 100 and 10^{12} are published, but the order of around 1000 to 10 000 seems to be accepted in more recent publications (Kneipp et al., 1997; Ren et al., 2011; Sweetenham et al., 2011; Weitz et al., 1983).

¹Although silver is known to be the better substrate, gold has the advantage of being chemically much more stable. Thus, especially for biosensors, where quantification can be very important, gold can be the better choice than silver.

Not only the exact enhancement factor, but also the exact process underlying the SERS effect is not agreed upon. Two mechanisms are thought to increase the signal. First, chemical binding changes the bonds and therefore the polarisability of the molecules. The influence of this effect is questionable as not all molecules bind to the surfaces used for SERS and some authors attribute no influence to it. On the second hand, electrical processes enhance the detected signal. This effect is generally given more importance and is sometimes referred to as the only relevant process (Kukushkin et al., 2013). The electric enhancement process is due to the fact that the signal obtained from a SERS setup is proportional to E^4 and this is used by enhancing the incident electric field locally through localised surface plasmons (LSPs). These are non-propagating electronic excitations in the free electron gas of the metallic structures.

In this work, the enhancement for SERS was generated using a NP on a mirror geometry (Eah et al., 2005). Gold NPs were used in conjunction with lipid membranes which were on a gold support. This lead to the coupling of the plasmon of the individual gold NP to their respective mirror images, as a charged particle in front of a metallic surface will result in the surface charges in the metal rearranging in such a way that the particle sees its mirror image in the surface (Wirth et al., 2014). The coupling of the plasmon leads to a strong electromagnetic field in the gap between the NP and its mirror image. As can be seen in figure 2.11, the strong field enhancement is produced in the region of the lipid membrane. Here, an HLM was used instead of an SLB. Vesicles do not spontaneously rupture and form bilayers on gold surfaces, therefore the surface had to be changed from being bare gold to hydrophobic SAM. The SAM allowed for the formation of a lipid monolayer on top of the SAM as the hydrophobic tails of the SAM interact with the hydrophobic tails of the lipid molecules. With this setup it is possible to sense changes in the lipid membrane with a very high sensitivity, possibly down to the single molecule level.

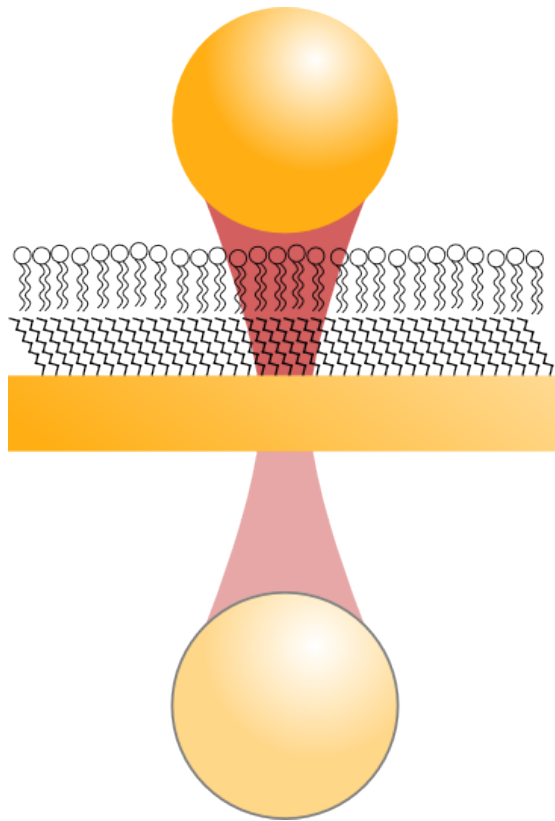


Figure 2.11: Gold NP on top of an HLM on a gold substrate modified with a SAM. The NP interacts with its mirror image on the other side of the gold surface and upon excitation a coupled plasmon (indicated in red) is produced. The size of the NP is not to scale.

For the theoretical analysis of this set-up, it is assumed that the NP has a diameter d which is much smaller than the wavelength λ of the incident light. This assumption is used to treat the particle as if it was in a constant electric field. Surprisingly this gives very good results already for visible light and particles of ≈ 100 nm in size although $d = \lambda/6$. For an ideal NP the extinction coefficient can be analytically determined and only depends on the permittivity of the surrounding medium ϵ_m , the permittivity of the material of the NP ϵ_r and the volume and shape of the structure. Also, the coupling between the NPs should be taken into account, as it mainly influences the shape of the plasmon resonance but also the exact position in the spectrum (Maier, 2010).

2.8.3 Applications

SERS was first discovered on chemically roughened silver in 1974 (Fleischmann et al., 1974) and the enhancement of the scattered signal was initially attributed to the aggregation of the detected species on the electrodes surface. It was in 1977 when the effect was explained through an electromagnetic and a charge transfer effect (Jeanmaire and Van Duyne, 1977; Landau, 1977).

As the enhancement makes Raman spectroscopy much more sensitive, SERS has found a wide range of applications, whenever the material to be detected is only available in very small amounts. Structures to obtain a surface enhanced signal are always based on metals which exhibit surface plasmon resonances. These can be roughened metal surfaces, NPs or nanostructures. While a roughened metal surface gives the strongest enhancement, it also gives the least spatial resolution. When either using NPs or -structures, the spatial resolution can be regained when the spectra are taken from a small amount of hot spots or from just a single hot spot. Especially the nanostructures have been investigated and optimised. The influence of size and spacing have been investigated thoroughly (Grand, 2003).

The approach can be used to a various amount of biophysical and biological applications. Silver NPs synthesised on the outside cell wall of bacteria have been used to obtain Raman signals from different bacteria in solution. This has allowed the researchers to not only reduce the amount of sample needed to detect bacteria in water, it also allowed for a distinction between *E. coli* and *S. epidermis* (Zhou et al., 2014).

Another way of using SERS is to determine the binding of ligands to receptors via the change in scattering spectra, as was shown using the example of biotin and streptavidin (Galarreta et al., 2011).

2.8.4 Single Molecule Detection

Despite the fact that bulk Raman spectroscopy needs a large amount of sample molecules, SERS is a very sensitive technique for molecules close to the surface which is enhancing the signal. Through the strong enhancement of rough metal surfaces, especially silver, the sensitivity of Raman spectroscopy can be enhanced up to the level of single molecules. The first report of SERS applied to single molecules is from 1997 (Kneipp et al., 1997), where colloidal silver was used to detect single molecules of crystal violet. This report took advantage of the silver particles forming clusters which resulted in a very broad band enhancement and a strong chemical enhancement. In the same year rhodamine 6G was used as a proof-of-concept molecule to show that individual silver NPs can be used to spectroscopically analyse single molecules (Nie, 1997).

Single molecule resolution has also been reached on bio-molecules. Silver NPs were used again to demonstrate the ability of SERS to detect individual hemoglobin protein molecules (Xu et al., 1999). In contrast to the previous reports, where the chemical enhancement was of importance as well as the electromagnetic enhancement, here only the latter seems responsible for the high sensitivity. This becomes especially evident with the main signal stemming from hemoglobin molecules which are between two NPs, allowing the plasmons to couple and lead to an especially strong enhancement in the gap. Here, the enhancement factor is estimated to be 10^{10} .

2.8.5 Probing Lipid Membranes

The enhancement from SERS can also be used to detect small changes in the lipid membrane. An interesting experiment was carried out, showing the mixture of lipids from vesicles to hybrid bilayers on nanoshells. Here, deuterated small unilamellar vesicles (SUVs) were formed via extrusion from MLVs. A gold nanoshell with an outer diameter of 85 nm was then used as the source of the Raman enhancement. The shells were also coated with an HLM from

hydrogenated lipids. In the Raman spectrum the difference between C-H and C-D vibrations is clearly visible, which allowed the system to sensitively and in real-time measure the exchange of deuterated lipids from the SUV to a coated nanoshell using the C-D vibration line. It was even possible to monitor the change of lipid composition in real-time, as SERS is a very sensitive analysis method (Kundu et al., 2009).

Another application of SERS on lipid membranes is the direct imaging of lipids in a membrane. This allows for a direct imaging of the composition of the membrane without the need for a lipid dye or a destruction of the membrane in mass spectroscopy. With the high spatial resolution of SERS it is even possible to map the distribution of different lipids inside the membrane (Ren et al., 2011). This idea has also been pursued by other groups and has been combined with the use of atomic force microscopy (AFM) to obtain height information using the same instrument as for the spectral information. This was achieved by using an AFM tip as a light guide towards the sample. Using this method it was possible to use differently structured substrates to optimise the surface enhancement obtained through the metal structures. Different molecules such as adenosine triphosphate (ATP) and Rhodamine 6G have been assembled in monolayers and successfully been imaged. In addition to that a lipid bilayer was formed between the structures and the SERS data from SLBs made from 1,2-dipalmitoyl-sn-glycero-3-phosphocholine (DPPC) were obtained (Sweetenham et al., 2011).

In addition to membrane components, it is also possible to detect their redox state. To show this, the redox couple NADH/NAD^+ was embedded into an HLM which was tethered to a gold electrode with ubiquinone terminated thiol SAMs. The ubiquinone mediated the redox reaction between the NADH and the NAD^+ as a mimic of the initial stage of the respiratory system. Cycling the voltage slightly over the respective redox potentials of NADH/NAD^+ led to changes in the SERS signal, which were attributed to the redox couple in the membrane (Ma et al., 2011).

2.9 Experimental Procedures

This section describes the details of the experiments presented in this work. It covers the experimental procedures needed to prepare the surfaces, bilayer formation on different substrates and the details of the FEA simulations.

2.9.1 Surface Preparation

In order to facilitate the formation of SLBs surfaces have to be cleaned on a molecular level and need to be hydrophilic. The glass surfaces used were No. 1 cover slips (thickness between 0.13 mm and 0.16 mm) and were obtained either from Menzel-Gläser, Germany or from VWR, UK. Initially, the surfaces were cleaned by sonication in an ultrasonic bath in a 2 % Decon solution, followed by MilliQ and isopropanol, each for 10 min. Subsequently, the cover slips were cleaned in a piranha bath (70 % sulphuric acid, 30 % hydrogen peroxide) for 10 min at around 80 °C. Finally, the surfaces were rinsed under a stream of MilliQ to remove any residual acid on the surfaces. Glass surfaces were stored in MilliQ and used within a week after preparation.

Polymer surfaces were cleaned using a reflux setup in which isopropanol was used as a cleaning agent. The samples went through at least five reflux cycles before they were stored in fresh MilliQ and used within a week.

Gold surfaces on cover slips for cyclic voltammetry and impedance measurements were prepared through template stripping (He et al., 2005; Naumann et al., 2003; Wang et al., 2010). Here, gold was evaporated onto the template of a silicon wafer using electron beam evaporation without an adhesive layer between the gold and the substrate. The glass cover slips were then glued to the gold surface using the low viscosity epoxy glue epo-tek 377 from Polyscience, Switzerland. The glass substrates were then mechanically stripped of the surface when they were needed. As the gold surface which is later used in the experiment is in contact with the silicon template until it is stripped off and was

evaporated onto the silicon in a vacuum chamber, these surfaces are intrinsically clean and do not require further treatment before use. In addition to that, the surfaces can also be stored for a long time and no deterioration was observed even after two months.

2.9.2 Vesicle Preparation

The preparation of SUVs was carried out using tip sonication. Initially, the desired amounts lipids obtained from Avanti Polar Lipids, Alabaster, US, were taken from a stock solution, which was kept at -20°C in a 50:50 solution of isopropanol:chloroform at concentration of 1 mg ml^{-1} . This solution was then dried under a continuous stream of nitrogen for at least 30 min to remove the solvents. The lipids were then desiccated for 2 h to remove any residual solvent. The dried lipid cake was then resuspended in the desired buffer for the experiment, usually phosphate-buffered saline (PBS), to a concentration of 1 mg ml^{-1} . This solution was then vortexed until the lipid cake had fully dispersed and the solution became cloudy. The solution of MLVs was then tip sonicated for 30 min to form SUVs of the desired lipids.

Fluorescent dyes were incorporated into the SUVs at different concentrations. Atto-Tec dyes have a high fluorescence yield and were used at 0.125 mol%. For TxRed, which has a lower fluorescence yield, the concentration was increased to 0.5 mol% while NBD based dyes were used at 2 mol% as this dye photobleaches quickly.

Binding Experiments

For the experiments where binding coefficients for different ligand-receptor combinations were measured, the composition of the vesicles and their respective preparation methods were varied as follows.

The cell wall precursor lipid II (Wiedemann et al., 2001) was incorporated into Egg PC (Avanti Polar Lipids, Alabaster, AL, US) vesicles at a concentration

of 2 mol%. The concentration of TxRed was 0.25 mol%. The preparation of the vesicles followed the same protocol as described above. The antibiotic vancomycin was obtained from Life Technologies, Paisley, UK and was labelled with boron-dipyrromethene (BODIPY). Vancomycin was dissolved in PBS and stock solutions were made with a concentration of $10 \mu\text{mol dm}^{-3}$. The solutions of varying concentration were prepared using PBS and kept at 4°C and used on the same day.

Biotinylated 18:1-12:0 PS was obtained from Avanti Polar Lipids, Alabaster, AL, US and was incorporated into the vesicles at a concentration of 0.1 mol%. Biotin PS is supplied as an ammonium salt and therefore carries a negative charge and behaves similar to negatively charged fluorescently labelled lipids, such as TxRed, in an SLB under the influence of electrophoretic forces. The fluorescent binding partner in this case was fluorescein isothiocyanate (FITC) labelled streptavidin, which was obtained from Life Technologies, Paisley, UK. Stock solutions were prepared with a concentration of 10 nmol dm^{-3} in PBS and were kept at 4°C for a maximum of 24 h.

The deoxyribonucleic acid (DNA) strands were synthesised by Eurogentec, Seraing, Belgium. Three different strands were used, two with cholesterol anchors for incorporation into vesicles and one with a fluorescent label but no cholesterol anchor. The DNA strands with a cholesterol anchor were incorporated into the vesicles at a concentration of 0.125 mol% each. The hybridisation of such a DNA pair in a membrane was shown previously (Pfeiffer et al., 2004). The fluorescently labelled DNA strands were dissolved in PBS to a concentration of $1 \mu\text{mol dm}^{-3}$ and stored at 4°C until used, the samples were stable over several months. The two DNA strands incorporated into the lipid membrane were 5'-CCC-AGG-CAG-CAC-GGA-GTG-ATA-TAC-AAG-CAA-3', with a cholesterol modification at the 5', 5'-TCC-GTG-CTG-CCT-CCC-3' with a cholesterol modification at the 3', respectively. The DNA strand with the fluorescent label was 5'-TTG-CTT-GTA-TAT-CAC-3' with an Atto 590 modification at the 5'.

All binding experiments were carried out in the same way. The SLB was formed and, where applicable, the charged SLB components were concentrated into trapping regions using electrophoresis. The electric field was then switched off and the solutions with different concentrations of the analyte were injected into the flow cell. After an incubation time of 5 min, the flow cell was rinsed with a flow speed of 7 ml min^{-1} for 2 min to 4 min until the background fluorescence had reached a level low enough to obtain a good signal to noise ratio. The rinsing time was kept constant for each ligand-receptor combination.

2.9.3 Surface Patterning

In addition to cleaning, some surfaces were also patterned to produce the patterned SLBs presented in chapters 3 and 4. This can be achieved in different ways such as patterning of a SAM on the surface (Han et al., 2007; Jenkins et al., 2002), μCP of proteins (Cheetham et al., 2011) or cross linking of polymerisable lipids (Morigaki et al., 2007). Here, μCP of fibronectin was used to change the surface properties in some regions, such that no SLB will form where the protein was deposited.

In order to produce the stamp which was used in the later process of producing a protein pattern on a surface, a mold was made first. This was done by standard UV-lithography of SU-8 on a silicon substrate. The patterned mold was then silanised using tridecafluoro-1,1,2,2-tetrahydrooctyl trichlorosilane by evaporation of three droplets at 120°C in a silanisation chamber. Then PDMS (Dow Corning Sylgard 184) was prepared by mixing 10 parts of monomer solution with 1 part by weight of the cross linking agent. After thorough mixing the air bubbles in the PDMS solution were removed through desiccation for 30 min. The PDMS was then poured onto the substrate and either left at 50°C for several hours or was cured on a hot plate at 120°C for 15 min. The resulting PDMS stamp was then stripped of the substrate and was used without further cleaning. The stamps were then incubated with a fibronectin (Invitrogen, Massachusetts,

US) solution with a concentration of 0.125 mg ml^{-1} in PBS. After 15 min incubation, the solution was blown off with nitrogen and the stamp was rinsed in MilliQ without the surface drying out completely. Just before stamping onto a cleaned substrate, the sample was then blown completely dry and manually placed onto the substrate. Complete contact between the stamp and the substrate was then induced by gently pressing the stamp onto the sample with a pair of tweezers. When complete contact was made, the stamp and the substrate were left in contact for 5 min. The stamp was then carefully removed from the substrate and the sample was used immediately. Whenever a stamp was used for the first time, the incubation time of the fibronectin solution on the stamp was increased to 1 h and the first print from a stamp was discarded since the first print always resulted in prints with defects and of lower quality than any subsequent prints. Stamps were reused up to 15 times or until deterioration of the prints was observed. Stock solution of fibronectin in PBS was kept at -80°C thawed solution was kept at 4°C , not re-frozen and used within a month.

2.9.4 Bilayer formation and Electrophoresis Experiments

After vesicle preparation, surface cleaning and, when applicable, surface patterning, the vesicle solution was injected into a flow cell. Vesicles and the surface were then incubated for at least 30 min to achieve vesicle rupture on the surface and the formation of an SLB. After the formation of the SLB, the vesicle solution was rinsed with at least 100 volumes of the flow cell at flow rates of up to 4 ml min^{-1} and the buffer solution was exchanged with MilliQ. This exerts osmotic pressure on the remaining vesicles on the surface and can induce rupture. To achieve high quality SLBs. MilliQ was then rinsed out and exchanged with the original buffer with another 100 flow cell volumes.

Electrophoresis experiments cannot generally be carried out in buffer solution. The high salt concentration will result in strong currents and low electric fields and therefore a small electrophoretic force. This can be overcome by either

special flow cell designs or by exchange of the buffer solution with MilliQ (Monson et al., 2011). Here, the buffer solution was exchanged with MilliQ by rinsing with another 100 flow cell volumes. The current was monitored throughout the experiments and was kept below 30 μA . The field was applied through two platinum wires in the flow cell. The platinum wires were 3.05 cm apart, the voltage applied was 190 V and the field strength therefore was 62 V cm^{-1} .

2.9.5 Surface Modification

For the formation of HLMS and tethered lipid bilayers, the surfaces used had to be modified by SAMs to form a monolayer of lipids on the SAM or tether the membrane to a gold surface.

The formation of HLMS for SERS experiments was carried out using 1-octadecanethiol (ODT) as a SAM molecule. The gold surfaces used were produced by the evaporation of 150 nm thick gold layers onto silicon substrates with 5 nm chromium as an adhesive layer. The SAM was formed by dissolving 5 mM ODT in ethanol and incubating the gold surface in the SAM solution for several hours. Excess SAM molecules were removed by thorough rinsing with ethanol. The surfaces were stored up to a week and before used rinsed with MilliQ. The SAMs were characterised using ellipsometry and contact angle measurements. The thickness was determined to be 2 nm and the water contact angle was measured to be 110° advancing and 104° receding which is in good agreement with literature values of 1.8 nm thickness (Jenkins et al., 2002) and 115° and 102° for the advancing and receding contact angle respectively (Abe et al., 2000).

Tethered lipid bilayers on gold were formed through the use of a mixture of SAMs. The molecules used for this were EO₃ cholesterol and 2-mercaptoethanol. The two components were mixed in a ratio 2:3 in isopropanol to a concentration of 1 mM. Gold surfaces were then immersed in the solution for 1 h. Remaining SAM molecules were then rinsed of with isopropanol and the surfaces were

used immediately after preparation. This protocols results in the formation of a mixed SAM were the 2-mercaptoethanol acts as a spacer between the gold and the tethered bilayer and the EO₃ cholesterol provides hydrophobic anchors for the tethered bilayer. The cholesterol molecules will replace some lipids in the proximal leaflet making while the distal leaflet remains a layer completely made from lipids.

Polymer surfaces for the formation of SLBs were grown on both gold and glass substrates. Growth was achieved through atom-transfer radical-polymerisation (ATRP) by the Armes group at the University of Sheffield (Blakeston et al., 2015).

2.9.6 Raman Experiments

Vesicles for SERS experiments were formed using 20 mol% DOTAP and 80 mol% 1-palmitoyl-2-oleoylphosphatidylcholine (POPC). The gold NPs have a negative zeta potential of around -40 mV (Mocanu et al., 2009). The positive charge from the DOTAP lipids in the HLM lead to binding of the NPs to the HLM (Pornpattananangkul et al., 2010). The gold NPs were observed through dark field microscopy and despite vibrations of the particles being observed, no net movement of the NPs across the surface was seen, indicating the formation of positively charged regions in the HLM under the NPs in which the NPs were bound.

The incubation time of the vesicles for HLM formation was increased over the incubation time on glass substrates. The vesicles were left in the flow cell for at least 2 h which lead to reliable formation of HLMs consisting of the pre-formed SAM and the lipid monolayer. The gold NPs with a diameter of 80 nm were obtained from BBI solutions, Cardiff, UK at a concentration of 1.10×10^{10} particles/ml or 2.89 mol l^{-1} of gold. The solution was diluted with 1:9 with PBS and then injected into the flow cell. The NPs were incubated on the HLM for at least 30 min the solution containing the NPs was then rinsed out with PBS.

Raman spectra were obtained with an acquisition time of 0.5 s and with a 10 mW laser with a wavelength of 680 nm. The spectra were smoothed using a Savitzky-Golay filter. The baseline was determined for each set of experiments and subtracted from each spectrum.

2.9.7 Finite Element Calculations

To predict the behaviour of charged components in an SLB under the influence of an external electric field and diffusion within the membrane FEA was used. The patterns under investigation were designed in COMSOL® Multiphysics (COMSOL) and the SLBs were simplified to 2D fluid geometries. Since the applied fields in the electrophoresis experiments are in parallel to the membrane, the assumption that no lipids leave or enter the membrane and are therefore confined to the 2D plane is reasonable.

The patterns were meshed using triangular meshes. The minimum mesh element size was always kept smaller than a third of the smallest feature in the pattern and the maximum mesh element size was set to 20 μm . The “chemical reaction engineering module” was used to set up the simulations. The combination of the “transport of diluted species” package with the “electrostatics” package allowed for the calculation of electric fields while at the same time the electrophoretic force on charged membrane components was calculated. The diffusion coefficient used by the simulation was set to 1.5 $\mu\text{m}^2 \text{s}^{-1}$, the charge was -1 elemental charge per molecule and the surface concentration of charged lipids was set to 1 mol%. To simulate the influence of an external electric field, the electric potential was changed across the y dimension of the simulation plane. The potential was calculated through

$$\Phi(y) = A \cdot y \cdot pw \quad (2.24)$$

where A denotes the amplitude of the electric field (6.2 V mm^{-1}) and pw is a piecewise function which was defined as

$$\text{pw}(t) = \begin{cases} -1 & : \text{concentration for } t < t_1 \\ 1 & : \text{reversal of the electric field for } t_1 < t < t_2 \\ 0 & : \text{free diffusion for } t_2 < t \end{cases}$$

For cases where the reversal of the field and the free diffusion were not investigated the piecewise function was replaced by a constant of either -1 or 1, depending on the direction of the electric field.

The potential, as described above, was applied to all simulation domains. The outside boundaries of the patterns were defined as no flux boundaries while flux through inner boundaries was allowed. The surface concentration c was then measured as a function of time in pre-defined regions of interest as a surface integral. The surface integral was normalised to the initial surface integral of the surface concentration to obtain a relative concentration.

References

- Abe, K., Takiguchi, H., and Tamada, K. (2000). Dynamic contact angle measurement of Au(111)-thiol self-assembled monolayers by the Wilhelmy plate method. *Langmuir*, 16(5):2394–2397.
- Abraham, T., Prenner, E. J., Lewis, R. N. a. H., Mant, C. T., Keller, S., Hodges, R. S., and McElhaney, R. N. (2014). Structure-activity relationships of the antimicrobial peptide gramicidin S and its analogs: Aqueous solubility, self-association, conformation, antimicrobial activity and interaction with model lipid membranes. *Biochimica et biophysica acta*, 1838(5):1420–1429.
- Acuña, a. U., Amat-Guerri, F., Morcillo, P., Liras, M., Rodríguez, B., Acuna, A., Amat-Guerri, F., Morcillo, P., Liras, M., and Rodriguez, B. (2009). Structure and formation of the fluorescent compound of lignum nephriticum. *Organic Letters*, 11(9):3020–3023.
- Axelrod, D., Koppel, D. E., Schlessinger, J., Elson, E., and Webb, W. W. (1976). Mobility measurement by analysis of fluorescence photobleaching recovery kinetics. *Biophysical Journal*, 16(9):1055–1069.
- Bao, P., Cheetham, M. R., Roth, J. S., Blakeston, A. C., Bushby, R. J., and Evans, S. D. (2012). On-Chip Alternating Current Electrophoresis in Supported Lipid Bilayer Membranes. *Analytical chemistry*, 84:10702–10707.
- Bayerl, T. M. and Bloom, M. (1990). Physical properties of single phospholipid bilayers adsorbed to micro glass beads. A new vesicular model system studied by 2H-nuclear magnetic resonance. *Biophysical journal*, 58(2):357–362.
- Bernard, A., Delamarche, E., Schmid, H., Michel, B., Bosshard, H. R., and Biebuyck, H. (1998). Printing Patterns of Proteins. *Langmuir*, 14(9):2225–2229.
- Bernard, A., Renault, J. P., Michel, B., Bosshard, H. R., and Delamarche, E. (2000). Microcontact Printing of Proteins. *Advanced Materials*, 12(14):1067–1070.
- Blakeston, A. C., Alswieleh, A. M., Heath, G. R., Roth, J. S., Bao, P., Cheng, N., Armes, S. P., Leggett, G. J., Bushby, R. J., and Evans, S. D. (2015). New Poly(amino acid methacrylate) Brush Supports the Formation of Well-Defined Lipid Membranes. *Langmuir*, 31(12):3668–3677.
- Cevc, G. and Marsh, D. (1987). *Phospholipid Bilayers Physical Principals and Models*. John Wiley & Sons, New York.

- Cheetham, M. R., Bramble, J. P., McMillan, D. G. G., Krzeminski, L., Han, X., Johnson, B. R. G., Bushby, R. J., Olmsted, P. D., Jeuken, L. J. C., Marritt, S. J., Butt, J. N., and Evans, S. D. (2011). Concentrating Membrane Proteins Using Asymmetric Traps and AC Electric Fields. *Journal of the American Chemical Society*, 133(17):6521–4.
- Cremer, P. S. and Boxer, S. G. (1999). Formation and spreading of lipid bilayers on planar glass supports. *The Journal of Physical Chemistry B*, 103(13):2554–2559.
- Cremer, P. S., Groves, J. T., Kung, L. A., and Boxer, S. G. (1999). Writing and erasing barriers to lateral mobility into fluid phospholipid bilayers. *Langmuir*, 15(11):3893–3896.
- Dodd, C. E., Johnson, B. R. G., Jeuken, L. J. C., Bugg, T. D. H., Bushby, R. J., and Evans, S. D. (2008). Native E. coli inner membrane incorporation in solid-supported lipid bilayer membranes. *Biointerphases*, 3(2):FA59.
- Eah, S. K., Jaeger, H. M., Scherer, N. F., Wiederrecht, G. P., and Lin, X. M. (2005). Scattered light interference from a single metal nanoparticle and its mirror image. *Journal of Physical Chemistry B*, 109:11858–11861.
- Fleischmann, M., Hendra, P., and McQuillan, A. (1974). Raman spectra of pyridine adsorbed at a silver electrode. *Chemical Physics Letters*, 26(2):163–166.
- Galarreta, B. C., Norton, P. R., and Lagugné-Labarthe, F. (2011). SERS detection of streptavidin/biotin monolayer assemblies. *Langmuir : the ACS journal of surfaces and colloids*, 27(4):1494–8.
- Grand, J. (2003). Optimization of SERS-active substrates for near-field Raman spectroscopy. *Synthetic Metals*, 139(3):621–624.
- Groves, J. T. (1997). Micropatterning Fluid Lipid Bilayers on Solid Supports. *Science*, 275(5300):651–653.
- Groves, J. T. and Boxer, S. G. (1995). Electric field-induced concentration gradients in planar supported bilayers. *Biophysical Journal*, 69(5):1972–5.
- Groves, J. T., Boxer, S. G., and McConnell, H. M. (1997). Electric field-induced reorganization of two-component supported bilayer membranes. *Proceedings of the National Academy of Sciences of the United States of America*, 94(25):13390–5.
- Hamai, C., Cremer, P. S., and Musser, S. M. (2007). Single giant vesicle rupture events reveal multiple mechanisms of glass-supported bilayer formation. *Biophysical Journal*, 92(6):1988–1999.
- Han, X., Cheetham, M. R. M., Sheikh, K., Olmsted, P. D., Bushby, R. R. J., and Evans, S. S. D. (2008). Manipulation and charge determination of proteins in photopatterned solid supported bilayers. *Integr. Biol.*, 1(2):205–211.
- Han, X. J., Achalkumar, A. S., Bushby, R. J., and Evans, S. D. (2009). A Cholesterol-Based Tether for Creating Photopatterned Lipid Membrane Arrays on both a Silica and Gold Surface. *Chemistry-A European Journal*, 15(26):6363–6370.

- Han, X. J., Critchley, K., Zhang, L. X., Pradeep, S. N. D., Bushby, R. J., and Evans, S. D. (2007). A novel method to fabricate patterned bilayer lipid membranes. *Langmuir : the ACS journal of surfaces and colloids*, 23(3):1354–8.
- He, L. H., Robertson, J. W. F., Li, J., Karcher, I., Schiller, S. M., Knoll, W., and Naumann, R. (2005). Tethered bilayer lipid membranes based on monolayers of thiolipids mixed with a complementary dilution molecule. 1. Incorporation of channel peptides. *Langmuir*, 21(25):11666–11672.
- Hovis, J. S. and Boxer, S. G. (2000). Patterning Barriers to Lateral Diffusion in Supported Lipid Bilayer Membranes by Blotting and Stamping. *Langmuir*, 16(3):894–897.
- Israelachvili, J. N., Marcelja, S., and Horn, R. G. (1980). Physical principles of membrane organization. *Quarterly reviews of biophysics*, 13(2):121–200.
- Jeanmaire, D. L. and Van Duyne, R. P. (1977). Surface raman spectroelectrochemistry Part I. Heterocyclic, aromatic, and aliphatic amines adsorbed on the anodized silver electrode. *Journal of Electroanalytical Chemistry*, 84:1–20.
- Jenkins, A. T. A., Bushby, R. J., Evans, S. D., Knoll, W., and Ogier, S. D. (2002). Lipid Vesicle Fusion on μ CP Patterned Self-Assembled Monolayers : Effect of Pattern Geometry on Bilayer Formation. (7):3176–3180.
- Johnson, J. M., Ha, T., Chu, S., and Boxer, S. G. (2002). Early steps of supported bilayer formation probed by single vesicle fluorescence assays. *Biophysical journal*, 83(6):3371–9.
- Johnson, S. J., Bayerl, T. M., McDermott, D. C., Adam, G. W., Rennie, A. R., Thomas, R. K., and Sackmann, E. (1991). Structure of an adsorbed dimyristoylphosphatidylcholine bilayer measured with specular reflection of neutrons. *Biophysical journal*, 59(2):289–94.
- Kalb, E., Frey, S., and Tamm, L. K. (1992). Formation of supported planar bilayers by fusion of vesicles to supported phospholipid monolayers. *Biochimica et Biophysica Acta - Biomembranes*, 1103(2):307–316.
- Kashimura, Y., Furukawa, K., and Torimitsu, K. (2011). Electrostatic control of lipid bilayer self-spreading using a nanogap gate on a solid support. *Journal of the American Chemical Society*, 133(16):6118–21.
- Kneipp, K., Wang, Y., Kneipp, H., Perelman, L., Itzkan, I., Dasari, R., and Feld, M. (1997). Single Molecule Detection Using Surface-Enhanced Raman Scattering (SERS). *Physical Review Letters*, 78(9):1667–1670.
- Koenig, B. W., Krueger, S., Orts, W. J., Majkrzak, C. F., Berk, N. F., Silverton, J. V., and Gawrisch, K. (1996). Neutron Reflectivity and Atomic Force Microscopy Studies of a Lipid Bilayer in Water Adsorbed to the Surface of a Silicon Single Crystal. *Langmuir*, 12(5):1343–1350.
- Kukushkin, V. I., Van'kov, A. B., and Kukushkin, I. V. (2013). Long-range manifestation of surface-enhanced Raman scattering. *JETP Letters*, 98(2):64–69.

- Kundu, J., Levin, C. S., and Halas, N. J. (2009). Real-time monitoring of lipid transfer between vesicles and hybrid bilayers on Au nanoshells using surface enhanced Raman scattering (SERS). *Nanoscale*, 1(1):114–7.
- Landau, L. (1977). Anomalously Intense Raman Spectra of Pyridine at a Silver Electrode. *Journal of the American Chemical Society*, pages 5215–5217.
- Lee, Y. K. and Nam, J.-M. (2012). Electrofluidic lipid membrane biosensor. *Small (Weinheim an der Bergstrasse, Germany)*, 8(6):832–7.
- Ma, W., Li, D.-W., Sutherland, T. C., Li, Y., Long, Y.-T., and Chen, H.-Y. (2011). Reversible redox of NADH and NAD⁺ at a hybrid lipid bilayer membrane using ubiquinone. *Journal of the American Chemical Society*, 133(32):12366–9.
- Mager, M. D. and Melosh, N. a. (2007). Lipid bilayer deposition and patterning via air bubble collapse. *Langmuir : the ACS journal of surfaces and colloids*, 23(18):9369–77.
- Maier, S. A. (2010). *Plasmonics, Fundamentals and Applications*. Springer Berlin / Heidelberg.
- Mennicke, U. and Salditt, T. (2002). Preparation of Solid-Supported Lipid Bilayers by Spin-Coating. *Langmuir*, 18(21):8172–8177.
- Michel, B., Bernard, A., Bietsch, A., Delamarche, E., Geissler, M., Juncker, D., Kind, H., Renault, J.-P., Rothuizen, H., Schmid, H., Schmidt-Winkel, P., Stutz, R., and Wolf, H. (2002). Printing Meets Lithography: Soft Approaches to High-Resolution Patterning. *CHIMIA International Journal for Chemistry*, 56(5):527–542.
- Mocanu, A., Cernica, I., Tomoaia, G., Bobos, L. D., Horovitz, O., and Tomoaia-Cotisel, M. (2009). Self-assembly characteristics of gold nanoparticles in the presence of cysteine. *Colloids and Surfaces A: Physicochemical and Engineering Aspects*, 338(1-3):93–101.
- Monson, C. F., Pace, H. P., Liu, C., and Cremer, P. S. (2011). Supported bilayer electrophoresis under controlled buffer conditions. *Analytical chemistry*, 83(6):2090–6.
- Morigaki, K., Schönherr, H., and Okazaki, T. (2007). Polymerization of diacylene phospholipid bilayers on solid substrate: influence of the film deposition temperature. *Langmuir : the ACS journal of surfaces and colloids*, 23(24):12254–60.
- Nakai, K., Morigaki, K., and Iwasaki, Y. (2010). Molecular recognition on fluidic lipid bilayer microarray corralled by well-defined polymer brushes. *Soft Matter*, 6(23):5937.
- Naumann, R., Schiller, S. M., Giess, F., Grohe, B., Hartman, K. B., Kärcher, I., Köper, I., Lübben, J., Vasilev, K., and Knoll, W. (2003). Tethered Lipid Bilayers on Ultraflat Gold Surfaces. *Langmuir*, 19(13):5435–5443.
- Nie, S. (1997). Probing Single Molecules and Single Nanoparticles by Surface-Enhanced Raman Scattering. *Science*, 275(5303):1102–1106.

- Pace, H. P., Sherrod, S. D., Monson, C. F., Russell, D. H., and Cremer, P. S. (2013). Coupling supported lipid bilayer electrophoresis with matrix-assisted laser desorption/ionization-mass spectrometry imaging. *Analytical chemistry*, 85(12):6047–52.
- Pfeiffer, I., Höök, F., and Ho, F. (2004). Bivalent cholesterol-based coupling of oligonucleotides to lipid membrane assemblies. *Journal of the American Chemical Society*, pages 10224–10225.
- Plant, A. L. (1993). Self-assembled phospholipid/alkanethiol biomimetic bilayers on gold. *Langmuir*, 9(11):2764–2767.
- Pompeo, G., Girasole, M., Cricenti, a., Cattaruzza, F., Flamini, a., Prospero, T., Generosi, J., and Castellano, a. C. (2005). AFM characterization of solid-supported lipid multilayers prepared by spin-coating. *Biochimica et biophysica acta*, 1712(1):29–36.
- Poo, M. and Robinson, K. R. (1977). Electrophoresis of concanavalin A receptors along embryonic muscle cell membrane. *Nature*, 265(17):602–605.
- Pornpattananangkul, D., Olson, S., Aryal, S., Sartor, M., Huang, C.-M., Vecchio, K., and Zhang, L. (2010). Stimuli-responsive liposome fusion mediated by gold nanoparticles. *ACS nano*, 4(4):1935–42.
- Poyton, M. F. and Cremer, P. S. (2013). Electrophoretic Measurements of Lipid Charges in Supported Bilayers. *Analytical chemistry*, 85(22):10803–10811.
- Ren, W., Liu, J., Guo, S., and Wang, E. (2011). SERS imaging for label-free detection of the phospholipids distribution in hybrid lipid membrane. *Science China Chemistry*, 54(8):1334–1341.
- Richter, R. P., Bérat, R., and Brisson, A. R. (2006). Formation of solid-supported lipid bilayers: an integrated view. *Langmuir : the ACS journal of surfaces and colloids*, 22(8):3497–505.
- Richter, R. P. and Brisson, A. R. (2005). Following the formation of supported lipid bilayers on mica: a study combining AFM, QCM-D, and ellipsometry. *Biophysical journal*, 88(5):3422–33.
- Schönherr, H., Johnson, J. M., Lenz, P., Frank, C. W., and Boxer, S. G. (2004). Vesicle adsorption and lipid bilayer formation on glass studied by atomic force microscopy. *Langmuir : the ACS journal of surfaces and colloids*, 20(26):11600–6.
- Seiffert, S. and Oppermann, W. (2005). Systematic evaluation of FRAP experiments performed in a confocal laser scanning microscope. *Journal of Microscopy*, 220(1):20–30.
- Stelzle, M., Miehl, R., and Sackmann, E. (1992). Two-dimensional microelectrophoresis in supported lipid bilayers. *Biophysical Journal*, 63(5):1346–1354.
- Stokes, G. G. (1852). On the Change of Refrangibility of Light. *Philosophical Transactions of the Royal Society of London*, 142:463–562.

- Subramaniam, V., Alves, I. D., Salgado, G. F. J., Lau, P.-W. W., Wysocki, R. J., Salamon, Z., Tollin, G., Hruby, V. J., Brown, M. F., and Saavedra, S. S. (2005). Rhodopsin reconstituted into a planar-supported lipid bilayer retains photoactivity after cross-linking polymerization of lipid monomers. *Journal of the American Chemical Society*, 127(15):5320–5321.
- Sucheta, A., Ackrell, B., Cochran, B., and Armstrong, F. (1992). Diode-like behaviour of a mitochondrial electron-transport enzyme. *Nature*, 356:361–362.
- Sweetenham, C. S., Larraona-Puy, M., and Notingher, I. (2011). Simultaneous Surface-Enhanced Raman Spectroscopy (SERS) and Atomic Force Microscopy (AFM) for Label-Free Physicochemical Analysis of Lipid Bilayers. *Applied Spectroscopy*, 65(12):1387–1392.
- Tsai, J., Sun, E., Gao, Y., Hone, J. C., and Kam, L. C. (2008). Non-Brownian diffusion of membrane molecules in nanopatterned supported lipid bilayers. *Nano letters*, 8(2):425–30.
- van Oudenaarden, A. and Boxer, S. G. (1999). Brownian Ratchets: Molecular Separations in Lipid Bilayers Supported on Patterned Arrays. *Science*, 285(5430):1046–1048.
- Wang, X., Shindel, M. M., Wang, S.-W., and Ragan, R. (2010). A facile approach for assembling lipid bilayer membranes on template-stripped gold. *Langmuir : the ACS journal of surfaces and colloids*, 26(23):18239–45.
- Weitz, D. A., Garoff, S., Gersten, J. I., and Nitzan, A. (1983). The enhancement of Raman scattering, resonance Raman scattering, and fluorescence from molecules adsorbed on a rough silver surface. *The Journal of Chemical Physics*, 78(9):5324.
- Wiedemann, I., Breukink, E., Van Kraaij, C., Kuipers, O. P., Bierbaum, G., De Kruijff, B., and Sahl, H. G. (2001). Specific binding of nisin to the peptidoglycan precursor lipid II combines pore formation and inhibition of cell wall biosynthesis for potent antibiotic activity. *Journal of Biological Chemistry*, 276(3):1772–1779.
- Wirth, J., Garwe, F., Bergmann, J., Paa, W., Csaki, a., Stranik, O., and Fritzsche, W. (2014). Tuning of Spectral and Angular Distribution of Scattering from Single Gold Nanoparticles by Subwavelength Interference Layers. *Nano letters*, 14(2):570–7.
- Xu, H., Bjerneld, E., Käll, M., and Börjesson, L. (1999). Spectroscopy of Single Hemoglobin Molecules by Surface Enhanced Raman Scattering. *Physical Review Letters*, 83(21):4357–4360.
- Yamada, M., Imaishi, H., and Morigaki, K. (2013). Microarrays of phospholipid bilayers generated by inkjet-printing. *Langmuir : the ACS journal of surfaces and colloids*, 29(21):6404–6408.
- Yoshina-Ishii, C. and Boxer, S. G. (2006). Controlling two-dimensional tethered vesicle motion using an electric field: interplay of electrophoresis and electroosmosis. *Langmuir*, 22(5):2384–91.

- Zhou, H., Yang, D., Ivleva, N. P., Mircescu, N. E., Niessner, R., and Haisch, C. (2014). SERS Detection of Bacteria in Water by in Situ Coating with Ag Nanoparticles. *Analytical chemistry*, 86(3):1525–33.
- Zhu, L., Gregurec, D., and Reviakine, I. (2013). Nanoscale Departures: Excess Lipid Leaving the Surface during Supported Lipid Bilayer Formation. *Langmuir : the ACS journal of surfaces and colloids*, 29(49):15283–15292.

Chapter 3

Diffusion in Lipid Membranes

Diffusion in biological membranes is the main means of transportation within the membrane for both lipids and proteins residing in the membrane. Membrane proteins can recruit specific lipids in their surroundings and membrane properties can be changed according to local diffusion coefficients. Even the energy transfer via ubiquinones is achieved through diffusion of these molecules in the hydrophobic core of the membrane. Therefore, it is important to understand diffusion in the membrane and how free diffusion interacts with external forces. Here, the experimental determination of the diffusion coefficient is discussed first, then special cases of diffusion in a membrane are shown, and finally Brownian ratchets for transporting membrane components are presented.

3.1 Measuring Diffusion in a Lipid Bilayer

In order to understand diffusion of lipids in SLBs better, it is important to know how the diffusion coefficient in the membrane varies with different parameters. Typically, FRAP (see section 2.6.3) experiments are carried out to measure the diffusion coefficient of fluorescently tagged components in the membrane. There is a variety of methods for the analysis of the experimental data: direct recording of the intensity in the bleaching area (Axelrod et al., 1976; Soumpasis, 1983), evaluating the change in the FWHM of the bleach spot (Seiffert and Oppermann,

2005) or by spatial Fourier analysis (Tsay and Jacobson, 1991). The first method, known as the Axelrod method and used widely, is further investigated here. Where firstly the influence of different parameters on the measured diffusion coefficient D is determined and secondly the variation in D with different dyes is shown.

3.1.1 Effect of the Bleach Time

When using a mercury arc lamp to bleach the fluorescence in a specific region of a lipid bilayer, the fluorophore molecules are not all bleached instantaneously but follow an exponential decay of remaining fluorescence with increase bleach time. To get a measure of the effect of the bleach time on the remaining fluorescence intensity, a lipid bilayer was formed and the remaining fluorescence intensity I_r was measured for different bleach times. The background was accounted for using

$$I_r(t) = \frac{I_m(t) - I_b}{I_0 - I_b}, \quad (3.1)$$

where I_m is the measured intensity after bleaching, I_b is the background fluorescence and I_0 is the initial fluorescence intensity from the same spot. I_b was determined by measuring the intensity of areas without fluorescing molecules, i.e. regions where no SLB was formed due to the patterning imposed on the membrane. The remaining intensity was then plotted against the bleaching time in figure 3.1. The graph shows that the remaining fluorescence does not reach 0 intensity. This is due to continuous back diffusion into the bleaching region. Therefore, the maximum bleach reached in the central region depends on the intensity of the lamp as this is directly related to the turn over of fluorescent to non-fluorescent molecules. The data points from this curve were then used to create a chemical reaction model in COMSOL . This meant solving a modified

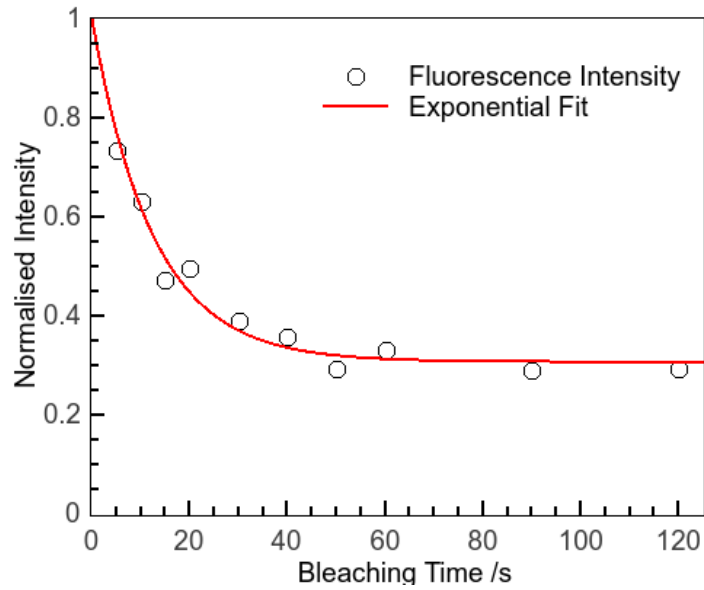


Figure 3.1: Experimentally determined remaining intensity I_r vs. bleaching time when a lipid bilayer is bleached with the same intensity for different times. The fit used is an exponential decay, the decay constant and the remaining intensity due to diffusion were obtained from the fit.

diffusion equation with a sink term to account for non-conservation

$$\frac{\partial c}{\partial t} + \nabla \cdot (-D\nabla c) = R_i, \quad (3.2)$$

which included a reaction term R_i in the bleach spot region. This reaction term was used as a representation of the bleaching process. Initial values were such that the whole simulated area had a fluorophore concentration of 1 mol m^{-3} . The reaction parameter R_i was determined from the interpolation of the data shown in figure 3.1. The simulation was set up to be a square with a side length of $400 \mu\text{m}$ and the bleach spot region had a radius of $28 \mu\text{m}$. The layout of the simulation is shown in figure 3.2. The diffusion coefficient defined for the fluorophore in the simulation was $1 \mu\text{m}^2 \text{ s}^{-1}$. The bleach time was then varied from 5 s to 180 s and the recovery in the bleach spot area was monitored for 20 min. As an example, the recovery curves for a very short bleaching time (5 s) and a long bleaching time (180 s) are shown in figure 3.3. This shows a clear difference in the two different bleaching times. While for the very short

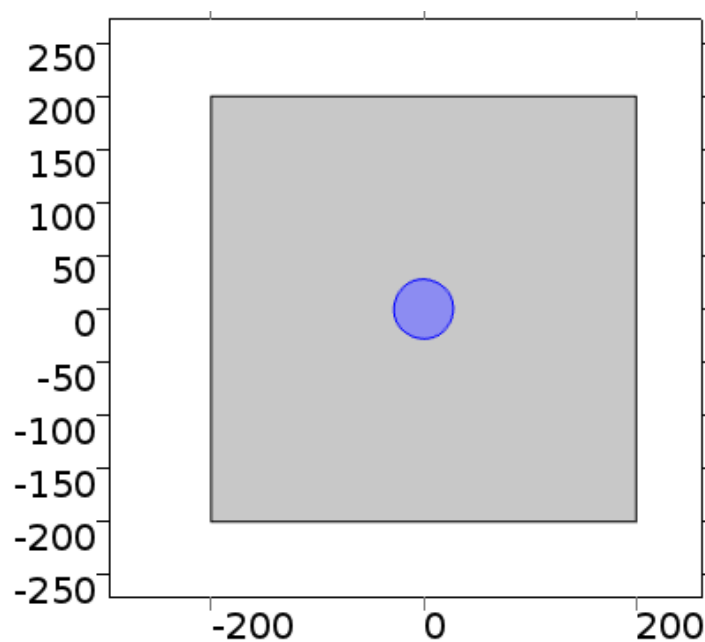


Figure 3.2: Simulation layout for bleaching calculations in COMSOL, the x and y axis are given in μm . The blue region shows the simulated bleach spot with a radius r of $28\ \mu\text{m}$.

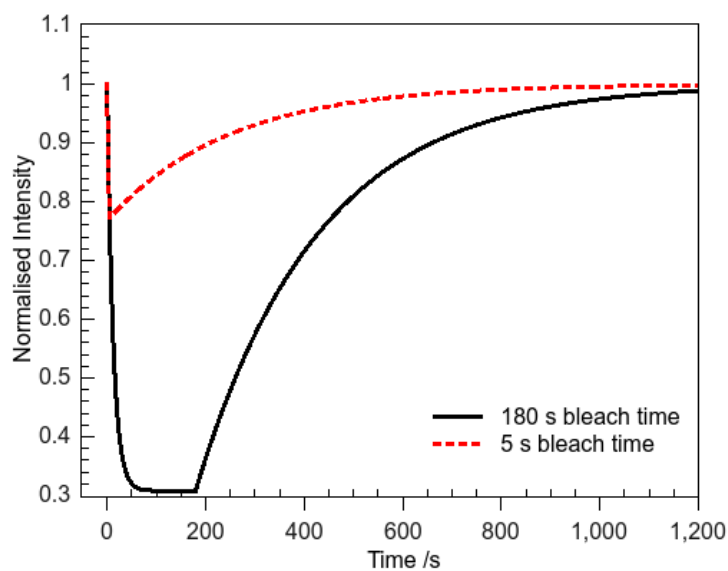


Figure 3.3: Simulated recovery curves in the bleach spot from COMSOL. The recovery curve is taken from the bleach spot and shown here for two different bleaching times. For short bleaching times a significant fraction of the fluorescent molecules remains active.

bleaching time the bleach is not complete and the recovery starts at around 75 %, the longer bleaching time shows an almost complete bleach as in the experimental data.

To obtain the respective diffusion coefficients, the data from the different bleaching times was then fitted to a Box-Lucas curve:

$$I(t) = MF(1 - e^{-(t-c)\tau}), \quad (3.3)$$

with MF being the perceived mobile fraction, τ the time constant and c a correction parameter for finite bleaching times. As the mobile fraction should be unity, since there is no immobile fraction in this simulation, the mobile fraction was set to be 100 %. This assumption can be made despite the finite size of the calculation region. When bleached molecules are confined within the calculation region, these cannot become fluorescent again and would appear as an immobile fraction. The bleach spot size of the calculations was 1.5 % of the overall pattern size and the overall area was scaled with the bleach spot area. Therefore, the assumption of having 100 % mobile fraction can be justified. In addition to that, the value for c when fitting equation 3.3 was monitored for the variation of the bleaching times. The results of the fit for c can be seen in figure 3.4. As c scales linearly with the bleaching time and therefore accounts for changes in finite bleaching times. Negative numbers for c indicate an incomplete bleach of the region of interest due to too short bleach times to achieve complete bleaching of all fluorescent molecules.

The diffusion coefficient D was calculated from the fitted value for τ and the known radius of the bleach area r

$$D = 0.88 \frac{r^2 \tau}{4 \ln(2)} \quad (3.4)$$

and was plotted for the different bleaching times. As can be seen from figure 3.5,

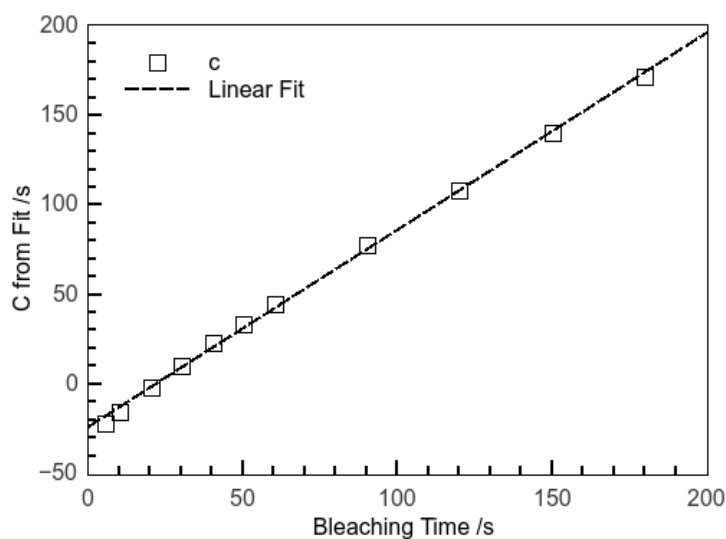


Figure 3.4: Value of the correction factor for finite bleaching time in the Box-Lucas fit (see equation 3.3) c for different bleach times determined from the fit of the recovery in the central bleaching region of the simulated data.

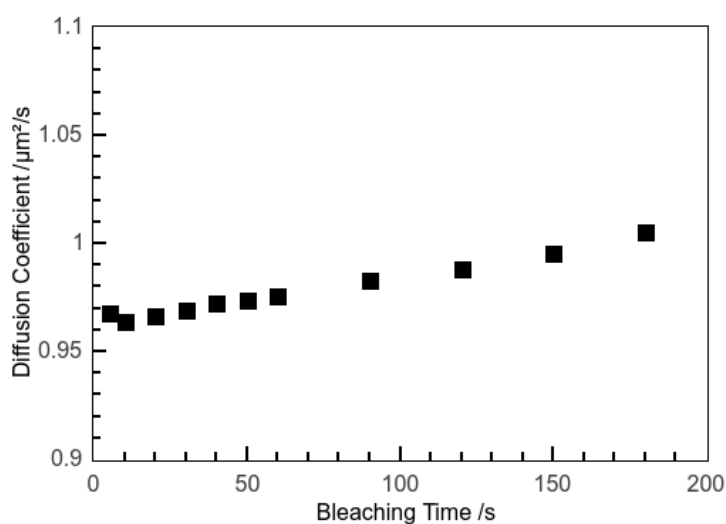


Figure 3.5: Observed variation of D from simulation data with increasing bleaching times determined by the Axelrod method. The observed diffusion coefficient increases slightly with increased bleaching times.

the variation of D with changing bleaching time is negligible. From the shortest to the longest bleaching time, the difference in D is around 4%. This small change in D is small compared to any other experimental error. Therefore, the calculations predict that the bleaching time and any associated incomplete bleaching should not influence the diffusion coefficient.

3.1.2 Experimental Effect of Bleaching Time and Spot Size on Diffusion Coefficient

To check the predictions and validity of the models used for the fitting of the diffusion coefficient, FRAP experiments were carried out. The same composition of lipid, 99.5 mol% POPC and 0.5 mol% TxRed, was used in several experiments to form a lipid bilayer on a glass support. The bilayer was then either bleached with a constant bleach spot diameter of 27 μm (constant spot, varying bleaching time) or bleached with a constant bleach time of 30 s (constant time, variable spot size).

For the experimental results, the Axelrod method was used as before for the simulations to determine the diffusion coefficient D . First, the bleaching time was kept constant while the size of the bleach spot was varied. The result of the fits is shown in figure 3.6. It can be seen that the diffusion coefficient seems to vary with the bleach spot size used for the experiment. This is counter-intuitive as the Axelrod method uses the parameter τ from the fit of the equation 3.3 and calculates D through equation 3.4 which takes the radius of the bleach spot r into account. Despite this it can be seen that the measured diffusion coefficient increases with an increase in the bleach spot diameter. The behaviour seems to indicate that the measured diffusion coefficient eventually levels off for very large bleach spot sizes. This is especially interesting as one might have assumed that smaller bleach spots result in higher values of the diffusion coefficient since small defects in the bilayer become more noticeable on a larger scale.

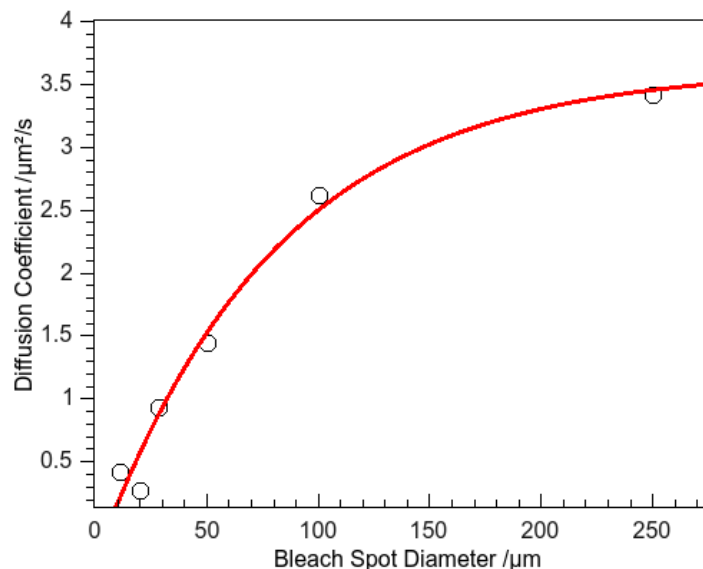


Figure 3.6: Experimentally obtained diffusion coefficients D obtained from the same sample using different bleach spot sizes. As the bleach spot diameter increases, the observed diffusion coefficient increases as well. The bleach time was kept constant at 30 s.

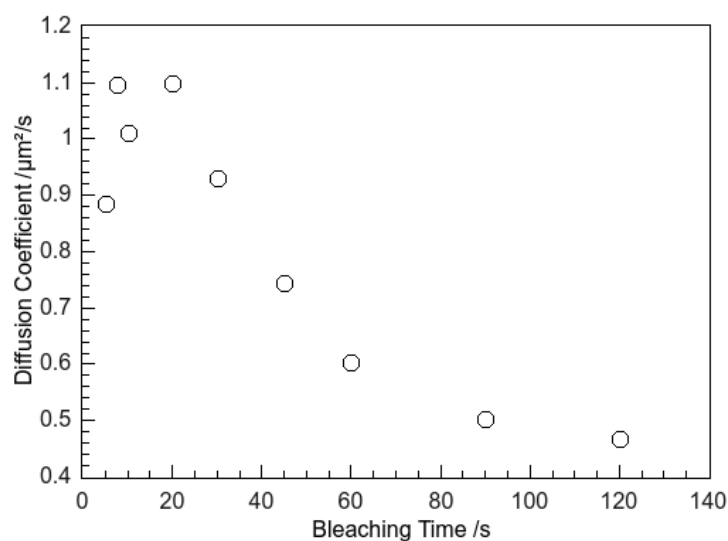


Figure 3.7: Experimental influence of the bleach time on the apparent diffusion coefficient as obtained from the Axelrod method. For short bleach times the observed diffusion coefficient is almost constant while it decreases for longer bleach times. The bleach spot diameter was kept constant at 27 μm .

In addition to the previous experiments, the effect of the bleaching time on the diffusion coefficient was also measured. An increasing bleach time in experiment seems, in contrast to the simulation, result in a decrease in the observed diffusion coefficient. The decay seems to follow an exponential curve.

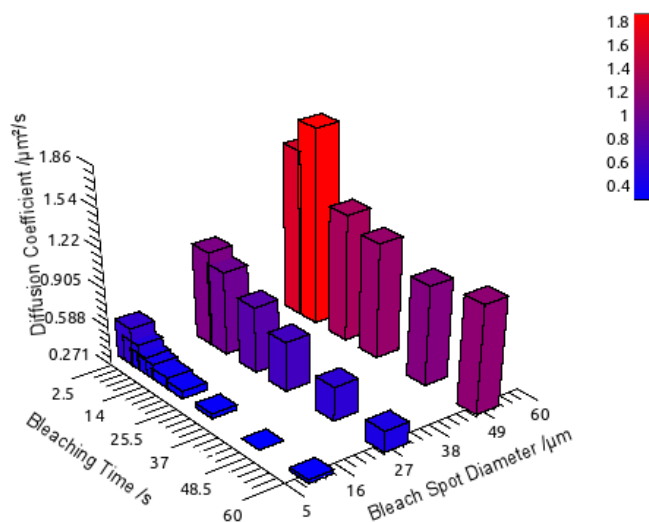


Figure 3.8: Experimentally observed influence of the bleach spot size and the bleaching time on the diffusion coefficient D . The influence of the bleach time and the bleach spot size on the observed diffusion coefficient shows a trend for all of the experimental data.

This is showing that, despite of fitting the parameter c the finite bleach time is not accounted for. The bleach time should therefore be kept as short as possible while still achieving a reasonable signal to noise ratio.

The combination of the results of variable bleaching time and bleach spot size into one graph, a clear trend in the effect of both, bleaching time and spot size on the diffusion coefficient can be seen in figure 3.8. The diagram shows how the apparent diffusion coefficient increases for larger bleach spots and shorter bleaching times while being minimal for small bleach spots and longer bleaching times.

3.1.3 Variation of Dye Molecules

Although the general assumption that labelled lipids behave like their non-labelled counterparts is made in the literature, this assumption does not always hold. It has been shown that TxRed interacts with the membrane (Skaug et al., 2009, 2011), and that different labels interact differently with lipid bilayers (Hughes et al., 2014). In a similar approach as taken in the work by Hughes *et al.*,

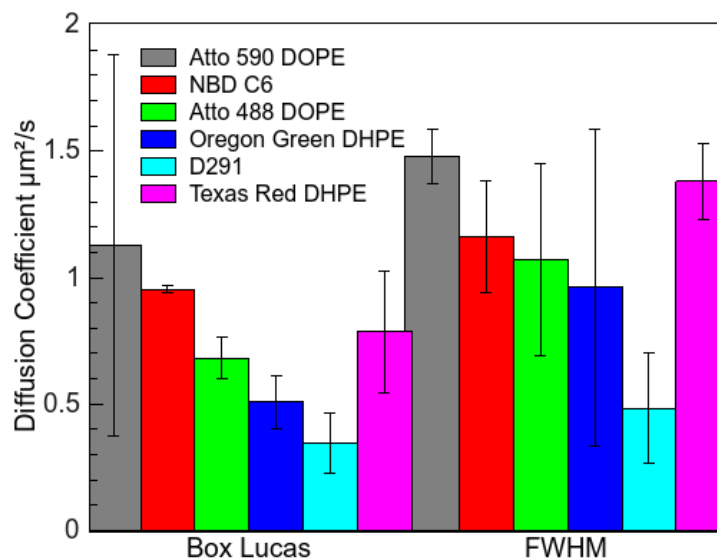


Figure 3.9: Diffusion coefficient determined by the Axelrod method and the measurement of the change of the FWHM of the bleach spot area over time from experimental data for different dyes. The error bars represent the standard deviation from at least five bleach experiments per sample.

the interaction of different dyes with a lipid bilayer is measured here. In contrast to the previous work, which was only looking at the interaction of water soluble dyes with membranes in the same solution, here the interaction of lipid bound dyes with the membrane is measured.

A variety of SLBs has been prepared using POPC as the main component and 1 mol % or 2 mol % of dye molecules. The dyes used were the head group labelled Atto 590 DOPE, Atto 488 DOPE, Oregon Green DHPE, Texas Red DHPE, the tail group labelled NBD PC (NBD C6) and the lipophilic dye 4-(4-(didecylamino)styryl)-n-methylpyridinium iodide (D291). The dyes cover different types of dyes, different attachment sites and different lipids they are attached to. If the assumption that the dye, when incorporated to a small amount, does not interact with the lipid membrane was true, the measured diffusion coefficients for all the dyes should be identical, as the host membrane always consisted of the same lipid, POPC. At least three separate FRAP measurements were carried out for each dye and the experimental data was analysed using the Axelrod method with a Box-Lucas fit (Axelrod et al., 1976) and the by

measuring the change in the FWHM over time (Seiffert and Oppermann, 2005). Despite the two different methods giving different results for each dye, the trend for the different dyes was the same for both of them. Figure 3.9 shows the diffusion coefficients obtained, it can be seen that even the two Atto dyes have significantly different diffusion coefficients, despite them being based on the same chemistry and being attached to the same lipid. The tail group labelled NBD C6 is diffusing faster than some of the head group labelled lipids but there seems to be no systematic difference here. The slowest diffusion coefficient was observed for D291. This may be due to the fact that this dye is not attached to a lipid but a lipophilic dye. Despite its clearly different behaviour compared to the rest of the lipids, and therefore probably also to the rest of the membrane, it can be a useful probe as it is one of the few positively charged dyes. The two methods for analysis seem to have a systematic difference between them. The Axelrod method always results in small diffusion coefficients than the FWHM method although the same data was analysed in both cases.

This shows again the importance of the dye in the membrane and the correction for experimental conditions when diffusion coefficients between different experiments are compared. Even though the lipid was the same in all experiments, the difference in measured diffusion coefficients was up to a factor of four.

3.2 Special Cases of Diffusion in a Membrane

In addition to the regular two-dimensional diffusion discussed previously, there are also some specific cases in which this behaviour changes. These cases are discussed in the following section.

3.2.1 Low Dimensional Diffusion

Although the lipid bilayer is a two dimensional sheet in which free diffusion can happen in both dimensions, this can be restricted further. In order to achieve diffusion in less dimensions, the movement in one of the dimensions has to be restricted. This can be achieved in different ways. It has been shown in the literature that small metal barriers effectively hinder diffusion in the lipid bilayer. Such small barriers can be produced on the nano scale using either electron beam or interference lithography (Tsai et al., 2008), or by the removal of thin bilayer-lines using an AFM tip (Shi et al., 2008). When a lipid bilayer is formed between these barriers, it can be shown that diffusion parallel to the barriers is much faster than the diffusion across the barriers. Through the use of thin chromium barriers it was shown that the diffusion coefficient perpendicular to the barriers can be tuned by a variation of the gap size between the barriers, while titanium barriers have proven to be less suitable for this task (Tsai et al., 2008).

Another way of experimentally limiting the diffusion in a membrane to effectively one dimension is the creation of thin lines of SLBs through the deposition of the lipid of an AFM tip. Similar experiments have been carried out using dip pen nanolithography (DPN), where a tip is moved into an ink reservoir region and then moved towards a writing region (Jackson and Groves, 2004; Lenhert et al., 2010). This process can be parallelised by the use of multiple tips and multiple reservoirs at one time (Lenhert et al., 2007). A combination of different microscopy methods has shown that the lipids can also form stacks on the substrate and that a monolayer of lipids on the hydrophilic substrate forms a wetting layer while further bilayers form on top (Hirtz et al., 2011). This method can also be expanded to different substrates such as graphene, where the lipids form inverse bilayers in air and monolayers when hydrated (Hirtz et al., 2013).

To deposit similarly small patterns of lipids, a similar approach was used here; lipids were dried from solvent onto an AFM tip. When rehydrated, the

tip can be used to draw a pattern of lipid onto the substrate. The pattern of lipid follows the path of the tip and is stable for a long time so that further experiments can be conducted on these patterns.

When lipids are patterned into thin membrane stripes, the diffusion along these lines is not hindered, but the diffusion across the lines is impossible. This leads to the bleaching area in a typical FRAP experiment looking like an oval instead of a circle. To investigate this effect further and to be able to compare theoretical with experimental results, the behaviour was modelled in a FEA model. The model consisted of zig-zag lines which were connected at their respective ends. This allowed for diffusion along the line but not across from one line to another. The bleaching was then simulated by generating a region of 0 mol m^{-3} of the component c in the centre, equivalent to the bleach spot, while the non bleached region was defined to have a concentration of 1 mol m^{-3} . Diffusion was then monitored in the overall pattern.

As can be seen in figure 3.10, the initial bleach spot is a circle, which then changes to an oval over time. Within the lines, the change from a clear cut to a gradual change of the concentration happens over less than 5 min. This indicates that diffusion is happening on a similar time scale as before. The line width for this simulation was set to be 53 nm, for this and the following simulations the diffusion coefficient was set to be $1.5 \mu\text{m}^2 \text{ s}^{-1}$ and the spacing of the lines was scaled according to the line width.

The width of the lines can easily be changed in simulation and can be changed in experiment through the change of the speed at which the tip is moving over the surface. This allows for an almost arbitrary change of the constriction of diffusion from very thin lines up to a line width at which two dimensional diffusion is happening again.

Figure 3.11 shows the variation in the apparent diffusion coefficient as determined by the Axelrod method with varying line width. The diffusion coefficient

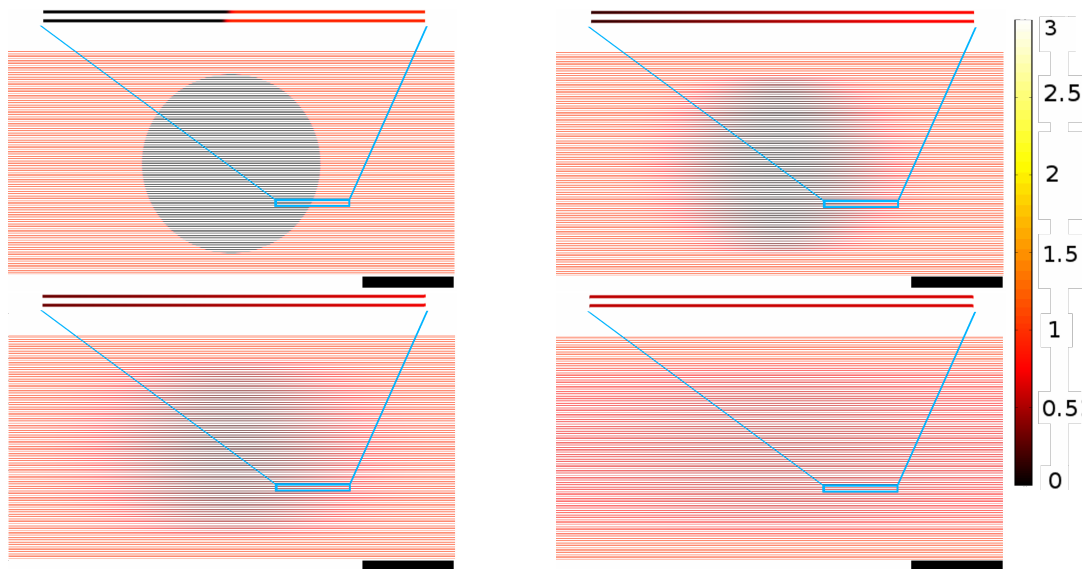


Figure 3.10: Succession of simulated FRAP images. Top left shows the intensity distribution directly after bleaching the bilayer. Top right, bottom left and bottom right are 25s, 75s and 300s after the bleach. The scale bar in each image is $10\ \mu\text{m}$, the colour map for the concentration of fluorescently marked molecules used for all subfigures is shown in on the right and shows the relative surface concentrations normalised to the initial concentration. On the top of each image is a magnification of two lines taken from the same region.

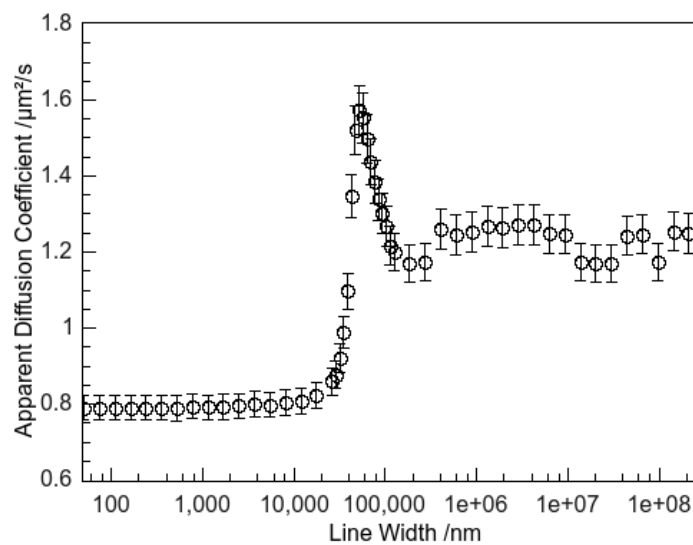


Figure 3.11: Variation of the apparent diffusion coefficient with the variation of the line width to show the influence of low dimensional diffusion obtained from the FEA calculations.

shows a step like change from one dimensional diffusion, where the apparent diffusion coefficient is lowered to almost regular two dimensional diffusion, where the apparent diffusion coefficient increases to almost its bulk value. The spike in D was not seen in experiment (Heath et al., 2014) and seems to be an artefact of the simulation when the finite element cells approach the same size as the patterned lines. Although the experimental data further reduces its diffusion coefficient when the lines are thinner, this effect is not seen in the calculations. The difference between experiment and calculation is most likely due to the simulation assuming the lipids to occupy a negligible surface area compared to the pattern size. This is assumption can be made for lines on the micron scale, but for lines approaching the size of a few lipid head groups, this assumption is no longer valid.

3.2.2 Reduced Mobility

In previous experiments an effect occurred which was attributed to the reduced mobility of TxRed in the SLB when it was concentrated to a high degree. This was seen especially in patterns used for AC experiments which were used to generate regions of high concentration of charged membrane components. Which is in contrast to simple line patterns in DC experiments where the concentration reached close to the barrier is not as high as in the concentration region of AC patterns such as the ones shown in figure 3.12 and 3.13.

As can be seen in figure 3.12, the reduced mobility in an AC experiment can be seen in regions in which the TxRed has been concentrated to a high degree. This is shown by a fraction of the fluorophore not moving or moving much slower than the bulk of it. The effect is not predicted by the solution of the Einstein-Smoluchowski equation, which is calculated by COMSOL. The difference between experiment and simulation shows that this is an effect which

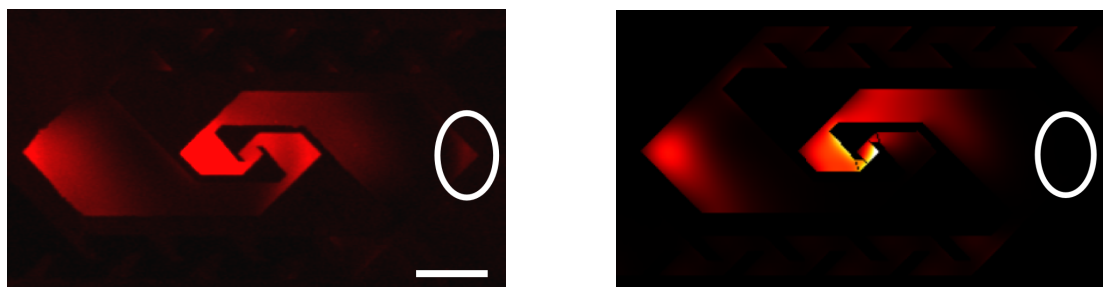


Figure 3.12: Reduced mobility as seen in a previous experiment (carried out by Matthew Cheetham). The left image shows the experimental result while the image on the right shows the calculated predictions. The difference in the marked area shows a region of high concentration of TxRed, which results in reduced electrophoretic mobility of the fluorophore. The scale bar in the left image is 200 μm .

does not stem from the diffusion and electrophoresis in the membrane but seems to be a result of concentrating TxRed in the membrane.

It was shown previously that TxRed can interact with the membrane and that the head group of it can fold into the membrane instead of being in the solution above it. Molecular dynamics simulations have shown that the aromatic head group of TxRed interacts with the hydrophobic core of the membrane and resides approximately 1.5 nm away from the centre of the membrane (Skaug et al., 2009). Using the same method, it was also shown, that TxRed also binds 1.2 DPPC molecules by charge–dipole and dipole–dipole interactions and that it has a mobility which is 30 % lower than the mobility of DPPC (Skaug et al., 2011).

Here, a different effect was observed, the mobility of a small amount of the TxRed, instead of all of the material, is reduced compared to the bulk of it, which behaves as expected. In order to investigate this further, a simpler pattern for the SLB was used, which allowed for the concentration of TxRed in a short time (although to a lower relative concentration) in a central region of interest. The pattern used to investigate the effect is shown in figure 3.13, the initial concentration of TxRed used in these experiments is 1 mol % and the bilayer is made of POPC.



Figure 3.13: Pattern used for the investigation of the effect of reduced mobility. The electric field of 62 V cm^{-1} is applied from left to right and causes the charged TxRed to concentrate in the centre. The scale bar is $100 \mu\text{m}$

Using this pattern for the recreation of the effect of reduced mobility of TxRed in a lipid bilayer was successful. The fluorescence signal detected after three cycles of an AC field of 62 V cm^{-1} for a period of 20 min can be seen in figure 3.14. Although all the TxRed in the lipid bilayer should have moved to the left, there is a significant amount of fluorescence signal coming from the right hand side corner of the trap. The line profile was taken from the central region of the pattern and shows clearly that the effect of reduced mobility occurs in the opposite corner of the main concentration, where the concentration of TxRed has been high before. When the field is reversed, the region of reduced mobility also changes the region of the trap in which it occurs, showing that this effect occurs whenever TxRed has been concentrated to a high degree.

The effect does not occur with all lipid dyes. The same experiment as before was carried out with NBD attached to lipid molecules. When 2 mol % of NBD 1,2-dioleoyl-sn-glycero-3-phosphoethanolamine (DOPE) were used in the same pattern of a POPC bilayer and the same field as before was applied, there was no effect of reduced mobility seen, as shown in figure 3.15 even though the concentration of NBD is even higher than the concentration of TxRed used in figure 3.14

As NBD DOPE is attached to a different lipid than TxRed, which is attached to 1,2-dihexadecyl-sn-glycero-3-phosphoethanolamine (DHPE), the experiment was also carried out using NBD DHPE. The experimental conditions were

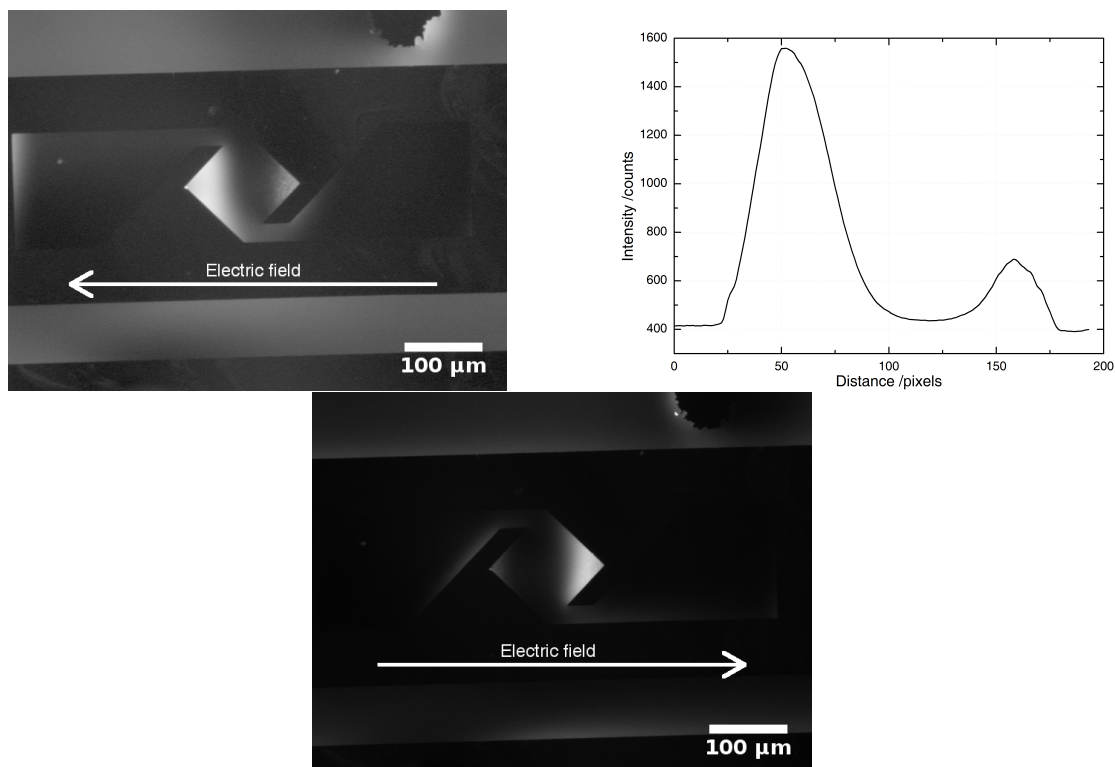


Figure 3.14: Experimental images and line profile of an area of reduced mobility in a trap device. The line profile on the right hand side shows an increase in fluorescence over the area of reduced mobility. The image on the bottom shows the region of reduced mobility on the opposite side of the trap region.

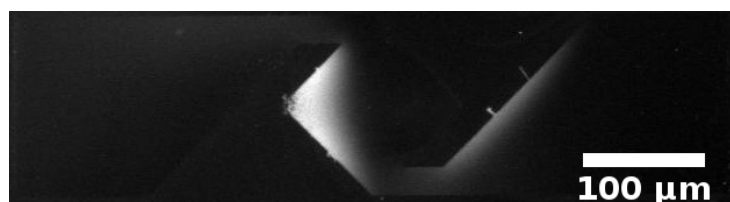


Figure 3.15: In contrast to figure 3.14, no reduced mobility is seen, when using NBD DOPE as a dye in the bilayer instead of TxRed. All other conditions (dye concentration, field strength and period of the electric field) were kept constant.

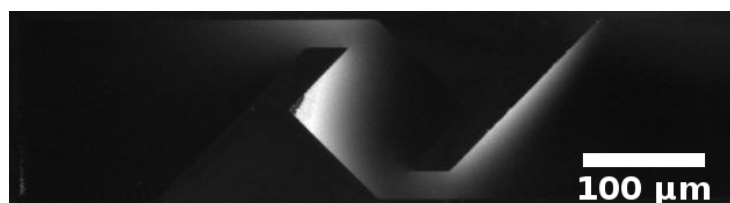


Figure 3.16: Fluorescence image of NBD DHPE showing no reduced mobility in contrast to the experiment where TxRed was used. Again, all conditions compared to the TxRed experiment were kept constant.

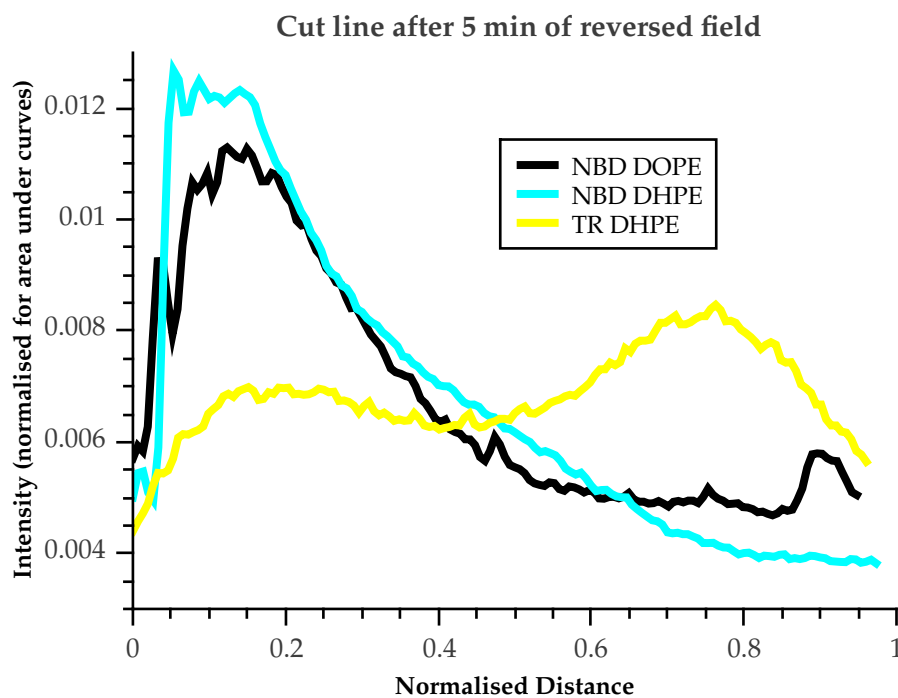


Figure 3.17: Comparing the different dyes in a bilayer. The dyes were concentrated in a central trap and the field was then reversed for five minutes. A line plot of the fluorescence intensity (normalised for areas under the curves) is given here. The mobility of the Texas Red is greatly reduced compared to NBD.

identical to the ones for NBD DOPE. Despite the lipid now being identical to the TxRed DHPE, again no reduced mobility was seen.

The results indicate that the reduced mobility is an effect which is unique to TxRed and does not depend on the lipid which it is attached to. The influence of the TxRed can also be seen when the line profiles obtained after a set time of field reversal between the different dyes are compared.

As seen in figure 3.17, while TxRed shows two peaks, one of “normal” mobility and one for the reduced mobility, neither of the line profiles for NBD based lipid dyes shows this behaviour. The higher mobility of NBD based dyes can also be seen, when the speed at which they move under the influence of the same electrophoretic force is measured. This was done by fitting a Gaussian curve to the peak corresponding to the non-reduced mobility before the field reversal and repeating this after three minutes of field reversal, and measuring

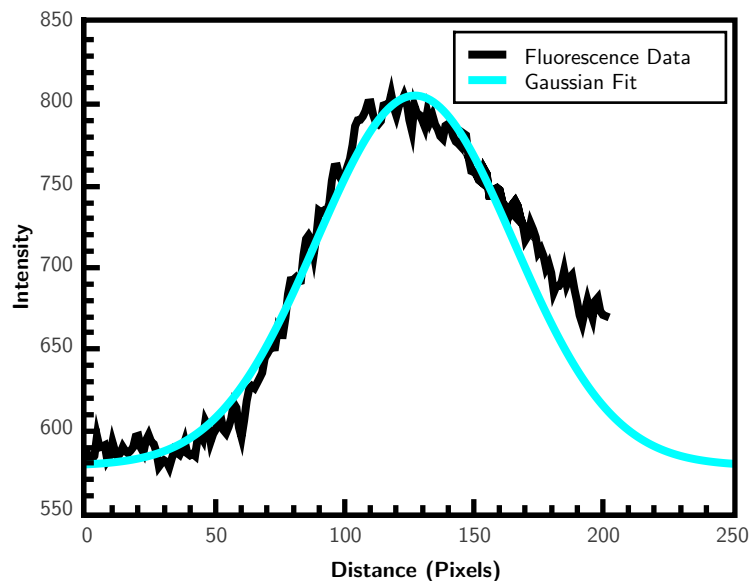


Figure 3.18: Typical line profile and a Gaussian fit used for the determination of the movement of the different dyes. The fit gave the centre of the peak at $x_C = 123$ pixels. The right hand side of the fit does not perfectly coincide with the measured data because this is the region where the trapping area started.

Dye - Lipid	Distance Travelled
NBD DOPE	135.8 μm
NBD DHPE	160.3 μm
Texas Red DHPE	54.0 μm

Table 3.1: Distance travelled by different dye-lipid combinations after three minutes of field reversal.

the distance in the different dye–lipid combinations have travelled, one example of the fitting can be seen in figure 3.18.

The distance, which the different dyes cover over the same time, is shown in table 3.1. It can easily be seen that NBD based dyes have double to triple the electrophoretic mobility of TxRed. This indicates that TxRed not only has a reduced mobility under some circumstances, but also in general is much slower in electrophoresis, as has been seen in other experiments as well (Cheetham et al., 2011; van Oudenaarden and Boxer, 1999) where the reduced mobility of TxRed has been given as 0.6 that of the membrane. Here, the reduced electrophoretic mobility compared to NBD based dyes is between 0.4 and 0.3 for NBD DOPE

and DHPE respectively. The difference in behaviour could be due to the two species of TxRed which are present in the samples, *ortho*- and *para*-TxRed. It was shown previously that the two species have different electrophoretic mobilities, even at pH 7.4 (Pace et al., 2013; Poyton and Cremer, 2013). This shows again that lipids with dyes attached do not behave identical to lipids without the dyes, although this assumption is often made in the literature.

3.3 Directed Brownian Motion

This section will show how Brownian motion can be combined with electric fields to result in movement of charged species perpendicular to the electric field. Firstly, Brownian motion in general will be discussed. Secondly, the idea of Brownian ratchets will be introduced. Combining this with electrophoretic movement in lipid bilayers will result in the ability to move and concentrate charged membrane components.

3.3.1 Discrete Diffusion

First discovered in pollen movement in 1827 by the Scottish botanist Robert Brown, Brownian motion was first thought to be some kind of life on the small scale. It quickly turned out that Brownian motion strongly depends on temperature and the material looked at. Molecules or particles which are free to move (i.e. not in a solid but in either a liquid or a gas) undergo the process of so called Brownian motion. In this process the particles or molecules are randomly hit by other molecules which move around due to the energy each of them has through temperature. This results in a random motion of particles in either liquids or gases.

When looking at a single particle undergoing a random walk in one dimension, in each time interval t_i the particle can either do one step to the left or a step to the right. The discrete steps are measured in distances l along the x -axis.

Without loss of generality we can assume that the number of steps taken n is even. In order to have arrived at the position $x_m = ml$, the particle must have taken $\frac{1}{2}(n + m)$ steps in positive x direction and $\frac{1}{2}(n - m)$ steps in negative x direction. The probability p to find the particle at a given position x_m after n steps can therefore be written as

$$p_n(m) = \frac{n!}{\left(\frac{1}{2}(n + m)\right)! \left(\frac{1}{2}(n - m)\right)!}. \quad (3.5)$$

Stirling's approximation $x! \approx \sqrt{2\pi n} \left(\frac{n}{e}\right)^n$ can be used for large values of n and m , resulting in

$$p_n(m) = \frac{2}{\sqrt{2\pi n}} e^{-\frac{m^2}{2n}}. \quad (3.6)$$

This is the well known Gaussian distribution centered around $m = 0$, with a mean square displacement $\langle m^2 \rangle = n$; in terms of x the mean square displacement is $\langle x^2 \rangle = nl^2$.

3.3.2 Continuous Diffusion

Instead of finite steps l we can also use a continuous space variable x ; the number of steps n is replaced by the time t , assuming there are n jumps in t . Thus, a probability distribution over space and time

$$p(x, t) = \frac{1}{\sqrt{4\pi Dt}} e^{-\frac{x^2}{4Dt}} \quad (3.7)$$

is obtained, where the diffusion coefficient $D = \frac{nl^2}{2t}$ was introduced. The mean square displacement in terms of x is now

$$\langle x^2 \rangle = 2Dt. \quad (3.8)$$

This can easily be expanded to more than just one dimension. With the extra degrees of freedom, the mean square displacement scales with dimensionality

$$\langle x_{1D}^2 \rangle = 2Dt \quad (3.9)$$

$$\langle x_{2D}^2 \rangle = 4Dt \quad (3.10)$$

$$\langle x_{3D}^2 \rangle = 6Dt \quad (3.11)$$

In this work most of the cases looked at are diffusion in two dimensions, thus $\langle x_{2D}^2 \rangle$ is governing the time dependence of the displacement of the material in question. Even if molecules are initially concentrated through an external force, this concentration will soon start dispersing, as the molecules will start spreading out over a bigger area with increasing time. This effect is increased through Fick's law of diffusion:

$$\mathbf{J} = -D\nabla\phi, \quad (3.12)$$

with the diffusive flux \mathbf{J} , the diffusion coefficient D , and the density of the diffusion material ϕ . This means that there is a net flux away from areas with a high concentration gradient ($\nabla\phi$) of a certain species driving the overall concentration into an equilibrium with an even distribution of all of the molecules.

The previous results can be combined into the diffusion equation. The continuity equation

$$\frac{\partial\phi}{\partial t} + \nabla \cdot \mathbf{J} = 0. \quad (3.13)$$

states that any change in the concentration of the diffusing material must be equal to the (negative) flow of material. This is called the continuity equation as it states that no material is either generated or destroyed. Using Fick's first law 3.12 and substituting \mathbf{J} into 3.13 gives:

$$\frac{\partial\phi}{\partial t} + \nabla \cdot (-D\nabla\phi) = 0 \quad (3.14)$$

In this equation the assumption is made that the diffusion coefficient is isotropic. Despite this not always being the case, it is the case in SLBs and therefore this can be justified for this case. Assuming that D is a constant and not depending on either density or spatial position, this equation can be further simplified to

$$\frac{\partial\phi(\mathbf{r}, t)}{\partial t} = D\nabla^2\phi(\mathbf{r}, t). \quad (3.15)$$

When an external electric field is applied to charged material, it is not only undergoing free diffusion, but also drift due to the electric field. The combination of drift and diffusion is accounted for in the Smoluchowski equation. It also can be derived from the continuity equation 3.13 (for this case no generation or consumption of material is assumed). The difference now is that the flux \mathbf{J} is written as the sum of two fluxes:

$$\mathbf{J} = \mathbf{j}_{\text{diffusion}} + \mathbf{j}_{\text{drift}} \quad (3.16)$$

$$\mathbf{j}_{\text{drift}} = \mathbf{v}\phi, \quad (3.17)$$

where \mathbf{v} denotes the velocity of the material.

With the diffusional flux still being the same as in 3.12, the continuity equation can be written as:

$$\frac{\partial\phi}{\partial t} + \nabla \cdot (-D\nabla\phi + \mathbf{v}\phi) = 0 \quad (3.18)$$

This equation does not take into account what causes the drift velocity but is a mere description of the effects of drift onto diffusion. Solving this differential equation allows for an accurate prediction of the behaviour of diffusing molecules.

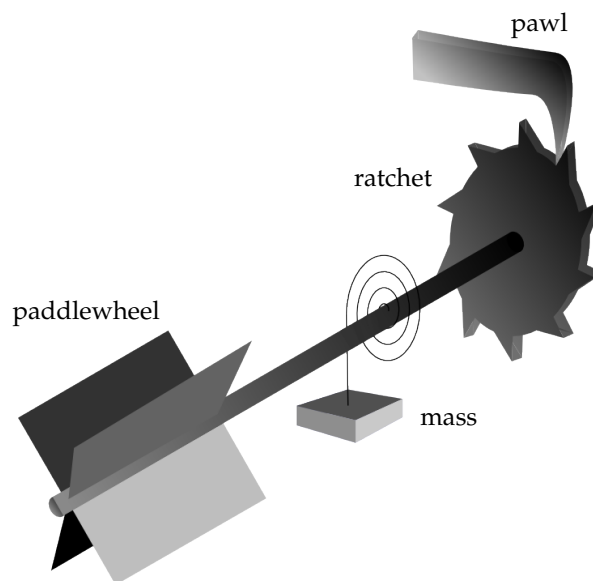


Figure 3.19: Brownian ratchet as proposed by Smoluchowski and discussed by Feynman. The paddlewheel on the left can get hit by molecules and thus rotate. The ratchet and pawl system on the right allows only for clockwise rotation and stops any anti-clockwise movement. Thus the ratchet can do work, like lifting the mass in the centre up.

3.4 Brownian Ratchets & Parrondo's Paradox

This section introduces Brownian ratchets and how they can be used to transport charged membrane components perpendicular to an applied electric field. It is also shown how these ratchets relate to Parrondo's paradox, which states that two individually losing games can be combined to an overall winning game. The "games" played here are diffusion and ratcheting in a membrane.

3.4.1 Brownian Ratchets

Brownian ratchets are built on the idea to generate work from Brownian motion only and therefore cooling down a single reservoir at any given temperature. The ratchet was investigated first by Smoluchowski in the early 20th century (Smoluchowski, 1912). This idea has been looked at in quite some detail by Feynman (Feynman, 1963). He proposed the idea of a microscopic paddlewheel with a ratchet and a weight on a string. Every time the paddlewheel is hit by

a molecule undergoing Brownian motion in a way that lifts up the weight, the paddlewheel moves one step ahead. If it is hit such that the weight would move down, the ratchet stops its movement so that no downwards movement of the weight is possible. This should allow for the weight to be lifted up while the heat reservoir is cooling down without having to rely on a temperature gradient. If this was possible, it would disprove the second law of thermodynamics, as stated by Planck (Planck, 1903):

It is impossible to construct an engine which will work in a complete cycle, and produce no effect except the raising of a weight and cooling of a heat-reservoir.

After some deeper analysis one finds out that although the manufacturing of such a device might be possible, it will have to be of the nano scale to be able to create a net movement from Brownian motion of single molecules. This also means that the ratchet and pawl device holding the paddlewheel in position if the paddlewheel was to go backwards also has to be on the nano scale and is subjected to random hits by the surrounding medium. Therefore the ratchet will fail every time the ratchet is being hit by a molecule while the paddlewheel is being hit in the undesired direction. Interestingly, the rate of failure of the ratchet is identical to the rate of success in the paddlewheel, meaning that no net movement can be generated (Feynman, 1963).

This effect could be overcome if the ratchet and the paddlewheel were in two reservoirs which are being kept at different temperatures with the ratchet and pawl being in the colder one. This would then be a heat engine working through the temperature difference between the two reservoirs. The warmer reservoir will cool down over time as the energy will slowly be taken out via the paddlewheel. The second reservoir could be kept at room temperature, but as the first reservoir with the paddlewheel approaches room temperature, the machine would stop working. Therefore external energy is needed to either

keep the second reservoir cooler than the first one or to continuously heat up the first reservoir.

3.4.2 Parrondo's Paradox

Parrondo's Paradox states that there is the possibility to combine two losing games into a single winning one. This may sound counter-intuitive but is based on the exact probabilities in the two games and works for games where there is a decision made on the basis of the results of the previous games.

One can imagine two different games, A and B. Game A is a simple coin toss with the probability of winning p_A and the probability of losing the game $1 - p_A$. If game A is played with a biased coin, such that $p_A < \frac{1}{2}$ then game A is a losing game. For the case discussed here, p_A was set to be

$$p_A = \frac{1}{2} - \epsilon, \quad (3.19)$$

with ϵ being small compared to p_A but $\epsilon > 0$. Game B is slightly more complicated than game A. It uses two biased coins and although the starting capital can be chosen arbitrarily, the choice of the coin used for the next coin toss depends on the current capital M . As expected, the capital is increased by 1, if the outcome of the coin toss is favourable and decreased by 1 if the outcome is unfavourable. The first coin c_1 is used if the current capital M is divisible by an integer i . If this is not the case, the second coin c_2 is used. The bias of c_1 is such that the probability of winning is $p_{B_1} = \frac{1}{10} - \epsilon$. Even if the probability of winning using c_2 is greater than $\frac{1}{2}$, this can still be outweighed by the fact that c_1 is used in more of the cases if i is greater than 2. Therefore, p_{B_2} can be set to $p_{B_2} = \frac{3}{4} - \epsilon$ and still game B remains an overall losing game.

The games were then "played" in a computer simulation. Each of the results is an average of playing the games multiple times and averaging the current capital over these iterations. Firstly, the games A and B were played individually.

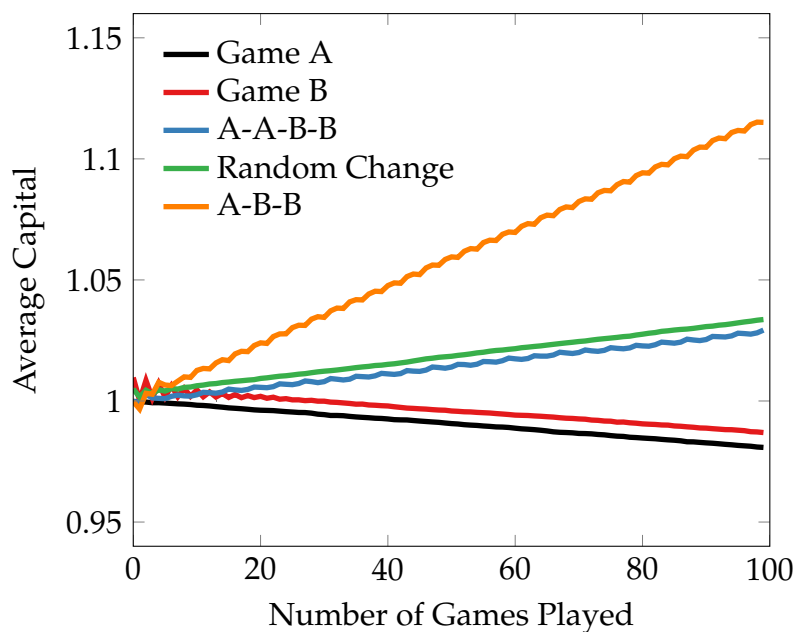


Figure 3.20: Average capital when games A and B are played individually and combined. The graphs show the average capital of 10.000 iterations obtained when playing each of the games or the combination of them. The individual games are losing games while different combinations show different rates of increase in the average capital.

Both of the individual games lead to an average loss of money over the time the games are played for. This can be seen from the black and red line in the graph for the individual games in figure 3.20, where the average capital goes down by about 2% over 100 played games. This is not the case if the two games are combined in the right way. When the player switches either randomly between the two games or plays them in the order AABB the combination of the two games results in winning game for the player. This results in a win of about 3% in 100 games. The average amount of money owned by the player can be increased even further when the games are played in the order ABB. The average result of 100 games then is a win of approximately 12%. This shows how the clever combination of two losing games can lead to a new, winning game when at least one of the games depends on the previous outcome (Harmer and Abbott, 1999; Parrondo et al., 2000).

Although the two “games” which are used in a Brownian ratchet as it has been used in this work are not alternated in a random way but just as ABAB, still

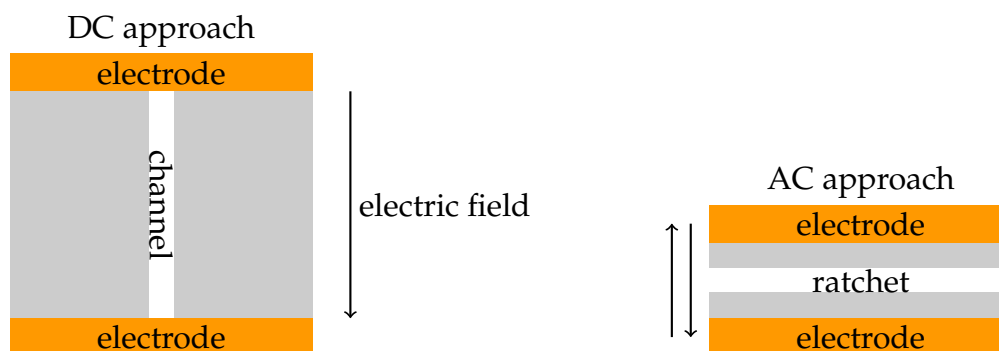


Figure 3.21: On the left a DC approach is shown, on the right an AC approach to transporting material is shown. In the DC case transport happens to in the direction of the electric field, in the AC case transport is achieved perpendicular to the electric field.

a winning game can be created from two individually losing games. The target, defined here as “winning” is the transport of a charged molecule perpendicular to an electric field. Transport in such a way allows for the electrodes to be much closer to the device used than in a more classical DC approach, where charged molecules are moved in the direction of the field. The DC approach requires the electrodes to be at least as far away from each other as the transport distance is. Using the ratchet approach, this can be minimised to the width of the ratchet. Such a small distance between the electrodes not only allows for a miniaturisation of the device, it also allows for a lower voltage which has to be applied to the electrodes, in order to still achieve the same field strengths as before.

The two “games”, which are “played” here, are free diffusion and movement into the ratchet under an electric field and winning is defined as the transport of charged molecules. Both of these games individually are losing games as neither of them results in effective transport perpendicular to the electric field. When the two “games” are combined into one overall game, efficient transport can be achieved. Figure 3.22 shows the working principle of a Brownian ratchet. Firstly, charged material is concentrated into the ratchet and has a sharp Gaussian distribution in the bottom of the ratchet. Then the charged material is moved out of the ratchet and free diffusion starts to happen which results in the Gaussian

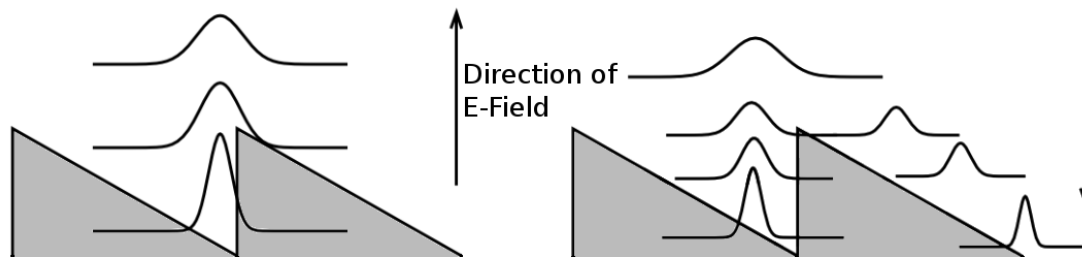


Figure 3.22: Principle of a Brownian ratchet used here. After charged molecules are concentrated into a ratchet and have a sharp Gaussian distribution in the bottom of the ratchet (left) the direction of the electric field is reversed and movement out of the ratchet starts to happen. During this time free diffusion can also happen and the Gaussian distribution widens. When the field is then reversed (right), the part of the Gaussian distribution that goes over the ratchet is "cut off" and goes one ratchet ahead. This is how transport in a ratchet is achieved.

distribution of the charged molecules broadening. When the charged material is then moved back into the ratchet, the part of the Gaussian distribution that has diffused over the next ratchet will move one ratchet ahead. The cycle then starts again and over many cycles transport perpendicular to the electric field can be achieved.

A simple way to imagine the working principle of two games in terms of a ratchet is to imagine a flashing ratchet, where the particles are free to diffuse along a line and this line can be turned into a ratchet shape at given time intervals (Amengual et al., 2004; Denisov et al., 2009; Makhnovskii et al., 2004). When the ratchet flashes up, the particles will move into the bottom of the individual teeth, while the ratchet is down, the particles will freely diffuse. A schematic of this process is shown in figure 3.23. As the ratchet flashes on and off, the particles are moving to the right of the ratchet. This process works using two mechanisms. Firstly the ratchets move all the particles into the bottom of their teeth. From there, when the ratchet is no longer present, the particles can diffuse freely to the left or the right. The asymmetry in the ratchet pattern leads to the transport of particles, as, on average, a particle will much more likely move the equivalent of one ratchet forward, than one ratchet backwards. After the ratchet is switched on, a particle that moves half a tooth length to the left will remain in the same

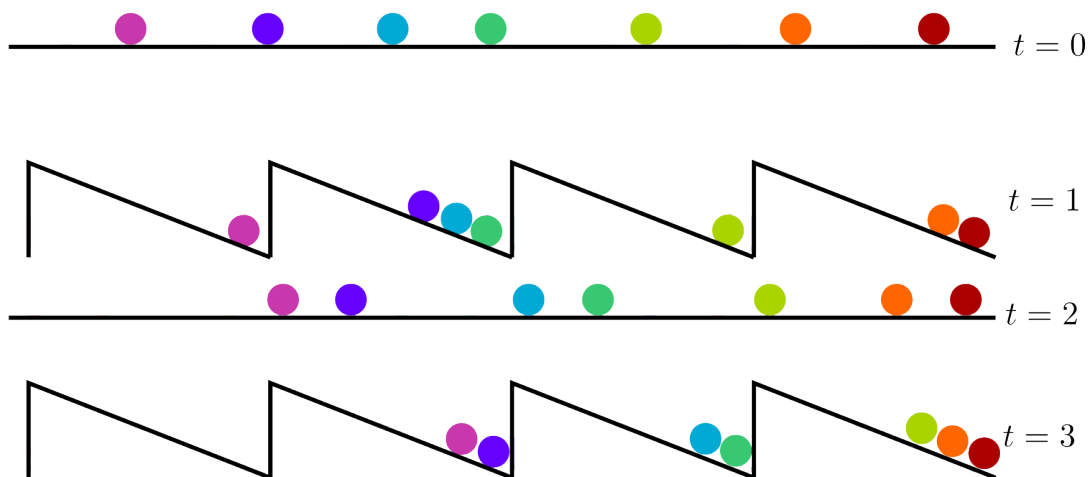


Figure 3.23: A flashing ratchet moving particles towards the right. The different particles are diffusing freely while the ratchet is not activated ($t = 0$, $t = 2$) and move into the bottom of the teeth while the ratchet is active ($t = 1$, $t = 3$). The combination of free diffusion and ratcheting potentials leads to a transport of particles to the right. .

tooth as it was in initially, while a particle which moves half a tooth length to the right will have moved one “step” forward.

The principle of flashing ratchets can be used in different applications. These include electrodes doing work in transporting organic molecules (Roeling et al., 2011), feedback controlled ratchets for improved transport (Lopez et al., 2008) and single particle transport (Bao and Zhuo, 1998).

The same principle, which applies to single particles in flashing ratchets applies to a distribution of material in a ratchet or in a lipid bilayer. The principle of a Gaussian distribution moving in a ratchet pattern is shown in figure 3.24. The overlay of a Gaussian distribution with the ratchet pattern demonstrates that the biggest fraction of the material in a specific tooth will remain in the tooth (yellow). Despite this disadvantage, the fraction of the material which will move forwards (green) is still much larger than the fraction which will move backwards (red), when one cycle is completed and the material moves back into the ratchet.

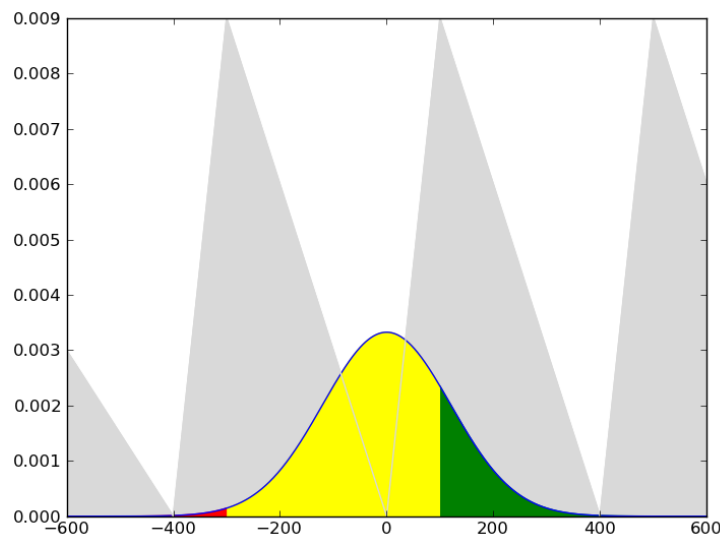


Figure 3.24: Gaussian distribution of material in a ratchet overlaid with a Brownian ratchet pattern. The green fraction of the Gaussian distribution will move one ratchet forward, the yellow fraction will remain in the same region while the red fraction will move one step backwards.

Even with such a simple model of a Brownian ratchet, predictions of its behaviour can be made. When assuming a constant fraction of the amount of material in a tooth is moving forwards the change in each ratchet can be calculated. For every cycle it is assumed that the fractions which are marked in the different colours in figure 3.24 moves into the predicted region. This results in the prediction for each tooth shown in figure 3.25. It can be seen that initially the transport out of each ratchet is equal to the transport into each ratchet apart from the first and the last ratchet. Therefore, the concentration decreases in the first ratchet and the increases in the last ratchet, initially. As transport continues, not only the first, but also the second tooth starts moving more material out of the tooth than is being back filled by the previous ratchet. This process continues until every tooth is emptied and there is equilibrium between the material diffusion backwards into the second to last tooth and the material being transported from the second to last tooth into the last tooth (from cycle 20 onwards).

Brownian ratchets and their possible uses have been investigated in the literature in some detail. It is possible to separate particles based on their

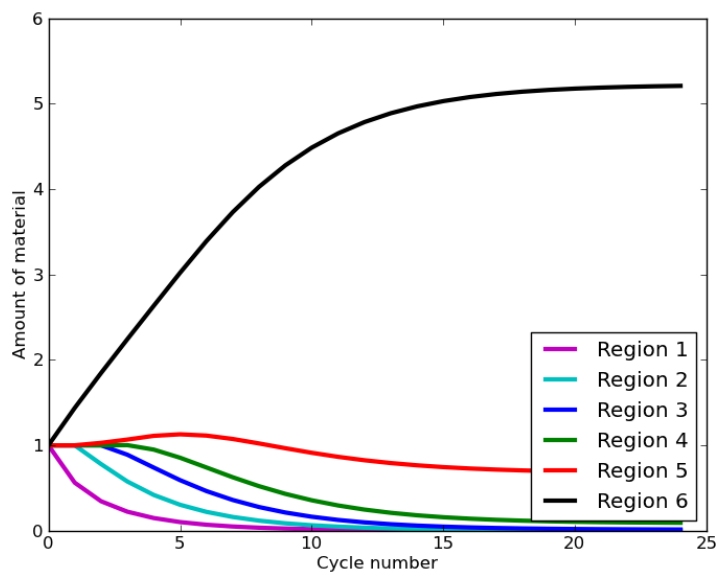


Figure 3.25: Calculation of the transport in Brownian ratchets based on a Gaussian distribution in each ratchet. The relative concentration in the last region increases while the relative concentration in the other regions decreases with the first regions decreasing before the last regions.

diffusion coefficients (Astumian et al., 1998), DNA can be transported (Bader et al., 1999) or separated (Huang et al., 2003) and pores can be used as sieves in either single channel setups (Verleger et al., 2012) or in parallel through many pores (Matthias and Müller, 2003). Brownian ratchets in lipid bilayers are based on the same principles as ratchets used for different applications and have been used for molecular separation (van Oudenaarden and Boxer, 1999) and concentration of membrane components (Cheetham et al., 2011).

3.5 Optimisation of Brownian Ratchets

In order to further understand the influence of different parameters on the efficiency of a Brownian ratchet, different patterns of lipid bilayers were simulated using finite element analysis. This allows for solving the Nernst-Planck equation in different geometries and obtain predictions for the behaviour of charged membrane components under the influence of an electric field and a ratcheting pattern.

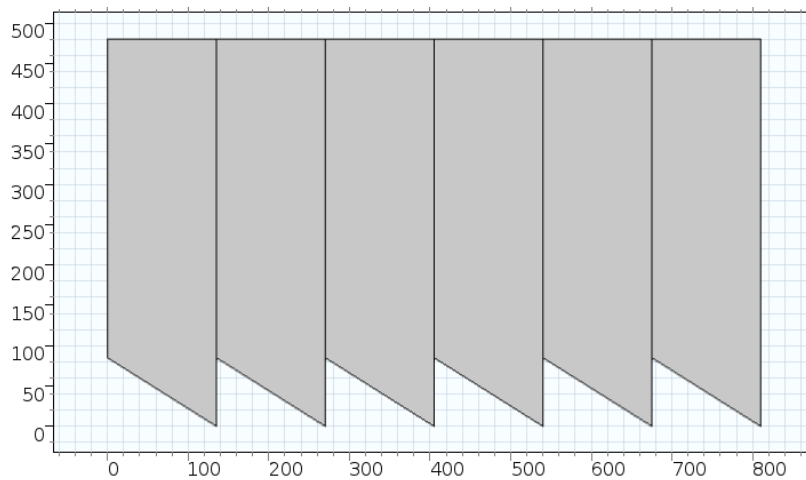


Figure 3.26: Patterned used for the calculation of transport in a patterned SLB. Six individual ratchets are combined into one geometry in COMSOL. The grey area represents the region which is simulated as the SLB region, where the effects of diffusion and electrophoresis are calculated. The outside barriers allow for no flux through them. The axis are in micro metres and show the overall dimension of the pattern.

3.5.1 Transport in a Brownian Ratchet

In order to show that a Brownian ratchet can achieve transport perpendicular to an applied electric field in a lipid membrane, a simple Brownian ratchet was simulated using the chemical engineering package in COMSOL. The simulated device consisted of six ratchets and transport was measured using the average surface concentration in the last ratchet normalised to the initial concentration in this ratchet. The layout of the ratchet pattern is shown in figure 3.26.

As discussed in part 2.5 the geometry and the size of the mesh is important when using FEA. A too coarse mesh will result in inaccurate results while a too fine mesh will give accurate results at high computational cost. To achieve optimal mesh size, the maximum size of a single mesh element was varied between $100\ \mu\text{m}$ and $1\ \mu\text{m}$ depending on the region of the pattern. Regions of high concentration were meshed fine (bottom of the teeth) while regions of less interest were meshed more coarsely (top of pattern).

The electric field used in both simulation and experiment can be seen in figure 3.27. Both, the electric field strength and the cycle time are normalised.

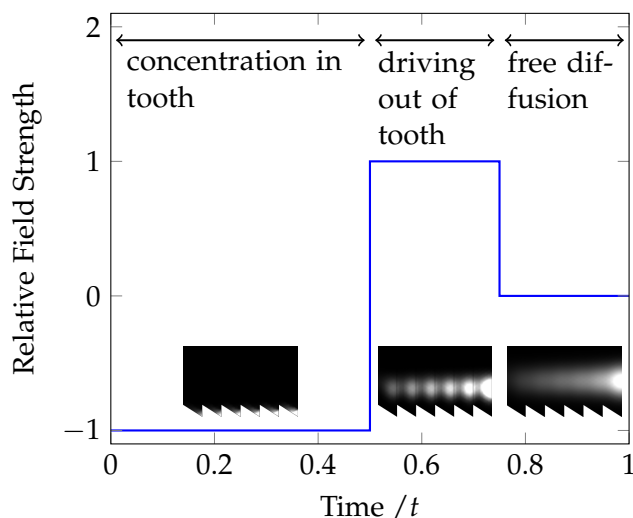


Figure 3.27: Applied electric field in a Brownian ratchet as a function of time normalised to the period time t . The insets show the behaviour of the charged material within the ratchet where the images are taken at the end of each of the three steps.

Parameter	Value	Description
a	$0 \mu\text{m}$	opposing edge on the ratchet
c	$480 \mu\text{m}$	height of the channel
e	60 V cm^{-1}	strength of electric field
h	$85 \mu\text{m}$	height of the ratchet
l	$810 \mu\text{m}$	length of the channel ($l = n \cdot (a + r)$)
n	6	number of ratchets
r	$135 \mu\text{m}$	individual ratchet length
t	0.67 h	period of the electric field

Table 3.2: Parameters used for the simulation and the experiment, unless stated otherwise. A schematic overview of the parameters is shown in figure 3.38.

For the first part of the cycle, the field is applied such that all of the charged material moves into the ratchet. In the second part the field is reversed and the charged material is moved out of the ratchet. The last step is the field being switched off and the material is allowed to diffuse freely for a given time. When the time for which the charged membrane component was driven out of the ratchet, τ , was changed, only the time of the second time step was changed while the others were kept constant.

For the simulations discussed in the following text the parameters were chosen (if not stated otherwise) to be as shown in table 3.2.

3.5.2 Prediction of the Ratchet Behaviour

The Brownian ratchets used here transports charged molecules perpendicular to the applied electric field. The field is applied in the y direction and transport happens in the x direction. This transport can be modelled using COMSOL. Brownian ratchets in a lipid bilayer were modelled as two dimensional objects, without diffusion in the third dimension. This is a very accurate model, as it is almost impossible for lipid molecules to leave the bilayer and possible, but very unlikely, to undergo flip-flop processes from one leaflet to the other, resulting in two-dimensional diffusion in the plane of the membrane.

This model is then exposed to an electric field with a strength of 62 V cm^{-1} , as it was done in the experiments, which makes the charged molecules move along the electric field lines. The general working principle of the ratchet is shown in figure 3.22. The initial state of the system is shown in figure 3.28a. The ratchet consists of two regions, one where chemical transport is modelled (red) and one where no transport is possible (white). These two regions correspond to the regions of lipid bilayer and fibronectin barriers in the experiments. Firstly the charged molecules are driven into the ratchet regions where an initial concentration happens (figure 3.28b). For the first cycle this is done for longer than during the rest of the cycles, as this is the only time where the full height of the channel has to be “emptied” of charged molecules. When all of the charged molecules have been driven from the channel into the ratcheting region, the field is reversed and the charged molecules are now being driven out of the ratchet again (figure 3.28c). This then allows for free diffusion to happen and for the molecules to diffuse in or against the direction of desired transport¹. As most charged molecules will accumulate in the bottom of a ratchet, the distance they need to diffuse over to reach the next ratchet in the direction of desired transport

¹The molecules can of course also diffuse in or against the direction of the electric field, but this motion will be cancelled out after one cycle as they are driven against the ratchet barriers in each cycle, effectively neutralising any transport which might have occurred in this direction.

is much smaller than the distance they need to diffuse against the direction of desired transport. Therefore, more molecules will diffuse one “step” forward than molecules diffusing one “step” backwards. The cycles of moving the charged molecules out of the ratchets and back into them are then repeated several times until finally the concentration of charged molecules in the ratchet on the right is much higher than in the ratchets on the left (figure 3.28d). Although there is significant build-up in the final ratchet, the first ratchets are not fully empty of charged material. This is because higher concentrations in any given ratchet result in higher back diffusion from this region since the diffusive flux is always away from areas of high concentration as can be seen from Fick’s law

$$\mathbf{J} = -D \frac{\partial c}{\partial x}. \quad (3.20)$$

The transport achieved with Brownian ratchets can be visualised through the concentration of charged material in each ratchet. The surface average of the concentration of charged material c_{av} is taken in each region of the ratchet (ratchets 1 to 6 in this case) by integrating the concentration of charged material in each ratchet at any given time $c(t)$ over the area of each ratchet A and dividing this value by the initial surface average:

$$c_{\text{av}}(t) = \frac{\int c(t) dA}{\int c(0) dA}. \quad (3.21)$$

Over several cycles this shows the expected behaviour. The first teeth (teeth 1 to 5 in figure 3.30) show a decrease of the charged material in them over time. It is worth mentioning that it is clearly visible how one ratchet after the other starts being “emptied” into the next one, until it is almost out of material and the next ratchet is being “emptied”. This continues until the molecules have moved

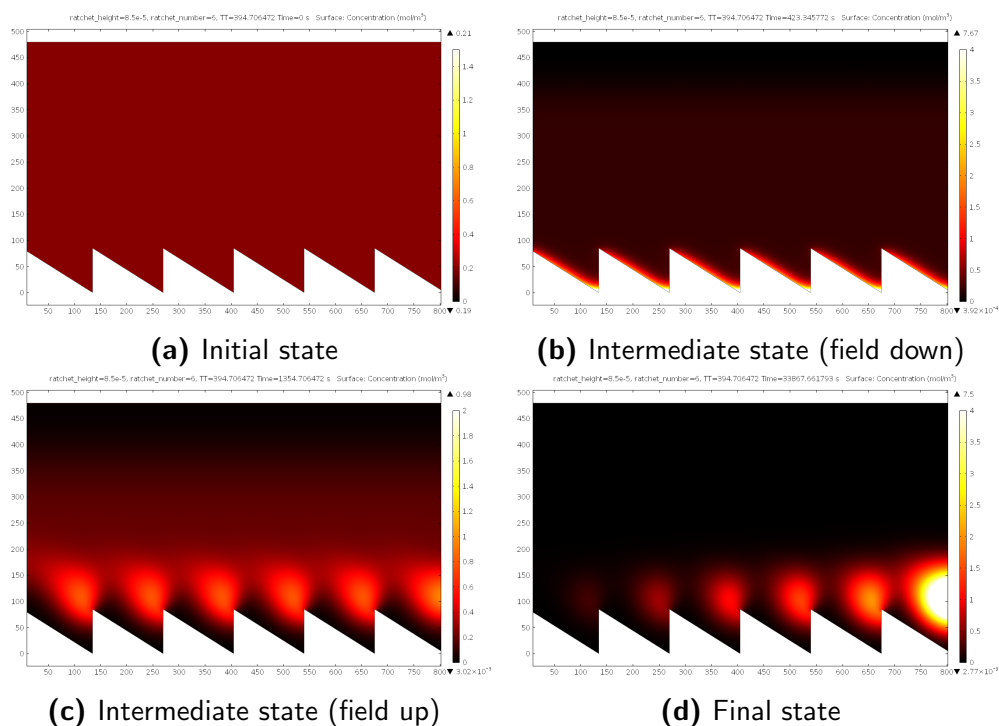


Figure 3.28: Different states of a Brownian ratchet, showing how transport is achieved from an initial equal distribution to the final state, where a higher concentration on the right is achieved. The top left image shows equal distribution, which is then driven into the teeth (top right) and when forced out of the teeth (bottom left) the probability of diffusing one step forward is higher than one step backwards leading to the final state (bottom right) which shows an increase in concentration in the last teeth.

into the last tooth of the ratchet, where they remain as the last ratchet does not have a neighbour in the direction of transport.

The profile of the applied potential can be varied in experiment and in calculation. A comparison of the effect of using different potentials (with the same amplitude between all of them) with the same pattern is shown in figure 3.29. The most efficient potential is a rectangular shaped curve while the triangular potential is the least efficient.

In figure 3.30, the first step taken before start of the cycles of ratcheting was to move all the charged molecules downwards into the teeth regions. The time for moving all the charged molecules, even from the very top of the pattern, into the bottom of the teeth was longer than the usual period of moving the charged molecules back into the teeth and can be seen as a decrease in tooth 6 for the

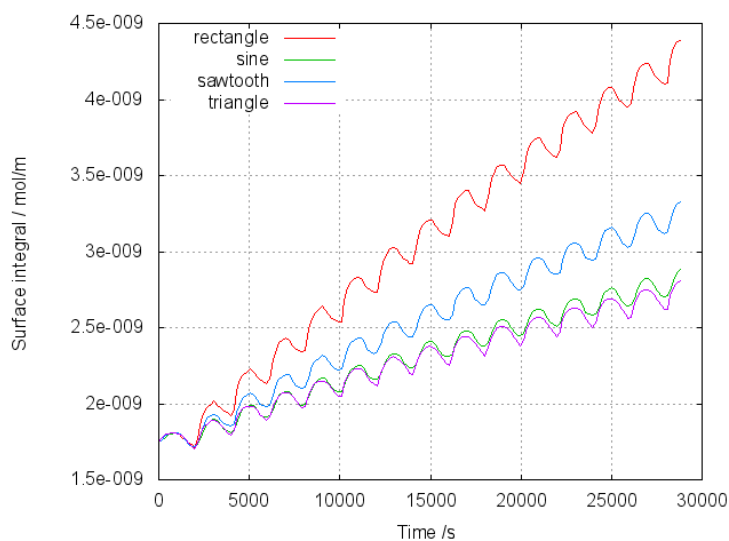


Figure 3.29: Calculated comparison of the effect of sine, sawtooth, triangular and rectangular shaped potentials on a Brownian ratchet. The pattern used is the same as shown in the previous figure. For all different field shapes the same period and amplitude was used.

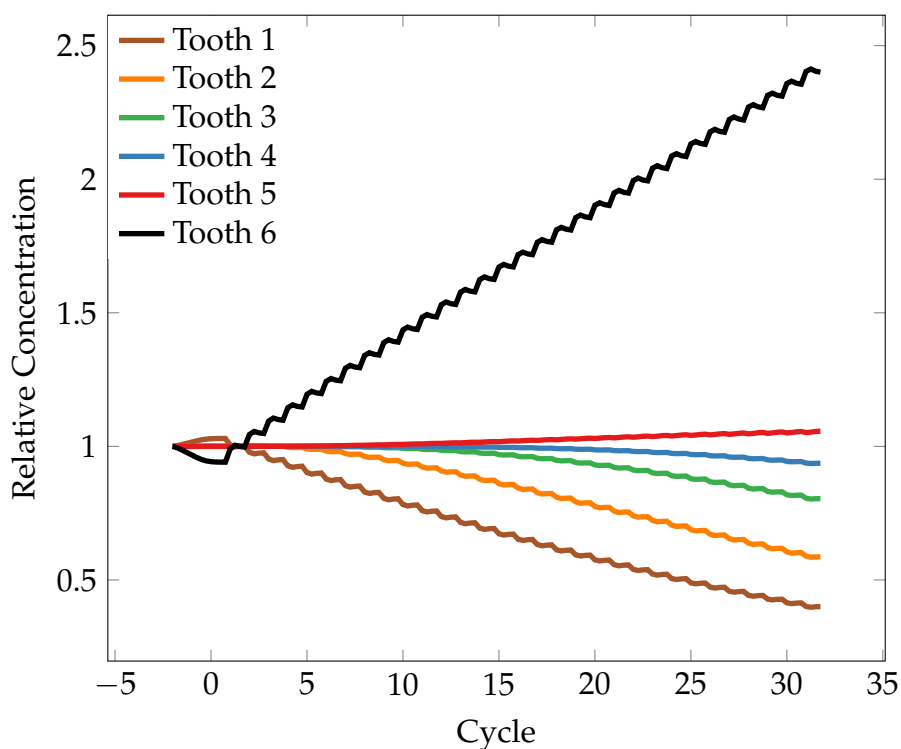


Figure 3.30: Calculated transporting behaviour of a Brownian ratchet from FEA shown for the different ratchet regions. As shown previously (see figure 3.25) the first teeth are emptied initially while the last tooth accumulates material.

time which is marked as negative cycles. Although it seems counter-intuitive that moving charged molecules from the channel region into the teeth regions results in a decrease in tooth 6 and an increase of charged material in tooth 1, this still happens and can be explained as follows.

As the charged molecules move out of the channel region and get concentrated in the trapping region, they start accumulating at the barrier of the teeth. This happens at the bottom of the teeth as well as at the top of each tooth before they move down into the tooth. As mentioned before, Fick's law (equation 3.20) describes how diffusion will always act against regions of high concentration. This means that charged molecules will move away from the regions they are being concentrated into. In the bottom of the teeth this means towards the top of the channel in the opposite direction in which they are driven through the electric field. At the top of each tooth the situation is different. Here the asymmetry of the concentration profile obtained through the concentration of the charged molecules against a diagonal barrier plays a much larger role. In the direction of the bottom of the same tooth the concentration of charged molecules is much higher than in the direction of the previous tooth, as the previous tooth is much deeper and the charged molecules have been driven to the bottom of the tooth. This results in a gradient in concentration and therefore a diffusive flux into the previous ratchet, as can be seen in the first cycles of figure 3.30. The total flux of the charged molecules in the teeth is shown in figure 3.31. The white streamlines at the top of the tooth are bending towards the previous tooth as they are driven by the diffusive flux from the red marked regions of high concentration at the top of the ratchet.

This effect causes every ratchet to lose some of the charged molecules into the previous ratchet. Although this is the same for all the ratchets, the first ratchet gains material from this process, as it has no neighbour it can lose molecules to, but gains molecules from the second tooth. The opposite is the case for the last tooth, which can only lose material to the second-to-last tooth but has no tooth

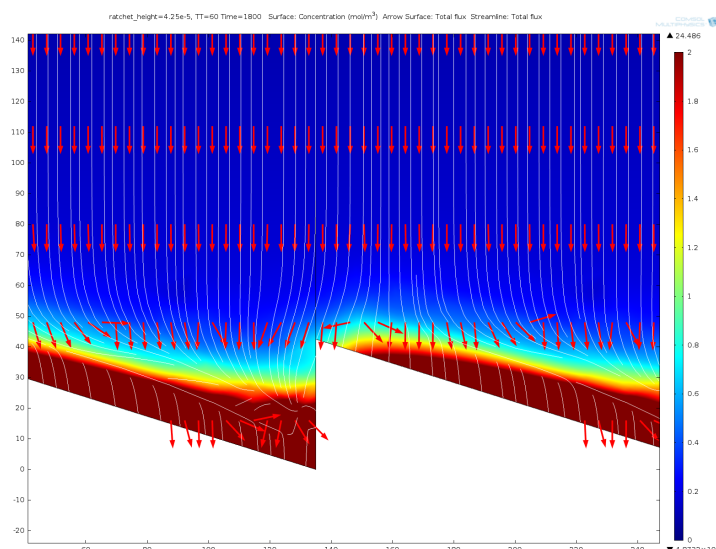


Figure 3.31: Total flux of charged molecules in a ratchet pattern when the field is applied such that the charges move into the trapping region initially. The flux towards the previous ratchet from the top of the ratchet on the right can be seen in the stream lines/arrows.

it gains molecules from. Therefore, the initial loss of charged molecules in the final tooth can be explained.

As discussed before, the transport is caused by the charged molecules driven out of the ratchet having enough time to encounter free diffusion and moving over the barrier for the next tooth. The effect of free diffusion combined with the effect of the electric field can be seen when a line profile of the concentration at different times after starting to move the charged molecules out of the ratchet is plotted, as seen in figure 3.32.

The effect shown in simulation can also be seen in experiment and is shown in figure 3.33. Initially, the distribution of the fluorophore is even throughout the pattern. When the electric field is applied, the negatively charged fluorophore is moved into the teeth of the ratchet where it is concentrated. The concentrated fluorophore is then moved out of the ratchet again and free diffusion starts to influence the material which was concentrated in the teeth of the ratchets. As the material diffuses parts of it will diffuse such that it is over the next tooth. When moved back into the teeth, this part of the material is then transported one step

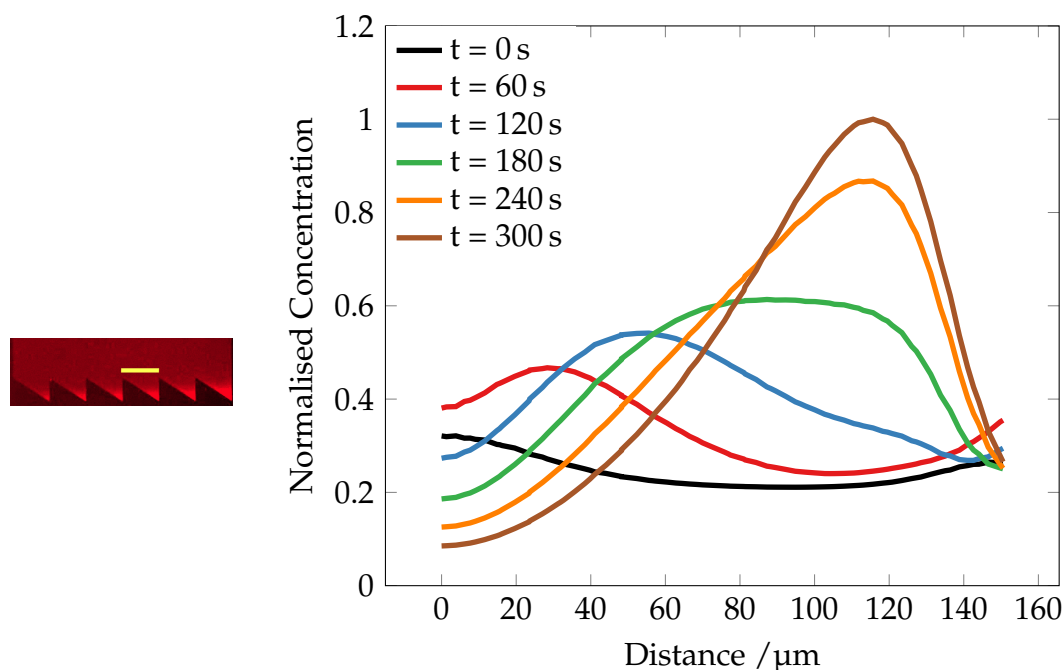


Figure 3.32: A fluorescence image of a Brownian ratchet realised as a lipid bilayer and the position of the line profile shown in red (left). Calculated values from FEA for the line profile at different times (right).

forward. The cycle is then repeated several times and the charged material is moved from the first ratchet towards the last. This effect, which was discussed in the simulation, can also be seen in the experimental results. The bottom image is taken after ten cycles and shows how the charged fluorophore has moved out of the first ratchet and into the last one.

To show that the ratcheting is the main cause for the transportation of membrane components and not a misaligned electric field, two opposing ratchets were printed onto the same sample. As the two ratchets are mirror images of each other, transport should occur in opposite directions. As can be seen in figure 3.34, the two ratchets have transported membrane components in opposite directions after only 15 cycles.

The concentration in each tooth can be followed through the amount of fluorescence detected through the camera. In figure 3.35 the comparison between the calculated results from COMSOL and the experimental results obtained from a patterned lipid bilayer are shown. It can be seen that the experimental values

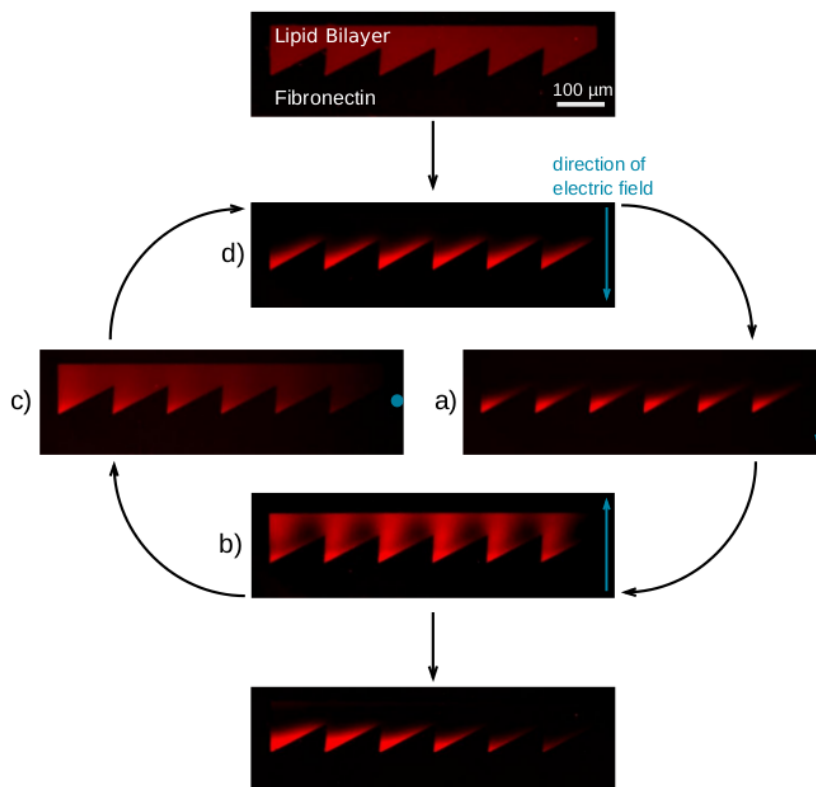


Figure 3.33: Fluorescence images of a Brownian ratchet showing the different states of the ratchet in experiment. The fluorescence is from the negatively charged TxRed in the membrane.

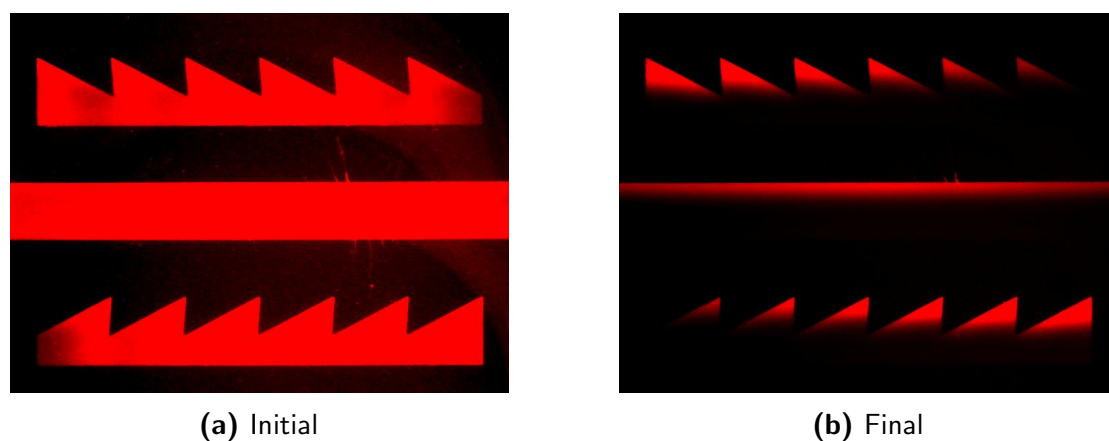


Figure 3.34: Two opposing ratchets showing the principle of Brownian ratcheting. The transport has occurred in different directions showing that it is caused by the ratchets. The length of an individual ratchet is 135 μm .

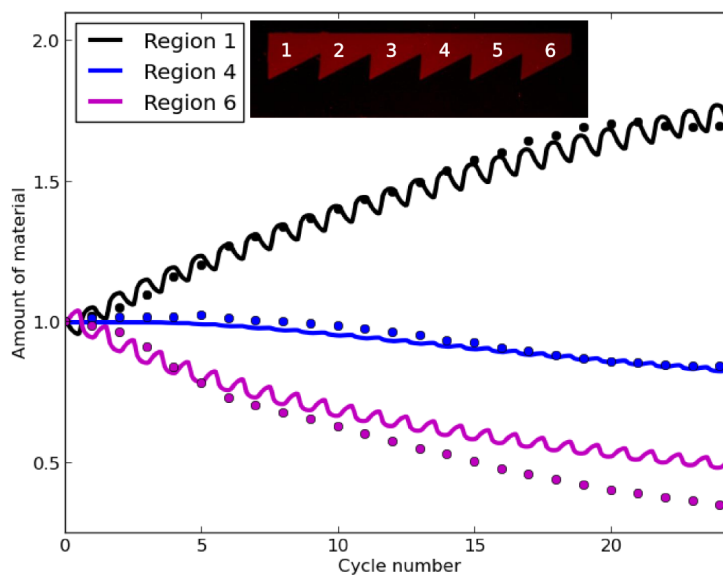


Figure 3.35: Comparison of experimental results and calculated predictions from FEA for different teeth of the ratchet. The solid lines represent the calculated results, the points are experimental results.

follow the predictions of the calculations. For the calculations a drag factor α for the electrophoretic mobility was introduced:

$$\mu = \alpha \frac{D}{k_B T}, \quad (3.22)$$

with the electrophoretic mobility reduced by $\alpha = 0.6$. The agreement between the calculated and the experimental values can also be seen when the final relative concentration in each tooth after 26 cycles is compared between calculation and experiment (see figure 3.36).

The line profiles shown in figure 3.32 show the normalised (to the highest concentration reached during the process of moving the charged material out of the ratchet) concentration of charged molecules just above the ratchet. The time is set to be zero when the field is reversed from moving charged molecules into the tooth to moving them back out into the open region. The distribution initially shows an almost even distribution of charged molecules along the line with a slightly higher concentration above the tip of the tooth (black line). This is expected, as the distance to be travelled for molecules which have not moved

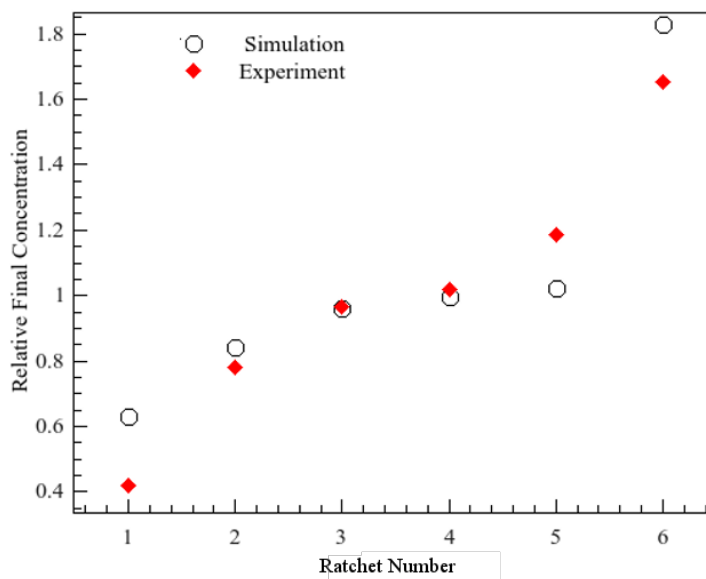


Figure 3.36: Comparison of the final relative increase in the different teeth in both, experiment and simulation.

into the bottom of the ratchet is much lower than for the molecules from the bottom of the tooth. As time increases, molecules from the regions of higher concentration from the bottom of the tooth start reaching the line and finally the highest concentration is reached after five minutes of field reversal (brown line).

A single tooth in this setup is $135\ \mu\text{m}$ long and as the line has been chosen to include parts of the previous and parts of the next tooth, the material that will move into the next ratchet can be seen under the final profile with an x value greater than $142.5\ \mu\text{m}$. This is where the next tooth starts and where the current tooth ends. The material which will move into the previous tooth is everything that is under the line at x values smaller than $7.5\ \mu\text{m}$. As expected this is considerably less than the amount that will move forward.

The results can also be compared with experiment when taking the same line profiles from fluorescence intensities at the same times and comparing the results with the calculated data. The agreement between experiment and calculation for the initial and the final time of the field reversal in figure 3.37 shows that the principle of the ratchet is the same in both, experiment and calculation. The increase of charged molecules in both cases occurs over the bottom of the

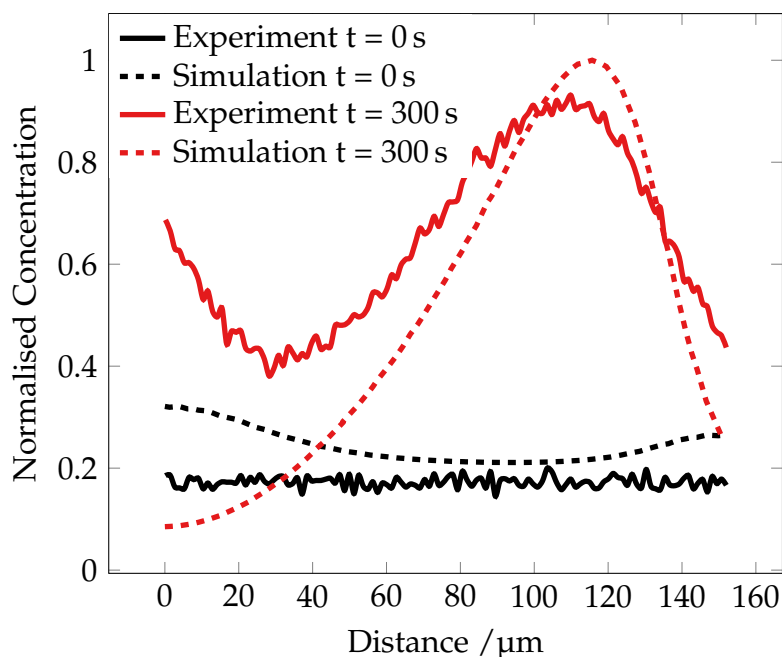


Figure 3.37: Comparison of the normalised fluorescence intensity (for the experimental data) and the normalised concentration (for the calculated data) of a line profile just above the ratchet.

tooth; when next the cycle begins, a bigger portion of charged material will move one step forwards than backwards. In the experimental data an increase in concentration is observed on the left hand side of the graph, which is not observed in the simulation results. This is due to the simulation not accounting for electrostatic repulsion and a limited maximum concentration in the bottom of a tooth. In the experiment not all charged lipids are concentrated into the bottom of the tooth, some remains on the slope of the tooth. When the field is then reversed, the lipids which were on the slope of the tooth are also moving into the region where the line profile was taken.

3.5.3 Influence of Ratchet Parameters

Different parameters influence the efficiency of a Brownian ratchet. Although Brownian ratchets have been used in a wide range of applications before (Amen-gual et al., 2004; Astumian and Bier, 1994; Astumian et al., 1998; Astumian and Derényi, 1998; Matthias and Müller, 2003; Parrondo et al., 2000; van Oudenaarden and Boxer, 1999; Verleger et al., 2012), the influence of the dimensions of the

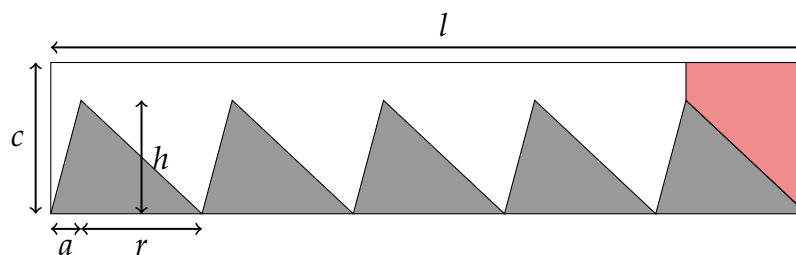


Figure 3.38: The design of a Brownian ratchet with the last region in which the transport is measured highlighted in red.

ratchet on its efficiency have not been investigated in detail. The design process started with the sizes of the ratchets being of the same order as designs used previously (Cheetham et al., 2011). From the basic design several parameters were changed so that their influence on the efficiency on the ratchet could be shown and an optimisation of the pattern and the period of the AC field was possible. The basic design parameters are shown in figure 3.38.

Height of the Channel c :

This parameter is decisive when the material in question is leaving the ratchet region and is allowed to freely diffuse. When c is chosen rather small (an example of this is shown in figure 3.38, where $c \approx 1.5h$), the material will move against the top barrier and will therefore be forced from a free two dimensional diffusion into one dimensional diffusion along this barrier. Although this may aid the transport process, this behaviour is undesired here as the interplay between free diffusion and the ratcheting through the pattern are to be observed. For a rather large c , as shown in the simulation design in figure 3.26, the material will, after once being concentrated in the bottom of the teeth, never reach the top of the channel and will always remain in free diffusion. To ensure that forced 1D diffusion is avoided here, c was chosen such that the distance covered by the “centre of mass”¹ d of the charged material fulfils $d < \frac{c}{2}$. The distance covered by the charged material can be calculated using the definition of the electrophoretic

¹The term *centre of mass* is chosen here, not because actual mass transport is achieved but because of its clarity for the reader as it can be easily imagined how many particles

mobility 3.23 and the Einstein relation 3.24

$$\mu = \frac{v}{E} \quad (3.23)$$

$$D = \mu k_B T, \quad (3.24)$$

where μ is the electrophoretic mobility of the material, v the speed of the material under the influence of an electric field, E the strength of the electric field, D the diffusion coefficient, k_B the Boltzmann constant and T the temperature. Therefore, one obtains for d :

$$d(t) = \mu E t \quad (3.25)$$

$$d(t) = \frac{DEt}{k_B T}, \quad (3.26)$$

where $d(t) = vt$, with t being the time the electric field is applied for, has been used together with equation 3.23. This allows for the calculation of the distance travelled by the “centre of mass” in the time t , assuming the diffusion coefficient D for the material in question is known. Therefore, c is mainly influencing the maximum value of the time τ the field is applied such that the molecules move out of the ratchet but does not influence the behaviour of the ratchet if $c > d(\tau)$

Length of the Channel l :

Although the schematic in figure 3.38 is showing six ratchets in the channel, the channel could consist of an arbitrary number of ratchets if the length l of the channel was changed, as the number of ratchets n is given by

$$n = \frac{l}{a + r}. \quad (3.27)$$

travel along the electric field and one therefore obtains a distribution of masses along the direction of transport.

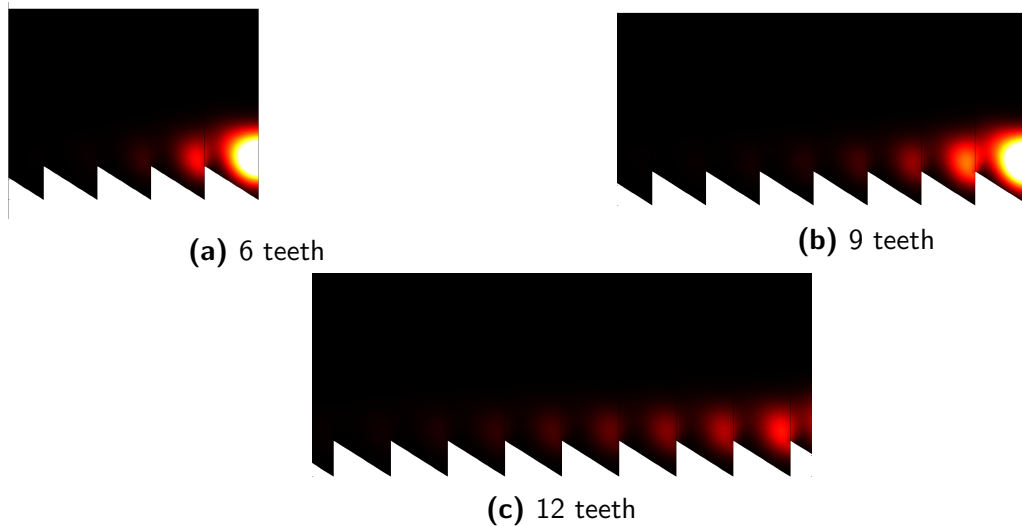


Figure 3.39: Final images of the concentration profile after 26 cycles for varied ratchet lengths.

A longer channel will therefore consist of more ratchets with the same geometrical parameters in each ratchet. The length of the channel does not influence the behaviour of the individual ratchet, but changes the overall concentration behaviour of the ratchet. An overview of the concentrations of channels with varying numbers of ratchets is shown in 3.39, where it can be seen that even for longer ratchets transport is still effective.

In figure 3.40, the normalised relative concentration c_n in the last tooth of ratchets with different length is shown. This was obtained from the surface average of the concentration in the final tooth c_{av} according to

$$c_n(t) = \frac{c_{av}(t)}{0.6 \cdot (u - 1)}, \quad (3.28)$$

where u is the total number of teeth in the ratchet and 0.6 is a normalisation factor which was the same for all different ratchet lengths. This takes into account that the concentration of the charged molecules can only increase by the amount of charged molecules which is in the overall pattern minus the last tooth.

Figure 3.40 shows that for a short ratchet (two or four teeth) the concentration in the final tooth plateaus rather quickly and then stays at that value for

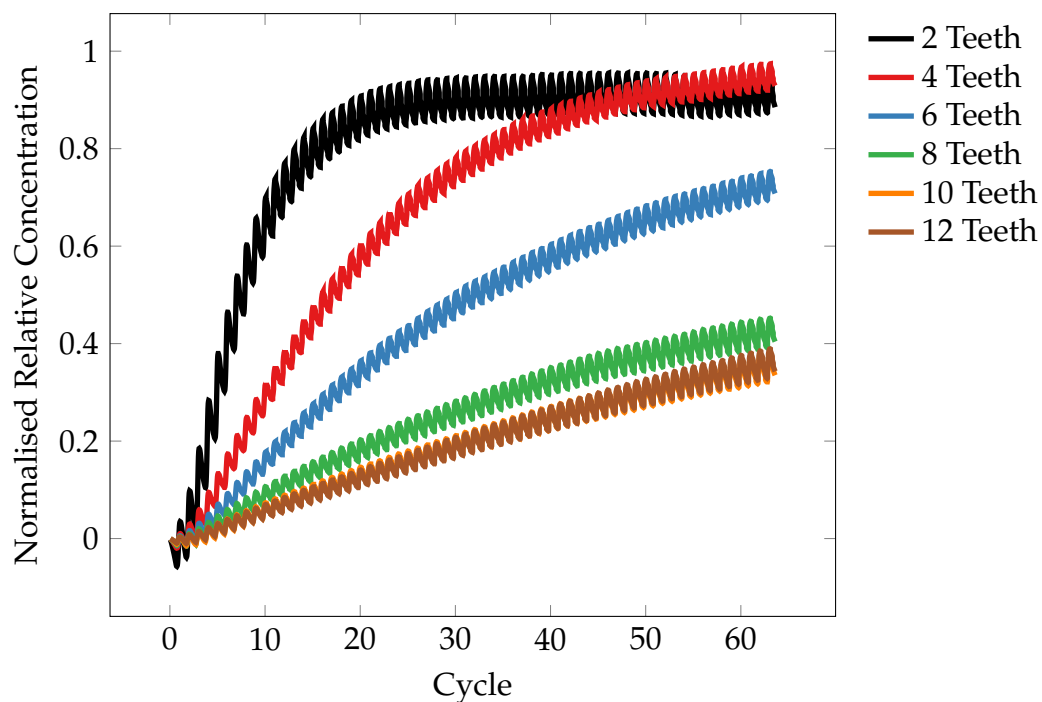


Figure 3.40: Normalised relative concentration in the last tooth of ratchets of varying length over 100 cycles. For the calculations only the number of teeth was changed while all other parameters were kept constant.

any further concentration. This means that most of the material which can be concentrated into the last tooth has now arrived and an equilibrium between “back” diffusion into the second to last tooth and “forwards” diffusion from the second to last tooth has been reached. For the longer ratchets this equilibrium has not yet been reached but they show a steady increase in the concentration in the final ratchet. If the calculation was run over more cycles, these ratchets would also start to plateau and reach an equilibrium state.

Not only does this idea show that the length of the overall pattern has no significant influence on the transport properties of an individual tooth, it also proves that transport can be achieved over long distances in arbitrarily long channels. This means that the idea proposed in figure 3.21 can be used to transport molecules perpendicular to the electric field, allowing for a lower voltage to be applied to the electrodes as large fields can still be achieved over the much smaller distances in this approach.

a [μm]	r [μm]	λ
0	135	0
16.9	118.1	0.125
12.7	88.6	0.125
21.1	147.7	0.125
25.3	177.2	0.125
33.8	101.3	0.25
25.3	75.9	0.25
42.2	126.6	0.25
50.6	151.9	0.25
50.6	84.4	0.375
38	63.3	0.375
63.3	105.4	0.375
75.9	126.6	0.375
67.5	67.5	0.5
50.6	50.6	0.5
84.4	84.4	0.5
101.2	101.2	0.5

Table 3.3: Table of the parameters used for the variation of λ .

Asymmetry Parameter λ

The asymmetry of the individual tooth is one of the most important factors when transport along the ratchet is desired. The asymmetry of the teeth is defined as

$$\lambda = \frac{a}{a + r}, \quad (3.29)$$

where a is the length of the rising edge of the tooth and r the length of the falling edge. This ratio can vary from 0, where the rising edge has a length of 0, to 0.5, where the rising and the falling edge have the same length and there is no asymmetry. The biggest asymmetry between the two edges is achieved when $a = 0$. If $a > r$, the values for λ could be larger than 0.5 but this is the identical case to a mirrored ratchet achieving transport in the opposite direction where a and r can then be swapped resulting in λ being smaller than 0.5 again.

Changes in λ can be achieved by either changing a or by changing r . The values used in the simulation for a and r are shown in table 3.3. The different

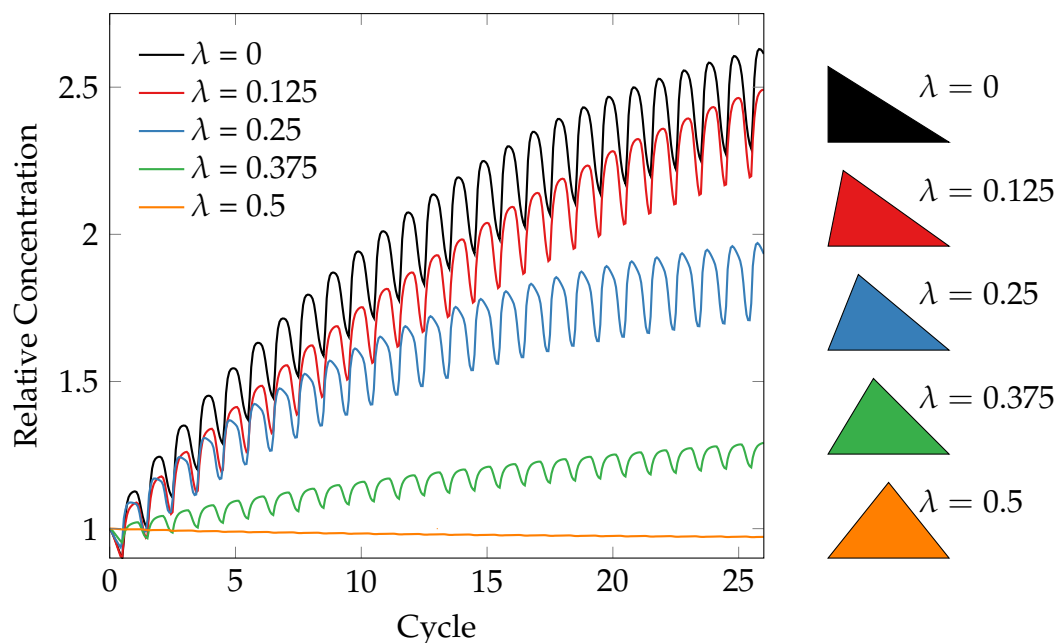


Figure 3.41: Relative concentration in the last tooth of a Brownian ratchet achieved for different values of the asymmetry parameter λ . Here $a + r$ was kept constant at $135 \mu\text{m}$ and only the ratio between a and r was changed.

curves obtained have been averaged for each value of λ to give an overview of the behaviour of the ratchet. As can be seen from figure 3.41, the relative concentration in the last tooth of the ratchet varies strongly with the value of λ . For the symmetric case ($\lambda = 0$) the relative concentration in the last tooth even decreases slightly. This is due to the effect of diffusive flux shown in figure 3.31, where the last ratchets loses a small amount of charged molecules in each cycle. When asymmetry is then introduced into the system, the ratchet starts to transport material. With an increase in asymmetry and therefore an increase in λ , the ratchet increases its efficiency. Although the changes in λ in figure 3.41 are chosen to all be of the same step size, the increase in the efficiency of the ratchet is not in equal steps. When going from a symmetric ratchet ($\lambda = 0.5$) to introducing a small amount of asymmetry ($\lambda = 0.375$), the increase in efficiency is much smaller than for the next two steps. The smallest increase in efficiency is then observed when the asymmetry changed from $\lambda = 0.125$ to $\lambda = 0$; here the increase in efficiency is only minimal. This is due to the fact that the distribution of the molecules in the bilayer will follow a Gaussian

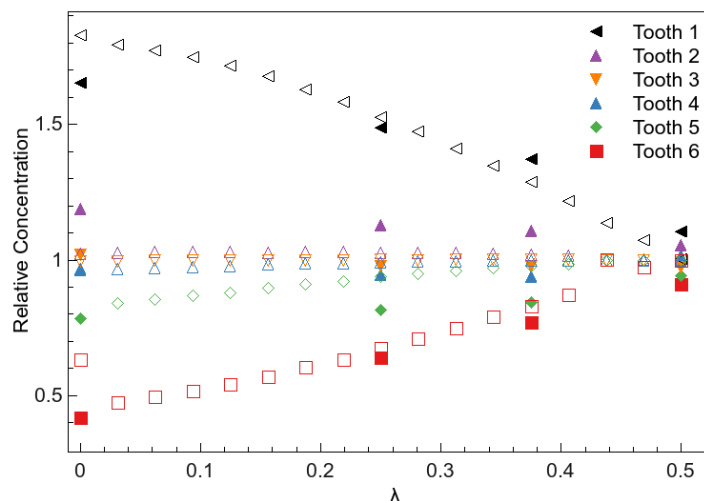


Figure 3.42: Comparison between experimental data from different patterns and simulated results for varied asymmetry parameter of the ratchet λ . The full symbols are experimental data while the hollow symbols are simulation results.

distribution once the electric field is reversed and they are free to diffuse. The first derivative of a Gaussian distribution has smaller values near the centre ($x = 0$) and towards large values of x , this means that the change in the efficiency is small when λ is changed from 0 to 0.125 or from 0.375 to 0.5. In contrast to that the first derivative of a Gaussian distribution is large on the flank therefore the changing λ from 0.125 to 0.25 or from 0.25 to 0.375 has a bigger influence on the efficiency.

This effect can also be seen in experiment. A Brownian ratchet was produced using μ CP of fibronectin onto a glass cover slip. The parameters for the teeth were varied the same way as in the calculations: $a + r$ was kept constant at $135 \mu\text{m}$ and the ratio of a to r was varied. To show the different efficiencies of the ratchet, the simulation and the experiment were executed for 16 cycles and the final concentration in each of the ratchets normalised to the initial concentration was plotted against λ in figure 3.42.

The comparison between experiment and calculation is very good if a drag parameter $\alpha = 0.6$ is introduced to the Einstein relation and equation 3.24 is

modified to

$$D_{\text{drag}} = \alpha \mu k_{\text{B}} T. \quad (3.30)$$

This drag parameter is well known in the literature (Cheetham et al., 2011; Groves and Boxer, 1995; Stelzle et al., 1992; van Oudenaarden and Boxer, 1999) and accounts for the fact that TxRed moves slower under the influence of an electric field than predicted through the Einstein relation (see also section 3.2.2). Although the diffusion coefficient D measures the mobility of the Texas Red labelled lipids in the bilayer, the Einstein relation does not take into account the fact that most of the fluorescence label protrudes out of the membrane and is therefore exposed to electrophoretic drag from the liquid around it or interacts with the membrane itself.

In figure 3.42, the expected behaviour of the ratchet can be seen. When the asymmetry is high ($\lambda = 0$), the relative concentration reached in the last tooth (number 6) after 16 cycles is the highest and the separation between the last tooth and the first tooth is at its maximum. This means that ratcheting for this case is most efficient. As can be seen in figure 3.41, the number of cycles the experiment and simulation are run for does not play a major role in determining the efficiency of a ratchet. Although there is a small influence of the number of cycles (especially when the build-up profile has not yet flattened), the order of the different values for λ does not change only the achieved relative concentration. Therefore, the comparison of the experimental results with the calculated values in figure 3.42, which was made after 16 cycles, would not change qualitatively, when the experiment and simulation were run for more or less cycles.

Height of the Ratchet h and Time Constant τ

When the electric field is applied to the charged molecules in the Brownian ratchet, the time for which the molecules are moved out of the ratchet plays an important role. The time τ and the height of the teeth h have to match. If

the molecules are not moving out of the ratchet for long enough, there will be no transport, as the “centre of mass” is still within the tooth and no diffusion into the next tooth happens. When the time τ is chosen too large in comparison to h , the ratcheting becomes inefficient again as the molecules will have too much time to diffuse freely and will therefore reach the previous tooth so “back diffusion” starts occurring at the same level at which “forward diffusion” occurs.

In the experiments and calculations discussed here, the cycle which the electric field undergoes consists of two parts. Firstly, the field is applied in the direction which causes the charged molecules to move downwards for a time t' (which was kept constant at 16 min). Then the charged molecules are moved out of the teeth for a variable time τ . This time governs whether the charged molecules will reach the top of the tooth or will stay within the tooth. Therefore, the efficiency of the ratchet is strongly influenced by τ . As can be seen in figure 3.43, with increasing τ the charged molecules start moving not only out of the teeth but also start having a wider distribution horizontally. This means that when they are moved back down into the tooth, the fraction of the molecules which has diffused over the next tooth increases. This also means that with an increase in τ there is the possibility for molecules undergoing “back diffusion”. This effect can be seen in figure 3.43d, where τ has been increased to 840 s and the molecules not only have the chance of moving one step forwards but can also diffuse for a long enough time to cover the distance to the tooth behind them. In an optimised ratchet these two counteracting effects have to be balanced so that maximum forward transport can be achieved.

To understand the optimisation of the time parameter τ in relationship to the height of the ratchet h , the movement of the charged lipids has to be further investigated. The distance covered by the “centre of mass” after the reversal of the electric field, so that the molecules start moving out of the ratchet, can be

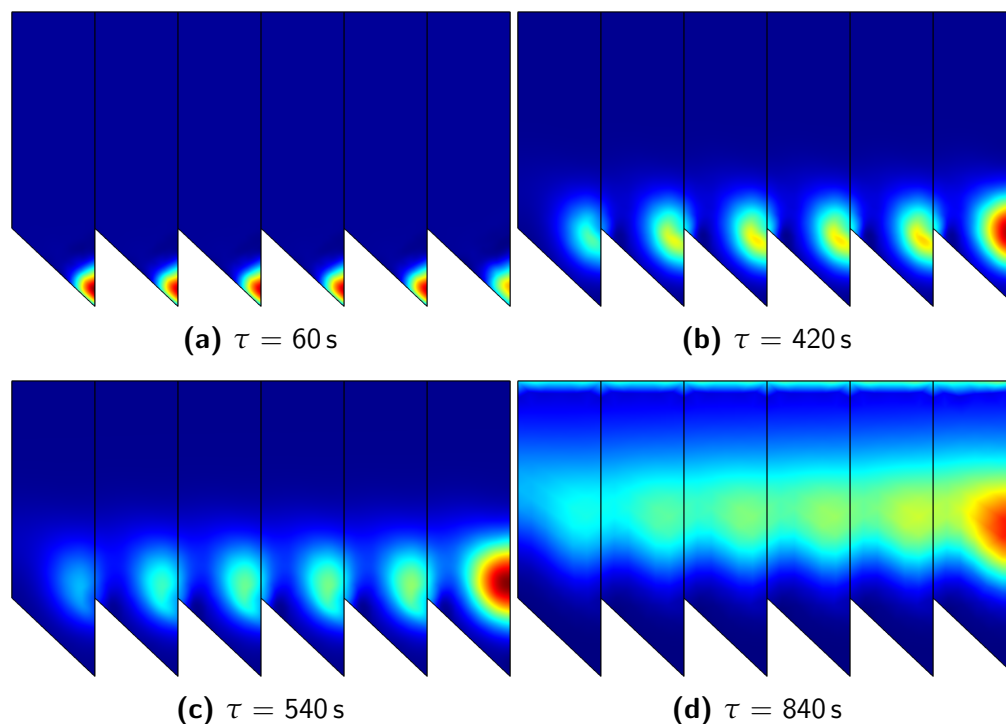


Figure 3.43: Calculated concentration distribution at the final stage of the field reversal for a variation of the time constant τ at constant ratchet height h of $127 \mu\text{m}$. As τ increases from top left to bottom right the charged molecules move further out of the tooth and eventually start showing “back diffusion”.

calculated easily. The distance s covered by each molecule is

$$s = \mathbf{v}t, \quad (3.31)$$

where \mathbf{v} is the velocity and t the time the molecule is moving for. In this case t is equal to the time parameter τ . The velocity of the molecules can be determined from equation 3.23. With the help of the modified Einstein equation 3.30 to express μ the distance covered by each molecule can be rewritten from equation 3.24 as

$$s = \frac{\alpha D}{k_B T} E \tau. \quad (3.32)$$

The distance travelled by the centre of mass s varies linearly with the time the time τ the electric field is reversed for. With this result, the dimensionless parameter $h' = \frac{s}{h}$ can be introduced. This parameter will be unity if the average distance travelled by the centre of mass is equal to the height of the tooth, smaller

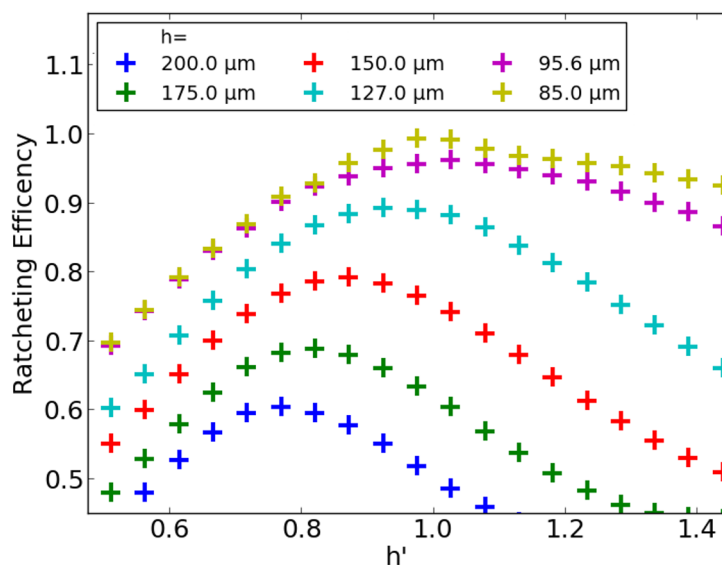


Figure 3.45: Variation of h' for different values of h obtained from FEA. Each colour represents a constant value for h while the time parameter τ is varied.

mass. In addition to that, the longer period also results in a larger fraction of the material undergoing “back diffusion”. The overall efficiency of the ratchet also decreases with an increase in h , since the larger ratchets require larger values of τ and the ratcheting efficiency is defined as transport over time.

When different experimental and calculated results are combined, it can be seen that for most values of h' a single curve is being followed (black line and points in figure 3.46). The only curve which follows a different line is the one representing $h = 42.5 \mu\text{m}$. For the smallest ratchet height, the efficiency is different to all other heights, as the assumption that all material is concentrated in the bottom of the ratchet does not hold here. The charged dye has an exponentially decaying distribution away from the barrier and for the smallest ratchet the finite decay is resulting in the material not being concentrated in the bottom of the teeth but also further towards the previous ratchet. Therefore, for smaller values of h' is very prominent and h' has to be chosen larger than unity for this ratchet height to be efficient.

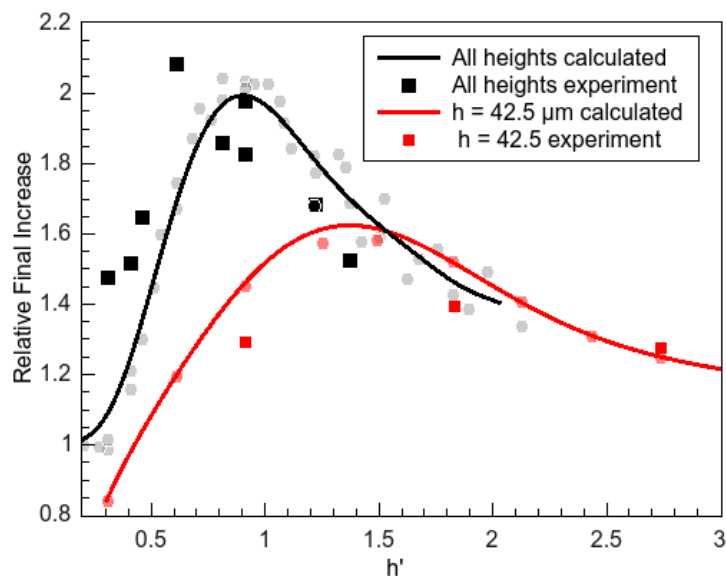


Figure 3.46: Comparison between experimental and calculated results for a variation in h' . The grey and light red points represent the individual points for the calculation and the lines are guide to the eye.

Angle of the Ratchet

In addition to the parameters discussed above, a Brownian ratchet can also be used at an angle to the electric field, this makes the top barrier, which is a straight line, more efficient at transporting charged species in the direction of transport. When used without an angle, the top barrier only acts as a way to spread out the charged species. The tilting of the ratchet in comparison to the electric field makes the top barrier contribute to the transport more efficiently, similar to having the top barrier patterned, as seen in other pattern designs (Cheetham et al., 2011).

A comparison between a ratchet which is perpendicular to the electric field and one which is offset by 30° compared to the electric field is shown in figure 3.47. It can be seen that in both cases the ratchets have moved material from the left towards the right. In case of the untilted ratchet, it can also be seen that the transporting effect clearly comes from the ratchet and not from an electric field, as the top ratchet has transported material to the right while the bottom ratchet, which is mirrored, has transported material to the left. This would not

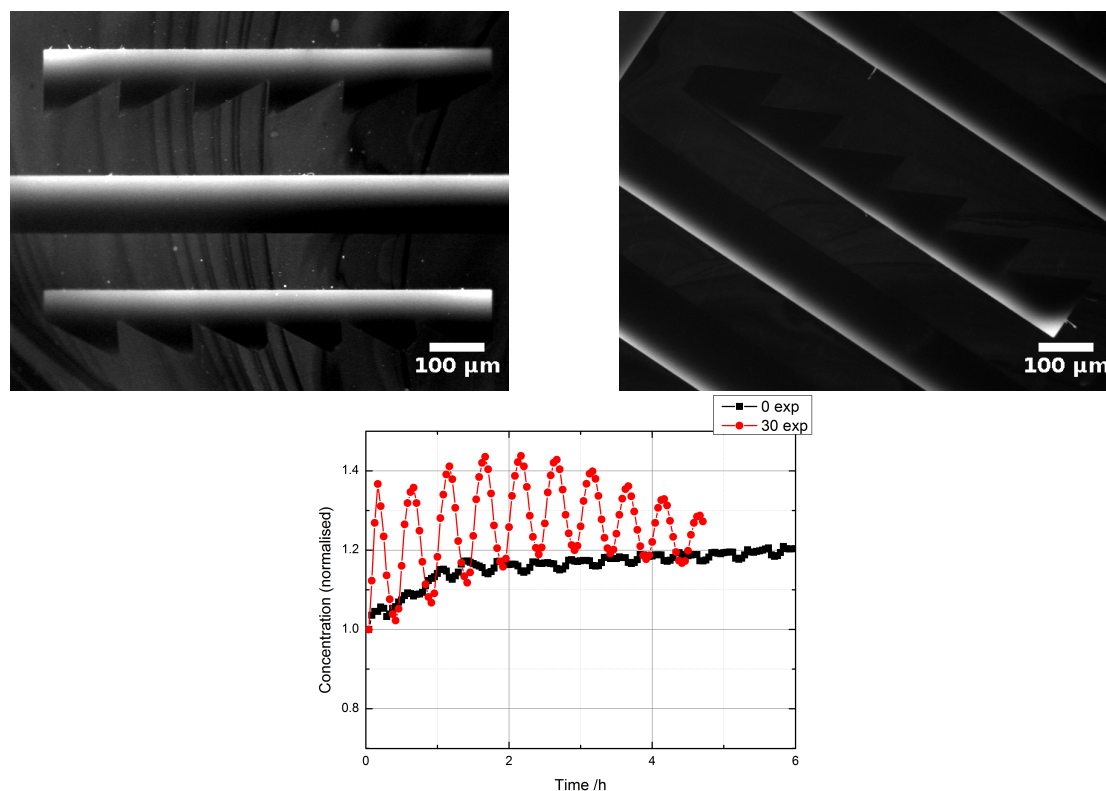


Figure 3.47: Comparison of the ratcheting achieved experimentally when the ratchet is perpendicular to the applied electric field (left) and when it is rotated by 30° (right). The bottom shows the relative concentration over time.

happen if the transport was due to the electric field only as this would be the same for both ratchets. From the comparison of the two ratchets, it can be seen that the tilted ratchet has worked more efficiently than the straight one.

Despite the advantage of a tilted ratchet when it comes to efficient transport, there is a problem when thinking of a channel to transport membrane components over a long distance. This would mean that the electrodes could not be positioned close to the pattern (which is an advantage, as discussed in section 4.2).

An approach to overcome this problem is shown in figure 3.48. Two tilted ratchets are combined to one single ratchet. This leads to efficient transport from left to right without the material moving in the perpendicular direction. Although this pattern is larger than the channel would be on its own, this would still allow for electrodes to be close to the channel so that lower voltages could

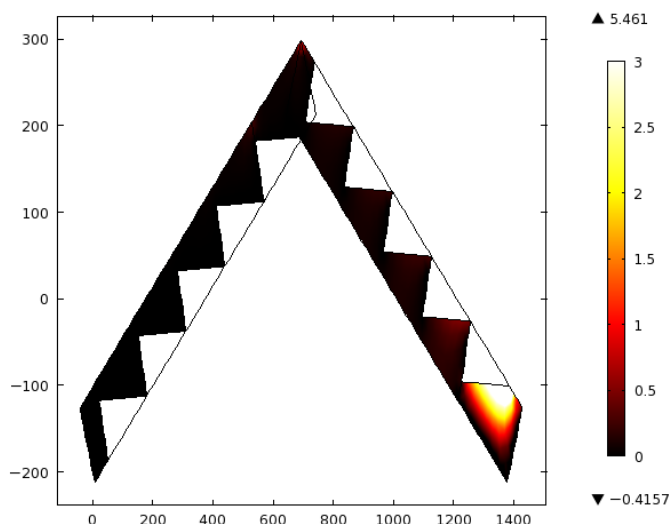


Figure 3.48: Combined tilted ratchet, showing how transport can be achieved with a double tilted ratchet.

still achieve transport. The result in figure 3.48 shows an increase in the charged material in the bottom right corner, as would be expected from a long, untilted ratchet.

3.6 Conclusion

Combining the results from both, experiment and calculation shows not only the validity of the calculations but also that it is possible to design efficient ratchets based on Parrondo's paradox. These ratchets allow transport perpendicular to the electric field. The efficiency of the ratchet is highly dependent on different parameters of the ratchet design. Especially the ratio of the diffusion coefficient to the size of the pattern and the ratio of the height of the individual teeth to the average distance travelled by the centre of mass play an important role.

As the transport of charged molecules within the membrane is proportional to the strength of the electric field, it is important to have thin channels, which allow electrodes to be close to the pattern, so that the voltage is low but the electric field is strong. Brownian ratchets can achieve this by allowing membrane components to be transported perpendicular to the electric field.

References

- Amengual, P., Allison, A., Toral, R., and Abbott, D. (2004). Discrete-time Ratchets, the Fokker–Planck Equation and Parrondo’s Paradox. *Proceedings of the Royal Society of London. Series A: Mathematical, Physical and Engineering Sciences*, 460(2048):2269–2284.
- Astumian, R. D. and Bier, M. (1994). Fluctuation driven ratchets: Molecular motors. *Physical review letters*, 72(11):1766–1769.
- Astumian, R. D., Dere, I., Derényi, I., Derényl, I., and Derényi, I. (1998). AC Separation of Particles by Biased Brownian Motion in a Two-Dimensional Sieve. *Physical Review E*, 58(6):7781.
- Astumian, R. D. and Derényi, I. (1998). Fluctuation driven transport and models of molecular motors and pumps. *European Biophysics Journal*, 27:474–489.
- Axelrod, D., Koppel, D. E., Schlessinger, J., Elson, E., and Webb, W. W. (1976). Mobility measurement by analysis of fluorescence photobleaching recovery kinetics. *Biophysical Journal*, 16(9):1055–1069.
- Bader, J. S., Hammond, R. W., Henck, S. a., Deem, M. W., McDermott, G. a., Bustillo, J. M., Simpson, J. W., Mulhern, G. T., and Rothberg, J. M. (1999). DNA transport by a micromachined Brownian ratchet device. *Proceedings of the National Academy of Sciences of the United States of America*, 96(23):13165–9.
- Bao, J.-D. and Zhuo, Y.-Z. (1998). Langevin simulation approach to a two-dimensional coupled flashing ratchet. *Physics Letters A*, 239(4–5):228–232.
- Cheetham, M. R., Bramble, J. P., McMillan, D. G. G., Krzeminski, L., Han, X., Johnson, B. R. G., Bushby, R. J., Olmsted, P. D., Jeuken, L. J. C., Marritt, S. J., Butt, J. N., and Evans, S. D. (2011). Concentrating Membrane Proteins Using Asymmetric Traps and AC Electric Fields. *Journal of the American Chemical Society*, 133(17):6521–4.
- Denisov, S., Lyutyy, T., Denisova, E., Hänggi, P., and Kantz, H. (2009). Directed transport in periodically rocked random sawtooth potentials. *Physical Review E*, 79(5):1–7.
- Feynman, R. P. (1963). *The Feynman Lectures on Physics Vol. 1*. Addison-Wesley, Massachusetts, 1 edition.
- Groves, J. T. and Boxer, S. G. (1995). Electric field-induced concentration gradients in planar supported bilayers. *Biophysical Journal*, 69(5):1972–5.

- Harmer, G. P. and Abbott, D. (1999). Losing Strategies Can Win by Parrondo's Paradox. *Nature*, 402(6764):1.
- Heath, G. R., Roth, J., Connell, S. D., and Evans, S. D. (2014). Diffusion in Low-Dimensional Lipid Membranes. *Nano Letters*, 14(10):5984–5988.
- Hirtz, M., Corso, R., Sekula-Neuner, S., and Fuchs, H. (2011). Comparative Height Measurements of Dip-Pen Nanolithography-Produced Lipid Membrane Stacks with Atomic Force, Fluorescence, and Surface-Enhanced Ellipsometric Contrast Microscopy. *Langmuir*, 27(18):11605–11608.
- Hirtz, M., Oikonomou, A., Georgiou, T., Fuchs, H., and Vijayaraghavan, A. (2013). Multiplexed biomimetic lipid membranes on graphene by dip-pen nanolithography. *Nat Commun*, 4.
- Huang, L. R., Cox, E. C., Austin, R. H., and Sturm, J. C. (2003). Tilted Brownian Ratchet for DNA Analysis. *Analytical Chemistry*, 75(24):6963–6967.
- Hughes, L. D., Rawle, R. J., and Boxer, S. G. (2014). Choose Your Label Wisely: Water-Soluble Fluorophores Often Interact with Lipid Bilayers. *PLoS ONE*, 9(2):e87649.
- Jackson, B. L. and Groves, J. T. (2004). Scanning Probe Lithography on Fluid Lipid Membranes. *Journal of the American Chemical Society*, 126(43):13878–13879.
- Lenhert, S., Brinkmann, F., Laue, T., Walheim, S., Vannahme, C., Klinkhammer, S., Xu, M., Sekula, S., Mappes, T., Schimmel, T., and Fuchs, H. (2010). Lipid multilayer gratings. *Nat Nano*, 5(4):275–279.
- Lenhert, S., Sun, P., Wang, Y., Fuchs, H., and Mirkin, C. (2007). Massively Parallel Dip-Pen Nanolithography of Heterogeneous Supported Phospholipid Multilayer Patterns. *Small*, 3(1):71–75.
- Lopez, B. J., Kuwada, N. J., Craig, E. M., Long, B. R., and Linke, H. (2008). Realization of a Feedback Controlled Flashing Ratchet. *Physical Review Letters*, 101(22):220601.
- Makhnovskii, Y. A., Rozenbaum, V. M., Yang, D. Y., Lin, S. H., and Tsong, T. Y. (2004). Flashing Ratchet Model with High Efficiency. *Physical Review E*, 69(2):21102.
- Matthias, S. and Müller, F. (2003). Asymmetric pores in a silicon membrane acting as massively parallel brownian ratchets. *Nature*, 424(6944):53–57.
- Pace, H. P., Sherrod, S. D., Monson, C. F., Russell, D. H., and Cremer, P. S. (2013). Coupling supported lipid bilayer electrophoresis with matrix-assisted laser desorption/ionization-mass spectrometry imaging. *Analytical chemistry*, 85(12):6047–52.
- Parrondo, J. J. M. R., Harmer, G. G. P. G. G. P., and Abbott, D. (2000). New Paradoxical Games Based on Brownian Ratchets. *Physical Review Letters*, 85(24):5226–5229.

- Planck, M. (1903). *Treatise on Thermodynamics*. Longmans, Green.
- Poyton, M. F. and Cremer, P. S. (2013). Electrophoretic Measurements of Lipid Charges in Supported Bilayers. *Analytical chemistry*, 85(22):10803–10811.
- Roeling, E. M., Germs, W. C., Smalbrugge, B., Geluk, E. J., de Vries, T., Janssen, R. A. J., and Kemerink, M. (2011). Organic electronic ratchets doing work. *Nat Mater*, 10(1):51–55.
- Seiffert, S. and Oppermann, W. (2005). Systematic evaluation of FRAP experiments performed in a confocal laser scanning microscope. *Journal of Microscopy*, 220(1):20–30.
- Shi, J., Chen, J., and Cremer, P. S. (2008). Sub-100 nm patterning of supported bilayers by nanoshaving lithography. *Journal of the American Chemical Society*, 130(9):2718–9.
- Skaug, M. J., Longo, M. L., and Faller, R. (2009). Computational studies of Texas Red-1,2-dihexadecanoyl-sn-glycero-3-phosphoethanolamine-model building and applications. *The journal of physical chemistry. B*, 113(25):8758–66.
- Skaug, M. J., Longo, M. L., and Faller, R. (2011). The impact of Texas red on lipid bilayer properties. *The journal of physical chemistry. B*, 115(26):8500–5.
- Smoluchowski, M. v. (1912). Experimentell nachweisebare, der üblichen Thermodynamik widersprechende, Molekularphänomene. *Phys. Zeitschr.*, 13:1069.
- Soumpasis, D. M. (1983). Theoretical analysis of fluorescence photobleaching recovery experiments. *Biophysical journal*, 41(1):95–97.
- Stelzle, M., Miehlisch, R., and Sackmann, E. (1992). Two-dimensional microelectrophoresis in supported lipid bilayers. *Biophysical Journal*, 63(5):1346–1354.
- Tsai, J., Sun, E., Gao, Y., Hone, J. C., and Kam, L. C. (2008). Non-Brownian diffusion of membrane molecules in nanopatterned supported lipid bilayers. *Nano letters*, 8(2):425–30.
- Tsay, T. T. and Jacobson, K. a. (1991). Spatial Fourier analysis of video photobleaching measurements. Principles and optimization. *Biophysical journal*, 60(2):360–8.
- van Oudenaarden, A. and Boxer, S. G. (1999). Brownian Ratchets: Molecular Separations in Lipid Bilayers Supported on Patterned Arrays. *Science*, 285(5430):1046–1048.
- Verleger, S., Grimm, A., Kreuter, C., Tan, H. M., van Kan, J. A., Erbe, A., Scheer, E., and van der Maarel, J. R. C. (2012). A Single-Channel Microparticle Sieve Based on Brownian Ratchets. *Lab on a chip*, 12(7):1238–1241.

Chapter 4

Novel Electrodes and Patterns for the Concentration of Membrane Components

In addition to the previously discussed methods for the movement and concentration of charged components within lipid bilayers, several advancements towards new methods can be made. The electrodes used previously consisted of platinum wires in the flow cell in which the experiment was conducted. By bringing the electrodes closer to the patterns in which they are effectively doing work, the applied voltage can be significantly reduced while the field strength can remain the same. Using different materials for the electrodes also allows for arbitrary designs of the electrodes, which could in the future even be printed using inkjet printing.

Another way of improving the way bilayer components are concentrated is to change the pattern which is used to a more time-efficient one. This allows for shorter experimental times and when applied to questions such as drug development, shorter experimental times can save considerable amounts of money. Finally, this chapter will also show, how the use of more than two electrodes can lead to the generation of two-dimensional electric fields, allowing

for the movement of charged material in any direction of the solid supported lipid bilayer (SLB) plane.

4.1 A Novel DC Pattern

In contrast to the approach taken in section 3.4, where the AC nature of an electric field was used to achieve transport perpendicular to the electric field, an alternative DC approach can also be taken. This means that the electrodes have to be further away from the pattern. Although this may seem like a disadvantage, such an approach can be useful for some applications. The main advantage of using the fields directly to obtain transport of charged molecules in the direction of the field itself. This makes the transport quicker but higher overall voltages are required to obtain the same field strengths as in the AC patterns.

4.1.1 Development and Calculations

A simple DC pattern, which allows for the concentration of charged material, is a reservoir and a triangular shaped region in which the material is concentrated. In this case the electric field is used to move the material out of the reservoir and into the tip. Such a pattern is shown in figure 4.1a. The charged material is moved from the left reservoir region into the right triangular region where it is concentrated. The graph in figure 4.1b shows the increase of charged material in the (red) triangular region over time for the first 2000 s. During this time, more and more charged material moves into the triangular trapping region. As the reservoir region empties, the amount of charged material in the trapping region starts flattening shortly before the field is switched off. When the field is switched off, free diffusion occurs and, as was shown in equation 3.12, concentrated material will spread out until an even distribution is reached. The exponential decay in figure 4.1b has a half-life of the diffusion out of the triangular region is approximately 3000 s.

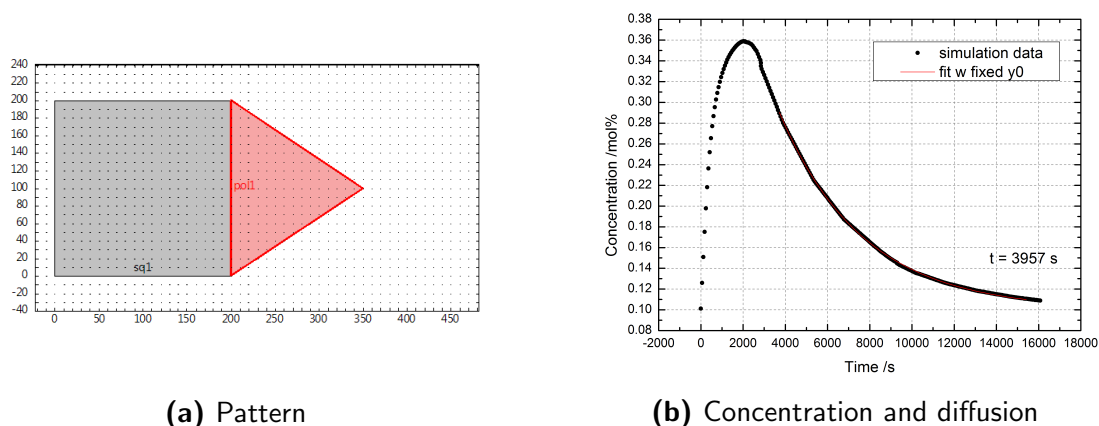


Figure 4.1: A simple triangular pattern (a) with the x - and y -axis in μm and the relative concentration in the tip of the pattern (red region) over time with and without the field applied. Concentration was simulated for the first 2000 s while free diffusion was observed afterwards. An exponential decay with a constant y offset y_0 of 0.1 mol% was fitted to the simulated data. The time shown in (b) is the decay constant of the fit.

This simple pattern allows for the concentration of charged material into a pre-defined region of high concentration. Through the replication of the pattern with different reservoir sizes, the final concentration in the end of the triangle can be varied with the reservoir size. The simulation of the concentration in such a pattern can be seen in figure 4.2a, where the electric field has been applied and concentration has occurred in the tips of the triangles. As figure 4.2b shows, the increase for all the different sub-patterns shows the same behaviour: initial increase until the reservoir is emptied and then the final flattening of the relative concentration.

Despite this pattern already being useful for concentrating charged membrane components to varied amounts and showing an improvement over simple barrier patterns (van Oudenaarden and Boxer, 1999; Yoshina-Ishii and Boxer, 2006), this pattern can further be improved. The simple triangular concentration region does not stop the concentrated material from moving out of the triangle once the electric field is switched off and therefore has very short retention times. By using a second triangle in a mirrored arrangement, as seen in figure 4.3a, and concentrating material into the added triangle instead of the first triangle, the re-

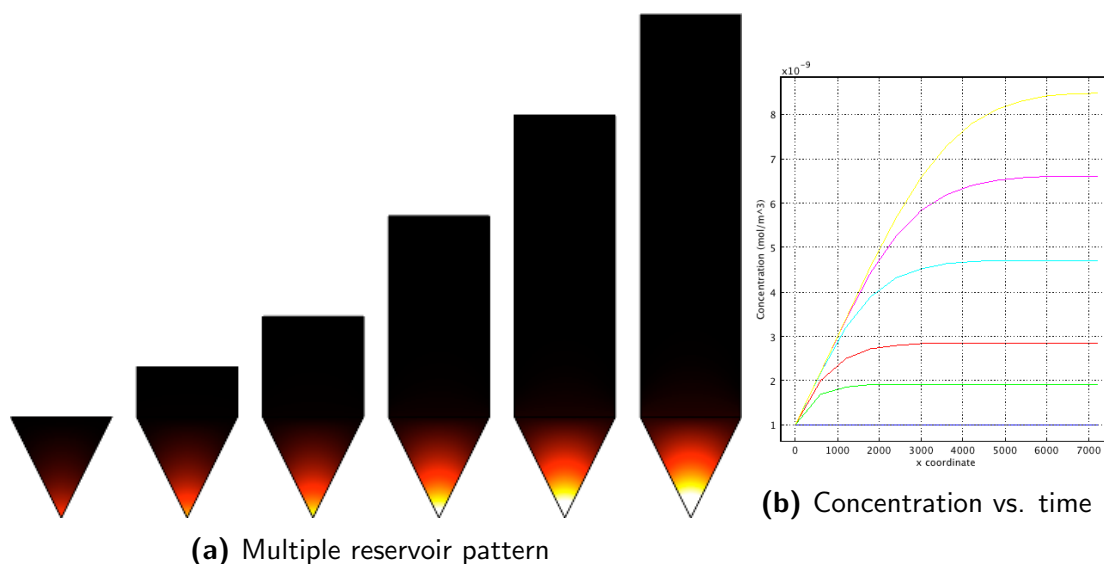
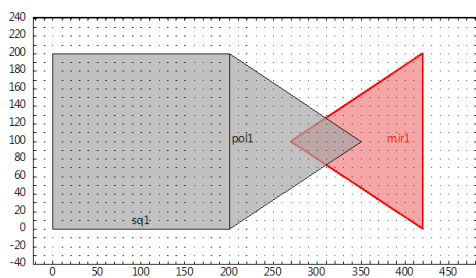


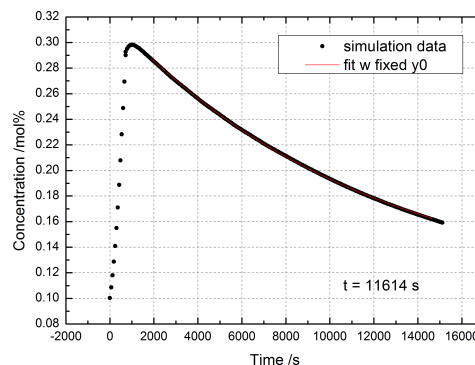
Figure 4.2: Several triangular concentration regions with different sized reservoirs and the concentration over time in the different triangular regions. The concentration into the bottom triangular regions is seen on the left. The plot on the right shows the relative concentration in the bottom region, the integration area for the determination of the relative concentration was identical to the first pattern for all six patterns, independent of the reservoir size.

tention time after the electric field is switched off is increased significantly. The increase is almost four fold, as can be seen from the fit in figure 4.3b. Another straight forward improvement can be made to the pattern. By making the overlap between the first and the second triangle smaller, and therefore hindering diffusion out of the second triangle, the material will stay in the concentration region even longer. The pattern is shown in figure 4.3c and the concentration and diffusion graph in figure 4.3d. Using this pattern improves the retention time by another 50 %. This shows how small improvements to the pattern can have a significant influence on the retention time in the concentration region.

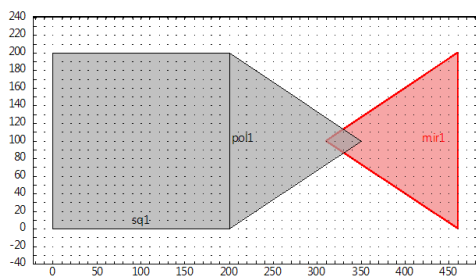
The increase in retention time in the concentration region can further be improved by hindering back diffusion even further. This can be useful as experiments such as binding experiment of charged analytes and antibodies require the electric field to be switched off but still need a significant amount of time to be carried out as the binding has to be in equilibrium and the charged



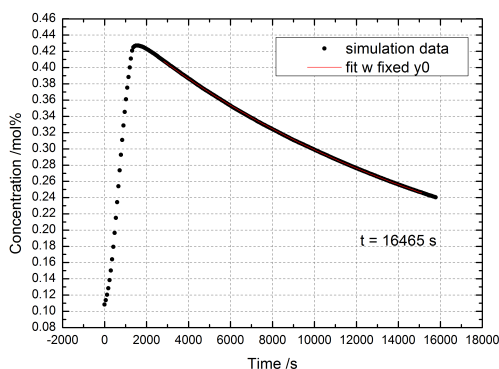
(a) Double triangle pattern



(b) Concentration and diffusion

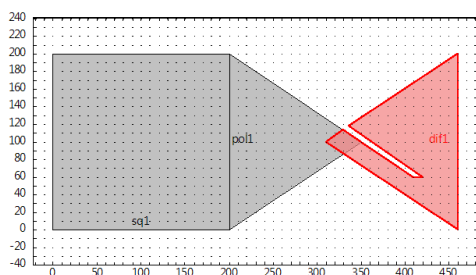


(c) Improved double triangle pattern

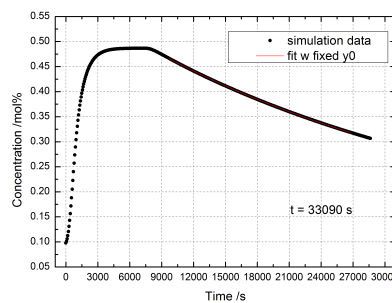


(d) Concentration and diffusion

Figure 4.3: Two double triangle patterns and their respective concentration and free diffusion behaviour. The fits were again carried out with the y offset fixed to the initial concentration y_0 , t in the inset depicts the time constant from the fit.



(a) Improved pattern



(b) Concentration and diffusion

Figure 4.4: Double triangle pattern with an added barrier to increase retention time and concentration graph. Fits were carried out as above and show an increase in the retention time in the trapping region over the previous patterns.

antibodies should not be influenced by an external electric field. The addition of a barrier into the added triangle can stop back diffusion even more efficiently.

As can be seen from figure 4.4a, the pattern has been changed only slightly from the pattern shown in figure 4.3c. A small region in the last triangle has been removed and is now a barrier for material which is in the concentration region and undergoes free diffusion. When the charged material starts spreading out in the concentration region, the diffusive flux will still drive the material out of the triangle, but as the barrier has now been put in place, it takes double the previous time to reach equilibrium.

As already shown, the pattern can be filled by reservoirs of different sizes, which will lead to different relative final concentrations in the trapping region. This idea was also applied to the improved pattern. In addition to the parallelisation, the pattern was slightly changed as well. The triangle, which acts as the concentration region, now has a lower boundary, which is slightly tilted in comparison to the electric field. This leads to the charged material moving away from the entrance of the concentration region and being concentrated in the opposite end of the triangle. Therefore, the time until the exit is reached is on average increased.

The initial state of the parallelised device is shown in figure 4.5a. As the electric field is applied, the charged material moves downwards and into the trapping region (figure 4.5b & figure 4.5c) until a final state is reached where all the reservoirs are empty and have expelled all their material into the bottom triangles (figure 4.5d). After the electric field is switched off free diffusion occurs. The retention can be seen in figures 4.5e and 4.5f for 1 h and 2 h after the field has been switched off, respectively. The analysis of the concentration in the different trapping regions shows that despite the added barrier, the concentration increase in the bottom triangle over time is (figure 4.6a) very similar to what was seen before in the simpler design (figure 4.1b) . When the electric field is switched off, the different trapping regions undergo free diffusion and each of them displays the same time constant for this process, as can be seen in figure 4.6b.

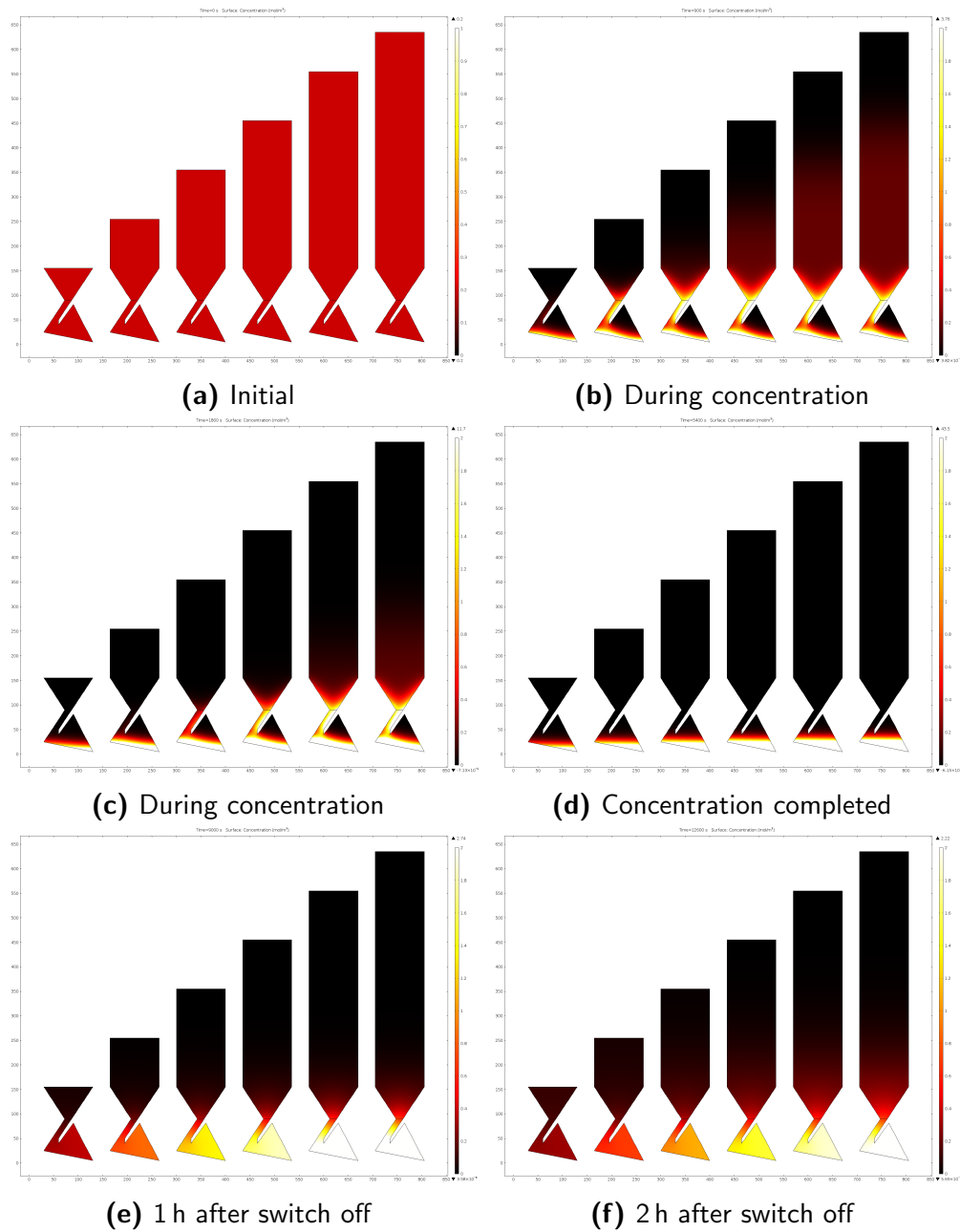


Figure 4.5: Initial state, concentration, final state and free diffusion after switch off of the electric field in a DC trap pattern. The first four images show the concentration into the different trapping regions while the last to images show the retention of the pattern under free diffusion.

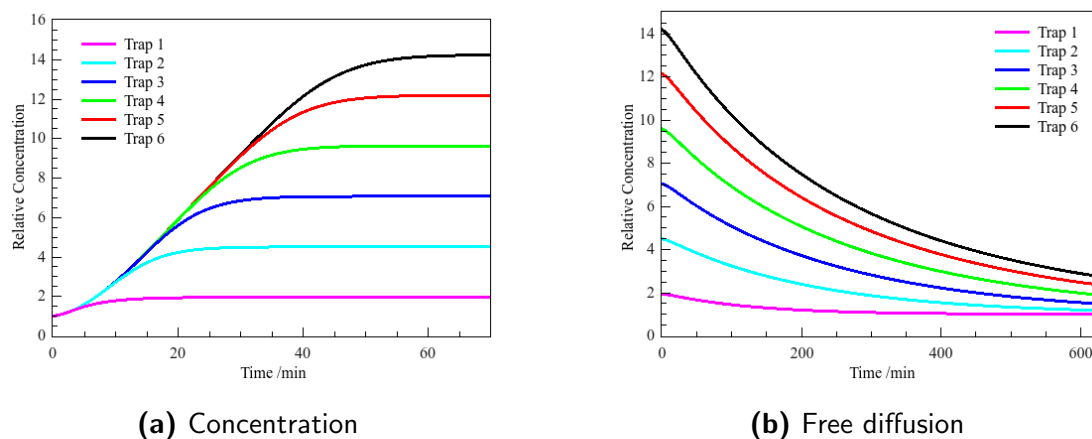


Figure 4.6: Concentration and diffusion profile for the trap shown in figure 4.5 over time. The increase follows a similar curve as for the patterns where the trapping region is just a triangle (see figure 4.1b) while the decrease in the trapping region due to free diffusion is slowed down.

In addition to the idea of parallelisation, the pattern can also be used to achieve higher concentrations in the trapping region. This can be achieved by increasing the size of the reservoir. As the reservoir regions empty out into the trapping regions, the relative increase of charged material in the trapping regions reached scales with the size of the reservoir. The previous patterns made the reservoirs longer which is useful when there are several patterns next to each other. In contrast to that, when only a single region of high concentration is needed, the reservoir can be expanded in two dimensions. A pattern with such an expanded reservoir and the trapping region opposite to it can be seen in figures 4.7c and 4.7d. They also show how even in such a large device the charged materials are not only concentrated but also trapped for more than 1 h. When compared with the initial pattern, which is shown in figures 4.7a and 4.7b, the significant improvement for the amount of charged material in the trapping region becomes clear.

4.1.2 Experimental Results

The pattern optimised in the previous section has also been realised experimentally. Both patterns, the parallelised traps seen in figure 4.5 and the increased

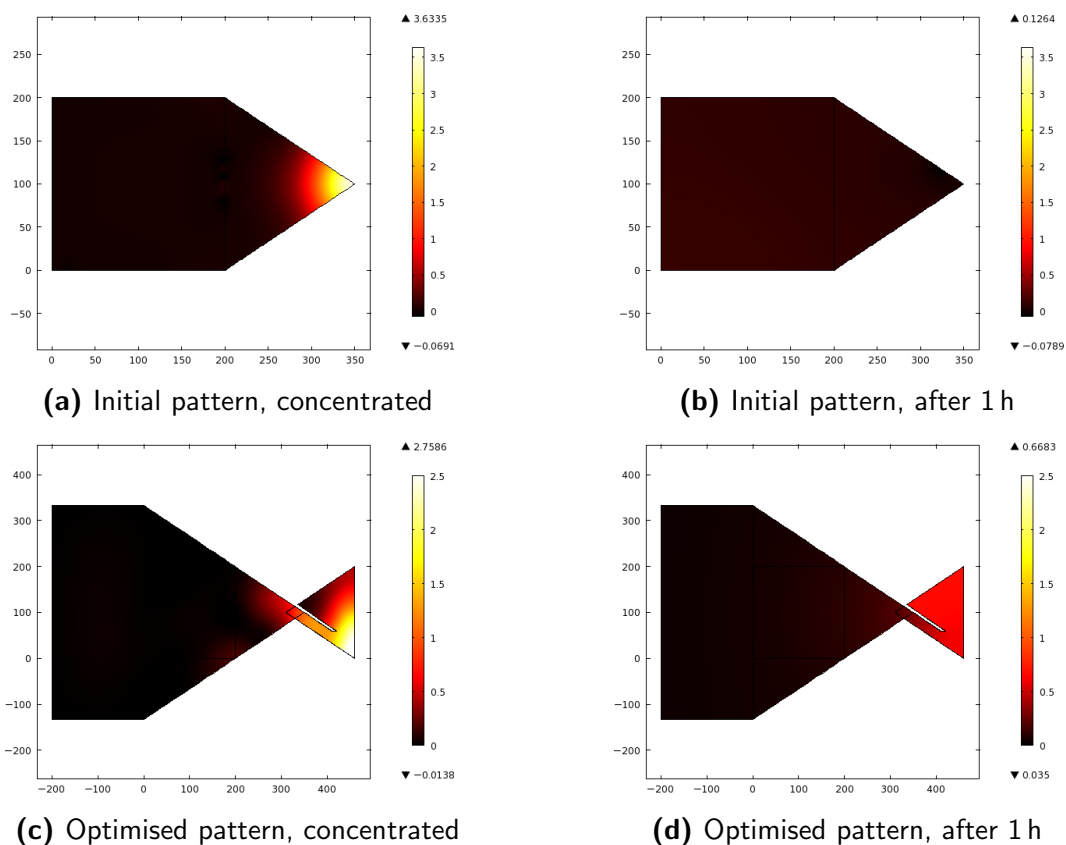


Figure 4.7: Optimisation of the pattern from the initial state to the final pattern. Images on the right show the effect of free diffusion after the field has been switched off for 1 h. It can be seen that both patterns can achieve similar concentrations in the region of interest while the improved design shows an increase of charged membrane components in the trapping region after 1 h, the triangle pattern shows an even distribution.

reservoir shown in figure 4.7c were used. The patterns were produced using either microcontact printing (μ CP) of a fibronectin pattern or through photolithography of SU-8 photoresist and lipid bilayers containing charged dyes were formed using the vesicle fusion method (see section 2.2). The vesicles consisted of 1-palmitoyl-2-oleoylphosphatidylcholine (POPC) and were labelled with 0.025 mol% Texas Red 1,2-dihexadecyl-sn-glycero-3-phosphoethanolamine (TxRed). The applied field had a strength of 62 V cm^{-1}

The experimental images in figure 4.8 show clean bilayer formation and good mobility when the electric field has been applied. All the charged, fluorescent molecules have moved into the bottom regions, showing that there are no major defects and no immobile molecules in the SLB. There is a small fluorescence

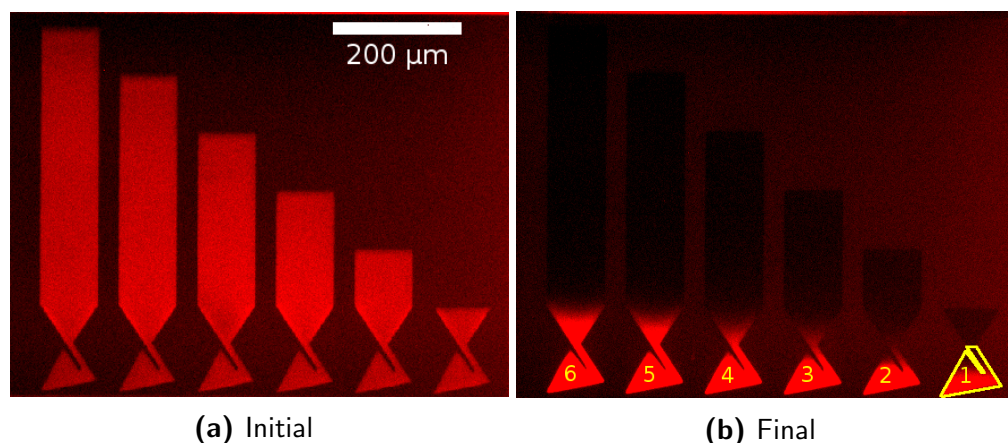


Figure 4.8: Fluorescence images for a DC trap pattern before the concentration of charged molecules and after. The region with the yellow outline depicts one of the trapping regions used for the determination of the increase in concentration in the trapping regions in the analysis.

signal coming from the region where no bilayer was formed. This is due to a small amount of non-specific binding of the lipids to fibronectin. This does not impede the experiment in any way, as the lipids, which are not in the SLBs are not moved by the electric field but only produce background fluorescence. This background from the non-specifically bound lipids is the reason why parts of the pattern appear black in figure 4.8b. When the charged molecules from the SLB have all moved out of the reservoir and into the trapping region, the reservoir appears darker than the region without an SLB with a small amount of non-specifically bound lipids in it.

The analysis of the fluorescence in the pattern shows very clearly that there is no fluorescence left in the reservoir regions, as can be seen from the line profiles in figure 4.9. In contrast to what was expected from the finite element method (FEM) calculations, these line profiles show very similar fluorescence intensities, independent of the reservoir size. It is even the case that the third and fourth largest reservoir generate the highest peak in the fluorescence signal, while the two patterns with the larger reservoir generate less fluorescence counts.

This behaviour can be attributed to the self-quenching of TxRed, when it is concentrated to a high percentage in the SLB. When two molecules of the fluo-

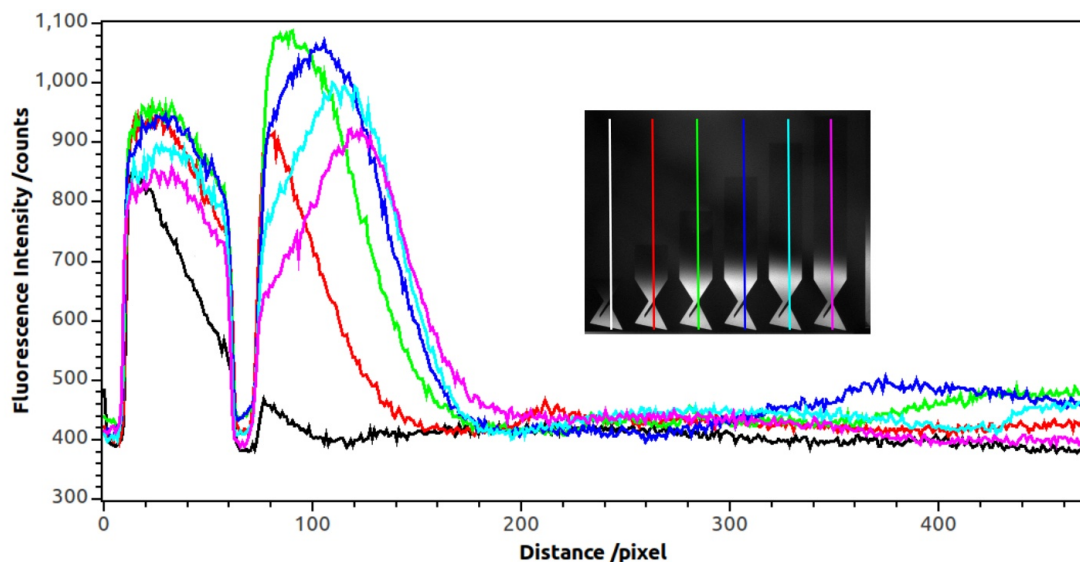


Figure 4.9: Line profiles of the fluorescence signal in all the sub-patterns after the concentration took place. The white line in the fluorescence image is represented by the black line in the line profiles. For small reservoirs the increase in the trapping region and before the neck follow an exponential curve while for larger reservoirs the line profiles show the influence of quenching due to a high concentration of fluorescent molecules.

rophore are very close together, self-quenching can occur. The self-quenching behaviour of TxRed can be better understood, when looking at the intermolecular distances depending on the concentration of TxRed in the membrane. Since the initial concentration used here was 0.2 mol% and the lipid head group area is 0.65 nm^2 (Marsh, 2012), the average distance between two TxRed molecules can be calculated. In addition to that the quenching efficiency was assumed to be a dipole-dipole interaction and therefore has an intensity of

$$I(r) = \frac{1}{1 + \left(\frac{r}{r_0}\right)^6}, \quad (4.1)$$

with r_0 being the interaction parameter specific to TxRed. The exponent of 6 is due to the dipole-dipole interactions of the two fluorophore molecules.

For the unquenched case, the intensity profile of a charged fluorophore, which is electrophoretically pushed against a barrier, should follow an exponential increase towards the barrier. When quenching is taken into account, the increase should initially still be exponential but when the molecules are so close

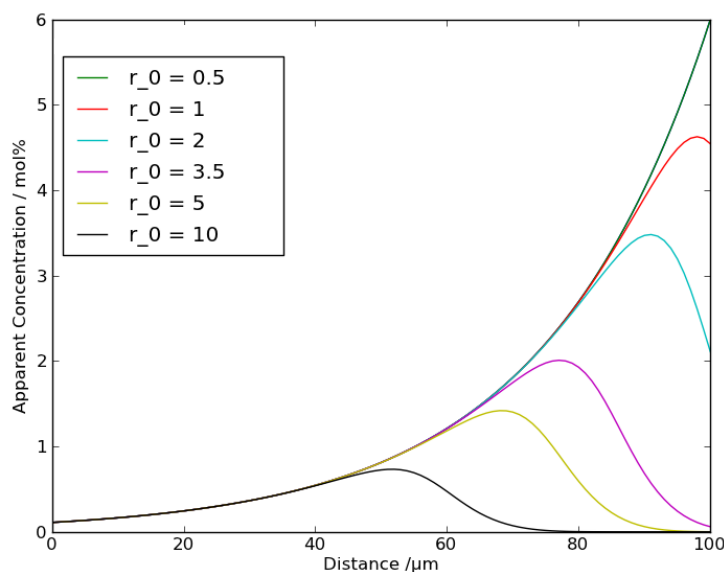


Figure 4.10: Expected intensity profile of fluorescence for different interaction parameters r_0 . The model assumes a barrier at $x = 100 \mu\text{m}$ and the distance from the origin towards the barrier is plotted against the apparent concentration which would be obtained through a fluorescence micrograph.

to each other that interaction becomes likely, the intensity can even decrease for higher intensities. To visualise this behaviour, an exponential increase of fluorescence towards a barrier $100 \mu\text{m}$ away from the origin was calculated. For this function, the expected quenching behaviour was then calculated using equation 4.1; the combination of the quenching and the exponential increase was then plotted in figure 4.10. It can be seen that for a very small interaction parameter the exponential increase of the intensity towards the barrier is not changed. With an increase in the interaction parameter, the quenching becomes stronger.

The comparison of the profiles obtained through the simple dipole-dipole interaction model and the experimental data indicates that quenching can explain the lower intensities for higher concentrations of the fluorophore in the trapping regions. The shapes of the curves in figure 4.9 agree with the graph in figure 4.10. For a small reservoir and therefore a low concentration of TxRed the black line is obtained in the experimental data, which is an exponential increase towards the barrier. As the concentration of TxRed increases and the reservoirs become larger (blue, cyan and pink line), the curves obtained experimentally follow the

shape of the predicted quenching curves with a peak before the barrier and a decay towards it instead of an increase.

With this explanation of the reduced intensity in some areas of the pattern, the increase in the different regions of the pattern was investigated. Initially, the intensity recorded $I(t)$ was corrected for background B , which is always collected through the camera:

$$I_B(t) = I(t) - B. \quad (4.2)$$

The corrected intensity was then multiplied with a further correction factor, which accounts for the reduction of intensity due to the quenching of the fluorophore. It is assumed that no fluorophore is lost during the concentration process. Therefore, the overall intensity captured from all of the pattern should remain constant. As self-quenching becomes a relevant process, the overall fluorescence intensity in each of the sub-patterns decreases. This is then accounted for by multiplying the reduced intensity by the factor by which the intensity has reduced:

$$I_Q^c(t) = I_B^c(t) \frac{I_B^a(0)}{I_B^a(t)}, \quad (4.3)$$

where c and a indicate the region of the pattern in which the intensity was recorded as either the concentration region or all of the pattern, respectively. With this correction for both background and quenching, the real increase in concentration in the triangular trapping regions can be determined.

The six different regions of interest are labelled in figure 4.8b; the outline over which the fluorescence signal was integrated for the regions marked with c is shown, as well. The increase over time in the different concentration regions is shown in figure 4.11. It can be seen that the concentration follows the same behaviour as predicted in figure 4.6b. Firstly, the concentration in the different trapping regions increases over time and secondly, the reservoirs start becoming empty and the concentration in the trapping regions flattens out. The relative

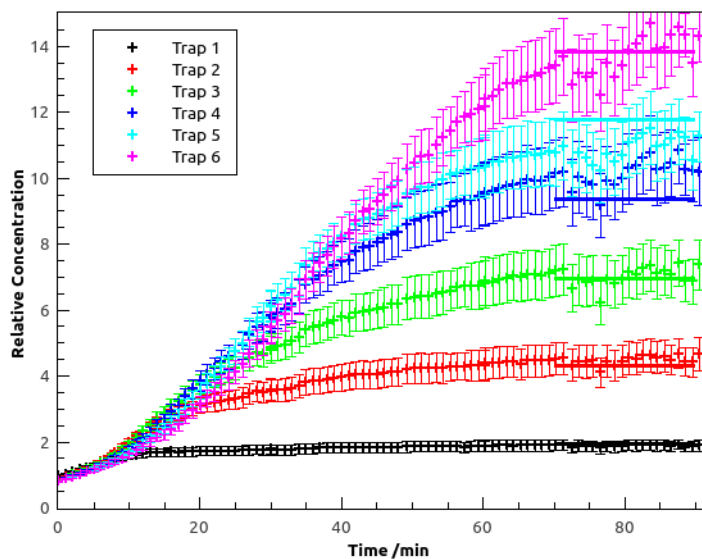


Figure 4.11: Experimentally obtained concentration I_Q^c over time in the different regions marked 1-6 in figure 4.8b. The straight lines on the right hand side show the increase expected from geometrical considerations assuming all charged molecules are transported into the trapping regions.

final increase, which can be achieved in the ideal case of all the fluorescently labelled lipids moving into the trapping, I_a region can be calculated through

$$I_a = A_r / A_t, \quad (4.4)$$

where A_r is the area of the reservoir and A_t is the area of the trapping region. The respective values of I_a are represented through the solid lines in figure 4.11. It can be seen that the concentration reached in the different trapping regions is very similar to the one calculated through geometrical considerations, indicating that almost all of the charged molecules have moved from the reservoir into the trapping region.

When the field is switched off and the trap is being used to carry out subsequent experiments, free diffusion can occur. As discussed and shown previously, this leads to the charged material diffusing back into the reservoir regions. The ratchet was designed such that the time it takes for the diffusion to drive charged molecules out of the trapping region is long compared to experimental times. In

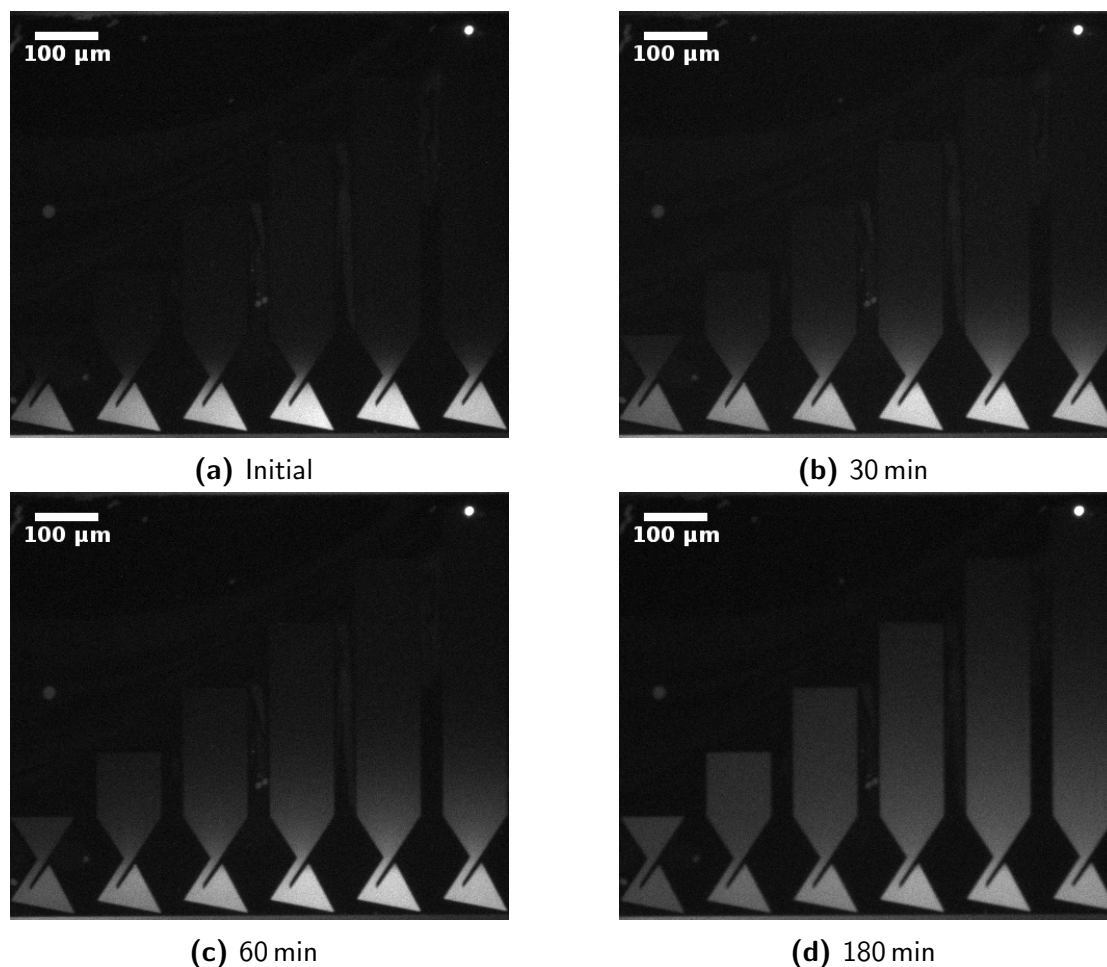


Figure 4.12: Behaviour of charged material in the trap region after the field has been switched off at different times. For up to 1 h the retention of the fluorescent molecules can be seen while after 3 h the observed fluorescence signal is almost even over the whole pattern.

contrast to the prediction made by the simulation, the pattern does not keep the charged molecules in the trapping region for several hours. In figure 4.12, it can be seen that over the course of three hours the concentration has been reversed and the charged components are distributed almost equally across the pattern. It can also be seen that within 30 min and 60 min, diffusion starts to occur but has a limited influence on the distribution of the charged molecules. Therefore, the pattern can be used for experiments, which can be carried out within this space of time.

4.1.3 Application for the Determination of Binding Coefficients

As more bacteria become resistant to the currently existing antibiotics, the development of new drugs is an important but also very expensive task. One reason for the high costs in this processes is the accurate determination of the potency of the drug. To determine the efficiency of a new drug's compound, the binding affinity of the drug to receptor is measured. As the majority of drug targets resides within the cell membrane (Overington et al., 2006), the determination of binding constants of molecules which bind to membrane proteins or membrane associated molecules is of high importance. Using SLBs as a model system for the cell membrane for the determination of the activity of ligands and analytes is a common practice (Cooper and Williams, 1999; Jung et al., 2009; Wittenberg et al., 2012).

Usually, the binding constant is measured by methods which involve the formation of an SLB and the subsequent addition of the ligand from solution. The ligand is added in different concentrations and the change in different quantities from the adsorption to the SLB is measured. This is then repeated for different concentrations of ligand in solution and a binding curve is obtained. This is a very time consuming and therefore expensive process, as the adsorbed mass has to be measured very accurately and the process has to be repeated for several different ligand concentrations. Currently, the methods used most commonly for the measurement of mass adsorption to a lipid bilayer are surface plasmon resonance (SPR) and quartz crystal microbalance with dissipation (QCM-D).

In SPR, a lipid bilayer is formed on the surface of a gold-coated prism. A laser is then used to excite a surface plasmon in the gold surface at a specific angle of incidence. This results in a dip in the reflectance of the prism at the resonance angle of the gold surface. Since the excited plasmon has an evanescent electric field which reaches into the solution, this method is very sensitive to changes close to the surface. When ligands adsorb to the surface of a prism, the refractive index of these ligands is in general different to the refractive index of

water. Therefore, the resonance frequency of the plasmon is changed and with it the angle of maximum absorption changes. This change can easily be detected and is regularly used in the literature (Campbell and Kim, 2007; Jung et al., 2000; Ladbury et al., 1995; Salamon and Tollin, 1996; Wittenberg et al., 2012).

Another method for the determination of mass adsorption and therefore binding constants is the use of QCM-D. This method uses the mechanical resonance frequencies of a quartz crystal. A quartz crystal between two electrodes is driven into oscillation by the application of an AC voltage. The voltage is then switched off and the oscillations of the quartz crystal are monitored. The resonance frequency can be measured very accurately and changes lower than 1 Hz can be recorded. The frequency change can then be used to gain information about the adsorbed mass. In addition to the frequency, the dampening of the oscillation is also measured. The dissipation of the oscillation gives information about the softness or stiffness of the material adsorbed to the crystal. In contrast to SPR, where the optical thickness of an adsorbed material is measured, QCM-D measures the mass which adsorbs to a surface. This method is especially useful when the adsorbing mass is of a similar optical density as the buffer solution in which it is measured. Applications for QCM-D range from specialised biosensors to the investigation of lipid adsorption on a surface (Hianik et al., 2005; Kastl et al., 2002; Pfeiffer et al., 2004; Richter et al., 2003).

As shown previously, the fluorescence intensity counts obtained from a sample can be used to quantify the amount of fluorescent material in a given region. When the lipid bilayer itself is not fluorescent, but the ligand, which is added from solution, is, the amount of ligand bound to the lipid bilayer can be assessed using the fluorescence intensity.

A proof of principle for this can be shown using a fluorescent ligand with a high quantum yield which binds very strongly to a surface. In this case deoxyribonucleic acid (DNA) strands which bind to their corresponding strands attached to lipids in an SLB were used. In order to increase the strength of the

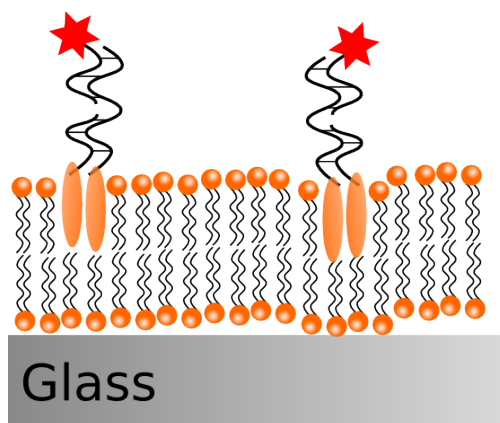


Figure 4.13: Principle of cholesterol modified DNA anchored in an SLB to which DNA is attached from solution. Two cholesterol modified anchors were used to bind the DNA to the SLB while a third, fluorescently labelled, DNA was used to determine the binding constant and the diffusion coefficient.

attachment of the DNA, especially under electrophoretic force, two cholesterol modified DNA strands were used. The cholesterol modification at the 5' for one of the strands and at the 3' for the other DNA strand led to the incorporation of the DNA into the lipid bilayer as cholesterol will insert itself into the small unilamellar vesicles (SUVs) during the preparation of the samples (Pfeiffer et al., 2004). The two anchor strands were designed such that one of the strands has 30 bases and the second has 15 bases. For the shorter strand, all the bases apart from the three closest to the cholesterol modification were chosen to be binding partners to the bases closest to the cholesterol modification in the longer strand. This leads to the incorporation of a double-anchor system into the lipid bilayer which still allows for another DNA strand to bind to the free 15 bases of the longer strand (Pfeiffer et al., 2004; Stengel et al., 2007). The principle of the experiment is shown in figure 4.13.

The DNA with the cholesterol modification was incorporated into the lipid bilayer and the DNA with the Atto 590 modification was added from solution to give a fluorescent signal when the DNA binds to the surface of the SLB. Similar to an SPR or QCM-D experiment, the concentration of the surface receptor was kept constant and the concentration of the ligand in solution was changed.

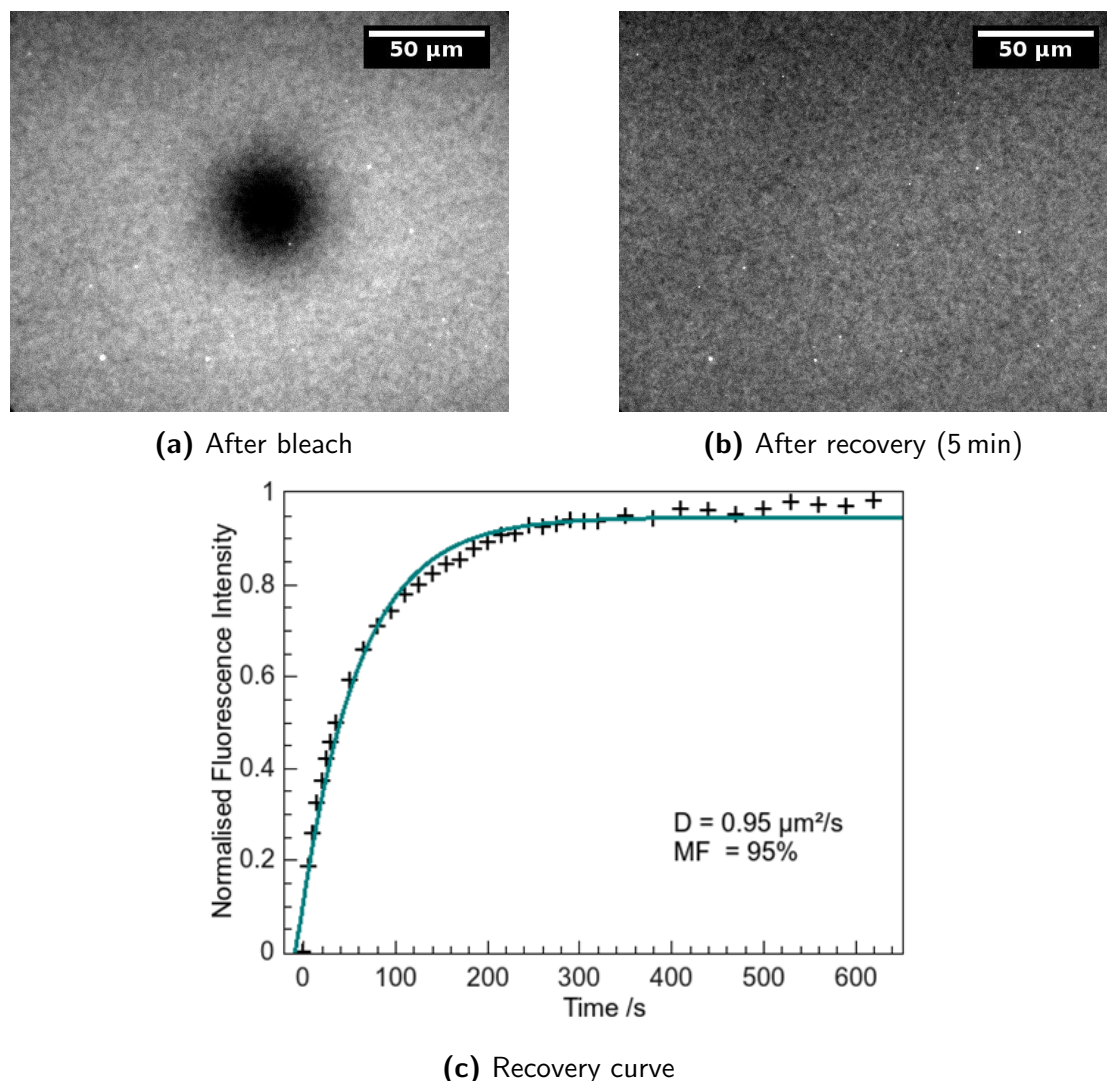


Figure 4.14: Fluorescence images from a FRAP experiment where fluorescently labelled DNA was bound to SLB anchored DNA strands and the corresponding recovery curve. The images and the graph show no indication of a significant immobile fraction and the diffusion coefficient is similar to that of lipids in an SLB.

In order to prove that the DNA was incorporated to the SLB and that fluorescently labelled DNA can bind it, a fluorescence recovery after photobleaching (FRAP) experiment was carried out. For this, the SLB was prepared as usual, with 0.025 mol% of cholesterol anchored DNA strand pairs.

As can be seen from figure 4.14a and figure 4.14b, the bleaching results in a circular spot and quick recovery in less than 5 min. The recovery curve and the corresponding fit in figure 4.14c result in a mobile fraction of more than 90% and a diffusion coefficient for the tethered DNA of almost $1 \mu\text{m}^2 \text{s}^{-1}$. These

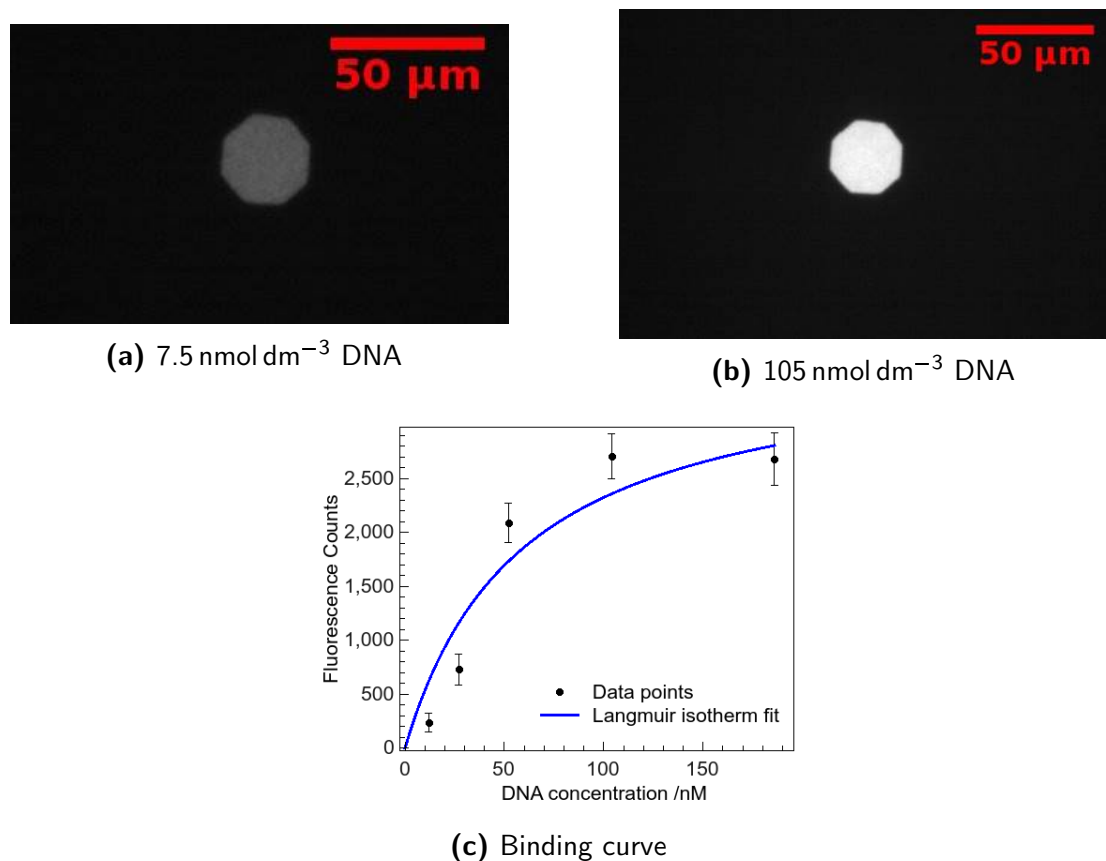


Figure 4.15: Fluorescence images obtained for increased DNA concentrations in solution while the concentration of DNA in the SLB was kept constant. The binding curve was obtained from the fluorescence counts of the labelled DNA bound to the SLB. The error bars are obtained from the standard deviation of the fluorescence counts.

results indicate the formation of an SLB of good quality and a mobility and mobile fraction of the DNA attached to the membrane close to the values of the membrane itself. As the DNA was incorporated into the membrane with no preferential orientation, the DNA with the cholesterol tethers could be in the proximal or in the distal leaflet of the SLB. When the diffusion coefficient of fluorescently labelled DNA bound to the SLB was measured, only one fast component was observed. If binding had occurred to both leaflets of the SLB, two significantly different diffusion coefficients would have been expected as the surface interaction of DNA with the substrate should not be negligible. Therefore, the DNA anchored to the SLB has either moved to the distal leaflet or

the DNA added from solution has not bound to the DNA in the proximal leaflet as this leaflet is inaccessible for the DNA in solution.

The following analysis of the binding constants of different molecular interactions is based on the Langmuir binding isotherm. The association constant k_A for two molecules A and B is given through

$$k_A = \frac{[AB]}{[A][B]} \quad (4.5)$$

where $[A]$ and $[B]$ are the concentration of the unbound molecules and $[AB]$ the concentration of the bound complex. The dissociation constant k_D is the inverse of k_A :

$$k_D = \frac{1}{k_A} \quad (4.6)$$

The Langmuir binding isotherm used for the fits is then calculated through

$$I([A]) = I_{max} \left(\frac{[A]}{[A] + k_D} \right) \quad (4.7)$$

where $I([A])$ denotes the fluorescence intensity with respect to the concentration of the binding partner in solution $[A]$ and I_{max} the fluorescence intensity observed when all binding sites are occupied Lodish (2013).

To determine the binding constant for the DNA pairs, the experiment was modified such that initially no fluorescent DNA was attached to the SLB. Then, different concentrations of fluorescently labelled DNA were injected to the flow cell, incubated for 5 min, and then rinsed thoroughly. This removed any non-bound DNA and resulted in fluorescence signal only from the DNA bound to the SLB. Since the fluorescence images were taken after 2 min to 4 min after the removal of non-bound DNA, the amount of DNA which has dissociated in this short amount of time is negligible compared to the still associated DNA. Two images for different concentrations of DNA in solution are shown in figure 4.15a and figure 4.15b. It can be seen that the fluorescence increase from the increased

amount of DNA results in a clear difference in the fluorescence intensity recorded by the camera. The binding curve for all DNA concentration used is shown in figure 4.15c. It shows the expected behaviour of an initial steep increase and a flattening out as the amount of ligand added is increased further. This effect is not due to self-quenching as the fluorophore concentration is much lower than the concentration used in the previous section and there is no decrease in fluorescence signal with increase in fluorophores, as it was seen in the model (figure 4.10) and the experiment (figure 4.9). From the graph and the fit to the obtained data the binding constant k_D can be determined as 35 nmol dm^{-3} . This value is in good agreement with the previously published value of 20 nmol dm^{-3} which was obtained using QCM-D (Pfeiffer et al., 2004).

The experiment was also carried out in a patterned SLB, in which the DNA modified cholesterol anchors were also incubated into the SLB. In addition to the DNA, nitrobenzoxadiazole (NBD) tagged lipids were incorporated into the vesicles which formed the SLB in order to facilitate the observation of bilayer formation. When this set-up was used, no movement of the DNA through electrophoresis was seen after the fluorescent DNA was bound to the SLB containing the non-fluorescent counterpart to the fluorescently labelled DNA. Despite the fluorophore labelled lipid incorporated into the bilayer having moved into the trapping region, the fluorescent DNA had bound uniformly to the SLB without any preference to either the trapping region or the top part of the pattern. This indicates that, despite the DNA being negatively charged and being mobile in the SLB as shown through the FRAP experiments, there was no movement of the unlabelled DNA under the application of an electric field. Although transport through electrophoresis was expected, the fact that the DNA was not transported into the trapping regions could be explained through electro-osmosis counteracting the electrophoretic forces on the DNA. This could also explain the transport of the dye-molecules since the DNA protrudes further into the liquid layer while the dye-molecules are shorter or even folded into the membrane

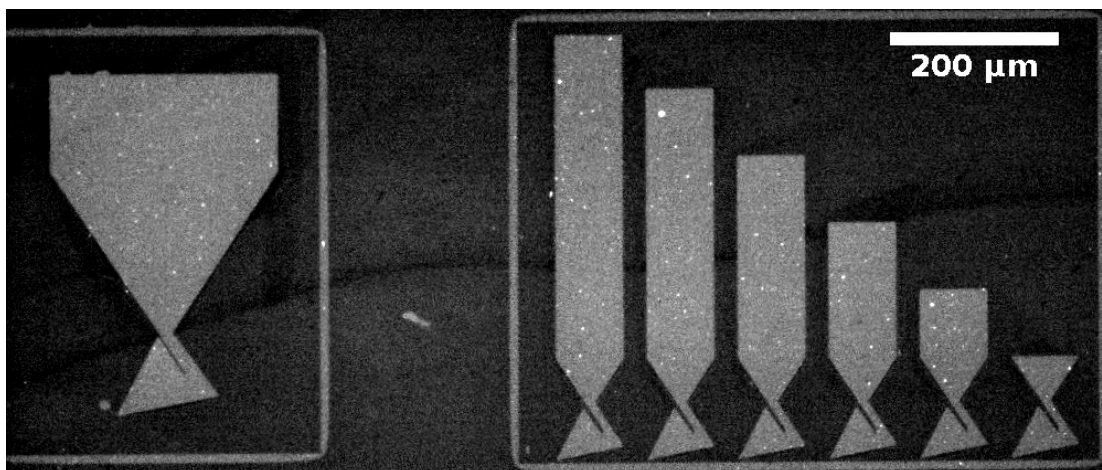


Figure 4.16: Fluorescence image of a pattern used for the determination of binding constants, including a single, large concentrator and a parallelised pattern with multiple concentrators. The SLB was formed using POPC vesicles tagged with a TxRed fluorophore at a concentration 0.25 mol%.

and are therefore influenced less by electro-osmosis. This effect could be further investigated in future work by changing the salt concentration in the buffer and therefore changing the strength of the electro-osmotic forces.

For ligand-receptor combinations, which have very low binding affinities, where the fluorophore has a lower quantum yield than the previously shown experiment, or where the incorporation into the SLB can only be achieved in a very small amount, the direct measurement of the binding coefficient through fluorescence is not always possible. For some cases the fluorescence signal obtained from an SLB to which the ligand is bound is too low and is hidden in the noise. For these cases the formation of the lipid bilayer with a low concentration of the receptor and subsequent formation of regions of high ligand concentration can be the solution. For such experiments a pattern having two main features was chosen. Firstly, there is a concentrator with a large reservoir and a single concentration region. Secondly, a pattern with six smaller reservoirs and a concentration region each was also present. The combination of both patterns can be seen in figure 4.16.

This approach was used to determine the binding constant of the antibiotic vancomycin to the cell wall precursor lipid II. Vancomycin is currently used as a

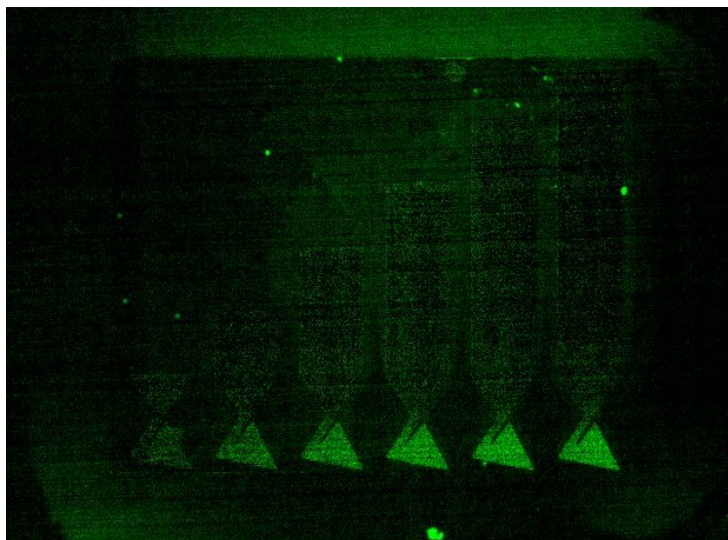


Figure 4.17: BODIPY labelled vancomycin bound to a lipid II containing SLB in which the charged bilayer components were moved into the trapping regions. Despite the lower contrast, the increase of the fluorescence signal in the trapping regions can be seen with the smallest reservoir producing the lowest fluorescence signal.

last resort antibiotic against some gram-positive bacteria. Despite its side effects, such as alleged nephrotoxicity and ototoxicity, it is a drug that can be used against some strains of MRSA bacteria or in cases where other drugs, such as penicillin, cannot be used. Vancomycin was obtained in a boron-dipyrromethene (BODIPY) modified version where a single fluorophore molecule was attached to each vancomycin molecule. The preparations for the experiment were as before: a patterned SLB was formed, the lipid II was concentrated into the trapping regions (monitored using TxRed in the SLB which has the same charge), and when the charged molecules were in the traps, the electric field was switched off. Different concentrations of fluorescently labelled vancomycin were then injected into the flow cell, incubated for 2 min, rinsed out and the fluorescence from the bound molecules was recorded. The image recorded using $1.25 \mu\text{mol dm}^{-3}$ vancomycin in solution is shown as an example in figure 4.17.

The data obtained from a single trapping region at a variation of concentrations of vancomycin in solution was then used to plot a binding curve. As can be seen from figure 4.18, the k_D for the binding of vancomycin to lipid II is around 700 nmol dm^{-3} . This compares well with the literature, where the value

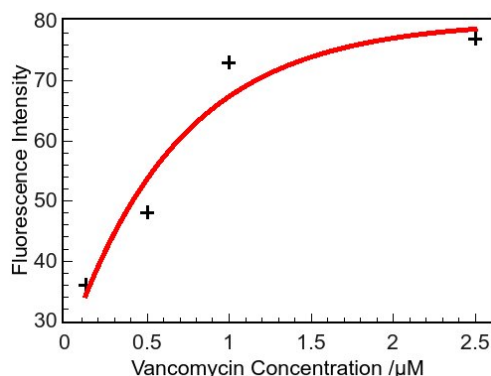


Figure 4.18: Binding curve of vancomycin binding to lipid II in an SLB. Lipid II was incorporated into the SLB at 2 mol% the fluorescence signal is obtained from the BODIPY label attached to the vancomycin.

for k_D is given between $0.3 \mu\text{mol dm}^{-3}$ (Al-Kaddah et al., 2010), $0.5 \mu\text{mol dm}^{-3}$ (Grabowicz et al., 2014), and can be as high as to $1.1 \mu\text{mol dm}^{-3}$ (Vollmerhaus et al., 2003).

The experiment using vancomycin shows that this approach can be used to measure the binding constant of fluorescently tagged drug molecules to their binding sites in the cell membrane. This shows how using SLBs can make the research into new antibiotics cheaper and less time consuming.

It can also be shown that using TxRed as an indicator for the concentration of lipid II is a good model. Both of the molecules are negatively charged and seem to concentrate in a similar fashion. Figure 4.19 shows the overlay of the fluorescence signal from TxRed and from fluorescently labelled vancomycin bound to lipid II in the same membrane. It can be seen that the overlap between the two colours is large and that there are only small regions where there is more TxRed than lipid II/vancomycin.

Another example for which the binding constant was measured is the interaction of biotin with streptavidin. The two molecules bind very strongly to each other and are one of the strongest non-covalent bonds (Green, 1975). Here, a fluorescently labelled streptavidin was used in combination with biotinylated

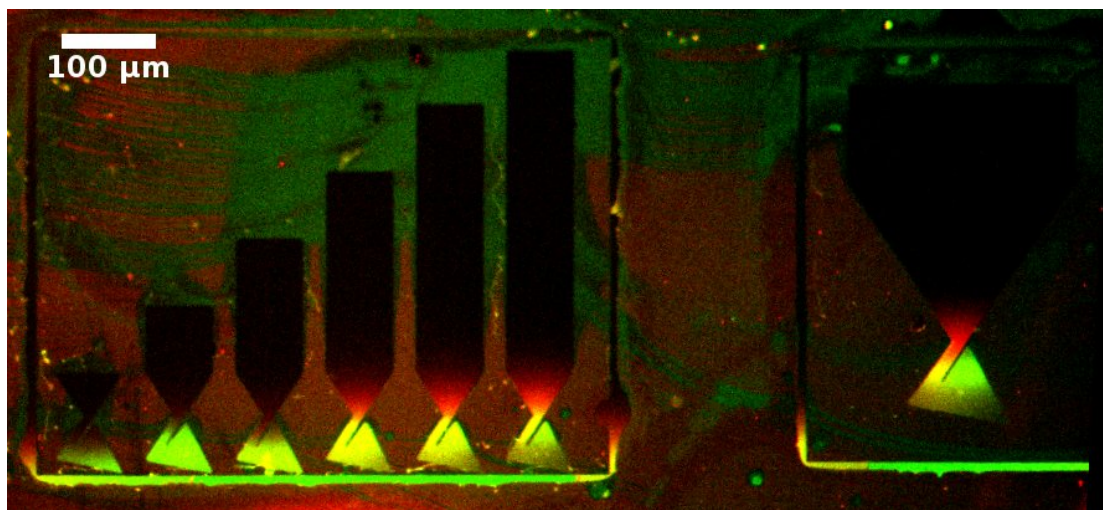


Figure 4.19: Overlap of the fluorescence signal obtained from TxRed and fluorescently labelled vancomycin bound to lipid II in the SLB. The regions in which concentration has occurred are identical for TxRed and vancomycin.

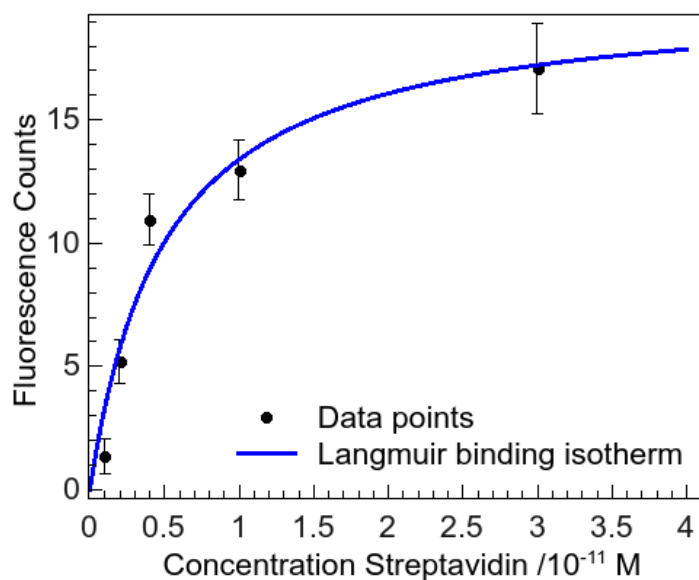


Figure 4.20: Binding curve for varied concentrations of streptavidin in solution. The fit was obtained from a Langmuir isotherm and gave a k_D of $(5 \pm 2) \times 10^{-12} \text{ mol dm}^{-3}$. The error bars are obtained from the standard deviation of the fluorescence counts in the trapping regions.

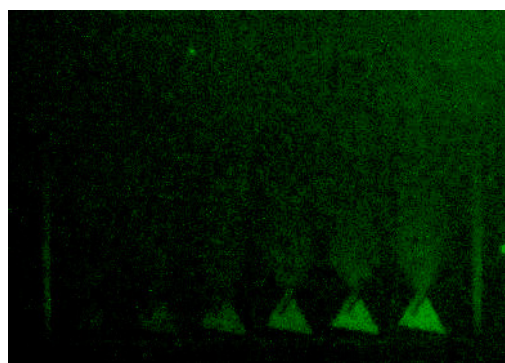
lipids which are negatively charged. The experiment carried out was the same as described earlier. The binding curve was then plotted and can be seen in figure 4.20. The binding constant derived from the graph is 52 pmol dm^{-3} , which is showing the significantly higher affinity of biotin to streptavidin compared to the affinity of vancomycin to lipid II. This is still several orders of magnitude away from the binding constant, which is usually given in the literature of $k_D = 10^{-14} - 10^{-15} \text{ mol dm}^{-3}$ (Green, 1966, 1975). This could be due to the fluorescence label attached to the biotin, which could reduce the binding affinity.

In addition to the use of single patterns to determine the binding constant by adding varying amounts of the ligand in solution, the variation in the receptor concentration in the different concentration regions can also be used. The pattern with several concentration regions and varying sizes of reservoirs allows for this to be done within a single image. Since the concentration of biotinylated lipids in the initial SLB is known, the surface concentration of biotinylated lipids in the concentration regions can be calculated, when it is assumed that all the charged molecules have moved out of the reservoir into the trapping region. It was shown in section 4.1.2 and in figure 4.11 that this assumption can be made.

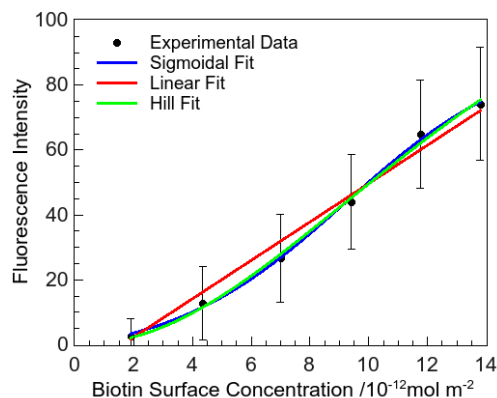
In order to fit the data where the surface concentration of biotin was changed, a different model was used. The fit for the fluorescence intensity follows a sigmoidal function given through

$$I(c) = B + \frac{M}{1 + e^{\frac{-c-k_D}{a}}} \quad (4.8)$$

where B is the background fluorescence, M the maximum fluorescence reached for full surface coverage and a the slope at $c = k_D$ (Keselowsky et al., 2003). The linear fit is shown for comparison and it can be seen in figure 4.21b that the sigmoidal curve fits the data better than the linear fit. This is also reflected in the R^2 values which are 0.998 for the sigmoidal curve and 0.989 for the linear fit. The value for k_D obtained from the fit is $(92 \pm 5) \times 10^{-13} \text{ mol/m}^2$. In other work, the sigmoidal nature of such binding curves has been attributed to electrostatic



(a) Fluorescence image



(b) Binding curve

Figure 4.21: Fluorescence image and binding curve obtained for streptavidin binding to a biotinylated SLB where the binding curve was obtained from a single image. The sigmoidal fit showed very good correlation with the experimental data while the linear fit is shown for comparison. The error bars are obtained from the standard deviation of the fluorescence counts.

interactions and the reduced dimensionality (Mosior and McLaughlin, 1991).

When fitting the Hill equation

$$I(c) = \frac{1}{\left(\frac{k_D}{c}\right)^n + 1} \quad (4.9)$$

with c being the concentration and n being the Hill coefficient, the curve is almost identical to the sigmoidal fit. The Hill coefficient obtained is 2.1 and therefore indicates cooperative binding (Boal, 2012).

As can be seen in figure 4.21a, the fluorescence intensity obtained from the smaller reservoirs is low and the data is noisy. Although the visual quality of the data is not very good, when subtracting background and plotting the fluorescence intensity for the different traps, the binding curve obtained in figure 4.21b agrees with the data from the varying ligand concentrations in solution in figure 4.20. This shows that it is possible to determine the binding constant using only a single fluorescence image, when different receptor concentrations are present in the image used. These receptor concentrations have to be known and well defined as they are in a pattern in which the charged molecules are trapped in pre-defined region of interest.

4.2 Patterned Electrodes

Classical electrodes are made from metals and are suspended in the bulk solution through which the electric field is applied to the SLB. Despite the fact that these methods have proven to be a reliable way to achieve electrophoretic movement for several different groups (Lee and Nam, 2012; Monson et al., 2011; Susan and Ling, 2011; Suzuki et al., 2008; Yoshina-Ishii and Boxer, 2006), there still is some advancement to be made in the choice of electrodes. Electrodes closer to the pattern which is being used for the creation of a gradient in the SLB would result in lower voltages needed to achieve the same field strength. This would make lab-on-a-chip devices much easier to produce as the lower voltages can be supplied by batteries much easier. In addition to this, being able to pattern electrodes so that more complex devices can be made is another advantage for the production of devices making use of electrophoresis in lipid bilayers.

4.2.1 Miniaturisation

Smaller devices could make the production of SLB based sensor devices much easier and could even see them going towards point-of-care applications. To produce such small devices the electrodes need to be closer to the region, in which the electrophoretic movement is generated to produce overall smaller devices. Electrodes which are closer together also need lower voltages to achieve the same field strength and therefore the same electrophoretic movement. Reducing the distance between two electrodes from classical sizes such as 2 cm to patterned electrodes with distance of the order of 0.1 mm to 1 mm immediately reduced the voltage needed by a factor of 20 to 200.

To produce such small electrodes, standard photolithography was used. Here, the photoresist is patterned through UV-light. Then gold is evaporated onto the surface and the remaining photoresist with the gold layer on top is removed resulting in a patterned layer of gold on the surface. A thin adhesive

layer of chromium was used between the cover slip and the gold layer. This should not influence any properties of the electrode as the chromium will not be in contact with the solution and is only a 5 nm thin layer. The pattern of the electrodes is such that interdigitated electrodes are produced where the patterns for the SLB are between the anode and the cathode.

When using two wires in a large flow cell, it can easily be assumed that the electric field between these electrodes is constant and that the potential difference varies linearly with the distance to the electrodes. This is no longer the case when the electrodes are 200 nm thick and a few mm in length and are also on the glass surface so that symmetry is broken, which will change the electric field significantly.

In order to understand potential problems in the variation of the electric field, the field distribution was calculated using finite element analysis (FEA). The electrodes were defined as gold with a potential difference of 10 V between them. The pattern in the experiments was made from SU-8 which has a permittivity of $\epsilon_r = 4$. This value was also used for the pattern in the calculation. The distance between the electrodes was chosen to be 200 μm as this is the smallest scale on which the electrodes were produced and any effects from the miniaturisation should be maximal for this case. Two regions of SU-8 were also incorporated into the simulation, they were position 100 μm and 150 μm away from the first electrode and had a width of 15 μm and 30 μm respectively.

The results of the calculation are seen in figure 4.22. It can be seen that the field distribution is not constant along the membrane; especially close to the electrodes an exponential decay is clearly visible. The further away from the electrode the more the field tends to be constant as it would be in an ideal case. Despite this not being perfect, this could even be used to aid the concentration of membrane components in some experiments. When the concentration regions are designed such that they are further away from the central regions than the reservoirs, the rise in the electric field towards the electrodes could be used to

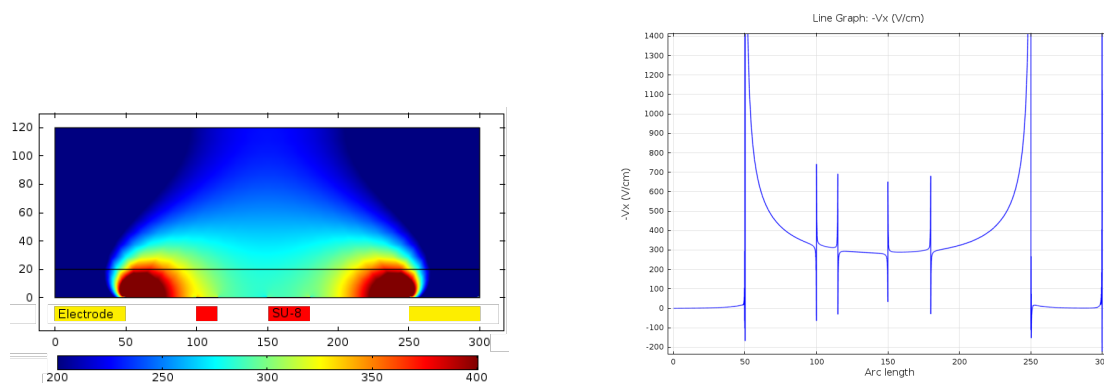


Figure 4.22: Left: Electric field (x component) caused by 10V applied to patterned electrodes on a glass surface in an aqueous environment. Right: line profile of the electric field 10 nm above the surface of the cover slip

make transport and concentration more efficient. The spikes in the electric field are in the regions where the transition from the SU-8 patterning the SLB to the water layer are made. These spikes are an artifact from the simulation as the sudden change in ϵ_r is the cause for the spikes in these regions. In reality a smooth transition of the electric field can be expected.

Using this model and the same pattern as shown in figure 3.12, the build up of charged material was predicted using this model. As can be seen in figure 4.23, the model accurately predicts the behaviour of the AC concentration pattern. There is a phase shift seen between the experimental results and the calculation as the simulated results exhibit peaks slightly before the experimental data but the overall increase over time follows the same behaviour. This shows that the calculations cannot only be used to predict the electrophoretic behaviour of charged membrane components in a lipid bilayer using macroscopic electrodes but that FEA also has the capability of accurately predicting the behaviour of electrophoresis in microscopically patterned electrode devices.

The patterned electrodes can also be used in DC patterns such as the previously presented one. The pattern used in the following experiments was the same one as shown in figure 4.8a. In order to compare the results between the larger and the smaller electrodes the same experiment, consisting of an SLB of 99.75 mol% POPC and 0.25 mol% TxRed in patterns of the same size, was car-

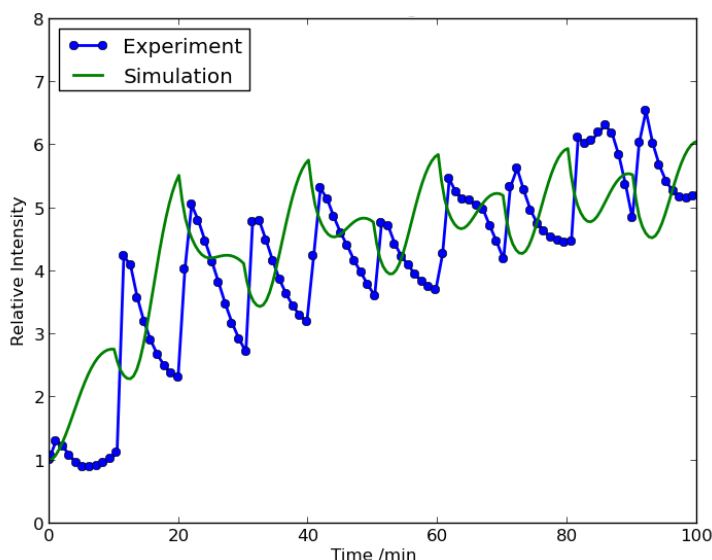


Figure 4.23: Relative increase in concentration/fluorescence intensity in the central region of a trapping device determined by calculation and experiment. (Experimental data courtesy of Peng Bao)

ried out for both electrode set ups. For the macroscopic electrodes the pattern was produced using μ CP, for the miniaturised version the pattern in the SLB consisted of SU-8 photoresist.

A comparison between the two systems is shown in figure 4.24. It can be seen, that after the same experimental time of 30 min the macroscopic electrodes have achieved more transport into the trapping regions than the microscopic ones. This effect could be overcome by increasing the voltage applied to the microscopic electrodes, as they were used with only 10 V applied between them. This voltage was chosen as the electric field strength was the same in the two different set ups using only this small voltage.

The time difference taken to achieve concentration in the trapping regions can be better understood, when the time behaviour of the concentration in the microscopic electrodes is investigated further. The fluorescence images obtained at different times after the electric field was applied can be seen in figure 4.25. In the first 10 min the tops of the reservoirs are already being emptied but it then takes more than 100 min to achieve complete transport into the trapping region of the pattern. This could be attributed to electrostatic repulsion of the

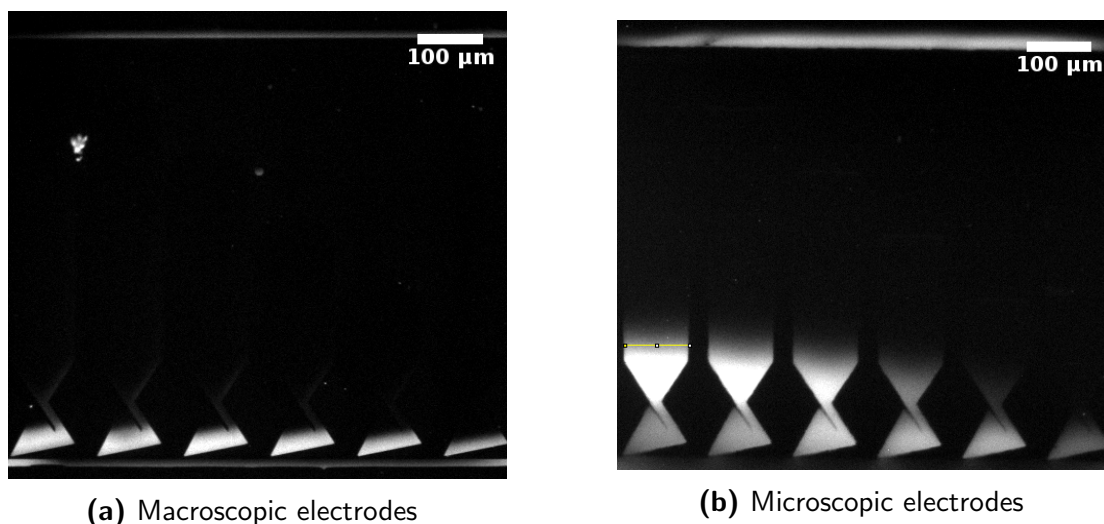


Figure 4.24: Comparison of the fluorescence images obtained for macroscopic and microscopic electrodes after the same concentration time. It can be seen that the microscopic electrodes have achieved less concentration. The electric field was 20 times lower for the microscopic electrodes.

fluorophore in the thin channel leading towards the trapping region. If this was the case, the same behaviour should also be observed for the macroscopic electrodes as the buffer, the concentration of the fluorophore and the strength of the electric field were identical. Therefore, it is more likely that this effect is due to the electric field between the patterned electrodes. As can be seen in figure 4.22, the electric field in the centre of the pattern is almost constant but when considering the field strength closer to the electrodes, an exponential decay of the field can clearly be seen. The top of the reservoirs is much closer to the top electrode than the bottom of the trapping region is to the bottom electrode. This leads to the electric field being much stronger in the top region of the pattern and weaker in the bottom region. Therefore, the slower movement of the charged fluorophore closer to the concentration region can be explained with the decay of the electric field in the same region. If shorter experimental times are required, the voltage applied can be increased two- or three-fold reducing the experimental time to several tens of minutes instead of hours.

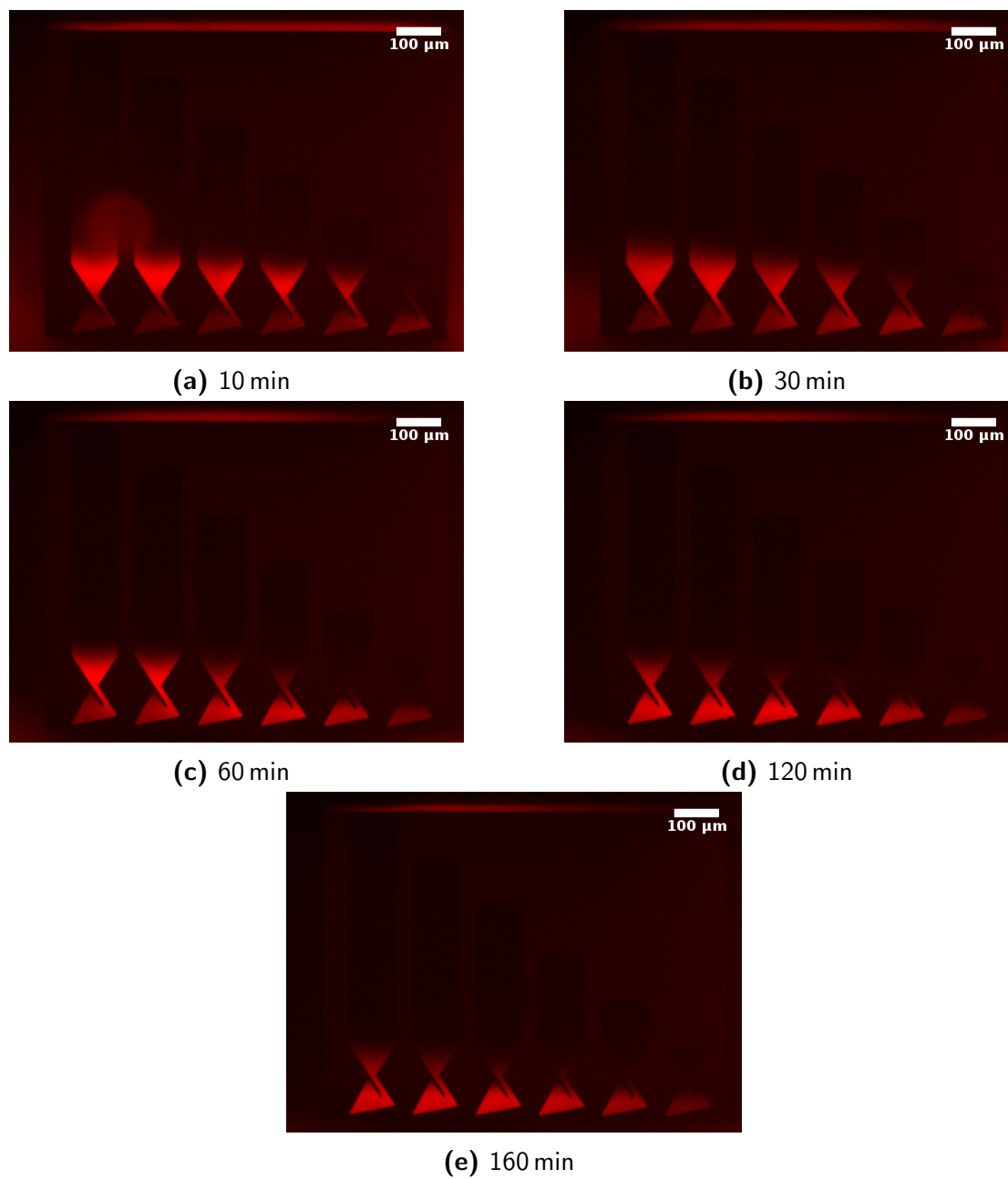


Figure 4.25: Fluorescence images taken at different times showing the achieved transport in a concentration pattern between microscopic electrodes. Transport out of the reservoir towards the trapping region is achieved quickly while the transport through the bottleneck into the trapping region is slow.

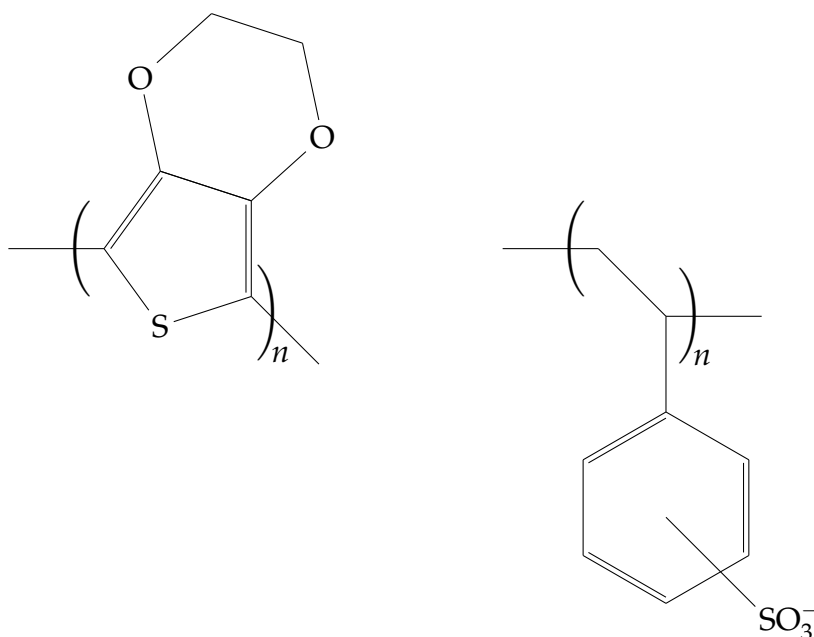


Figure 4.26: Chemical structure of the two isomers in PEDOT:PSS. Poly(3,4-ethylenedioxythiophene) (PEDOT) is shown on the left and polystyrene sulfonate (PSS) is on the right.

4.2.2 New Electrode Material

Instead of using metals as the electrode material other electrodes could also be used as patterned electrode materials. A good candidate for such a material is poly(3,4-ethylenedioxythiophene) polystyrene sulfonate (PEDOT:PSS). It is a polymer which can be used in a water-based solution consisting of two individual ionomers, as can be seen in figure 4.26.

Using this polymer from a dispersion of gelled particles in water allows for a wide range of applications for patterning the polymer onto a surface. It can be spin-coated (Jönsson et al., 2003), ink-jet printed (Xiong and Liu, 2012), microcontact printed (Kaufmann and Ravoo, 2010), or applied through drop-casting (Nardes et al., 2007; Pasquier et al., 2005).

Here drop-casting was used to produce two large electrodes on a glass cover slip. Then, μ CP of fibronectin was used to produce a pattern for subsequent bilayer formation. A schematic of the setup is shown in figure 4.27

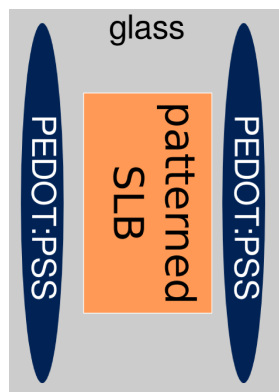


Figure 4.27: Schematic of the use of a PEDOT:PSS electrode patterned directly on a glass cover slip. The glass cover slip has a width of 22 mm and the pattern is approximately 10 mm wide.

Initial experiments were promising but a break down of the current between the electrodes occurred. This is due to the PEDOT:PSS only being able to store a limited amount of charge. When this amount of charge has been transported through the current in the solution, the electrodes degrade and the field, and therefore the current, breaks down. To avoid this, the PEDOT:PSS electrodes were fabricated thicker by depositing more material on the surface initially. In addition to this, diethylene glycol was added to the PEDOT:PSS solution at 5 % by weight. Diethylene glycol acts as a secondary dopant in the PEDOT:PSS layer and increases the conductivity of the electrode (Erlandsson and Robinson, 2011).

The concentration of TxRed using PEDOT:PSS electrodes with an applied potential of 20 V for 30 min can be seen in figure 4.28. This not only shows the successful use of polymeric electrodes but also the influence of a small defect on the trap pattern used in these experiments. The second trap from the left has a small defect in the channel towards the trapping making the channel therefore even thinner. This defect results in less charged material going through the neck and therefore more of it still being above the trap region because of charge repulsion between the different fluorophore molecules in the high concentration regions. The difference becomes especially evident when comparing the two patterns to the left and right of the pattern with the defect. There, the concentration into the trapping region has advanced much further.

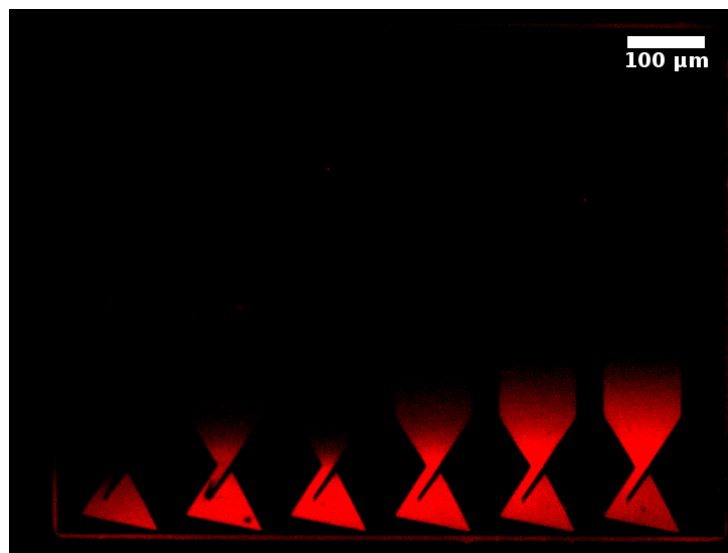


Figure 4.28: Concentration of TxRed in a fibronectin pattern using PEDOT:PSS electrodes. The image was taken 15 min after the electric field was applied. The electric field strength was 24 V cm^{-1} .

This result presents the first time that PEDOT:PSS has been used as a polymeric electrode material in conjunction with electrophoresis on lipid bilayers. It was possible to show that the material can successfully be used to concentrate TxRed in a pattern produced by μCP after the electrodes had been patterned onto the cover slip by drop-casting. This has made the use of a significantly lower voltage (20 V instead of 200 V) possible while still maintaining the ability to transport membrane components based on the electrophoretic force.

4.3 Two-Dimensional Electric Fields

So far, electrophoresis in lipid bilayers has only been used in conjunction with one-dimensional electric fields, where the charged components of a membrane are moved in direction of the electric field. This has led to the patterns being limited to designs where the use of the electric field is limited. Such patterns include lines (Liu et al., 2011; Poyton and Cremer, 2013; Tanaka et al., 2007), squares (Hovis and Boxer, 2000; Lee and Nam, 2012; Pace et al., 2013; Yoshina-Ishii and Boxer, 2006), ratchets (van Oudenaarden and Boxer, 1999), or ratchet based traps (Cheetham et al., 2011).

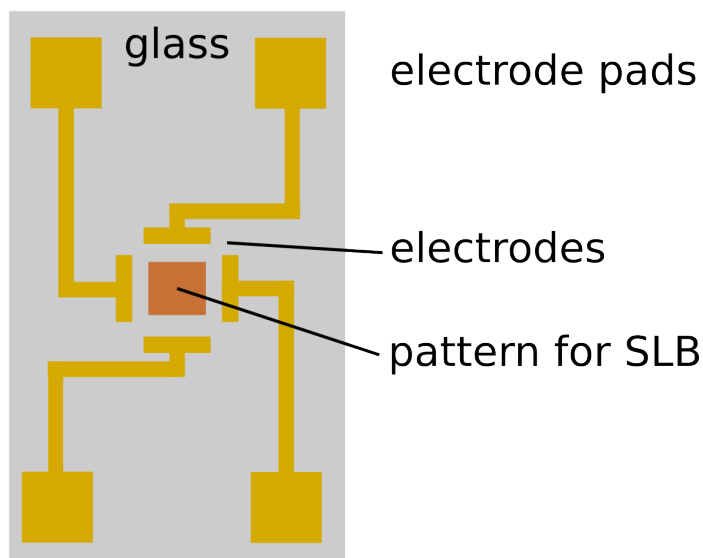


Figure 4.29: Schematic for the electrode patterning to obtain two dimensional electric fields. The large pads in the corners allow for electrical contact to the electrodes on the glass surface via push-pins. The region in the centre is exposed to a variable electric field.

In order to advance towards two dimensional fields, the need for more than two electrodes arises. The electrode design can be seen in figure 4.29. The pads are contacted through four separate push pins in the flow cell, allowing for individual control of the potential of each electrode pair while the liquid volume is in a sealed and well controlled environment.

Using four electrodes, which are both offset in x - and in y -direction from the central region where the pattern for the lipid bilayer is, allows for control of the electric field in both x - and y -direction. To assess the quality of the electric field in the central region of the pattern, the field was simulated using COMSOL® Multiphysics (COMSOL) for a sine wave on both pairs of electrodes including a phase difference. With a 90° phase difference, the two fields overlap such, that the overall electric field effectively moves in a circle.

It was shown before (see section 4.2.1) that electrodes can be patterned onto a glass surface in order to achieve one dimensional electric fields. It is clear that the electric field lines between two parallel, long electrodes are uniform and parallel. When using four electrodes close together, the influence of the pattern

of the electrodes on the electric field lines is not as obvious. When a potential is applied only to the electrodes in x or only to the electrodes in y direction, the field lines will behave as before where only two electrodes were used. Since the aim of using four electrodes is to not only be able to apply fields in x or y direction but also to combine the two components in order to achieve arbitrary fields in two dimensions.

4.3.1 FEA Calculations

To show that the electric field can truly be varied in two dimensions with an arbitrary direction of the field, the electric field distribution was calculated in COMSOL. The field distribution in figure 4.30 shows the results of the calculation. The electric potential is shown colour coded for the pattern with the electrodes (top row) and as a zoom-in of the patterned region (bottom row). The case of only two electrodes having an applied voltage of 10 V is seen in the left column and the case where there are different potentials applied to both the electrode pairs is shown in the right column. For the case of only two electrodes having an applied potential it can be seen that the electric field is linear across the pattern region. The arrows show the electric field direction and strength and are parallel across the pattern region. When both pairs of electrodes are being used, the field becomes starts to vary across the pattern region and some of the field drops off between the electrodes. The central region is less influenced by this effect and shows more linear behaviour. Therefore, the central region, in which the pattern lies, can be used for applications in which a constant electric field is needed.

As an example of a pattern which requires arbitrary fields, a spiral was used here. The pattern can already be seen in figure 4.30. The spiral in the centre needs a rotating field to achieve efficient transport of material along the spiral into the centre. With each rotation of the electric field the charged material also undergoes one rotation as well and is moved towards the centre. Since the

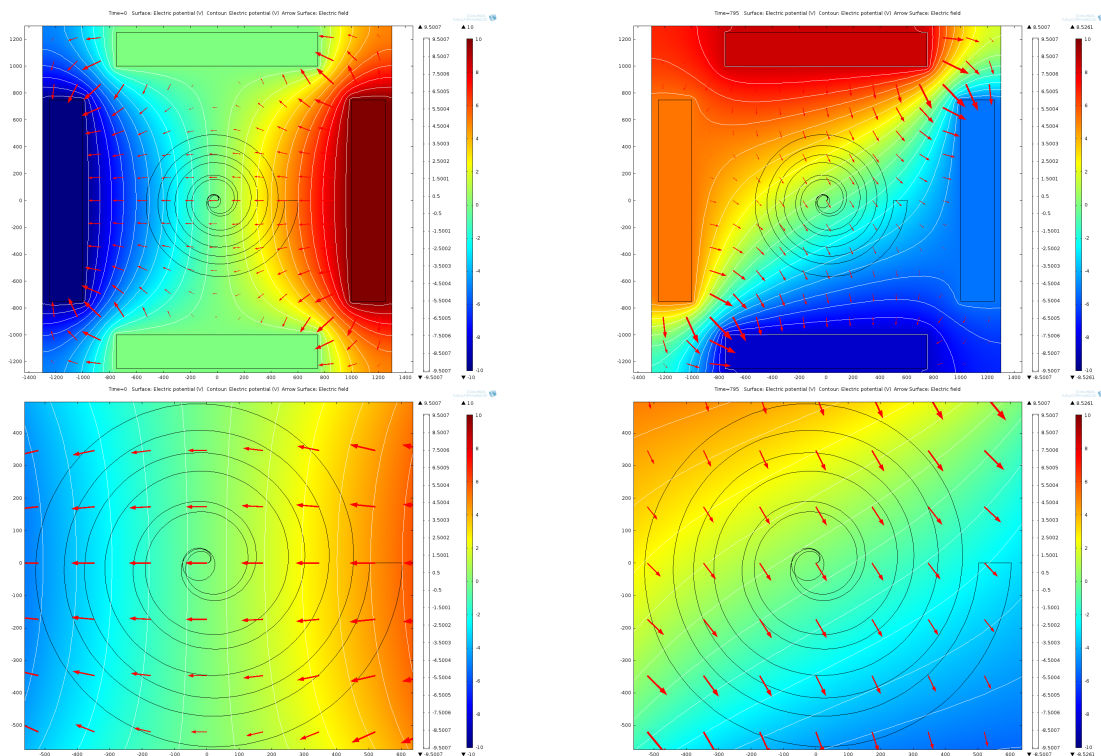


Figure 4.30: Calculation of the electric field caused by four electrodes close to each other. The top row shows an overview including the electrodes themselves, bottom row shows a zoom in into the region where the pattern (spiral) for the lipid bilayer is. The electric field can point either in a horizontal direction (left) or, when all four electrodes are used, in an arbitrary direction (right).

pattern is clockwise, charged material will be moved into the central region if the electric field is also rotating in a clockwise direction but when the electric field is rotating counter clockwise the charged material is expelled from the central region and moved towards the outside of the spiral. Therefore, the spiral can either be used as a concentrating device or for the controlled release of material which has previously been concentrated into the central region.

Before an experimental realisation of the spirals was attempted, the use of the two-dimensional electric fields was optimised. The first parameter which was considered was the phase shift between the two electrodes. The two pairs of electrodes are independently accessible and can therefore be used to obtain any phase shift desired, not only in a simulation but also in experiment. In figure 4.31, the relative increase of the charged material in the central region after 10h is plotted against the phase shift for different period times of the overall

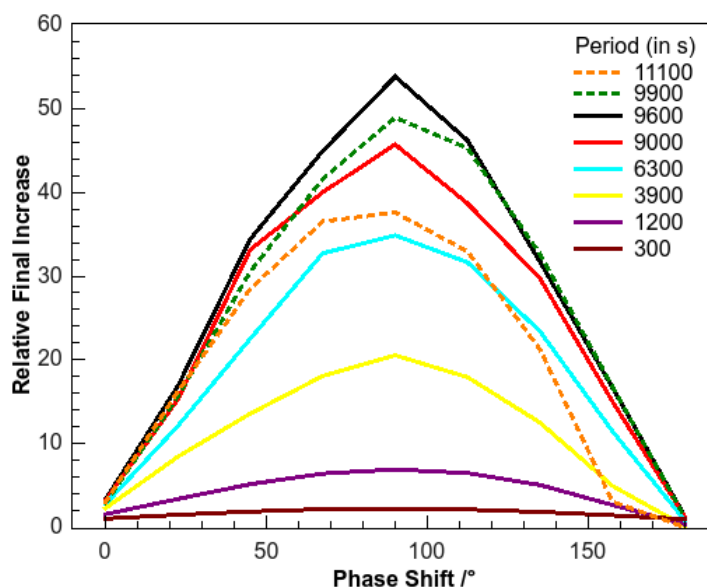


Figure 4.31: Relative increase of charged material in the central region of a spiral after 10 h experimental time for different period times (shown in seconds) plotted against phase shift. The optimal condition for any period is a 90° phase shift between the electrodes. The relative concentration increases with increase of the period until a period time of 2.67 h after which it decreases.

rotation. It can clearly be seen that the most efficient phase shift is independent of the period chosen for the experiment and is at 90° . The overall efficiency increases with the period time until the period reaches 9600 s. Further increases in the period time results in decreases in the final concentration in the central region, as can be seen from the dashed lines. From this graph the optimum period is 9600 s with a phase shift of 90° .

The 10 h overall time T for the experiment assumed in the simulation so far is rather long and it can be beneficial to have optimum concentration in shorter overall experimental times. To analyse the situation for shorter experimental times, the relative final concentration in the central region was plotted against the period ω . In this case, the different data sets correspond to different overall experimental times. Immediately, it can be seen from figure 4.32 that the final relative concentration increases for longer overall experimental times. The graph also shows that for each given overall experimental time there is an increase in the final concentration until the optimum value is reached. The final concentration then drops off in steps and does not increase again. A close

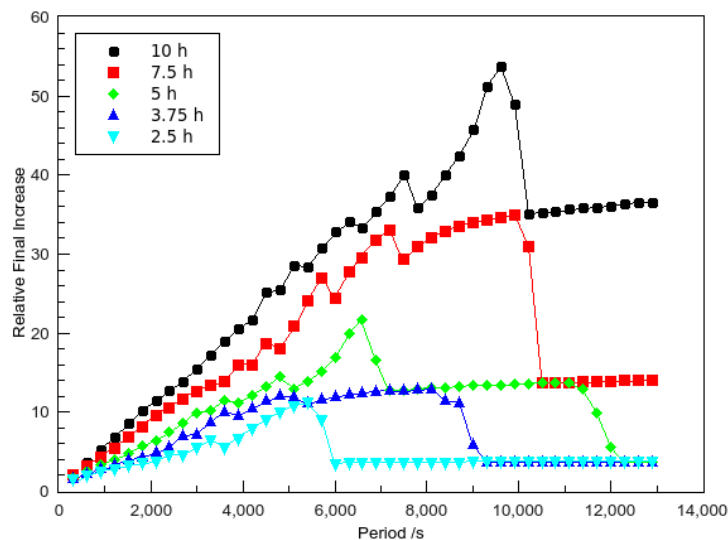


Figure 4.32: Relative final increase in the centre of a spiral pattern plotted against the period of the electric field for different overall experimental times. For any given overall experimental time, the optimal period is such that 3.75 rotations of the field are reached.

analysis shows that the optimum for the relative final concentration is reached when

$$\frac{\omega}{T} = 3.75. \quad (4.10)$$

The reason for this is the shape of the pattern. Charged lipids initially located at the outer end of the spiral have to cover 3.75 revolutions in the spiral to reach the central region. When less rotations are achieved (i.e. the period is longer than the optimum) within the experimental time, the charged lipids from the outside do not reach the central region and the relative final concentration therefore is lower. For shorter periods and thus more rotations of the field, not all of the charged lipids follow the electric field quick enough and are left behind, making the spiral less efficient for shorter periods.

In conclusion, the spirals highest efficiency depends on the maximum experimental time T . When this is known, the period should be chosen such that $\omega = \frac{T}{3.75}$ to get the maximum amount of charged material into the central region.

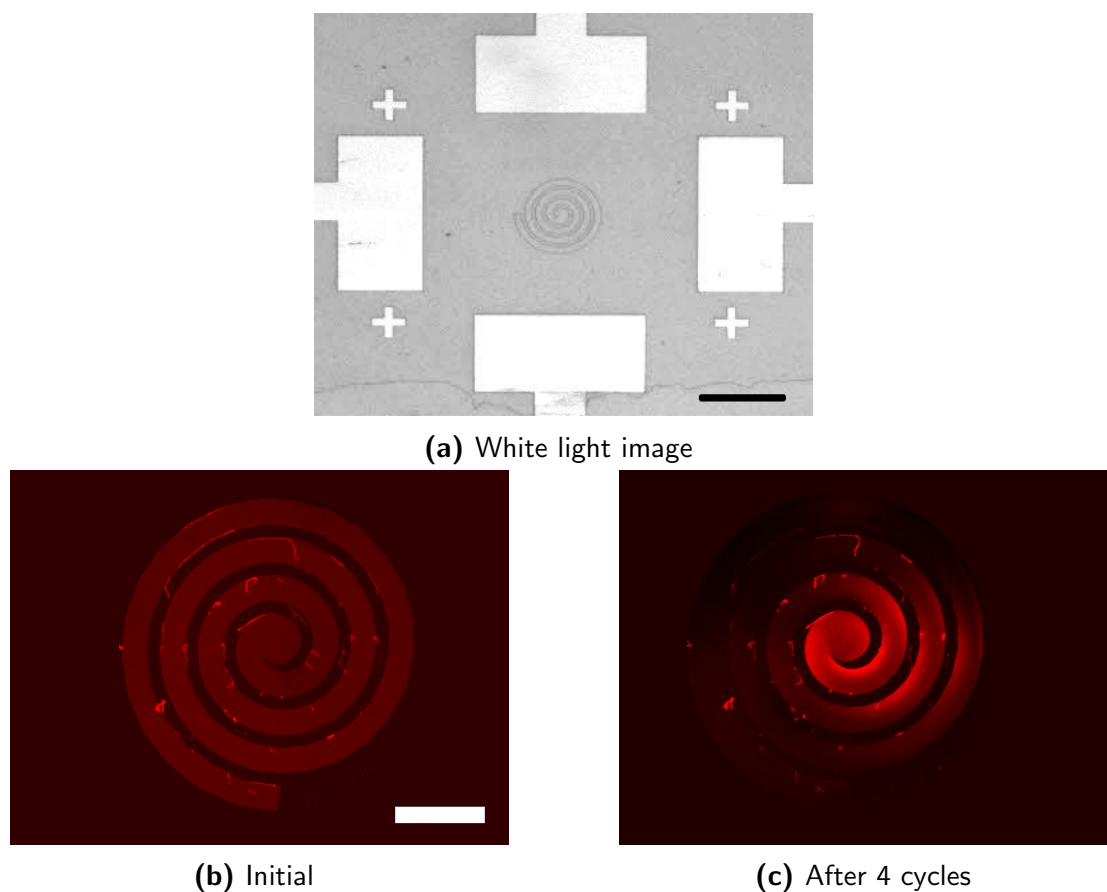


Figure 4.33: Experimental realisation of the spiral pattern. The black scale bar is 100 μm , the white scale bar is 50 μm , the fluorescence signal is from TxRed in the lipid bilayer. It can be seen that the use of two dimensional electric fields lead to an increase of charged, fluorescent lipids in the central region of the pattern. (Images taken by Ying Zhang)

4.3.2 Experimental Realisation

The spiral pattern has also been realised experimentally. The pattern was fabricated using SU-8 photoresist as a barrier material and glass as a support for bilayer formation between the SU-8 barriers. The overall design of the pattern and the electrodes next to the pattern is shown in figure 4.33a

As a charged membrane component TxRed was chosen at a concentration of 0.025 mol%. The pattern with the SLB formed as described in the previous section can be seen in figure 4.33b. After four cycles a significant part of the TxRed has been transported to the central region (figure 4.33c).

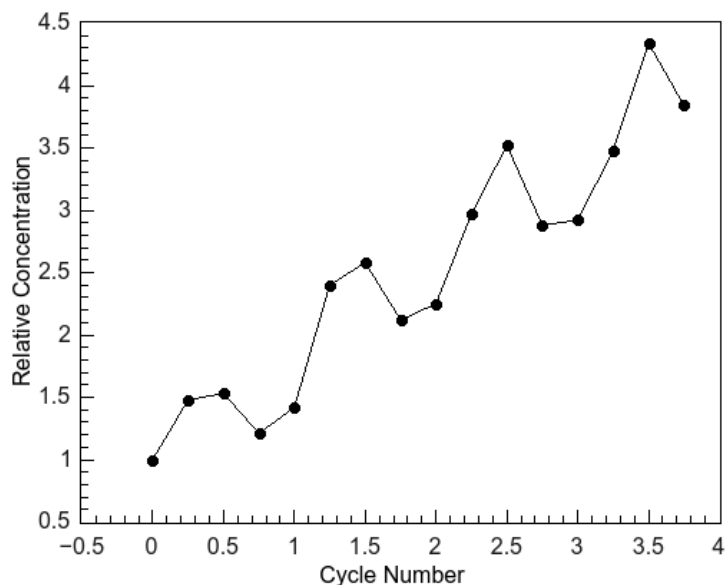


Figure 4.34: Relative increase in concentration of the TxRed fluorophore in the central region of a spiral pattern. The pattern used for this experiment is shown in figure 4.33. With every full rotation of the electric field, the relative concentration in the central region increases.

The analysis of the spiral pattern shows that the behaviour is as expected from the calculations. With every full cycle of the field, more charged material is moved into the central region. In figure 4.34 the relative increase of the fluorophore in the central region is plotted against the cycle number. The steps towards higher concentration in the central region coincide with the completion of the cycles of the electric field and the final relative increase in concentration is almost 4.5 fold

It can also be seen in figure 4.34, that in each cycle a small portion of charged material is lost after an increase was reached previously. This is due to a portion of the charged material, which has been concentrated into the central region, moving out of the centre again. The pattern could be improved by changing the pattern such that moving out of the central region would be made more difficult once charged material has been concentrated in the centre. This would be achieved by adding a small barrier into the inlet, making the pattern more like a fish trap, which allows for easy access into the trap region but prevents an easy exit from the same region.

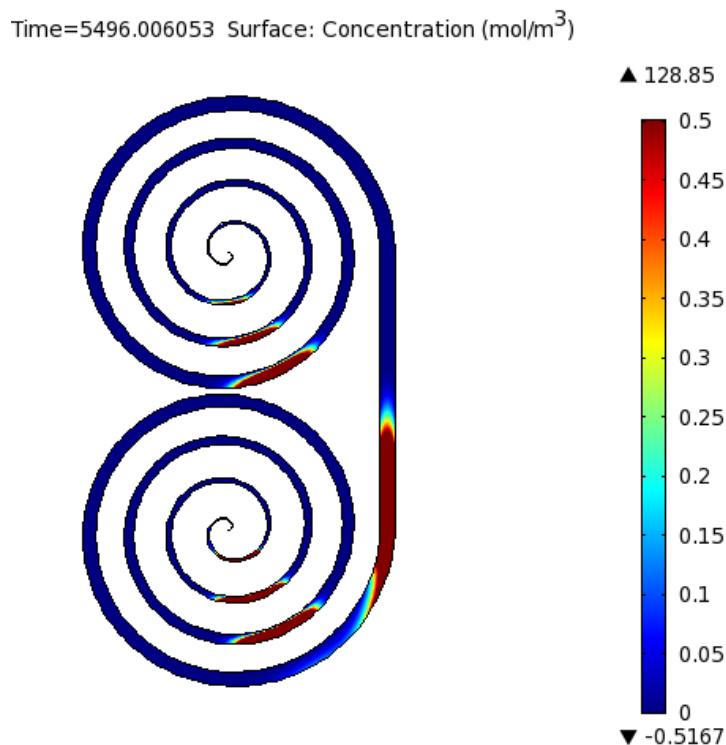


Figure 4.35: Two spirals connected to each other. The bottom spiral is wound up clockwise, the top spiral counter clockwise. The top spirals releases material into the bottom spiral. As the electric field also forces charged material through the connector part, the relative concentration reached in the central region of the bottom spiral can be increased by using this pattern over a single spiral. The charged material in the connector region is behind the charged material in the spiral region as the field is optimised to move material in a spiral pattern.

The spiral pattern can also be used twice in a bigger overall pattern. When two spirals are arranged such that one of the spirals is wound up counter clockwise and one is wound up clockwise and the two spirals are connected to each other, one spiral can be used to feed charged material into the other spiral. The electric field will make the charged material follow its pattern in both the spirals. Depending on the orientation of the spiral, this will either lead to an increase in the concentration in the centre of the spiral or to an expulsion of material from the spiral. A pattern with two spirals can be seen in figure 4.35. The result was obtained after four cycles of the electric field rotation. Since more than one rotation was completed, the top spiral has expelled material towards the bottom ratchet. This can be seen as the red region in the connection between the two spirals.

4.4 Conclusion

This chapter presents new methods of manipulating charged membrane components. New electrode materials, electrode patterns and ways for applying electric fields are discussed. The toolbox has been expanded from means of transportation using Brownian ratchets to compact patterns, which make use of two-dimensional electric fields, and can be used for either concentration or controlled release. In addition to that, a pattern for the fast concentration of material using DC fields and subsequent capture is shown. The applications for the latter are also presented and it is shown that it can be used to determine binding coefficients quickly with only a single fluorescence image.

References

- Al-Kaddah, S., Reder-Christ, K., Klocek, G., Wiedemann, I., Brunschweiler, M., and Bendas, G. (2010). Analysis of membrane interactions of antibiotic peptides using ITC and biosensor measurements. *Biophysical Chemistry*, 152(1–3):145–152.
- Boal, D. H. (2012). *Mechanics of the cell*, volume 2. Cambridge University Press, Cambridge; New York.
- Campbell, C. T. and Kim, G. (2007). SPR microscopy and its applications to high-throughput analyses of biomolecular binding events and their kinetics. *Biomaterials*, 28(15):2380–2392.
- Cheetham, M. R., Bramble, J. P., McMillan, D. G. G., Krzeminski, L., Han, X., Johnson, B. R. G., Bushby, R. J., Olmsted, P. D., Jeuken, L. J. C., Marritt, S. J., Butt, J. N., and Evans, S. D. (2011). Concentrating Membrane Proteins Using Asymmetric Traps and AC Electric Fields. *Journal of the American Chemical Society*, 133(17):6521–4.
- Cooper, M. a. and Williams, D. H. (1999). Binding of glycopeptide antibiotics to a model of a vancomycin-resistant bacterium. *Chemistry & biology*, 6(12):891–9.
- Erlandsson, P. G. and Robinson, N. D. (2011). Electrolysis-reducing electrodes for electrokinetic devices. *Electrophoresis*, 32(6-7):784–90.
- Grabowicz, M., Andres, D., Lebar, M. D., Malojčić, G., Kahne, D., and Silhavy, T. J. (2014). A mutant *Escherichia coli* that attaches peptidoglycan to lipopolysaccharide and displays cell wall on its surface. *eLife*, 3(1):e05334.
- Green, N. M. (1966). Thermodynamics of the binding of biotin and some analogues by avidin. *Biochemical Journal*, 101(3):774–780.
- Green, N. M. (1975). Avidin. *Advances in protein chemistry*, 29(5):85–133.
- Hianik, T., Ostatná, V., Zajacová, Z., Stoikova, E., and Evtugyn, G. (2005). Detection of aptamer–protein interactions using QCM and electrochemical indicator methods. *Bioorganic & Medicinal Chemistry Letters*, 15(2):291–295.
- Hovis, J. S. and Boxer, S. G. (2000). Patterning Barriers to Lateral Diffusion in Supported Lipid Bilayer Membranes by Blotting and Stamping. *Langmuir*, 16(3):894–897.

- Jönsson, S. K. M., Birgersson, J., Crispin, X., Greczynski, G., Osikowicz, W., Denier van der Gon, A. W., Salaneck, W. R., and Fahlman, M. (2003). The effects of solvents on the morphology and sheet resistance in poly(3,4-ethylenedioxythiophene)-polystyrenesulfonic acid (PEDOT-PSS) films. *Synthetic Metals*, 139:1–10.
- Jung, H., Robison, A. D., and Cremer, P. S. (2009). Detecting protein-ligand binding on supported bilayers by local pH modulation. *Journal of the American Chemical Society*, 131(3):1006–14.
- Jung, L. S., Shumaker-Parry, J. S., Campbell, C. T., Yee, S. S., and Gelb, M. H. (2000). Quantification of Tight Binding to Surface-Immobilized Phospholipid Vesicles Using Surface Plasmon Resonance: Binding Constant of Phospholipase A2. *Journal of the American Chemical Society*, 122(17):4177–4184.
- Kastl, K., Ross, M., Gerke, V., and Steinem, C. (2002). Kinetics and Thermodynamics of Annexin A1 Binding to Solid-Supported Membranes: A QCM Study. *Biochemistry*, 41(31):10087–10094.
- Kaufmann, T. and Ravoo, B. J. (2010). Stamps, inks and substrates: polymers in microcontact printing. *Polymer Chemistry*, 1:371.
- Keselowsky, B. G., Collard, D. M., and García, A. J. (2003). Surface chemistry modulates fibronectin conformation and directs integrin binding and specificity to control cell adhesion. *Journal of biomedical materials research. Part A*, 66(2):247–259.
- Ladbury, J. E., Lemmon, M. A., Zhou, M., Green, J., Botfield, M. C., and Schlessinger, J. (1995). Measurement of the binding of tyrosyl phosphopeptides to SH2 domains: a reappraisal. *Proceedings of the National Academy of Sciences*, 92(8):3199–3203.
- Lee, Y. K. and Nam, J.-M. (2012). Electrofluidic lipid membrane biosensor. *Small (Weinheim an der Bergstrasse, Germany)*, 8(6):832–7.
- Liu, C., Monson, C. F., Yang, T., Pace, H., and Cremer, P. S. (2011). Protein separation by electrophoretic-electroosmotic focusing on supported lipid bilayers. *Analytical chemistry*, 83(20):7876–80.
- Lodish, H. (2013). *Molecular cell biology*, volume 7. W.H. Freeman, Basingstoke; New York.
- Marsh, D. (2012). Thermodynamics of Phospholipid Self-Assembly. *Biophysical Journal*, 102(5):1079–1087.
- Monson, C. F., Pace, H. P., Liu, C., and Cremer, P. S. (2011). Supported bilayer electrophoresis under controlled buffer conditions. *Analytical chemistry*, 83(6):2090–6.
- Mosior, M. and McLaughlin, S. (1991). Peptides that mimic the pseudosubstrate region of protein kinase C bind to acidic lipids in membranes. *Biophysical journal*, 60(1):149–159.

- Nardes, A., Kemerink, M., Janssen, R., Bastiaansen, J., Kiggen, N., Langeveld, B., van Breemen, A., and de Kok, M. (2007). Microscopic Understanding of the Anisotropic Conductivity of PEDOT:PSS Thin Films. *Advanced Materials*, 19(9):1196–1200.
- Overington, J. P., Al-Lazikani, B., and Hopkins, A. L. (2006). How many drug targets are there? *Nat Rev Drug Discov*, 5(12):993–996.
- Pace, H. P., Sherrod, S. D., Monson, C. F., Russell, D. H., and Cremer, P. S. (2013). Coupling supported lipid bilayer electrophoresis with matrix-assisted laser desorption/ionization-mass spectrometry imaging. *Analytical chemistry*, 85(12):6047–52.
- Pasquier, A. D., Unalan, H. E., Kanwal, A., Miller, S., and Chhowalla, M. (2005). Conducting and transparent single-wall carbon nanotube electrodes for polymer-fullerene solar cells. *Applied Physics Letters*, 87(20):203511.
- Pfeiffer, I., Höök, F., and Ho, F. (2004). Bivalent cholesterol-based coupling of oligonucleotides to lipid membrane assemblies. *Journal of the American Chemical Society*, pages 10224–10225.
- Poyton, M. F. and Cremer, P. S. (2013). Electrophoretic Measurements of Lipid Charges in Supported Bilayers. *Analytical chemistry*, 85(22):10803–10811.
- Richter, R., Mukhopadhyay, A., and Brisson, A. (2003). Pathways of lipid vesicle deposition on solid surfaces: a combined QCM-D and AFM study. *Biophysical journal*, 85(5):3035–47.
- Salamon, Z. and Tollin, G. (1996). Surface plasmon resonance studies of complex formation between cytochrome c and bovine cytochrome c oxidase incorporated into a supported planar lipid bilayer. I. Binding of cytochrome c to cardiolipin/phosphatidylcholine membranes in the absence of oxida. *Biophysical journal*, 71(2):848–57.
- Stengel, G., Zahn, R., Ho, F., and Höök, F. (2007). DNA-induced programmable fusion of phospholipid vesicles. *Journal of the American Chemical Society*, (129):9584–9585.
- Susan, D. and Ling, C. (2011). Supported Lipid Bilayer Electrophoresis for Separation and Analytical Studies of Cell Membrane Biomolecules. In *Interfaces and Interphases in Analytical Chemistry*, volume 1062, chapter 4, pages 99–121. American Chemical Society.
- Suzuki, K., Hosokawa, K., and Maeda, M. (2008). Electrophoresis of membrane-associated molecules in packed beds of bilayer-coated particles. *Journal of the American Chemical Society*, 130(5):1542–3.
- Tanaka, M., Hermann, J., Haase, I., Fischer, M., and Boxer, S. G. (2007). Frictional drag and electrical manipulation of recombinant proteins in polymer-supported membranes. *Langmuir : the ACS journal of surfaces and colloids*, 23(10):5638–44.

- van Oudenaarden, A. and Boxer, S. G. (1999). Brownian Ratchets: Molecular Separations in Lipid Bilayers Supported on Patterned Arrays. *Science*, 285(5430):1046–1048.
- Vollmerhaus, P. J., Breukink, E., and Heck, A. J. R. (2003). Getting Closer to the Real Bacterial Cell Wall Target: Biomolecular Interactions of Water-Soluble Lipid II with Glycopeptide Antibiotics. *Chemistry – A European Journal*, 9(7):1556–1565.
- Wittenberg, N. J., Im, H., Xu, X., Wootla, B., Watzlawik, J., Warrington, A. E., Rodriguez, M., and Oh, S.-H. (2012). High-Affinity Binding of Remyelinating Natural Autoantibodies to Myelin-Mimicking Lipid Bilayers Revealed by Nanohole Surface Plasmon Resonance. *Analytical chemistry*.
- Xiong, Z. and Liu, C. (2012). Optimization of inkjet printed PEDOT:PSS thin films through annealing processes. *Organic Electronics*, 13(9):1532–1540.
- Yoshina-Ishii, C. and Boxer, S. G. (2006). Controlling two-dimensional tethered vesicle motion using an electric field: interplay of electrophoresis and electro-osmosis. *Langmuir*, 22(5):2384–91.

Chapter 5

Read-out Methods for Light Harvesting Proteins in Lipid Bilayers

This chapter presents several steps taken towards the incorporation and detection of light harvesting proteins in solid supported lipid bilayers (SLBs). Firstly, novel supports are discussed, which allow for the incorporation of membrane proteins with significant extramembranous domains. Secondly, surface enhanced Raman scattering (SERS) is shown to be a useful, label-free method of investigation of SLBs. Finally, electrochemical read-out methods are presented.

5.1 Novel Polymeric Supports For Lipid Bilayers

One of the main disadvantages of using SLBs for the investigation of lipid bilayers is their proximity to their support. Between the SLB and the substrate there is a water reservoir of only around 1 nm thickness (Cremer and Boxer, 1999; Johnson et al., 1991; Min et al., 2010; Ogawa et al., 2009). Membrane proteins which have extramembranous domains larger than the water cushioning layer will interact with the substrate, become immobile, and can even be denatured. To overcome this problem, various novel supports for lipid bilayers have been

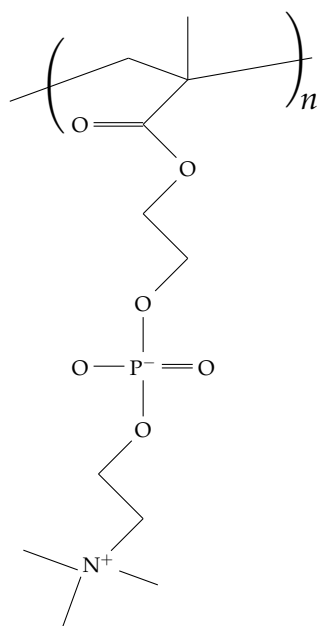


Figure 5.1: Structure of PMPC. The head group closely resembles the the polar head group of POPC. The polymeric chains are made of carbon chains, similar to lipid tails.

investigated in the literature (Smith et al., 2005; Zhang et al., 2010) . Independent of the specific support used, the materials have common properties: they are hydrophilic to mimic an aqueous environment, they are biocompatible so that no strong interactions between the SLB and the support occur and they are soft, allowing membrane proteins to protrude into the polymer without denaturing.

5.1.1 PMPC

Here, the zwitterionic brush poly(2-methacryloyloxyethyl phosphorylcholine) (PMPC) is investigated for its possible use as a support for SLBs. It is well known to be biocompatible, biomimetic, and hydrophilic (Blanazs et al., 2009; Lomas et al., 2010) and could therefore be used in experiments involving membrane proteins with large extramembranous domains. The growth of PMPC is achieved by atom-transfer radical-polymerisation (ATRP) and was done by the Armes group in Sheffield. The structure of PMPC is shown in figure 5.1 and it can be seen that the structure resembles the head group of a lipid molecule.

Vesicle Fusion

Initially, the attempt was made to form SLBs on PMPC brushes using the vesicle fusion method, which allows for the incorporation of proteins using proteoliposomes instead of vesicles containing only lipids. This would be an easy method to incorporate light harvesting proteins into SLBs, which has been used for several other proteins (Dewa et al., 2006; Karatekin and Rothman, 2012; Trépout et al., 2007). First experiments were carried using only 1-palmitoyl-2-oleoylphosphatidylcholine (POPC) vesicles. This led to no significant coverage of SLBs on the polymer brush, as can be seen in figure 5.2. The top image is a typical image of POPC vesicles on the PMPC brush. The vesicles adsorb in small numbers on the surface but do not rupture to form a continuous SLB. The bottom images in figure 5.2 show the rare example of a patch of SLB formed on a PMPC brush. This could be because the random distribution of vesicles led to a very high concentration of them in this specific region, resulting in rupture of the vesicles limited to this region or even a defect in the polymer substrate.

Since the experiments with POPC vesicles did not lead to a significant coverage of the brush with SLB, the vesicle composition was changed. Despite the surface being neutral at pH 7, the PMPC brush is zwitterionic and has an amine group at the surface. This led to the assumption that charged lipids might increase the interaction of the brush with the vesicles and therefore lead to a higher surface coverage of vesicles on the brush, finally resulting in the formation of SLBs. To test this hypothesis, lipid vesicles containing 25 mol% of either 1,2-dioleoyl-3-trimethylammonium-propane (DOTAP) or 1,2-dioleoyl-sn-glycero-3-phospho-(1'-rac-glycerol) (DOPG) were used to give the vesicles a positive or a negative net charge. The vesicles were then incubated with the polymer substrates for up to 24 h. The results are shown in figure 5.3. It can be seen that for the case of DOPG no significant adsorption of vesicles to the sur-

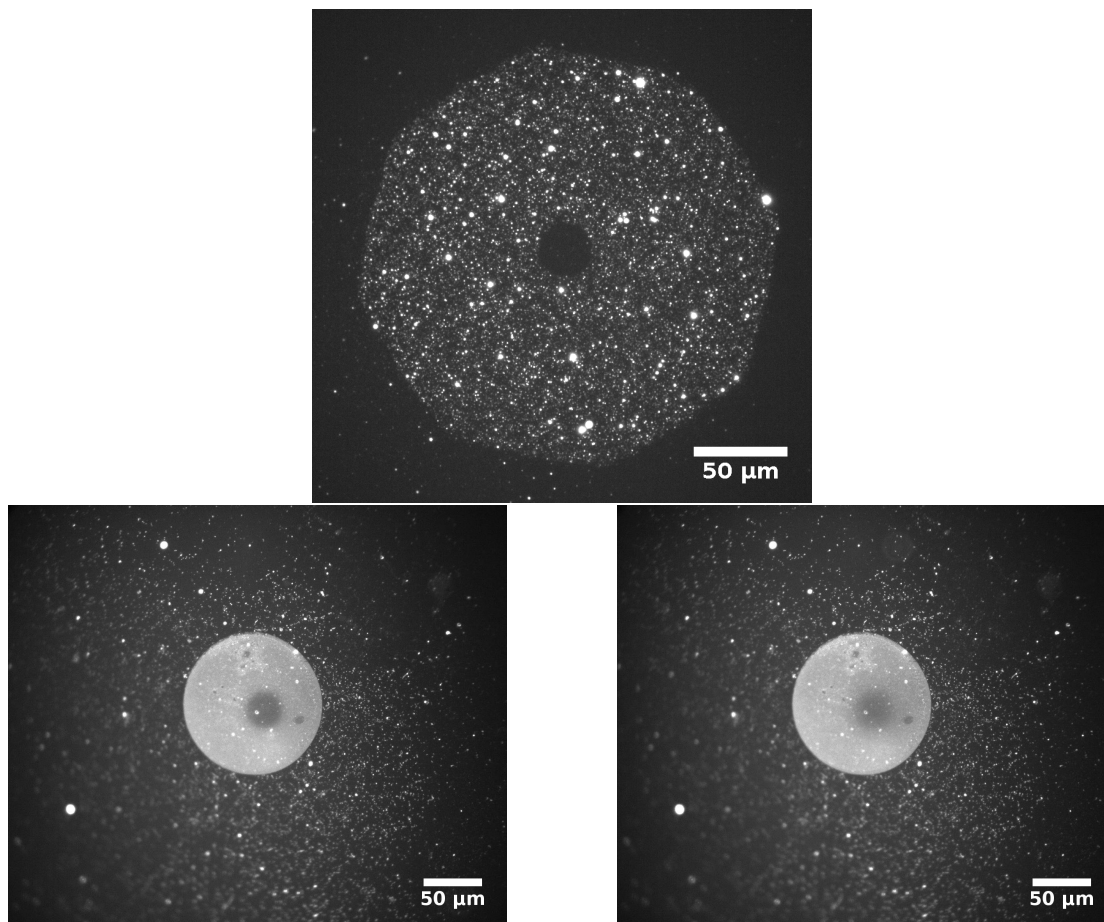


Figure 5.2: Results of vesicle fusion experiments using POPC only in vesicles on a PMPC brush. Vesicles were incubated overnight on the samples and patches like in the bottom to images were observed in few cases, most of the surface was covered in unfused and unruptured vesicles as seen in the top image.

face occurred. In contrast to that, when using DOTAP in the vesicles there are regions of varying density of vesicle coverage visible.

Using charged vesicles, the interaction between the surface and the lipids seems to have increased, especially for the positively charged lipids; but so far the formation of a continuous SLB has not been observed. To increase the attractive forces between the negatively charged vesicles, Ca^{2+} ions were introduced to the solution. It is well known that the two positive charges on the Ca^{2+} can add to the attraction and subsequent fusion of two vesicles (Kataoka-Hamai et al., 2010; Richter et al., 2003; Vequi-Suplicy et al., 2010). In order to promote the fusion of the positively charged lipids, NaCl was dissolved in the buffer solution to increase the shielding between the different charges and reduce the effects of

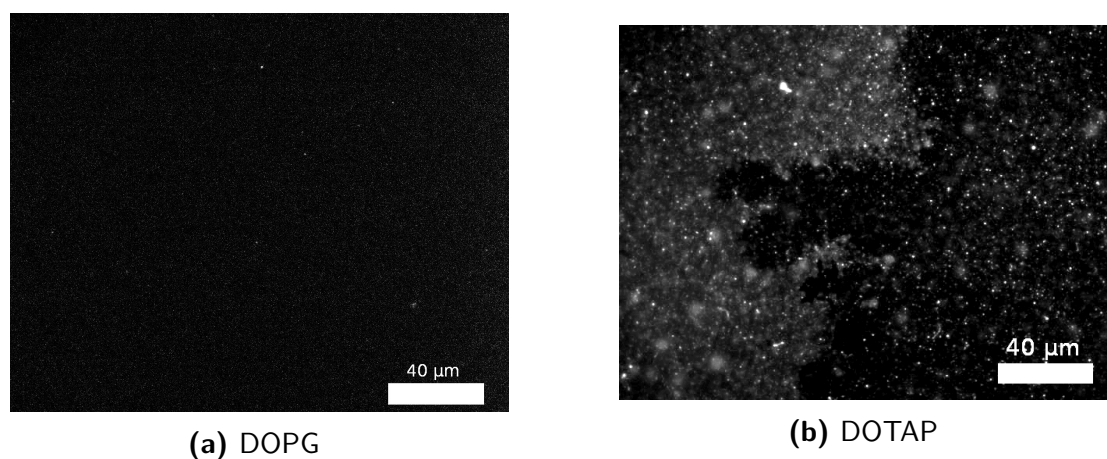


Figure 5.3: Comparison of the results of using the charged lipids DOPG and DOTAP in combination with PMPC supports. DOTAP and DOPG were added to 25 mol% to the vesicles. The dye used was TxRed.

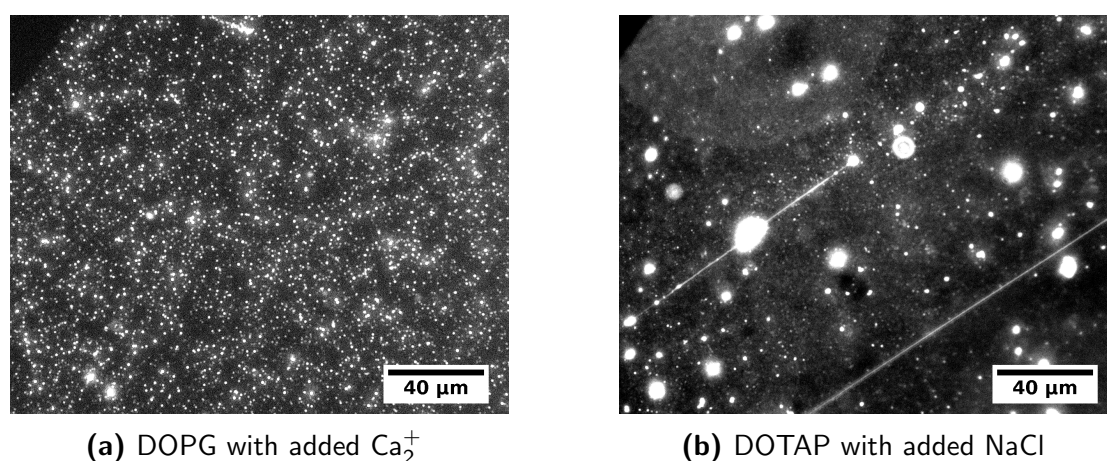


Figure 5.4: Comparison of the results when adding either Ca²⁺ or Cl⁻. Both were added in steps from 10 mM up to 2 M and were incubated for at least 2 h per step. The images shown were taken after incubation with the the strongest ion concentration.

electrostatic repulsion. In figure 5.4 it can be seen that in both cases a difference to the previous results is visible. For the case of vesicles with DOPG, the surface coverage of vesicles has increased, but still there is no bilayer formation visible. In the case of the vesicles partially made from DOTAP, the surface shows a much higher coverage of vesicles and regions which indicate a combination of SLB formation and vesicles adsorbed to the surface. In addition to that, more, larger vesicles and lipid tubules are visible now, showing that the reduction of electrostatic repulsion increases the probability of vesicles fusing to form larger aggregates.

Since the experiments using DOPG had so far produced only vesicles adsorbed to the surface and no bilayer formation has been achieved, not even in small regions of a sample, further efforts focussed on using vesicles with a combination of DOTAP and POPC. The previous results showed that bilayer formation under the conditions tested seemed possible, but not favourable and no continuous SLB was formed so far.

Freeze Thaw

To increase the possibility of vesicle fusion and rupture, the samples with the vesicle solution were also exposed to up to five freeze thaw cycles. This method is normally used in vesicle preparation to homogenise the vesicles (Jackman et al., 2014; Morigaki et al., 2012; Richter et al., 2003; Schönherr et al., 2004). Especially when using charged lipids in combination with an uncharged lipid species, it can be of importance to have an even distribution of charges between the vesicles. The flow cell containing both the vesicle solution and the polymer substrate, was then exposed to several freeze thaw cycles where it was cooled down to -20°C and then heated up to room temperature.

The freeze thaw cycles significantly increased the amount of ruptured vesicles. As can be seen in figure 5.5a and figure 5.5b, the vesicles started rupturing after a single freeze thaw cycle and patches of bilayer were formed on the PMPC support. Interestingly, the SLBs consisted not only of single layers, but also of double layers of bilayers. The intensity profile in figure 5.5c shows that most of the patches are single layers and the step like increase when the second bilayer is crossed. The position of the line profile is marked in yellow in figure 5.5b.

More freeze thaw cycles led to further coverage of the surface with SLBs. The influence of multiple freeze thaw cycles is shown in figure 5.6. After three freeze thaw cycles the patches of lipid became much larger and, as seen in figure 5.6a and figure 5.6b, recovery can be seen in fluorescence recovery after photobleaching (FRAP) experiments. It can also be seen that the mobile fraction

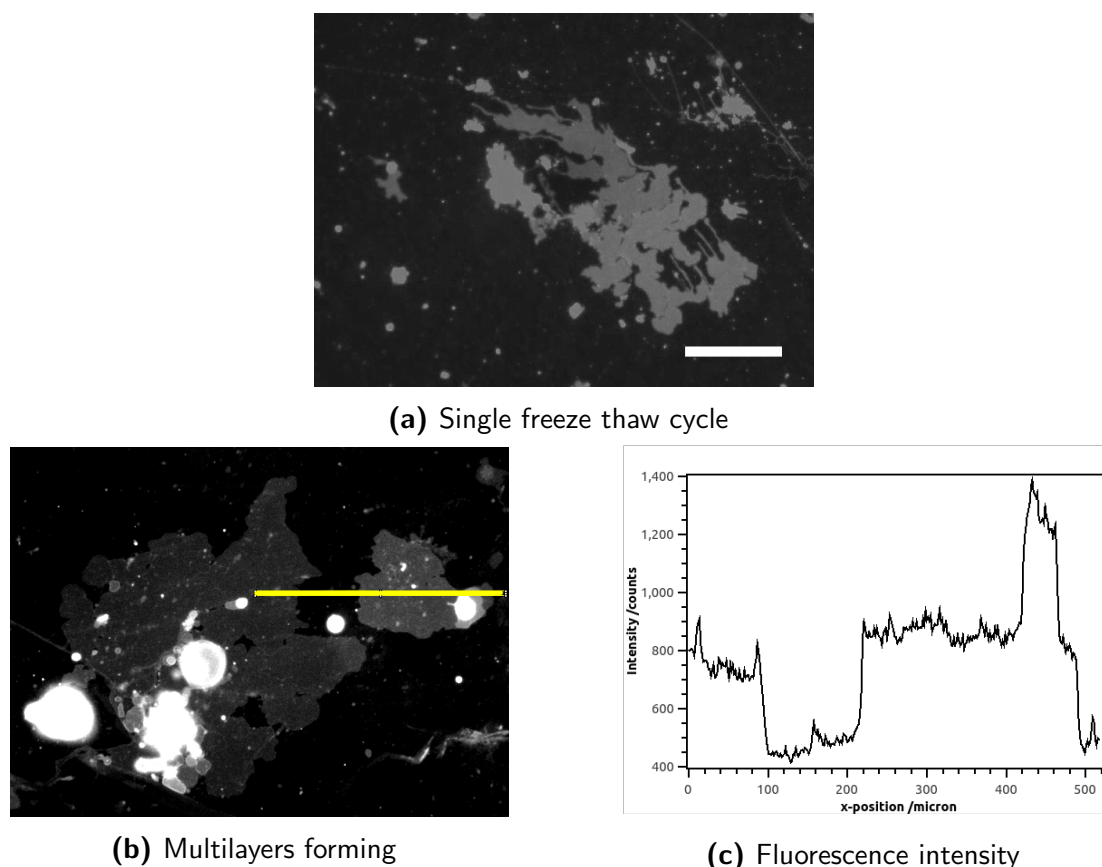


Figure 5.5: Patches of an SLB on a PMPC support after a single freeze thaw cycle. The intensity profile (taken from the yellow line) shows that most of the patches are single layers but that double bilayers are also present. The scale bar is $40\ \mu\text{m}$.

is rather low; even 5 min after the bleaching pulse there is still a significant amount of bleached molecules in the initial bleaching region. The diffusion coefficient obtained from this experiment was $0.2\ \mu\text{m}^2\ \text{s}^{-1}$, which is lower than what would be expected from an SLB of good quality but is also higher than what would be expected from vesicles rolling on the surface.

When the amount of freeze thaw cycles is further increased to five, the coverage of the SLB over the surface of the PMPC becomes almost complete (see figure 5.6c). From the image taken 5 min after the bleaching occurred, it can also be seen from the line profile in the inset that there still is a significant immobile fraction. This is also reflected in the recovery graph shown in figure 5.6e where it can be seen that the mobile fraction is approximately 80%. The diffusion coefficient for this experiment was $0.5\ \mu\text{m}^2\ \text{s}^{-1}$. Despite this method showing some progress towards the formation of SLBs on PMPC, there is also a significant

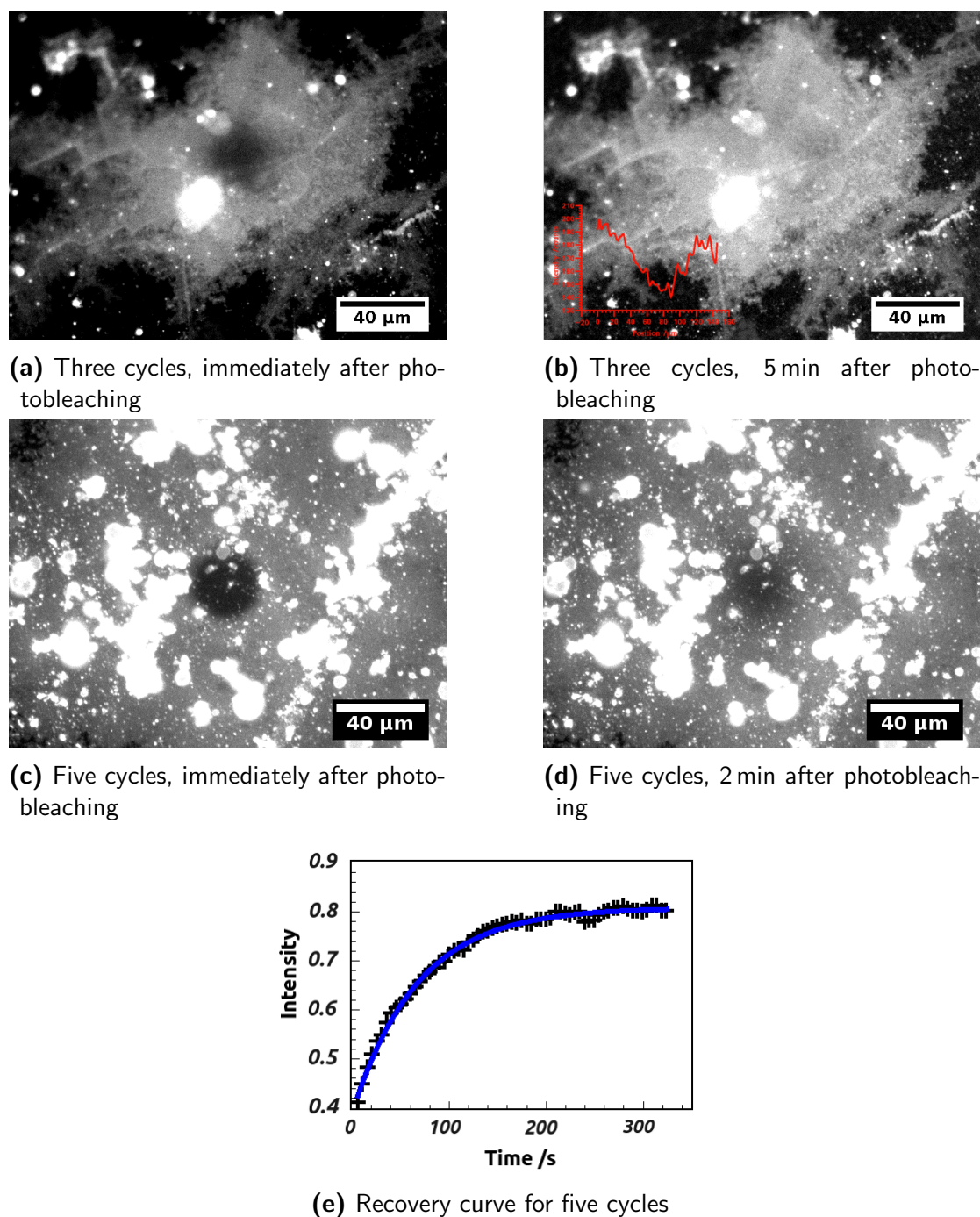


Figure 5.6: Fluorescence images immediately after photobleaching and five minutes after bleaching for different numbers of freeze-thaw cycles. The inset in 5.6b shows the intensity profile across the bleach spot showing that recovery has occurred but that an immobile fraction is present. The bottom image shows the recovery curve for five freeze-thaw cycles.

amount of vesicles attaching to the surface. The vesicles were immobile and could not be removed through rinsing, even when the salt concentration of the buffer was varied to induce osmotic shock.

Another interesting effect when freeze thawing SLBs on PMPC is the changing of the size of the lipid bilayer patches during imaging. This effect was especially visible when FRAP experiments were carried out. A possible explanation for this effect is that the heat of the focussed white light on the sample results in an increased free energy and therefore increased bilayer formation. The process of bilayer growth can be seen in figure 5.7. The growth process of the SLB becomes especially clear when the first image is subtracted from the final image, as shown in figure 5.7e. It can be seen that the growth of the SLB is on the edges of existing bilayer regions and that these regions expand. The region of biggest growth is the centre of the image, where the FRAP experiment delivers most of its energy (i.e. heat) and that the areas away from this region only experienced little growth. This indicates that the formation of SLBs on PMPC needs more driving force than the usual formation of SLBs on solid supports or self-assembled monolayers (SAMs).

Spin Coating

Despite these experiments showing progress towards the formation of SLBs on biocompatible surfaces, the method still needed improvement so that more continuous SLBs are formed on the substrate. Another method of depositing SLBs onto solid substrates is spin coating lipids from solvents. Several solvents can be used for this process as long as they evaporate quickly and dissolve lipids easily. It was shown in the literature, that the number of SLBs deposited on a surface can be modified by the spin speed, the solvent used and the concentration of lipid in the solvent (Mennicke and Salditt, 2002). Here, the lipids chosen were 75 mol% POPC and 25 mol% DOTAP in isopropanol, spun at 3000 rpm from a concentration of 1 mg mL^{-1} . This is expected to result in the formation of a single SLB without any multilayers.

After the spin coating a dry layer of lipids is obtained on the PMPC surface. When this layer is kept dry and is not allowed to rehydrate, not even from

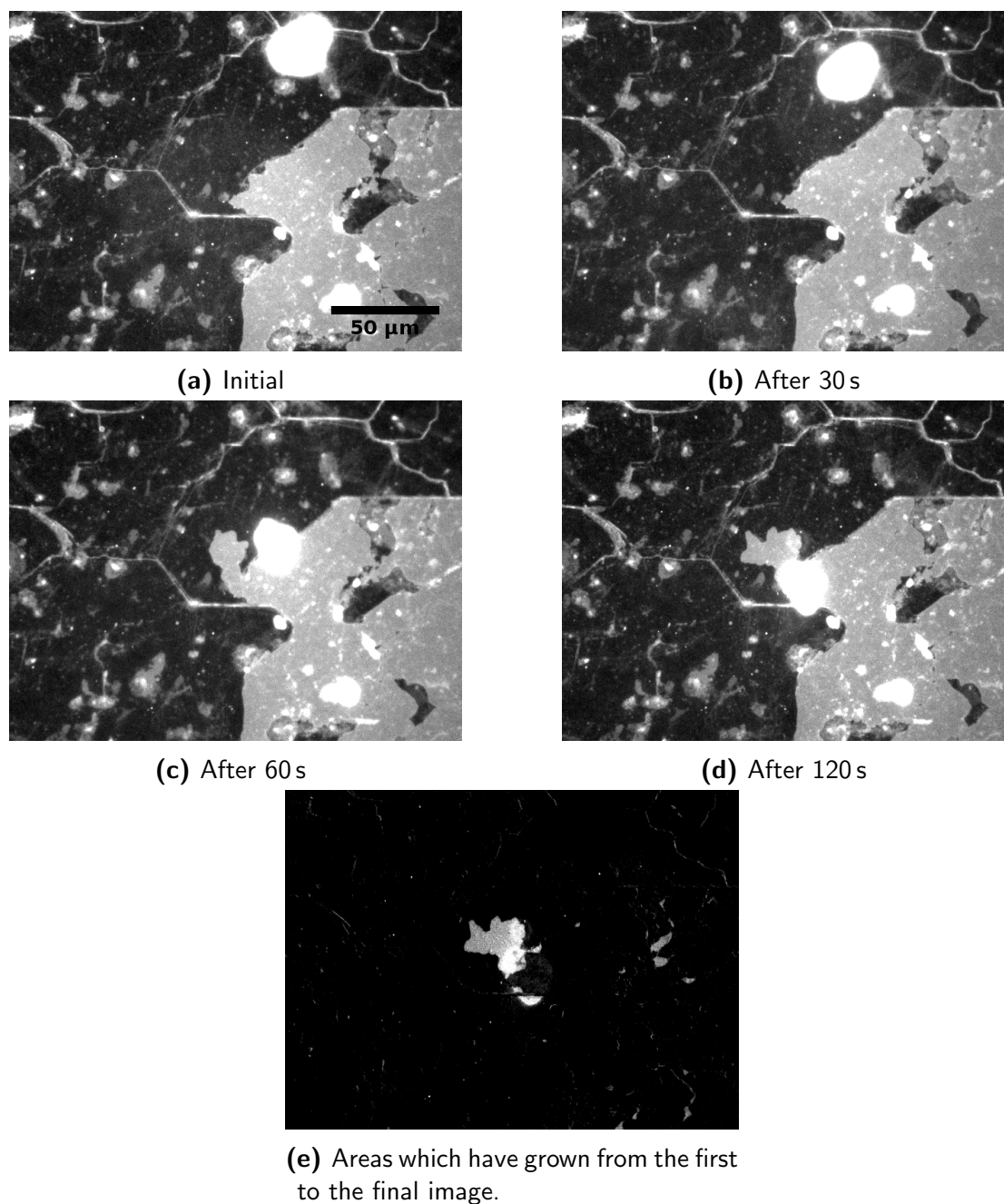


Figure 5.7: Growth process of an SLB produced by freeze thaw cycles of vesicle solution on PMPC. The final image shows the areas of growth by showing only the difference between the first and the final image produced by subtracting the first image from the last.

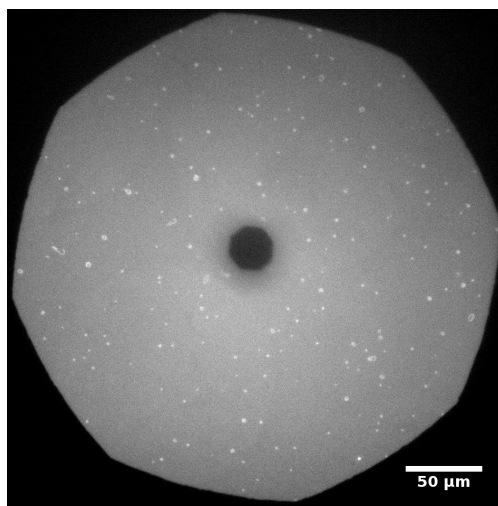


Figure 5.8: Spin coating of fluorescently labelled lipids onto a PMPC support. The lipid is dry and shows good coverage of the substrate. Since the sample has not been rehydrated there is no mobility in the lipid layer and the bleach spot shows the characteristic octagon shape of an immobile layer bleached through an aperture with the same shape.

humidity from the surrounding air, no bilayer formation is obtained. The lipids stay on the surface in a disordered, immobile arrangement. When bleaching a part of the lipid layer formed on the support, no recovery is seen. Figure 5.8 even shows the octagon structure of the aperture used for the bleaching. This means that no diffusion happens, as the edges should start smearing out, even when only slow diffusion occurs.

In order to obtain an SLB from the adsorbed lipids, the layer has to be rehydrated. When the flow cell was flushed with phosphate-buffered saline (PBS) solution, the lipids started to come off the surface and leave behind a layer of lipids with many defects. The defects obtained when rehydrating the lipid are seen in 5.9. In the central regions, the lipids have been bleached for a FRAP experiment. In the second image, a small amount of recovery can be seen but the majority of the lipids is still immobile.

A similar behaviour to the growth of the SLB when using the freeze thaw method (see figure 5.7) can be seen in the defects after the rehydration of spin coated lipids on PMPC. Many small defects occurred upon the rehydration

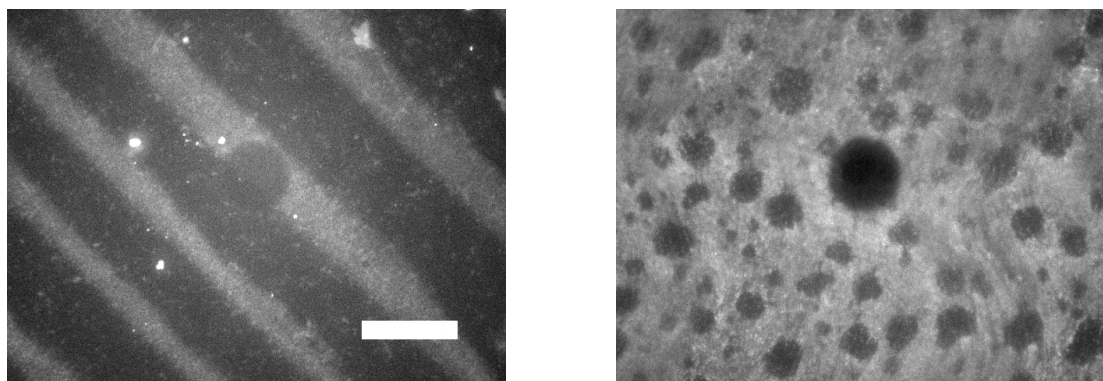


Figure 5.9: Defects obtained when rehydrating lipids adsorbed onto PMPC using spin coating. Despite the rehydration, the layer is still immobile. The scale bar is 40 μm and both bottom images are to the same scale.

of the lipids on PMPC. Before the FRAP experiment, the defects are evenly distributed over all of the sample (see figure 5.10). Even in the image directly after the bleaching, the “repair” of the bilayer can be seen, the dark region in the centre is more continuous than would be expected from an SLB with many defects. When the recovery is completed in the final image, the central region became a single SLB. This shows that the attribution of the repair of the bilayer to the added energy from heating the bilayer during the bleaching of the FRAP process is a potential explanation for the healing and growth of bilayers formed on PMPC.

To improve the quality of the SLB formed after spin coating and rehydrating, the process of rehydration was carried out very slowly. Initially, only the bottom of the flow cell, which was not in contact with the PMPC, was brought into contact with water. This led to a higher moisture in the atmosphere of the flow cell from which the lipids on the surface accumulated enough liquid to form an SLB. The FRAP experiment shown in figure 5.11 shows that this led to a mobile bilayer with almost no defects.

In order to accommodate proteins in the SLB, full hydration has to be achieved. Therefore, after the slow hydration from the humidity from the atmosphere full hydration has to be achieved. This was done by slowly ($20 \mu\text{L min}^{-1}$

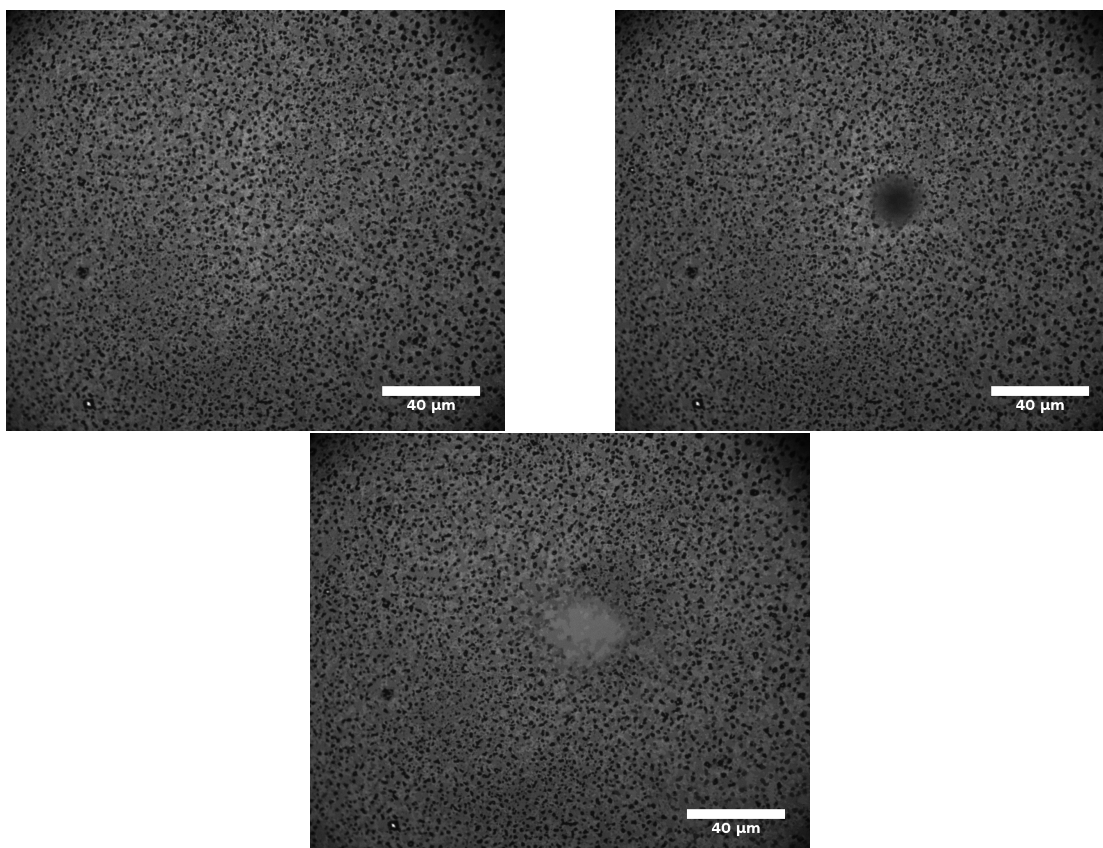


Figure 5.10: Fluorescence images from a FRAP experiment on a spin coated, rehydrated lipid layer on PMPC. The images show the before, immediately after bleach and the recovered image. The SLB is mobile and in addition to the mobility shows the previously seen growth effect and heals in the region which has been bleached.

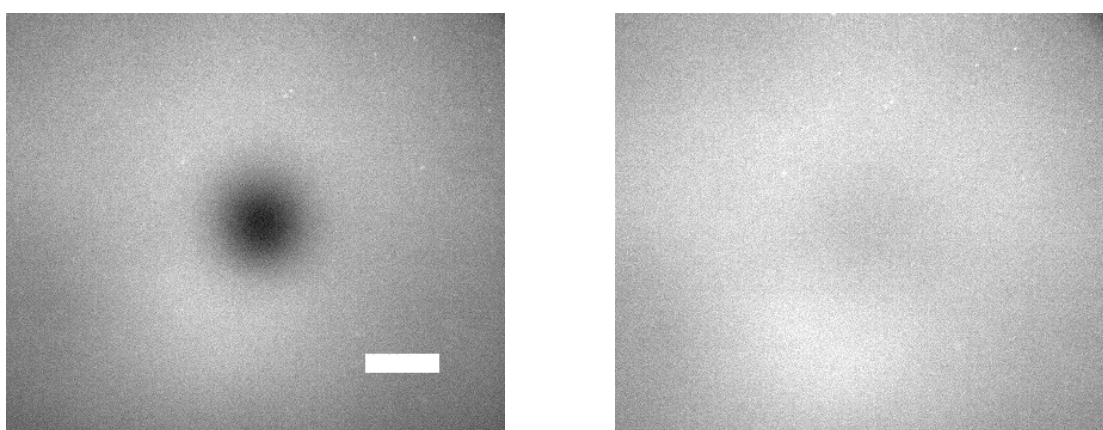


Figure 5.11: Lipid bilayer on PMPC formed by rehydration using moisture from the atmosphere. The left image was taken directly after the bleaching while the second image was taken 60 s later. The images show almost full recovery in a short time indicating good mobility after the gentle rehydration process. The scale bar is 30 μm.

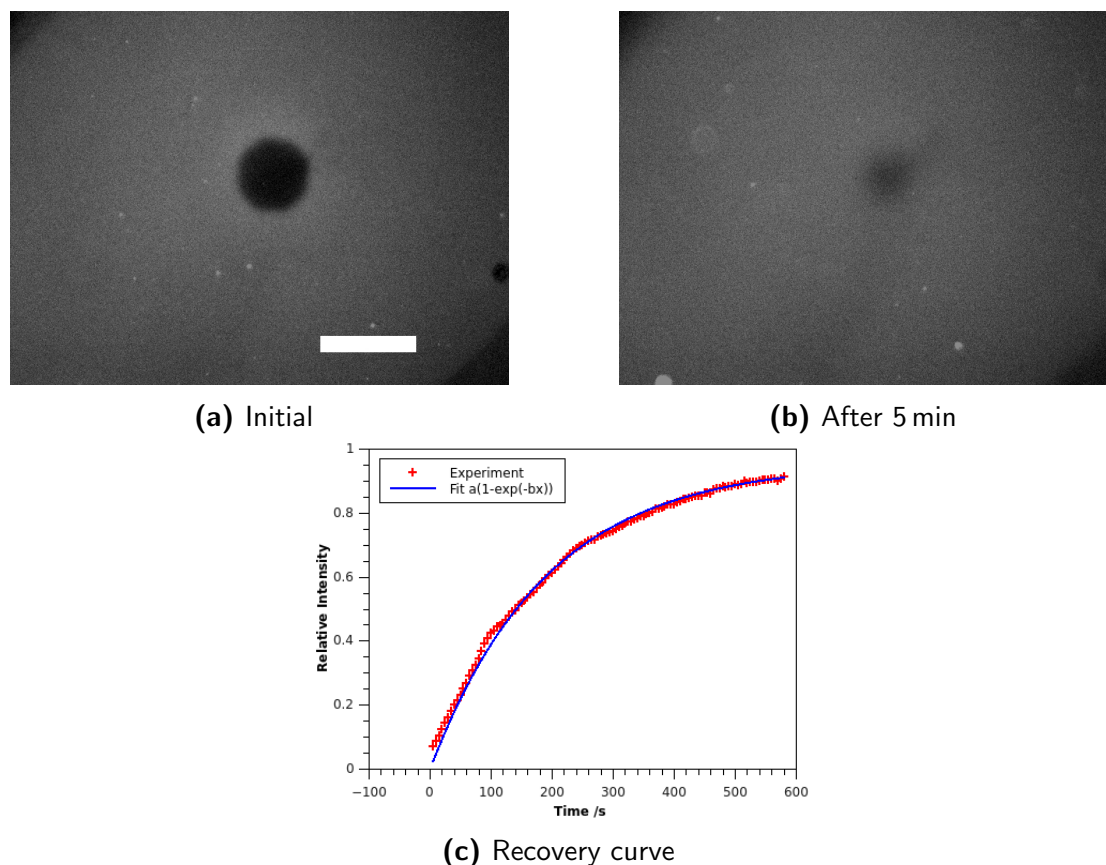


Figure 5.12: Fully rehydrated SLB on a PMPC support. The FRAP experiment showed almost full recovery and the bilayer showed good mobility. The scale bar is $40\ \mu\text{m}$. The diffusion coefficient obtained from the fit was $1.1\ \mu\text{m}^2\ \text{s}^{-1}$ indicating the formation of mobile SLB on the polymeric support.

flow speed) adding buffer to the flow cell. The slow rehydration lead to a defect free SLB. The diffusion coefficient obtained from a FRAP experiment was $1.1\ \mu\text{m}^2\ \text{s}^{-1}$, which is of the same order as what we expected from an SLB on a glass support (see figure 5.12).

This shows how spin coating of lipids can be used to obtain a defect-free SLB on a PMPC support. This method can be controlled to achieve the formation of a single SLB without the formation of multilayers by choosing the concentration and spin speed carefully. The SLB showed good mobility and over 90 % mobile fraction.

Short-Chain Lipids

Using spin coating of lipids onto the solid support has shown to be a viable method for the formation of SLBs. This method gave good results but does not allow for the incorporation of membrane proteins directly as these would denature in the solvent needed for spin coating. The proteins could still be incorporated into the SLB using vesicle fusion to the pre-existing SLB (Karatekin and Rothman, 2012; Trépout et al., 2007). A more direct method for the incorporation of proteins into the SLB would be preferable over the indirect method of bilayer formation and subsequent vesicle fusion. Therefore, short chain lipids were introduced to reduce the energy needed for the formation of SLBs. The short chain lipids act like a detergent and enhance the formation of small patches of bilayers as the energy required for bilayer formation is reduced. The short-chain lipids aggregate at the edges of the bilayer patch and significantly reduce the energy associated with the formation of a bilayer edge compared to the use of long chained lipids only (Hauser, 2000; Morigaki et al., 2012).

Here 1,2-hexanoyl-sn-glycero-3-phosphocholine (DHPC-C6) was chosen as a short-chain lipid. It was used at a concentration of 5 mmol dm^{-3} in the vesicle solution. The solution containing the DHPC-C6 was then rinsed out. This leads to slow detergent removal where more and more of the detergent molecules leave the SLB and are dissolved in the solution. The detergent concentration in the solution is constantly driven out of equilibrium with the SLB and therefore more and more detergent molecules are removed from the SLB. This method has been used with other detergents as well and can be used to incorporate proteins into an SLB (Bayburt, 2003; Kataoka-Hamai et al., 2010; Ranaghan et al., 2011).

Using this method resulted in the formation of patches of varying sizes of SLBs on the PMPC. As can be seen in figure 5.13, the patches formed were very clean patches of SLB without vesicles attached to them. The SLB showed a high

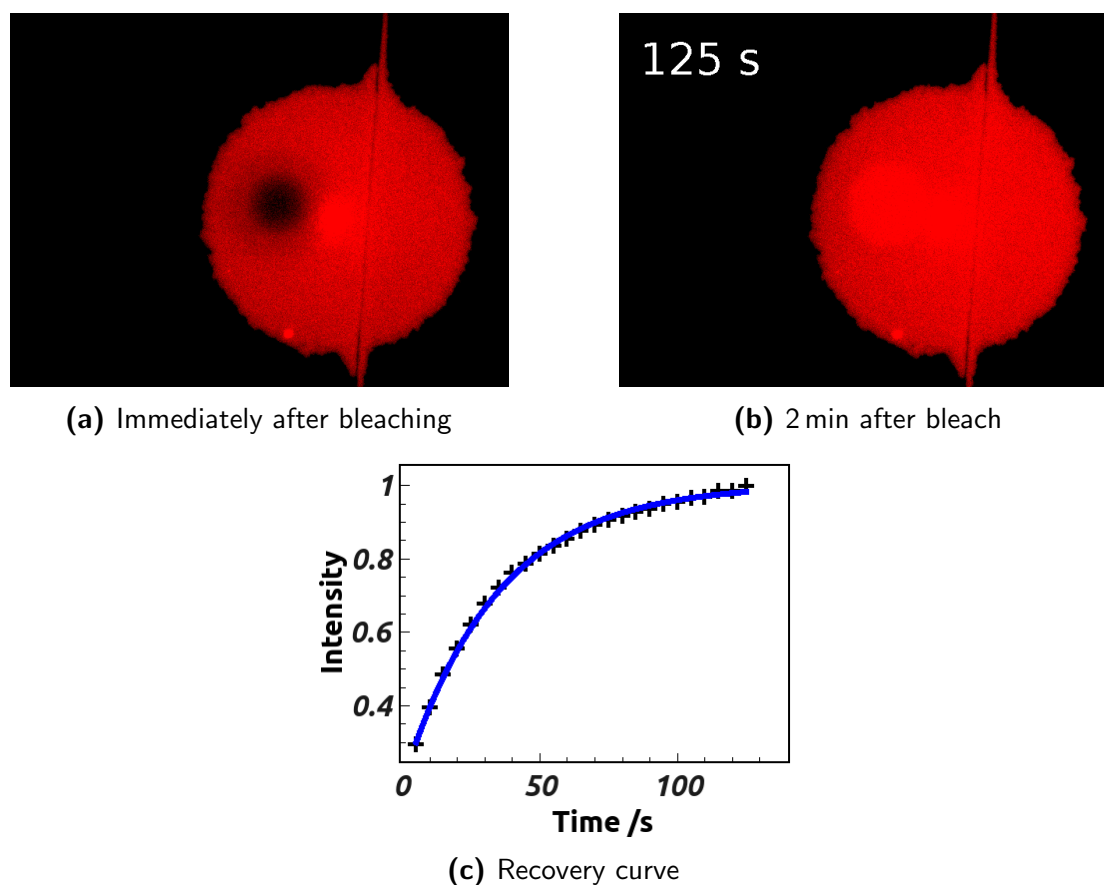


Figure 5.13: Bilayer patches formed using DHPC-C6 at a concentration of 5 mmol dm^{-3} and the recovery curve of the associated FRAP experiment. The SLB shows good mobility in the patch and the final intensity is close to unity.

mobility and almost no immobile fraction, as shown in the recovery curve of the FRAP data.

Longer rinsing with solution containing lower concentration of DHPC-C6 did not increase the surface coverage of the patches. Therefore, the substrate together with the lipid/DHPC-C6 solution were heated up to 50°C to increase thermal energy and remove the short-chain lipids from the patches. The heating was carried out in a sealed atmosphere at 50°C for at least 3 h. This avoided the drying out of the flow-cell while it was heated up, and ensured the full flow-cell having an increased temperature.

The heating of the samples lead to full coverage of the surface with SLBs. The results can be seen in figure 5.14. The lipids used here were again consisting of 25 mol% DOTAP and 75 mol% POPC. The result was a good quality SLB

with diffusion coefficients around $1 \mu\text{m}^2 \text{s}^{-1}$, as can be seen from the recovery curve (see figure 5.14e) with mobile fractions greater than 80 %. Although the quality of the bilayer was good using this method, the defects on the PMPC became evident, when a bilayer of good quality would otherwise form. As seen in figure 5.14d, the surface of the PMPC support has many microscopic scratches. The scratches are due to the production process and inter-sample variability was very high.

The results shown here present a viable method to deposit SLB from an aqueous solution directly onto a PMPC support only using a heating step at 50°C . Such a heating step may not be ideal for all membrane proteins but is more likely to result in functional protein incorporation than spin coating from a solvent.

5.1.2 PCysMA

A second polymer has also been investigated for the formation of SLBs on a polymer support. Despite the result of PMPC being promising the substrates proved to be difficult to produce to a high quality, as needed for bilayer formation and the conditions needed were very specific. Therefore, another polymer, poly(cysteine methacrylate) (PCysMA) was investigated for its ability to support SLB formation. The structure of PCysMA is shown in figure 5.15. As PCysMA exhibits a negative surface zeta potential of around -10 mV at physiological pH (Alswieleh et al., 2014), this polymer support was also combined with positively charged lipids.

Vesicles were formed using 25 mol% DOTAP and 75 mol% POPC and then incubated with the PCysMA polymer surfaces. The vesicles and the polymer surfaces were then heated to 50°C for at least 1 h. This resulted in the formation of clean SLBs on the surfaces. The bilayer can be seen in figure 5.16a and figure 5.16b. The data from the FRAP experiments shows a diffusion coefficient of

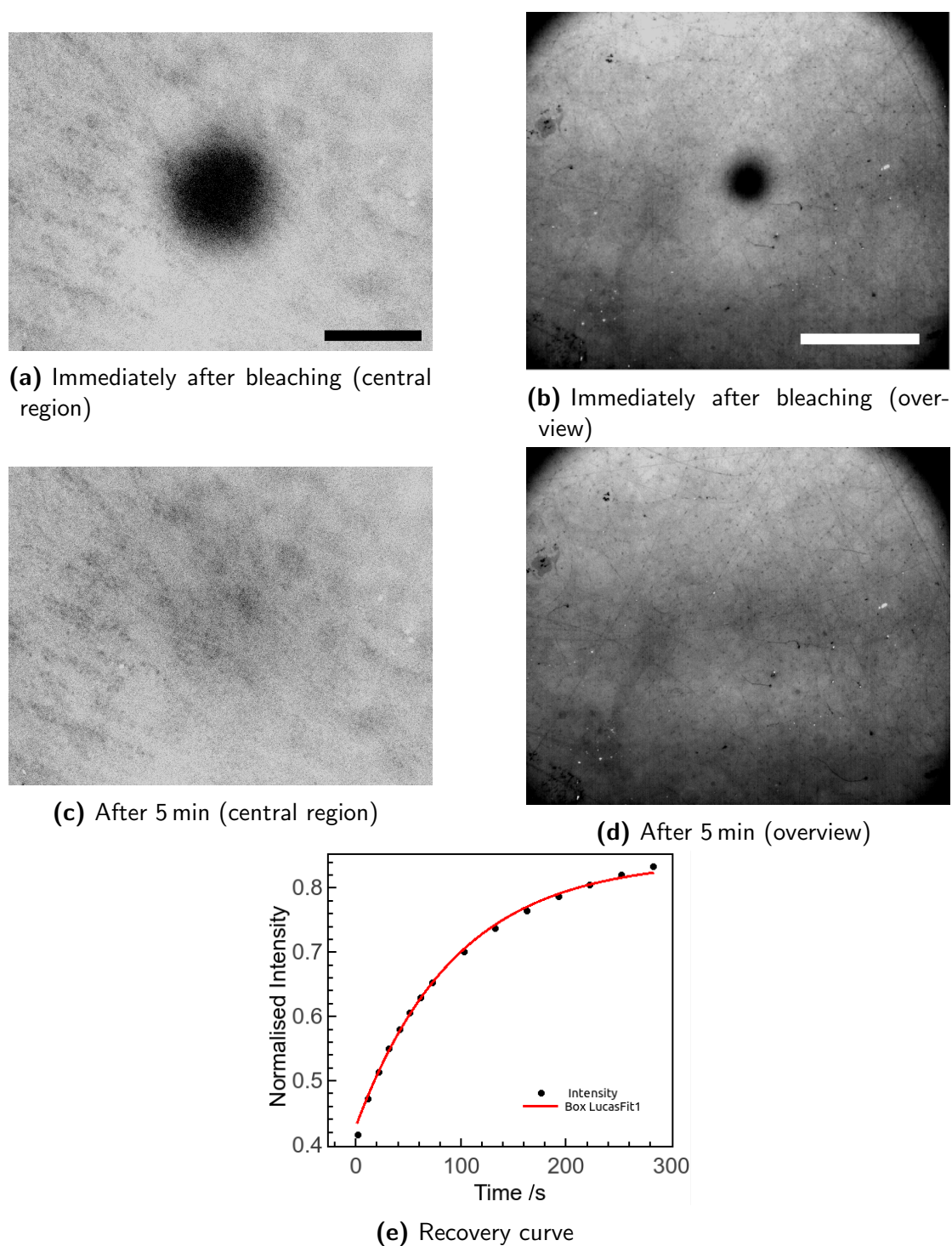


Figure 5.14: Zoom in and overview of SLB formation on a PMPC support. A heating procedure was used to form the SLB. The scale bars are $40\ \mu\text{m}$ (left) and $100\ \mu\text{m}$ (right). The close up view shows the recovery of the bleach spot area while the overview shows the defects occurring on a larger scale. A diffusion coefficient of $1\ \mu\text{m s}^{-1}$ was obtained from the fit (bottom).

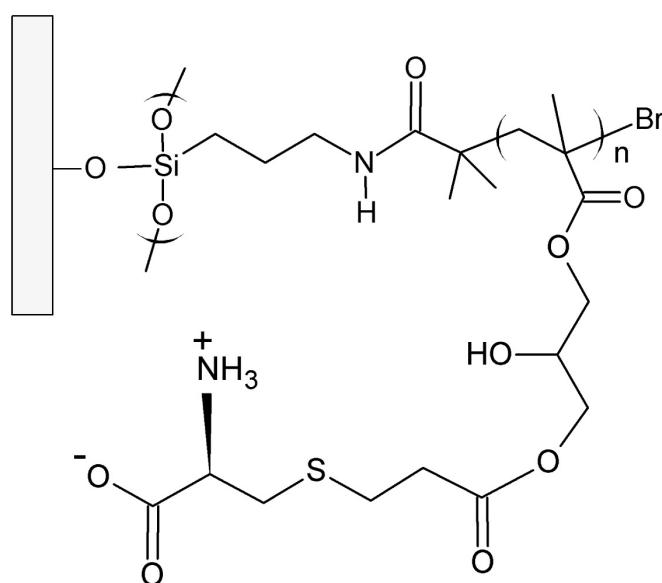


Figure 5.15: Structure of PCysMA, which was used as a polymer support.

$0.9 \mu\text{m}^2 \text{s}^{-1}$ which is within the expected value of an SLB on a glass surface. Although a polymer support may be expected to have a higher diffusion coefficient than an SLB formed on a glass surface, this was not seen here. A reduced mobility of the lipids can be explained with the increased interaction of the SLB with the underlying polymer support as both of them are charged and electrostatic interactions can play a major role here.

In order to develop a read-out method for the light harvesting proteins in SLBs, the PCysMA was not just grown on glass surfaces but also on a gold surface. The conductive substrate allows for electric read-out methods to be applied to the bilayer and the containing proteins. Here, electrochemical impedance spectroscopy (EIS) was used (see section 2.4) to monitor potential SLB formation on PCysMA grown on conductive surfaces. As before, these surfaces were incubated with 25 mol% DOTAP and 75 mol% POPC vesicles, and were heated up to 50°C for 1 h. The EIS spectra were recorded for the bare gold, gold with PCysMA, and gold with PCysMA after it has been heated up for 1 h.

The results in figure 5.17 show a decrease in the impedance when comparing the bare gold and the PCysMA results as it would be expected for the addition

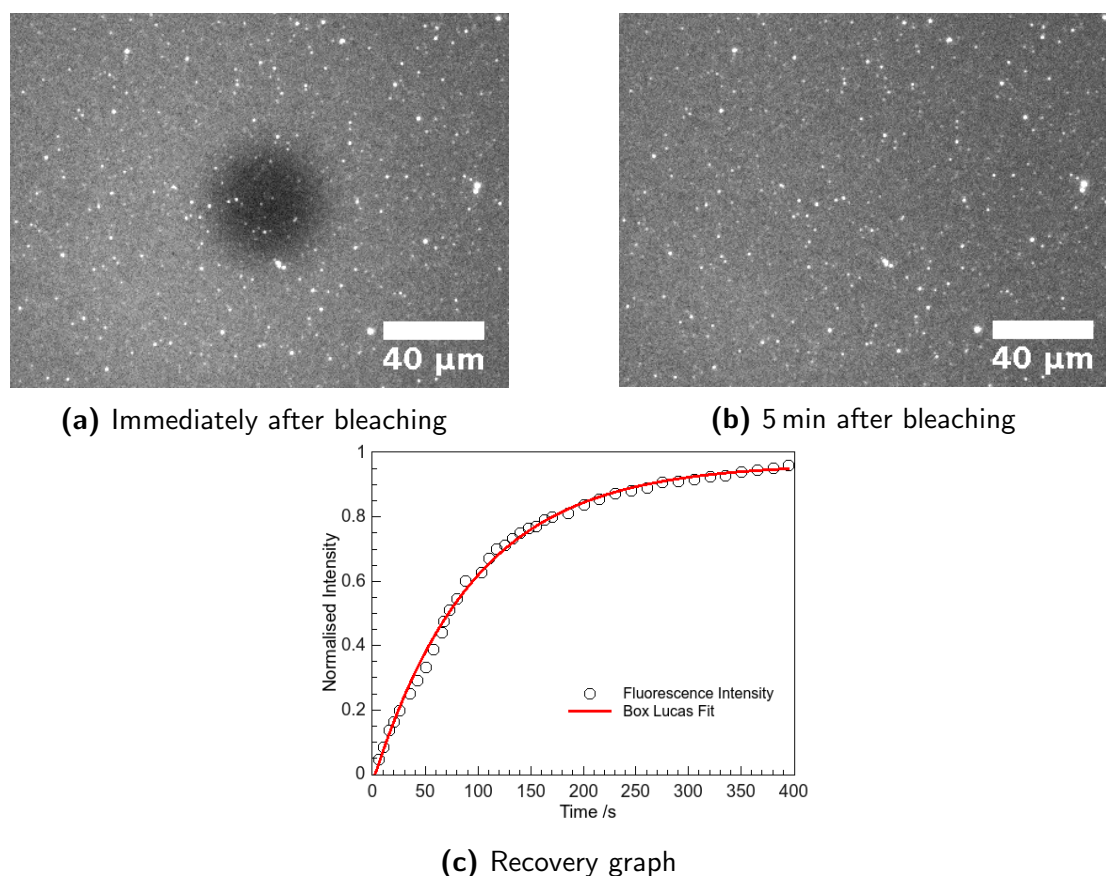


Figure 5.16: Formation of an SLB on a PCysMA surface using elevated temperature and the recovery graph of a FRAP experiment. The fluorescence images show the formation of an SLB with a diffusion coefficient obtained from the fit of $0.9 \mu\text{m}^2 \text{s}^{-1}$. In addition to the bilayer several unruptured vesicles can also be seen in the fluorescence images.

of an extra layer on a surface. After the addition of vesicles in solution a small, additional decrease in the impedance occurred (cyan triangles). This can be attributed to the further adsorption of material. After heating the sample to 50°C for 1 h, impedance increased significantly and almost reached the value of the initial gold layer. An increase in the measured impedance does not agree with the formation of an SLB; if one was formed, a layer with a capacitance of approximately $0.5 \mu\text{F cm}^{-2}$ to $1 \mu\text{F cm}^{-2}$ for the added SLB would be expected. To understand the behaviour of the polymer and the added vesicle solution, any possibly lipids attached to the PCysMA were removed by thoroughly washing the surface with isopropanol. The impedance measured after the wash was identical to the data obtained before, indicating that there were no lipids attached

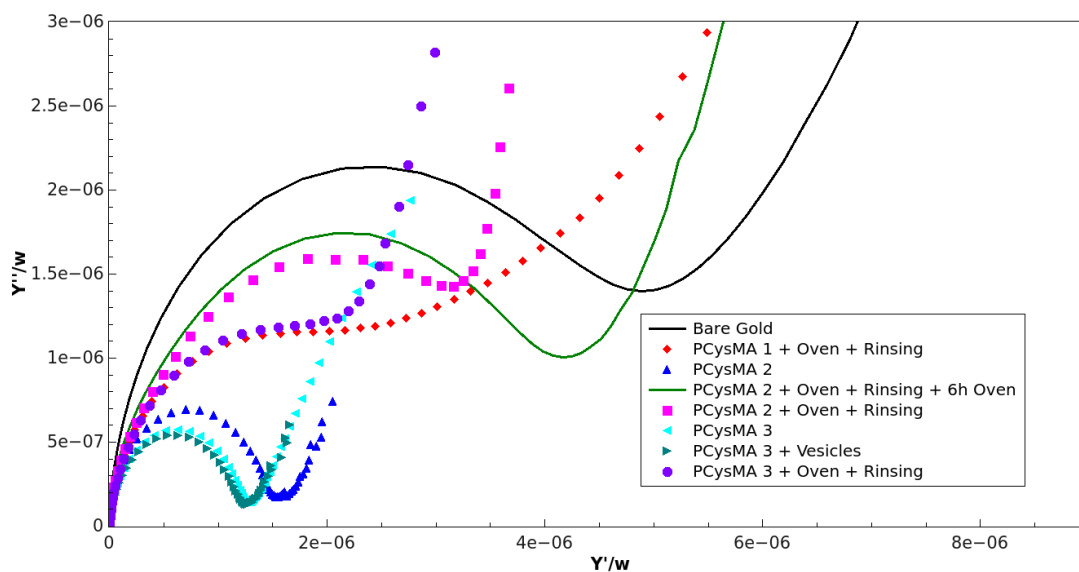


Figure 5.17: Heating of PCysMA with vesicles investigated using EIS for three individual experiments. The electrode area was 0.8 cm^2 . The numbers in the legend refer to different samples showing only small differences between the samples.

to the polymer. This assumption was confirmed when the polymer on gold was heated to 50°C without lipids in the solution. The data obtained from this also agreed with the previously recorded data. Accordingly, the heating step does not seem to form an SLB when PCysMA is grown on a gold surface. On the contrary, the data suggests that the heating step removes the polymer from the surface and thus, the impedance curve moves away from the curve obtained from the polymer towards the one obtained from a clean gold surface.

Since the heating method seemed to remove the PCysMA from the surface instead of forming a supported SLB, the method for bilayer formation on a conductive surface was changed. Instead of using lipid vesicles on the surfaces, a detergent, n-Dodecyl β -D-maltoside (DDM), was added to the lipid solution. The concentration of DDM was 10 mg ml^{-1} and it was always ensured that the solution of multi-lamellar vesicles (MLVs) became clear when adding the detergent showing that the MLVs have broken up and are solubilised through the detergent. The solution was then incubated on the polymer support for at least 1 h and slowly rinsed out. The slow rinsing process should remove

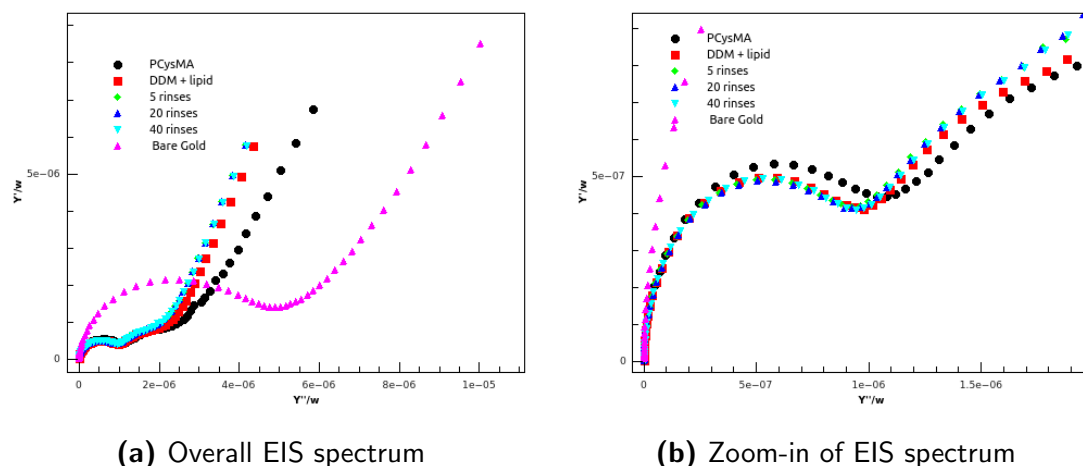


Figure 5.18: Impedance spectrum obtained for the detergent removal method on PCysMA. In this case the impedance remains low after the addition of the lipids which is in contrast to what was seen after the incubation and heating steps in 5.17.

the detergent and lead to SLB formation similar to the process described in section 5.1.1.

As can be seen from figure 5.18, the impedance after the addition of lipids with a detergent remained in the same region as the PCysMA on its own. This shows that in this case the polymer is not removed by the deposition method of the lipids. Despite the method not removing the polymer from the surface, it also shows no clear indication of bilayer formation. The impedance drops slightly after 40 exchanges of 80 % of the liquid volume. During the exchange of the liquid volume a decrease in the recorded impedance can also be seen, this indicates that the lipids are forming a more sealing layer as the detergent is slowly washed out.

5.1.3 Polyethylene Glycol

Another method of forming SLBs on a polymer support is the use of polyethylene glycol (PEG). Pegylated lipids are commercially available and PEG is a well studied and biocompatible polymer (Karatekin and Rothman, 2012). When pegylated lipids are used, the SLB will have a polymer cushion underneath the

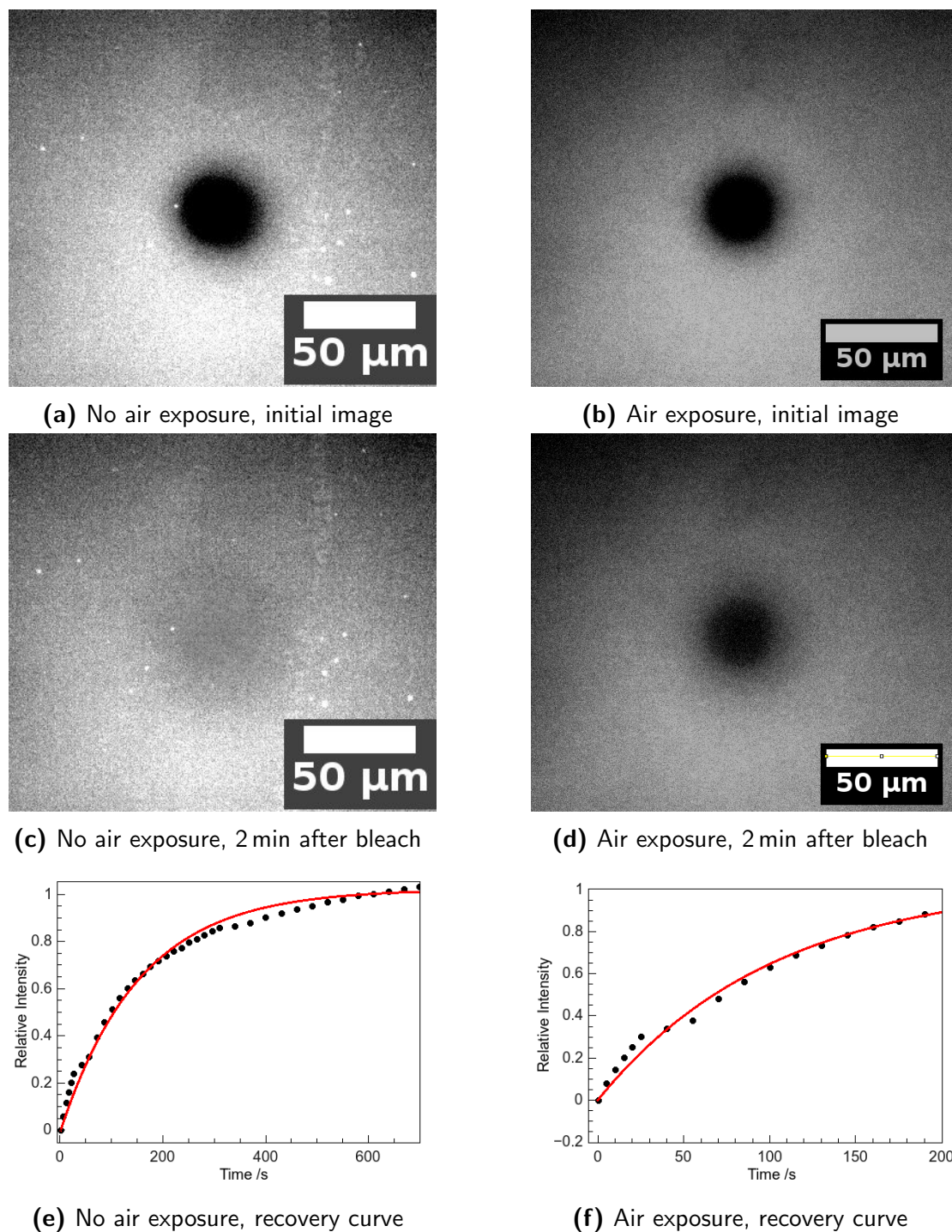


Figure 5.19: Different conditions of a PEG supported bilayer: before (left column) and after (right column) exposure to air. The images from FRAP experiments and their respective recovery curves are shown. The sample has a diffusion coefficient of $0.8 \mu\text{m}^2/\text{s}$ before the exposure to air and $0.4 \mu\text{m}^2/\text{s}$ after

bilayer and above it. This means that the bilayer will not only be supported by a soft cushion but also has a water retaining layer on top of it.

As can be seen in figure 5.19, the SLB forms when the vesicles are incubated on the surface. When the sample is dried down and rehydrated (figure 5.19b), there are a few defects occurring in the SLB, but the sample is still mostly covered in an SLB. The FRAP data shows that the diffusion constant for the PEG supported SLB has a mobility of $0.8 \mu\text{m}^2 \text{s}^{-1}$ when kept hydrated and a lower mobility of $0.4 \mu\text{m}^2 \text{s}^{-1}$ when the SLB is exposed to air and subsequently rehydrated. The mobile fraction in both cases is very high and exhibits values above 80 %. It is higher when the substrate has not been dried out indicating that the quality of the bilayer decreases slightly when the water is removed from the flow cell and later reintroduced.

5.2 SERS as a Read-Out Method

So far fluorescence has been used as the main read-out method for localisation of molecules in lipid bilayers. This method is advantageous because of the ease of use and the inexpensive equipment and material that is needed. The disadvantages of fluorescence microscopy are that it does not give information about the molecules which are surrounding the fluorescent molecule and that adding a fluorescent of around the same size as the molecule investigated can significantly change the properties of the molecule. Therefore, a label-free method would be advantageous for many applications. Raman spectroscopy offers the aforementioned advantages but requires, as discussed in section 2.8.2, a lot of molecules to give good signal to noise. An improvement can be made, when SERS is used. This method requires modified substrates but can give significant enhancement over bulk Raman spectroscopy.

5.2.1 Nanopatterned Surfaces

There are different ways to obtain surface enhancement from different samples. Instead of using rough metal substrates, which give strong enhancement but no

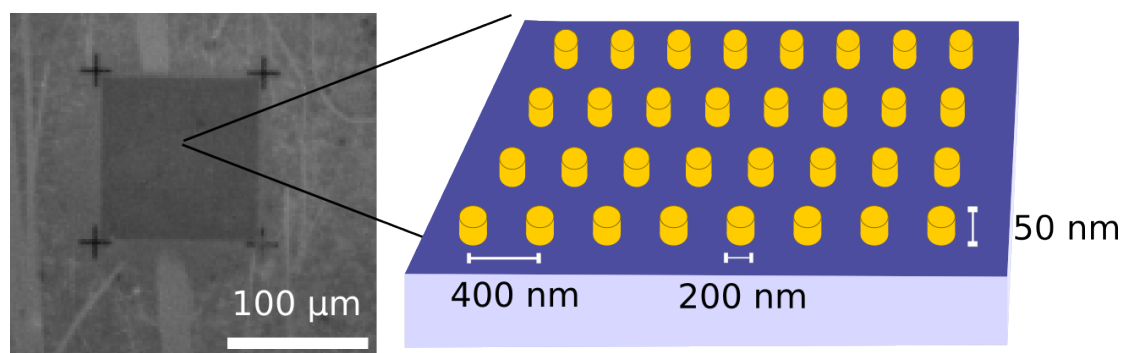


Figure 5.20: Microscope image and schematic of the gold nanodot pattern used. The underlying support is from SiO_2 which was chosen over silicon to prevent fluorescence quenching.

control over the exact resonance, patterned gold on a silicon dioxide substrate was used here. The substrates were either gold nanodots or gold nanorods, similar to structures which have been used before (Felidj et al., 2002, 2003; Grand et al., 2005; Tian et al., 2012). The structures give a controlled resonance, which can be adjusted to the laser wavelength and the scattering of the sample. The structures initially investigated were gold nanodots of 200 nm diameter with a spacing of 400 nm between them, a schematic and a microscope image are shown in figure 5.20.

The substrate was first tested for its capability to support lipid bilayer formation on it, especially in the region with the nanopattern. Since the substrate was silicon dioxide, POPC was used as a lipid, which has been used on glass in several previous experiments and was expected to also work on silicon dioxide. After an SLB was formed from vesicle fusion and a FRAP experiment was carried out on the region with the nanopattern. The recovery was monitored and the change in the variance of the bleach spot was monitored over time. The diffusion coefficient was measured to be $0.9 \mu\text{m}^2 \text{s}^{-1}$, which is lower than for an SLB undergoing free diffusion. A lower value can be expected as the nanopattern hinders the diffusion of the SLB. This shows that an SLB can be formed around a pattern of gold nanodots which should in turn allow for the recording of SERS spectra.

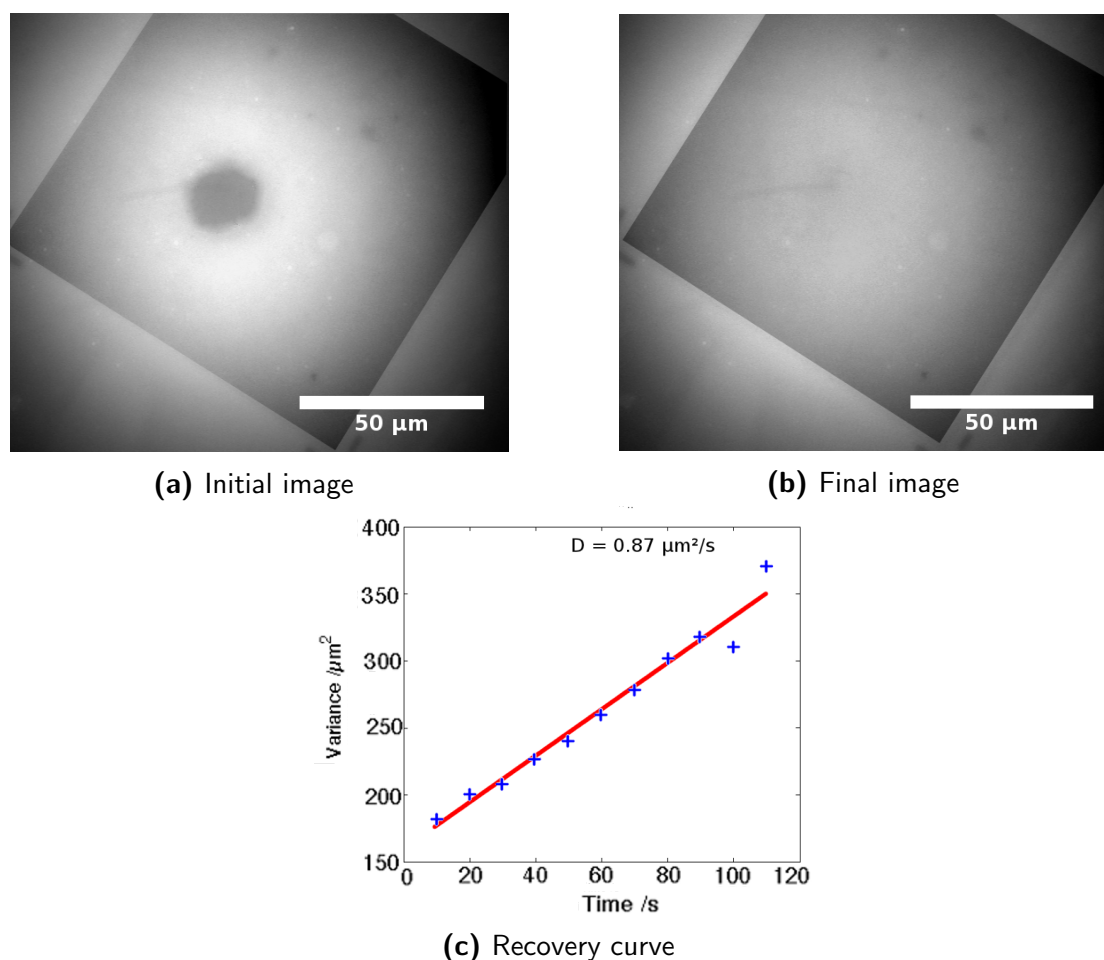


Figure 5.21: An SLB was formed on a nanodot pattern, the FRAP experiment showed good mobility of the lipids in the pattern. The recovery within the region of the pattern of the nanodots shows the mobility of the SLB is maintained despite the posts hindering full mobility. The diffusion coefficient is reduced to $0.9 \mu\text{m s}^{-1}$.

Raman spectra were taken using a 633 nm laser which is expected to excite the localised surface plasmons (LSPs) in the substrate (Walsh and Negro, 2013). The enhancement in the sample caused by the strong electric fields around the nanoposts is then used to obtain the spectra from the sample. Initial testing of the setup resulted in a weak enhancement but a signal from the bilayer. Two different structures, nanodots and nanobars which were 100 nm wide and 200 nm long, were used. The data is shown in figure 5.22 and shows a clear difference between the signal obtained from the silicon substrate without and with POPC and the regions with the nanopatterns.

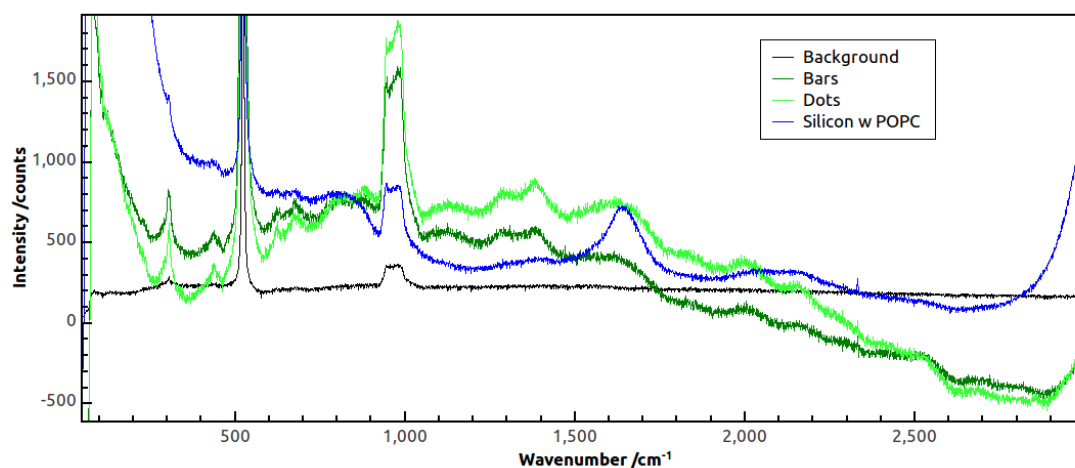


Figure 5.22: SERS data from a POPC SLB formed around gold nanoposts and nanobars on a silicon dioxide substrate. The sample used is shown in figures 5.20 and 5.21.

Component	Wavenumber	Vibration	Source
Silicon	303 cm ⁻¹		(Jorio et al., 2001)
	521 cm ⁻¹		
	963 cm ⁻¹		
Water	1640 cm ⁻¹		(Tian et al., 1994)
	3400 cm ⁻¹		
POPC	963 cm ⁻¹	C–C all trans chain	(Saint-Pierre Chazalet et al., 1994)
	1130 cm ⁻¹	C–C all trans chain	
	1300 cm ⁻¹	CH ₂ twist	
	1375 cm ⁻¹	C–O (partially broken)	

Table 5.1: Assignment of some of the bonds seen in the SERS spectrum.

As seen in table 5.1, the observed bands can be assigned to a combination of the signals expected from an SLB, a silicon substrate and the water layer above the SLB. The vibration observed at 1375 cm⁻¹ can be assigned to a partially broken bond, this is a bond where the association between the atoms is weaker and therefore the distance larger than normally expected. If the bond was not broken, the vibration would be expected to be at 1700 cm⁻¹.

The enhancement seen from the pattern is present but not very strong. To increase the signal, different sizes of nanodots were tested for their ability to generate surface enhancement. The spacing between the dots was kept constant and their diameter was varied between 100 nm and 200 nm. As seen in figure 5.23,

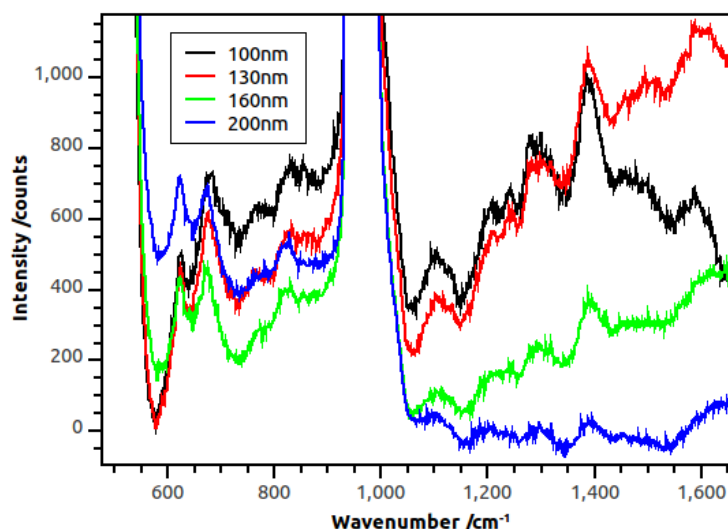


Figure 5.23: Raman spectra of nanodots surrounded by lipid bilayers with varying diameters of the nanodots. The SLB was formed using POPC vesicles.

Diameter (in nm)	1100 cm ⁻¹	1400 cm ⁻¹
100	2.9	6.1
130	2.33	3.4
160	1	1.8
200	1	1

Table 5.2: Relative peak height of the Raman peaks seen at 1100 cm⁻¹ and 1400 cm⁻¹ both columns were individually normalised to the peak obtained from nanodots with a diameter of 200 nm.

the signal to noise ratio increases as the size of the nanodots decrease in size. The increase in the enhancement can also be seen from table 5.2, where the peak height was normalised to the peaks taken from the 200 nm dots. Although the relative peak height varies between the two different peaks, the nanodots with a diameter of 100 nm have the biggest enhancement of the signal.

5.2.2 SERS using Nanoparticles

To further improve the enhancement generated from the nanostructures on the surface, the experimental set-up was changed. As discussed in section 2.8.2, the enhancement from a nanoparticle on a metal surface is generated in the plasmonic hot spot region which occurs between the nanoparticle and the

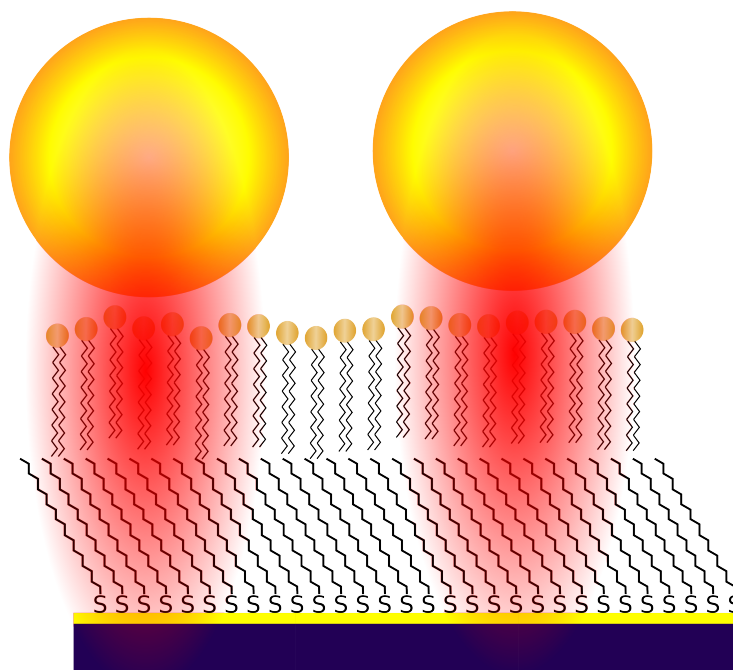


Figure 5.24: Schematic of the nanoparticle on a mirror arrangement with an HLM in the hot spot region.

surface (Eah et al., 2005). The system was realised by firstly depositing and 1-octadecanethiol (ODT) SAM on a freshly evaporated gold surface on a silicon wafer. Secondly, vesicles were injected into the flow cell and through fusion of the vesicles on the hydrophobic SAM surface an hybrid lipid membrane (HLM) of lipids consisting of 75 mol% POPC and 25 mol% DOTAP and the SAM was formed. Gold nanoparticles with a diameter of 80 nm were then added from solution. Since the nanoparticles have a citrate coating, the charge on the nanoparticles is negative, while the bilayer is positively charged. The electrostatic interaction between the nanoparticle and the bilayer were sufficient to obtain nanoparticles bound to the surface. A schematic of the set-up and the localisation of the plasmonic hot spot is shown in figure 5.24.

Since the plasmon resonance is very sensitive to the distance of the nanoparticle to its mirror image, the spectrum of the scattered light can also give information on the spacing of the nanoparticle and the surface. The dark field microscopy image in figure 5.25a shows that individual nanoparticles can be seen on the surface and scattering spectra were obtained for single nanoparti-

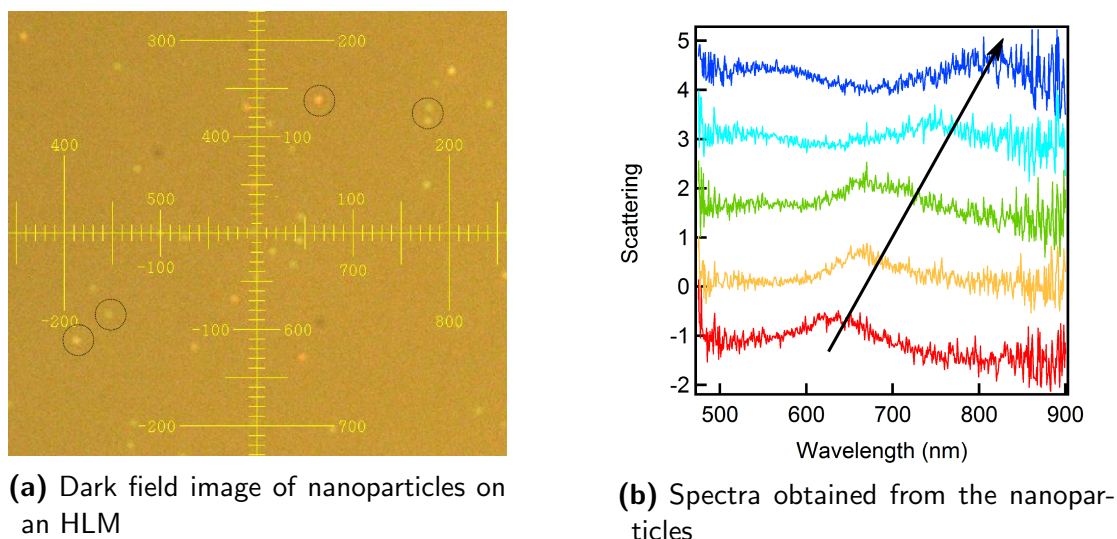


Figure 5.25: Dark field image of nanoparticles on an HLM and the scattering spectra obtained from the nanoparticles circled in the dark field image. The circled nanoparticles on the left correspond to the spectra shown on the right.

cles and are showing in figure 5.25b. It can be seen that the peak position varies for different nanoparticles. Assuming a refractive index of $n = 1.5$ between the nanoparticle and the surface, the resonance frequency for a gap of 10 nm is predicted as 660 nm and for a gap of 4 nm is 720 nm (Mock et al., 2003). Since the distance between the nanoparticle and its mirror image is double the distance of the nanoparticle to the surface, the distance expected for a nanoparticle on a bilayer to its mirror image is 10 nm and when the nanoparticle is on the SAM where there is a defect in the bilayer, the distance would be 4 nm. The predicted resonance frequencies for these distances can be seen in the green and cyan curve respectively in figure 5.25b. The other graphs could be due to nanoparticles being further away from the surface than 5 nm if they are not strongly bound to the surface.

The system improved by the nanoparticles was then used to obtain SERS spectra. As can be seen in figure 5.26, the signal obtained was significantly increased in this system compared to the previous results. This is attributed to the more localised plasmons which are now more focussed on the SLB compared to the previous system, where the nanodots have a height of 50 nm and the

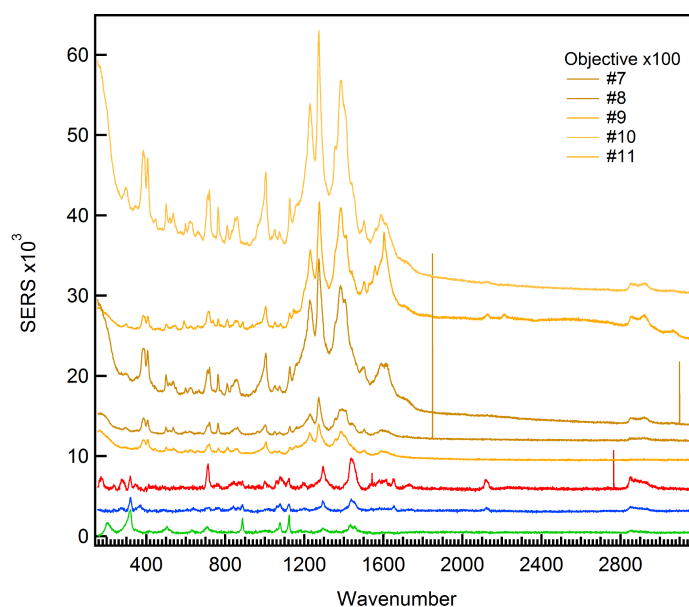


Figure 5.26: SERS spectra obtained from an HLM consisting of DOTAP and POPC from different nanoparticles on the HLM. The green, blue and red curve represent the bulk Raman spectra from ODT, POPC and DOTAP respectively.

plasmon is therefore on average 25 nm above the surface. The more localised and more focussed plasmon can be seen in the enhancement of the signal.

The yellow spectra shown in figure 5.26 are taken from different nanoparticles on the same sample. The spectra show that SERS is a very sensitive technique, which can result in the enhancement of different bonds in different conditions. Some of the peaks are very clear and pronounced in some spectra, while being much smaller in other spectra. When comparing the SERS spectra from the HLM with the bulk spectra from ODT (green), POPC (blue) and DOTAP (red), it can be seen that the obtained spectrum is the result from the combination of the three spectra. As typical with SERS not all of the vibrations seen in the bulk spectra are enhanced and not all of the vibrations which are seen are also seen in the bulk spectra (Kneipp et al., 1997; Weitz et al., 1983). The assignment of the highest peaks is shown in table 5.3.

To show the spectra obtained were mainly due to the HLM and not due to organic contamination, the experiments described above were carried out with deuterated lipids. Changing the C–H bonds to C–D bonds gives rise

Vibration	Wavenumber
ν C–N	720 cm^{-1}
ω CH ₂	762 cm^{-1}
ν choline	907 cm^{-1}
ν C–C	1003 cm^{-1}
ν C–C	1126 cm^{-1}
ν_{as} PO ₂ ⁻	1229 cm^{-1}
δ_{sym} CH ₃	1378 cm^{-1}
ν_{sym} CH ₂	2853 cm^{-1}
ν_{as} CH ₂	2923 cm^{-1}
ν_{as} CH ₃	2955 cm^{-1}

Table 5.3: Main Raman peaks seen in figure 5.26 and their assignment.

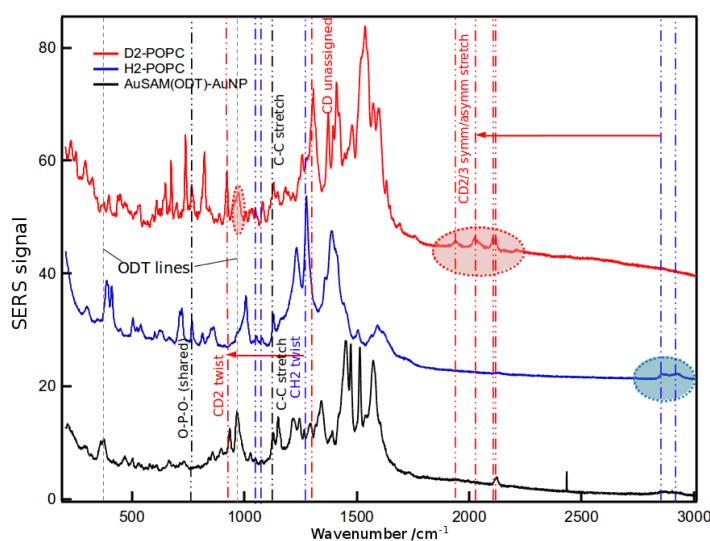


Figure 5.27: SERS spectra obtained from an HLM consisting of deuterated lipids. For comparison the spectra from the non-deuterated lipids and the SAM alone are also shown.

to significant changes in the Raman spectrum. The C–H vibrations seen in the region of 3000 cm^{-1} are shifted by around 1000 cm^{-1} to 2000 cm^{-1} while the vibrations observed by the C–C or O–P–O vibrations do not change their positions. The spectra obtained with assigned peaks can be seen in figure 5.27.

This method also has the ability to distinguish between different membrane components. When used with a membrane consisting of POPC, gramicidin and 1-palmitoyl-2-(10,12-tricosadiynoyl)-sn-glycero-3-phosphocholine (DiPC), the different membrane components can be identified individually in the spectra. Figure 5.28 shows the bulk spectra for the lipids POPC and DiPC and for the

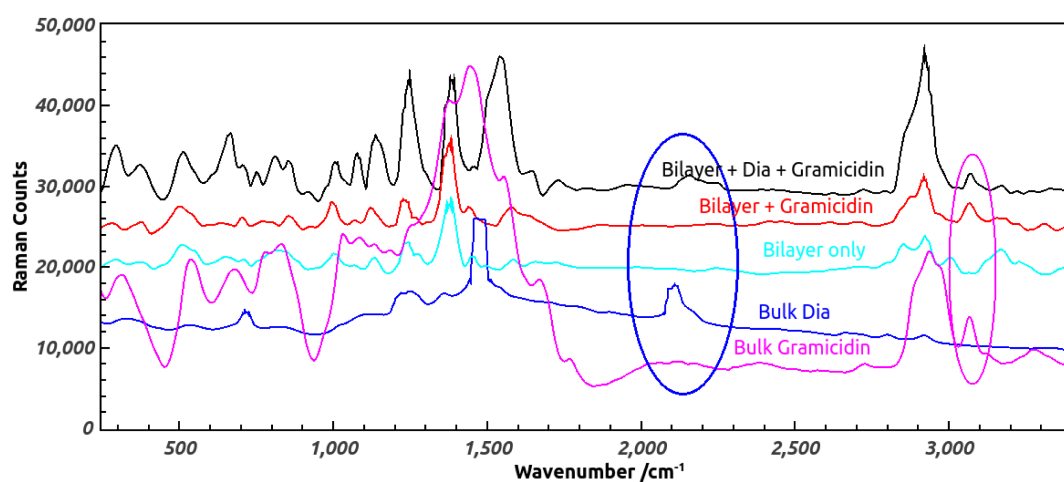


Figure 5.28: SERS spectra of HLMs containing different membrane components, gramicidin and DiPC. The bilayer was formed from POPC with 2 mol% DiPC. Gramicidin was added from solution after the formation of the SLB.

polypeptide gramicidin. In addition to that, it can be seen that upon the addition of either DiPC or gramicidin the peak in the fingerprint region for each of them appears. The peak around 2100 cm^{-1} occurs only upon the addition of DiPC while this region is free of any peaks otherwise. Gramicidin can be identified through the peak at 3100 cm^{-1} which is also unique to gramicidin and is not present in either the lipid or the DiPC spectrum.

5.2.3 Cyclic Voltammetry with Nanoparticles

An interesting observation was made, when gold nanoparticles of the same size as the ones used for the SERS experiments, were used for cyclic voltammetry (CV) experiments. The nanoparticles seemed to increase the oxidation and reduction peaks obtained from different samples significantly, as seen in figure 5.29. Here the CV curves obtained from SLBs containing of POPC and a mixture of POPC and ubiquinone Q10 (UQ) were compared. In all cases the addition of gold nanoparticles lead to a significant increase in the peaks and even added a second peak to the data. The nanoparticles seem to add extra electrode area to the SLB allowing for an increase in the oxidation and reduction peaks. In addition to that, the citrate coating of the nanoparticles itself is responsible for

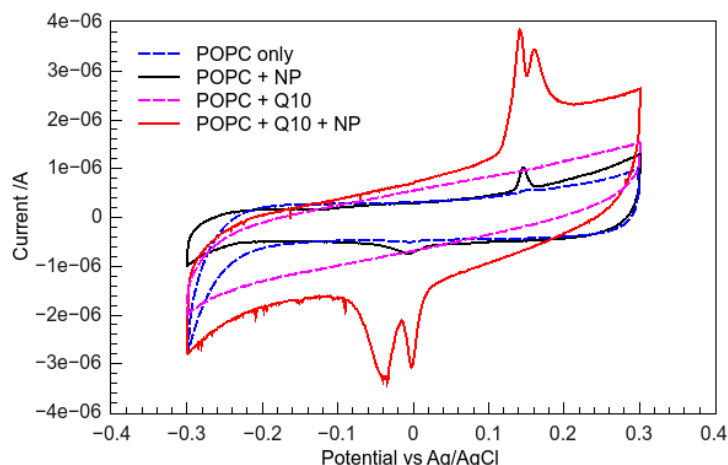


Figure 5.29: Nanoparticle enhanced CV experiments on bilayers and bilayers containing UQ taken at a scan speed of 25 mV s^{-1} . Despite an increase in the peak height upon the addition of gold nanoparticles, the UQ oxidation and reduction peaks cannot be seen.

one of the oxidation and reduction peaks. The potentials found here, agree well with potentials for the citrate coating given in the literature (Van Hoonacker and Englebienne, 2006).

As the nanoparticles significantly enhanced the reduction and oxidation peaks obtained from SLBs, the influence of the nanoparticles on the SLBs was investigated further. When the charged nanoparticles are on top of the SLB and a potential is applied, it is not clear what happens to the nanoparticle and the SLB. The different configurations possible are shown in figure 5.30. With the significant enhancement from the nanoparticles it would be possible that the bilayer is penetrated by the nanoparticle and is now either within the SLB or has removed the lipids partially, as shown in figure 5.30c and figure 5.30d.

To further understand the influence of an electric field applied to an SLB with nanoparticles attached, impedance spectra were taken at different time points. When the EIS spectrum was taken from the SLB with attached nanoparticles (NPs) before the CV data was taken (black data points in figure 5.31), the capacitance from the bilayer was below $1 \mu\text{F cm}^{-2}$, which is expected from a good quality SLB (Lin et al., 2012). The CV experiment conducted here was the

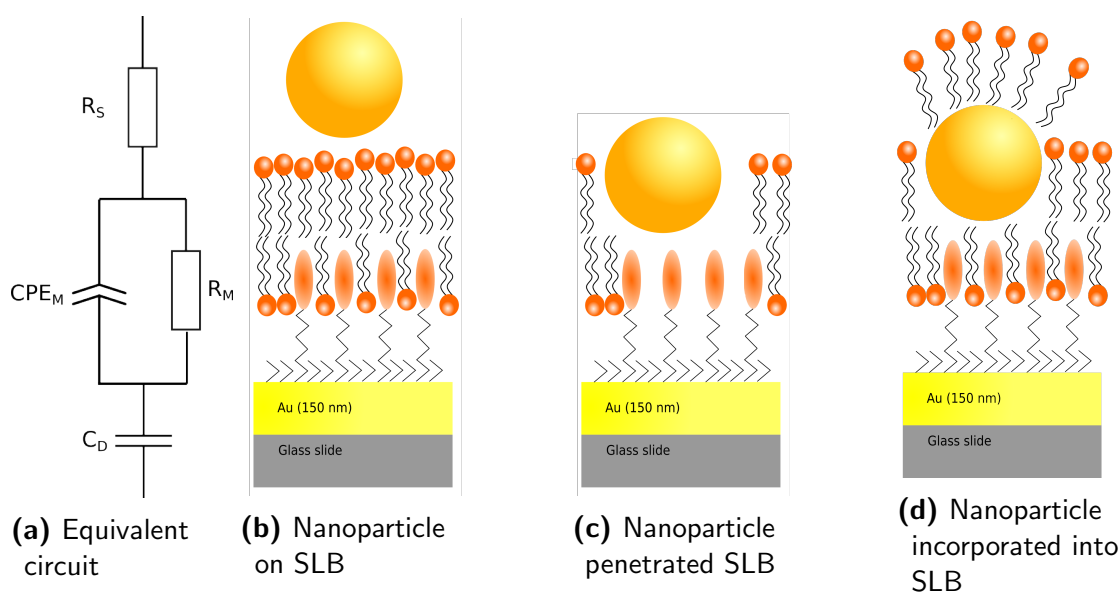


Figure 5.30: Equivalent circuit used for fits and three different configuration a nanoparticle can take on or in cholesterol tethered SLBs.

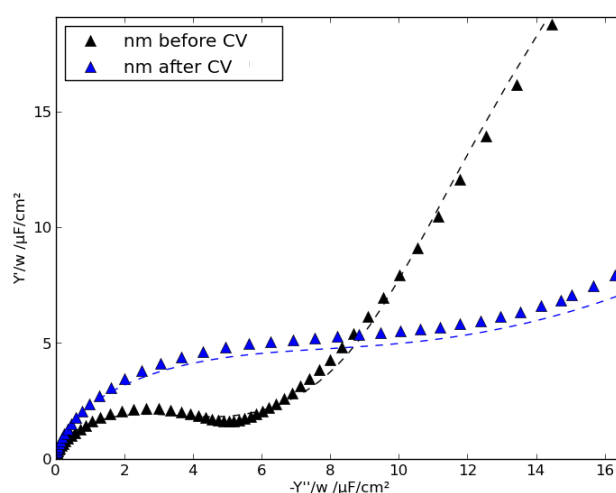


Figure 5.31: Impedance spectra of an HLM with 80 nm gold NPs attached to the surface before and after taking CV data. The electrode area was 0.8 cm^2 .

same as shown in figure 5.29, i.e. a scan from -0.3 V to 0.3 V scanned at a speed of 50 mV s^{-1} .

After the CV measurement has taken place, the EIS data obtained from the SLB has significantly changed. As can be seen in figure 5.31, the capacitance of the SLB has increased and the curve is much less similar to a full semi circle and more like a quarter circle (blue data points). This indicates not only a change

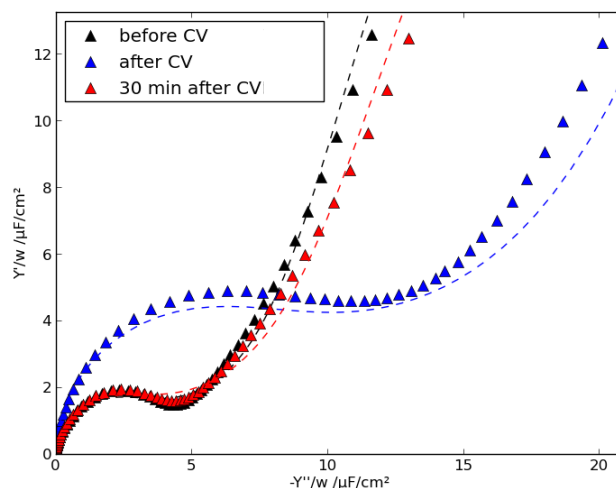


Figure 5.32: Impedance spectra of an SLB with 80 nm gold NPs attached to the surface before the CV measurements, 5 min after and 30 min after the CV measurements. The electrode area was 0.8 cm^2 .

to the SLB, but also a decrease in the quality of the capacitor. The decrease in quality is attributed to the NPs penetrating the SLB.

After the electric field is switched off, the NPs are no longer forced into the SLB and the lipids are also free to diffuse. Therefore, changes to the SLB can occur over time. To investigate the change in the bilayer over time, EIS spectra were taken before, 5 min and 30 min after the CV measurement. As can be seen from figure 5.32, the change in the properties of the SLB is reversing with time. The spectrum taken after 30 min is almost identical to the initial spectrum while the spectrum taken after 5 min shows the differences discussed before. This indicates that, although taking the CV influences the SLB and the NPs, the induced change is fully reversing and the configuration is the same as it has been initially, as shown in figure 5.30b. The results for the resistance R_{SLB} and capacitance C_{SLB} of the membrane are shown in table 5.4. It can be seen that there is a significant change in the capacitance of the membrane when the CV data has been taken while the resistance of the membrane remains within a 10 % variation of the initial measurement and is consistent with resistances obtained

	Q_{SLB}	R_{SLB}
Before CV	$0.62 \mu\text{F cm}^{-2}$	$240 \text{k}\Omega \text{cm}^{-2}$
5 min after CV	$1.69 \mu\text{F cm}^{-2}$	$260 \text{k}\Omega \text{cm}^{-2}$
30 min after CV	$0.59 \mu\text{F cm}^{-2}$	$280 \text{k}\Omega \text{cm}^{-2}$

Table 5.4: Resistances and capacitances obtained from the fits to the data shown in figure 5.31 and figure 5.32. The equivalent circuit used consisted of a serial circuit of a resistance for the solution, a capacitance for the interface between the surface and the solution and a constant phase element and a resistor in parallel to represent the membrane with potential defects, as shown in figure 5.30a.

in the literature (Naumann et al., 1999). The final capacitance 30 min after the CV procedure is almost identical to the initially recorded one.

5.3 Towards Light Harvesting Proteins in Lipid Bilayers

Different steps have been taken towards the incorporation of light harvesting proteins into SLBs. Here an overview of different experiments is presented.

5.3.1 Light Harvesting Systems

The choice of detergent can be very important when working with membrane proteins. The detergent can either ensure the membrane protein can become water soluble with the detergent molecules ensuring that the membrane domains of the protein are enclosed by detergent molecules or can change the properties of the membrane protein by denaturing the protein. The light harvesting complex IIs (LH2s) from *Rhodobacter sphaeroides* were produced in DDM containing buffer solution. The DDM solubilised the membrane proteins. The disadvantage of using DDM is its low critical micelle concentration (CMC). The low CMC makes methods involving rapid dilution of detergent for the formation of vesicles very difficult, as the dilution has to be to a very high degree. Therefore, it was investigated if octyle glucoside (OG) could be used as a detergent for LH2.

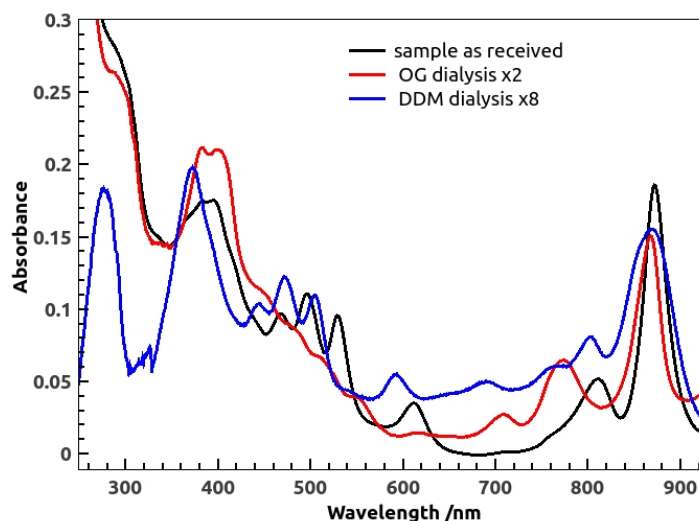


Figure 5.33: UV-Vis spectrum of LH2 in the DDM containing solution as received and after dialysis in different solutions containing either DDM or OG. The structural change in DDM buffer is reversed upon dialysis into an OG containing solution.

Despite OG having been used in combination with LH2 before, only membrane incorporation and organisation and not the functionality of LH2 was shown (Dewa et al., 2006).

In figure 5.33, it can be seen that after dialysis of the LH2 containing solution from a DDM buffer (black) to an OG containing buffer (red). The peak of the reaction centre (RC) at 800 nm has blue-shifted by around 40 nm, the triple peaks around 500 nm have also reduced and almost became invisible. This shows that the detergent can have a big influence on the protein structure and therefore on the protein function. The graph also shows that, when re-dialysing the sample into a DDM buffer (blue), the peaks move back to their original position. The changes due to the detergent have thus been reversed and the protein has changed its structure back to the original structure, showing that OG can be used as a detergent in combination with LH2 and that the structure might change when OG is introduced but that this change is reversible upon removal of OG. This removal of OG would also be the case when the protein is incorporated into an SLB when the formation of the SLB is completed.

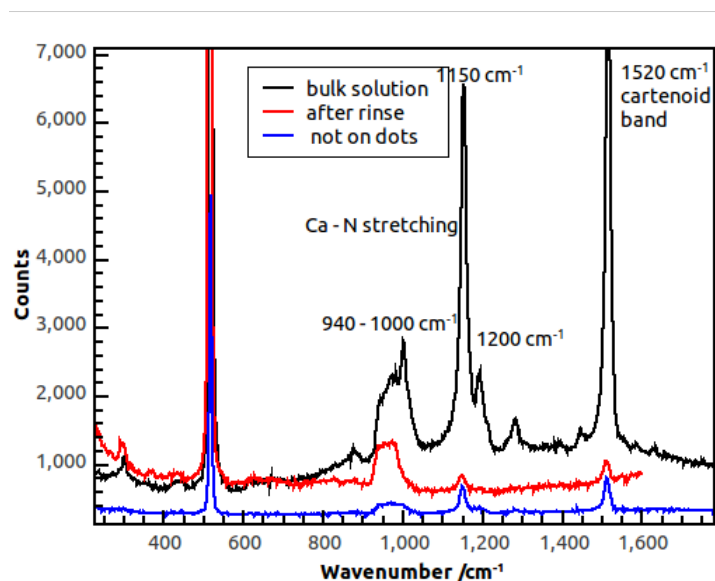


Figure 5.34: Raman spectra of the bulk vesicle solution containing vesicles from *Rhodobacter sphaeroides* and POPC, the surface region with nanodots and the surface without nanodots. The vesicle solution shows a Raman spectrum which can be assigned to the components of the light harvesting complex but the nanodots show no enhancement of the Raman signal over a region of the substrate without gold nanodots.

As samples containing the full vesicles of *Rhodobacter sphaeroides* with all the components of the light harvesting cycle could be able to form SLBs, especially when mixed with POPC vesicles (Dodd et al., 2008). Therefore, the natural membrane vesicles were mixed with 80 % by weight tip sonicated POPC vesicles and were incubated on a sample with nanodots with a diameter of 100 nm. When an SLB is formed, this should allow for the detection of the proteins using SERS from the nanodots.

As seen in figure 5.34, the bulk spectrum (black) of the solution containing the vesicle mixture clearly shows features of the membrane proteins involved in the light harvesting cycle. When the solution is then rinsed out to be able to measure the Raman spectrum from the surface only, most of these features disappear (red) and only the peaks which were the strongest initially are still seen. This indicates that the either surface enhancement from the nanoparticles is too weak to obtain scattering from the SLB or that the SLB has not formed. The latter is more likely since samples with the same geometry have produced

surface enhancement from SLBs formed from lipids only. In addition to that the signal obtained did not change when the spectrum was taken from bare silicon not from the region of the nanodots (blue). This indicates that the peaks obtained were from dilute vesicles still present in the solution or on the surface but not from an SLB on the surface.

Despite the SLB of full vesicles from the *Rhodobacter sphaeroides* membrane not forming, the incorporation of RCLH1 into SLBs could be achieved using rapid dilution of lipids and proteins dissolved in an OG solution (Stamouli et al., 2003). Using a YFP-tagged variant of the light harvesting proteins, fluorescence images showing the YFP in the membrane were recorded. The final concentration of the protein in the membrane was lower than expected but the yellow fluorescence of the YFP can still be seen in figure 5.35. The FRAP experiment carried out showed a diffusion coefficient of $0.35 \mu\text{m}^2 \text{s}^{-1}$. The lowered diffusion coefficient when comparing this result with FRAP experiments carried out without the light harvesting proteins indicates that the actual concentration of protein in the membrane is probably higher than seen from the fluorescence image, especially when comparing the 2 % by weight of the protein to the 0.5 mol% for the TxRed used in the SLB and the obtained fluorescence signal from each of them.

5.3.2 Cytochrome bc1

The incorporation of cytochrome bc1 into a membrane can be measured in different ways. Controlling the incorporation of the protein is easiest, when it is tagged with a marker. Here, two different labelled versions of cytochromes are discussed, one with a fluorescent marker and one with a gold bead attached to it.

Using gold beads as a marker for a proteins allows the protein to be seen in different imaging methods such as atomic force microscopy (AFM), electron microscopy (Cartron et al., 2014) or dark field microscopy. When the gold

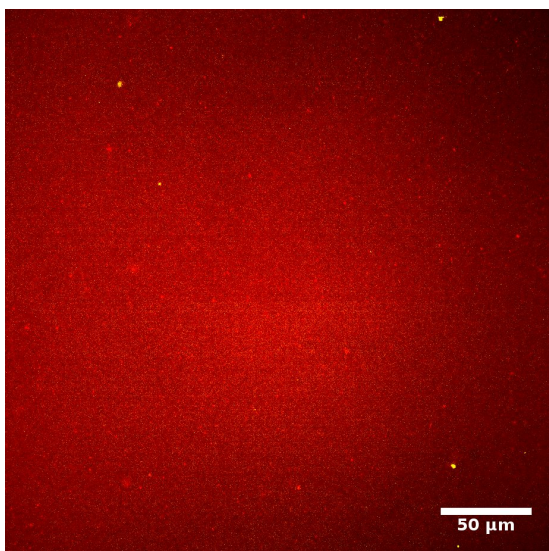


Figure 5.35: Overlay of two fluorescence images of a TxRed labelled SLB with YFP-tagged RCLH1 incorporated into the membrane. The red background shows the formation of an SLB while the yellow dots show potential regions with YFP-tagged light harvesting proteins.

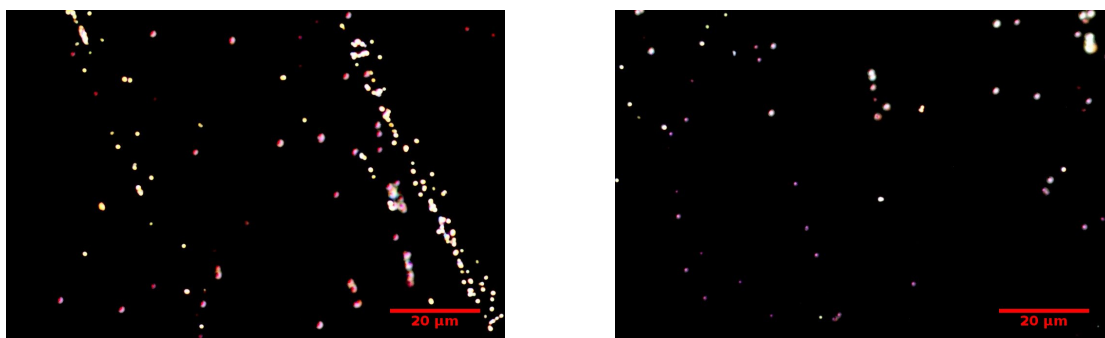


Figure 5.36: Dark field image of gold NPs with 5 nm diameter in solution. The different colours in the image can be attributed to different aggregate sizes and distances between aggregates gold nanoparticles resulting in different resonance frequencies.

nanoparticles are attached to the cytochrome bc1, the location of the cytochrome either in solution or in the membrane can be determined.

The cytochrome bc1 used in this case was labelled with 5 nm gold nanoparticles. To demonstrate the ability of visualising such small particles, which are much smaller than the diffraction limited resolution limit of an optical microscope, gold nanoparticles of the same size in solution were used initially. The NP solution was drop casted onto a glass cover slip and then observed through a dark field microscope.

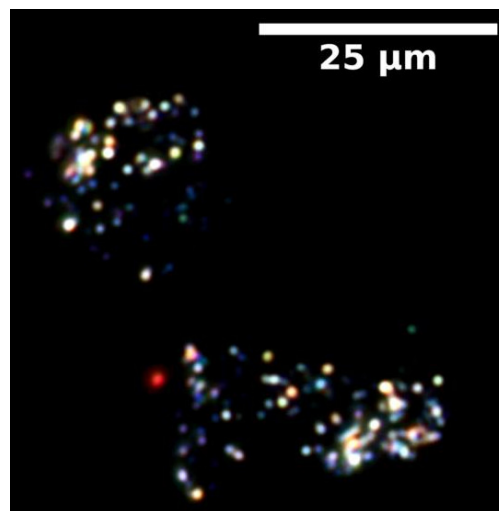


Figure 5.37: Cytochrome bc1 labelled with 5 nm gold NPs in solution as seen under a dark field microscope. The images suggest that the cytochrome forms clusters in the membrane.

As can be seen in figure 5.36, the NPs show up clearly. The different colours associated with them are due to either single NPs (red) or clusters of NPs (blue and yellow). The same experiment was then carried out with the solution containing cytochrome bc1 with gold NPs attached. As seen in figure 5.37, the gold NPs can also be seen clearly in this case. Compared to the gold NPs on their own, the colour of the scattered light has shifted from the red towards more blue and yellow clusters. This indicates that many of the particles, and therefore of the proteins, aggregate in small regions.

The incorporation of cytochrome bc1 into SLBs could also be shown using this method. The SLBs were formed using the detergent removal method, where lipids, detergent and proteins are mixed with detergent and the detergent is slowly washed out (Trépout et al., 2007). The dark field image of the incorporation of gold labelled cytochrome bc1 into an SLB is shown in figure 5.38a. The advantage of using the gold label is its clear visibility under the dark field microscope.

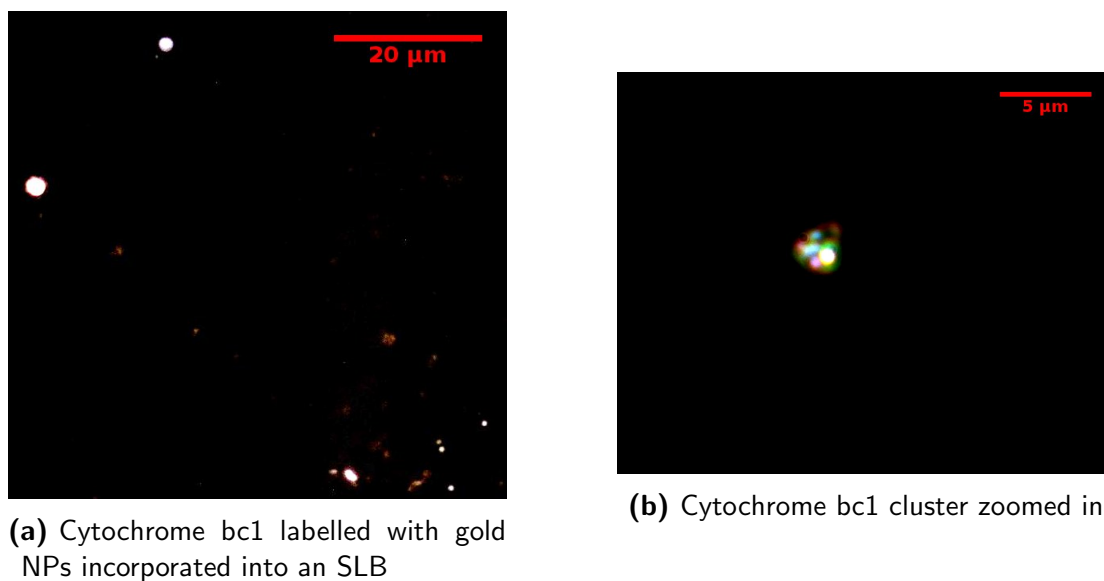


Figure 5.38: Cytochrome bc1 incorporated into SLBs observed by dark field microscopy. The images show clusters of the gold NPs indicating a clustering of the cytochrome in the SLB.

5.4 Conclusion

In conclusion, this section has shown that there are several methods to deposit SLBs on different polymer surfaces. The vesicle rupture method was not successful in all cases but alternatives to this method were found and presented. The formation of SLBs on polymers on conductive surfaces showed less promising results than the formation of them on glass. This is due to the bond between the glass and the polymer being stronger than the bond between the gold and the polymer which requires more gentle treatment.

Nanopatterned substrates were used as an initial method to obtain SERS spectra of SLBs on solid supports. The use of NPs and binding them via electrostatic interactions to the membrane was shown to improve the SERS signal obtained from the membrane. Different membrane components could be detected through their respective fingerprint regions. This presents a label-free method of detecting lipids and membrane components.

First steps towards the incorporation of light harvesting components into SLBs were also taken. The incorporation of light harvesting systems was shown using a fluorescently tagged proteins. Cytochrome bc1 with a gold label was

also incorporated into the membrane and was observed through dark field microscopy.

References

- Alswieleh, A. M., Cheng, N., Canton, I., Ustbas, B., Xue, X., Ladmiral, V., Xia, S., Ducker, R. E., El Zubir, O., Cartron, M. L., Hunter, C. N., Leggett, G. J., and Armes, S. P. (2014). Zwitterionic poly(amino acid methacrylate) brushes. *Journal of the American Chemical Society*, 136(26):9404–9413.
- Bayburt, T. H. (2003). Self-assembly of single integral membrane proteins into soluble nanoscale phospholipid bilayers. *Protein Science*, 12:2476–2481.
- Blanazs, A., Armes, S. P., and Ryan, A. J. (2009). Self-Assembled Block Copolymer Aggregates: From Micelles to Vesicles and their Biological Applications. *Macromolecular Rapid Communications*, 30(4-5):267–277.
- Cartron, M. L., Olsen, J. D., Sener, M., Jackson, P. J., Brindley, A. A., Qian, P., Dickman, M. J., Leggett, G. J., Schulten, K., and Neil Hunter, C. (2014). Integration of energy and electron transfer processes in the photosynthetic membrane of *Rhodobacter sphaeroides*. *Biochimica et Biophysica Acta - Bioenergetics*, 1837(10):1769–1780.
- Cremer, P. S. and Boxer, S. G. (1999). Formation and spreading of lipid bilayers on planar glass supports. *The Journal of Physical Chemistry B*, 103(13):2554–2559.
- Dewa, T., Sugiura, R., Suemori, Y., Sugimoto, M., Takeuchi, T., Hiro, A., Iida, K., Gardiner, A. T., Cogdell, R. J., and Nango, M. (2006). Lateral organization of a membrane protein in a supported binary lipid domain: direct observation of the organization of bacterial light-harvesting complex 2 by total internal reflection fluorescence microscopy. *Langmuir : the ACS journal of surfaces and colloids*, 22(12):5412–8.
- Dodd, C. E., Johnson, B. R. G., Jeuken, L. J. C., Bugg, T. D. H., Bushby, R. J., and Evans, S. D. (2008). Native *E. coli* inner membrane incorporation in solid-supported lipid bilayer membranes. *Biointerphases*, 3(2):FA59.
- Eah, S. K., Jaeger, H. M., Scherer, N. F., Wiederrecht, G. P., and Lin, X. M. (2005). Scattered light interference from a single metal nanoparticle and its mirror image. *Journal of Physical Chemistry B*, 109:11858–11861.
- Felidj, N., Aubard, J., Levi, G., Krenn, J., Salerno, M., Schider, G., Lamprecht, B., Leitner, A., and Aussenegg, F. (2002). Controlling the optical response of regular arrays of gold particles for surface-enhanced Raman scattering. *Physical Review B*, 65(7):1–9.

- Felidj, N., Aubard, J., Levi, G., Krenn, J. R., Hohenau, A., Schider, G., Leitner, A., and Aussenegg, F. R. (2003). Optimized surface-enhanced Raman scattering on gold nanoparticle arrays. *Applied Physics Letters*, 82(18):3095.
- Grand, J., de la Chapelle, M., Bijeon, J.-L., Adam, P.-M., Vial, a., and Royer, P. (2005). Role of localized surface plasmons in surface-enhanced Raman scattering of shape-controlled metallic particles in regular arrays. *Physical Review B*, 72(3):1–4.
- Hauser, H. (2000). Short-chain phospholipids as detergents. *Biochimica et biophysica acta*, 1508(1-2):164–81.
- Jackman, J. A., Zhao, Z., Zhdanov, V. P., Frank, C. W., and Cho, N.-j. (2014). Vesicle Adhesion and Rupture on Silicon Oxide: Influence of Freeze-Thaw Pretreatment. *Langmuir : the ACS journal of surfaces and colloids*, 30(8):2152–2160.
- Johnson, S. J., Bayerl, T. M., McDermott, D. C., Adam, G. W., Rennie, A. R., Thomas, R. K., and Sackmann, E. (1991). Structure of an adsorbed dimyristoylphosphatidylcholine bilayer measured with specular reflection of neutrons. *Biophysical journal*, 59(2):289–94.
- Jorio, A., Saito, R., Hafner, J., Lieber, C., Hunter, M., McClure, T., Dresselhaus, G., and Dresselhaus, M. (2001). Structural (n, m) Determination of Isolated Single-Wall Carbon Nanotubes by Resonant Raman Scattering. *Physical Review Letters*, 86(6):1118–1121.
- Karatekin, E. and Rothman, J. E. (2012). Fusion of single proteoliposomes with planar, cushioned bilayers in microfluidic flow cells. *Nature protocols*, 7(5):903–20.
- Kataoka-Hamai, C., Higuchi, M., Iwai, H., and Miyahara, Y. (2010). Detergent-mediated formation of polymer-supported phospholipid bilayers. *Langmuir : the ACS journal of surfaces and colloids*, 26(18):14600–5.
- Kneipp, K., Wang, Y., Kneipp, H., Perelman, L., Itzkan, I., Dasari, R., and Feld, M. (1997). Single Molecule Detection Using Surface-Enhanced Raman Scattering (SERS). *Physical Review Letters*, 78(9):1667–1670.
- Lin, J., Motylinski, J., Krauson, A. J., Wimley, W. C., Searson, P. C., and Hristova, K. (2012). Interactions of Membrane Active Peptides with Planar Supported Bilayers: An Impedance Spectroscopy Study. *Langmuir*, 28(14):6088–6096.
- Lomas, H., Du, J., Canton, I., Madsen, J., Warren, N., Armes, S. P., Lewis, A. L., and Battaglia, G. (2010). Efficient Encapsulation of Plasmid DNA in pH-Sensitive PMPC–PDPA Polymersomes: Study of the Effect of PDPA Block Length on Copolymer–DNA Binding Affinity. *Macromolecular Bioscience*, 10(5):513–530.
- Mennicke, U. and Salditt, T. (2002). Preparation of Solid-Supported Lipid Bilayers by Spin-Coating. *Langmuir*, 18(21):8172–8177.

- Min, Y., Pesika, N., Zasadzinski, J., and Israelachvili, J. (2010). Studies of bilayers and vesicle adsorption to solid substrates: development of a miniature streaming potential apparatus (SPA). *Langmuir : the ACS journal of surfaces and colloids*, 26(11):8684–9.
- Mock, J. J., Smith, D. R., and Schultz, S. (2003). Local Refractive Index Dependence of Plasmon Resonance Spectra from Individual Nanoparticles. *Nano Letters*, 3(4):485–491.
- Morigaki, K., Kimura, S., Okada, K., Kawasaki, T., and Kawasaki, K. (2012). Formation of substrate-supported membranes from mixtures of long- and short-chain phospholipids. *Langmuir : the ACS journal of surfaces and colloids*, 28(25):9649–55.
- Naumann, R., Schmidt, E. K., Jonczyk, a., Fendler, K., Kadenbach, B., Liebermann, T., Offenhäusser, a., and Knoll, W. (1999). The peptide-tethered lipid membrane as a biomimetic system to incorporate cytochrome c oxidase in a functionally active form. *Biosensors and Bioelectronics*, 14(7):651–662.
- Ogawa, M., Kosaka, N., Choyke, P. L., and Kobayashi, H. (2009). H-type dimer formation of fluorophores: a mechanism for activatable, in vivo optical molecular imaging. *ACS chemical biology*, 4(7):535–546.
- Ranaghan, M. J., Schwall, C. T., Alder, N. N., and Birge, R. R. (2011). Green proteorhodopsin reconstituted into nanoscale phospholipid bilayers (nanodiscs) as photoactive monomers. *Journal of the American Chemical Society*, 133(45):18318–27.
- Richter, R., Mukhopadhyay, A., and Brisson, A. (2003). Pathways of lipid vesicle deposition on solid surfaces: a combined QCM-D and AFM study. *Biophysical journal*, 85(5):3035–47.
- Saint-Pierre Chazalet, M., Masson, M., Bousquet, C., Bolbach, G., Ridente, Y., and Bolard, J. (1994). Surface-enhanced Raman scattering studies of lipid planar bilayers in water. *Thin solid films*, 244(1-2):852–856.
- Schönherr, H., Johnson, J. M., Lenz, P., Frank, C. W., and Boxer, S. G. (2004). Vesicle adsorption and lipid bilayer formation on glass studied by atomic force microscopy. *Langmuir : the ACS journal of surfaces and colloids*, 20(26):11600–6.
- Smith, E. A., Coym, J. W., Cowell, S. M., Tokimoto, T., Hrubby, V. J., Yamamura, H. I., and Wirth, M. J. (2005). Lipid bilayers on polyacrylamide brushes for inclusion of membrane proteins. *Langmuir : the ACS journal of surfaces and colloids*, 21(21):9644–50.
- Stamouli, A., Kafi, S., Klein, D. C. G., Oosterkamp, T. H., Frenken, J. W. M., Cogdell, R. J., and Aartsma, T. J. (2003). The ring structure and organization of light harvesting 2 complexes in a reconstituted lipid bilayer, resolved by atomic force microscopy. *Biophysical Journal*, 84(4):2483–2491.

- Tian, L., Chen, E., Gandra, N., Abbas, A., and Singamaneni, S. (2012). Gold Nanorods as Plasmonic Nanotransducers: Distance-dependent Refractive Index Sensitivity. *Langmuir : the ACS journal of surfaces and colloids*, 28(50):17435–17442.
- Tian, Z., Sigalaev, S., Zou, S., Mao, B., Funtikov, A., and Kazarinov, V. (1994). The observation of sers of water in a wide potential range from the Ag/NaClO₄ system. *Electrochimica acta*, 39(14):2195–2196.
- Trépout, S., Mornet, S., Benabdelhak, H., Ducruix, A., Brisson, A. R., and Lambert, O. (2007). Membrane protein selectively oriented on solid support and reconstituted into a lipid membrane. *Langmuir : the ACS journal of surfaces and colloids*, 23(5):2647–54.
- Van Hoonacker, A. and Englebienne, P. (2006). Revisiting silver nanoparticle chemical synthesis and stability by optical spectroscopy. *Current Nanoscience*, 2(4):359–371.
- Vequi-Suplicy, C. C., Riske, K. A., Knorr, R. L., and Dimova, R. (2010). Vesicles with charged domains. *Biochimica et biophysica acta*, 1798(7):1338–47.
- Walsh, G. F. and Negro, L. D. (2013). Engineering Plasmon-Enhanced Au Light Emission with Planar Arrays of Nanoparticles. *Nano letters*.
- Weitz, D. A., Garoff, S., Gersten, J. I., and Nitzan, A. (1983). The enhancement of Raman scattering, resonance Raman scattering, and fluorescence from molecules adsorbed on a rough silver surface. *The Journal of Chemical Physics*, 78(9):5324.
- Zhang, Y., Chen, Y., and Jin, G. (2010). PEGylated phospholipid membrane on polymer cushion and its interaction with cholesterol. *Langmuir : the ACS journal of surfaces and colloids*, 26(13):11140–4.

Chapter 6

Conclusions and Future Work

6.1 Concluding Remarks

This work investigated the diffusion in membranes, the use of electrophoresis in solid supported lipid bilayers (SLBs), and how surface enhanced Raman scattering (SERS) can be used in SLBs as a label free read-out method for different components of the membrane.

6.1.1 Diffusion in Membranes & Brownian Ratchets

Diffusion in membranes has been investigated and the influence of different factors on the observed diffusion coefficient has been shown. The variation in the diffusion coefficients in SLBs by different groups can be accounted for by some of these influencing factors. In addition to that, the influence of different dye molecules on the perceived diffusion coefficient has been investigated. In agreement with previous publications (Hughes et al., 2014), it could be shown that different dyes interact with membranes differently and therefore have not only different interaction factors, but also alter the measured diffusion coefficient significantly.

With the investigation of the efficiency of Brownian ratchets depending on the size and time parameters used on both the ratchet itself and the applied

electric field, the use of Brownian ratchets can be increased. This does not only include Brownian ratchets in SLBs (Motegi et al., 2012; van Oudenaarden and Boxer, 1999), but also Brownian ratchets used for other applications such as sorting of molecules (Bader et al., 1999; Huang et al., 2003; Roeling et al., 2011) or the transportation using flashing ratchets (Amengual et al., 2004; Lopez et al., 2008; Makhnovskii et al., 2004). With the increase in efficiency, these ratchets can be used more effectively and with smaller experimental times.

6.1.2 Novel Electrodes & Patterns

This work has shown that the classical system of wires in the buffer solution is a feasible but also improvable method of achieving electrophoresis in an SLB. With classical electrodes, the potentials required to achieve field strengths which allow significant transport rates are very high and are far beyond what would be achievable in lab-on-a-chip devices. To improve this situation, it has been shown that electrodes can be miniaturised and that their behaviour can still be predicted using finite element analysis (FEA), despite the electric field not being perfectly constant in the patterned region of the membrane.

Through the use of differently patterned electrodes, which, instead of having two, have four electrodes, one on each side of the pattern, it was shown that two dimensional fields can also be controlled and used for the transport and concentration of charged membrane components in regions of interest. This work has presented the use of four electrodes in conjunction with SLBs for the first time.

To improve on the time taken to concentrate membrane components in trapping patterns, instead of using the AC approach used in previous work (Cheetham et al., 2011), a pattern for SLBs was developed here which not only allows for the concentration of membrane components, as a simple barrier would as well, but also allows for significant trapping of the charged molecules in the trapping regions. The increased trapping times have been used to determine

binding coefficients of different molecules and deoxyribonucleic acid (DNA) in a quicker way than using previously used methods such as quartz crystal microbalance with dissipation (QCM-D) or surface plasmon resonance (SPR).

6.1.3 Polymer Supports

Different novel polymer supports for the formation of SLBs have been investigated. The formation of SLBs on both, poly(2-methacryloyloxyethyl phosphorylcholine) (PMPC) and poly(cysteine methacrylate) (PCysMA) has been shown using different methods. For PMPC methods involving short chain lipids, such as 1,2-hexanoyl-sn-glycero-3-phosphocholine (DHPC-C6), acting as detergent and heating the sample to 50 °C have been shown to be the most promising. Other methods like spin coating of lipids and subsequent gentle rehydration have also been shown to form SLBs but make the incorporation of membrane proteins into the SLB more complex. For PCysMA, the formation of SLBs from vesicle solutions is less complex and could be achieved using elevated temperatures and positively charged lipids without the need for detergent molecules or spin coating where solvents would be needed. Such polymers allow for the incorporation of membrane proteins into the SLB even for proteins with a large extramembranous domain. Denaturing or immobilisation, as it would occur for a glass support, is avoided using these polymers.

As the methods used involved elevated temperatures, the formation of SLBs on polymers on conductive supports was less successful. In these cases it could be shown, that the elevated temperatures remove the polymer off the surface and therefore are not suitable. Slow detergent removal has been shown to be a good candidate for an alternative SLB formation method on these surfaces.

6.1.4 Read out Methods

Although fluorescence microscopy can be used as a read-out method for different questions, it also has several disadvantages. When working with proteins, these

have to be fluorescently tagged, which is not always a straight-forward process. Fluorescently labelled lipids are easier to obtain; but with the fluorophore being of the same molecular weight as the lipids, the properties of the lipid can be significantly changed. Some of these changes were shown in section 3.1.3 and 3.2.2. The development of a label-free read-out method is therefore of importance for the investigation of membranes and membrane components.

Here, a method to interrogate hybrid lipid membranes (HLMs) on gold supports was developed. The combination of the conductive surface with the addition of gold nanoparticles which are close to the surface creates strong plasmonic hot-spots between the gold nanoparticle and the conductive surface. With the HLM being located between the surface and the nanoparticle, the HLM is in the region of the strong enhancement of the electric field. The spectra obtained from this set-up allowed for the distinction between different lipids and membrane components, such as gramicidin.

This method does not only allow for the determination of membrane components without damaging or influencing the membrane, as other methods like mass spectrometry would (Pace et al., 2013); it also gives high spatial resolution as the hot spots created by the nanoparticles are of the order of tens of nm in diameter. Such a resolution cannot be achieved by optical microscopy. In addition to the spatial resolution, the spectra are also taken on a very short time scale and therefore temporal resolution on a second time scale can be achieved (Taylor et al., 2014).

6.1.5 Light Harvesting Proteins

The investigation of polymer supports for the formation of SLBs has led to the development of several methods which allow for the formation of SLBs on different substrates, a neutral and a negatively charged polymer. The methods include the heating of the vesicles and the polymer; therefore it has to be ensured that the substrate is suitable for these conditions. The substrates support the

formation of high quality SLBs with diffusion coefficients of the same order as a solid substrate, such as glass (Blakeston et al., 2015).

6.2 Future Work

Brownian ratchets have been shown to be efficient transporters of membrane components. The ratchets can be optimised in different applications and in the future can be used in more complex devices. The optimisation of the transport structure for a given diffusion coefficient could also be used to separate membrane components by their respective diffusion coefficient as this relates to their electrophoretic mobility through the Einstein equation. Separation of membrane components has so far only been achieved based on the charge of the lipids (Groves et al., 1997) or in linear patterns (Pace et al., 2013).

More complex devices could include the initial concentration and subsequent transport of membrane components away from concentration regions. The combination of transport and concentration devices has so far not been shown in the literature. Patterned electrodes could also be used to have electric field based gates which allow for the initial concentration of membrane components against the gate, which can then be opened through switching off the external potential.

The potential of using two dimensional electric fields can also be explored further. The pattern shown in this work was a proof of concept and opens up the field to more complex patterns requiring the accurate control of the electric field applied to the membrane. The patterns can now become much more intricate as the control over the electric field has increased; with the ability to individually address each of the electrodes, the charged membrane components can also be moved in any direction for an arbitrary amount of time.

The DC approach for the concentration and trapping of charged molecules has proven its ability to be used in the determination of binding coefficients.

This is an important tool for further development of drugs acting on membrane components. The approach can be used for the development of new drug formulations and has the ability to cut down on the cost of research and development of new drug molecules.

Polymer supports in future can be used in variety of ways. It has been shown that PMPC can be used as a support for SLBs under certain conditions, while under different conditions it stops bilayer formation very well. It can therefore be used as a method of patterning SLBs when the conditions are chosen such that an SLB forms on the remaining substrate but not on the SLB. In addition to that, PMPC can also be used as a neutral, polymeric support for SLBs, when the conditions for bilayer formation are met.

The use of SERS as an *in-situ*, label-free read-out method for membrane components can lead to the development of easier ways of detecting membrane components. The combination of the work presented here with HLMs and cyclic voltammetry in future can be combined to detect oxidised and reduced states of membrane components such as ubiquinone Q10 (UQ). With the possibility of time resolved SERS the natural turn over rates of reduced to oxidised states and vice-versa can be observed in a label-free and direct way. The change in the Raman spectrum from benzoquinone to hydroquinone can be observed in the bulk spectrum and could therefore also be observed in SERS spectra of a membrane.

After gold labelled cytochrome bc1 has been incorporated into an SLB this method can be explored further. The combination of SERS with the incorporation of gold labelled proteins could be used for the detection of the proteins in the membrane. In addition to that, the local lipid environment of the protein in the membrane could also be investigated.

References

- Amengual, P., Allison, A., Toral, R., and Abbott, D. (2004). Discrete-time Ratchets, the Fokker–Planck Equation and Parrondo’s Paradox. *Proceedings of the Royal Society of London. Series A: Mathematical, Physical and Engineering Sciences*, 460(2048):2269–2284.
- Bader, J. S., Hammond, R. W., Henck, S. a., Deem, M. W., McDermott, G. a., Bustillo, J. M., Simpson, J. W., Mulhern, G. T., and Rothberg, J. M. (1999). DNA transport by a micromachined Brownian ratchet device. *Proceedings of the National Academy of Sciences of the United States of America*, 96(23):13165–9.
- Blakeston, A. C., Alswieleh, A. M., Heath, G. R., Roth, J. S., Bao, P., Cheng, N., Armes, S. P., Leggett, G. J., Bushby, R. J., and Evans, S. D. (2015). New Poly(amino acid methacrylate) Brush Supports the Formation of Well-Defined Lipid Membranes. *Langmuir*.
- Cheetham, M. R., Bramble, J. P., McMillan, D. G. G., Krzeminski, L., Han, X., Johnson, B. R. G., Bushby, R. J., Olmsted, P. D., Jeuken, L. J. C., Marritt, S. J., Butt, J. N., and Evans, S. D. (2011). Concentrating Membrane Proteins Using Asymmetric Traps and AC Electric Fields. *Journal of the American Chemical Society*, 133(17):6521–4.
- Groves, J. T., Boxer, S. G., and McConnell, H. M. (1997). Electric field-induced reorganization of two-component supported bilayer membranes. *Proceedings of the National Academy of Sciences of the United States of America*, 94(25):13390–5.
- Huang, L. R., Cox, E. C., Austin, R. H., and Sturm, J. C. (2003). Tilted Brownian Ratchet for DNA Analysis. *Analytical Chemistry*, 75(24):6963–6967.
- Hughes, L. D., Rawle, R. J., and Boxer, S. G. (2014). Choose Your Label Wisely: Water-Soluble Fluorophores Often Interact with Lipid Bilayers. *PLoS ONE*, 9(2):e87649.
- Lopez, B. J., Kuwada, N. J., Craig, E. M., Long, B. R., and Linke, H. (2008). Realization of a Feedback Controlled Flashing Ratchet. *Physical Review Letters*, 101(22):220601.
- Makhnovskii, Y. A., Rozenbaum, V. M., Yang, D. Y., Lin, S. H., and Tsong, T. Y. (2004). Flashing Ratchet Model with High Efficiency. *Physical Review E*, 69(2):21102.
- Motegi, T., Nabika, H., and Murakoshi, K. (2012). Enhanced Brownian Ratchet Molecular Separation Using a Self-Spreading Lipid Bilayer. *Langmuir : the ACS journal of surfaces and colloids*.

- Pace, H. P., Sherrod, S. D., Monson, C. F., Russell, D. H., and Cremer, P. S. (2013). Coupling supported lipid bilayer electrophoresis with matrix-assisted laser desorption/ionization-mass spectrometry imaging. *Analytical chemistry*, 85(12):6047–52.
- Roeling, E. M., Germs, W. C., Smalbrugge, B., Geluk, E. J., de Vries, T., Janssen, R. A. J., and Kemerink, M. (2011). Organic electronic ratchets doing work. *Nat Mater*, 10(1):51–55.
- Taylor, R. W., Benz, F., Sigle, D. O., Bowman, R. W., Bao, P., Roth, J. S., Heath, G. R., Evans, S. D., and Baumberg, J. J. (2014). Watching individual molecules flex within lipid membranes using SERS. *Sci. Rep.*, 4.
- van Oudenaarden, A. and Boxer, S. G. (1999). Brownian Ratchets: Molecular Separations in Lipid Bilayers Supported on Patterned Arrays. *Science*, 285(5430):1046–1048.